THE FATIGUE PROPERTIES OF PRESSURE DIECAST ZINC - ALUMINIUM BASED ALLOYS

KAMEEL SAWALHA

Doctor of Philosophy

THE UNIVERSITY OF ASTON IN BIRMINGHAM
May 1991

THE UNIVERSITY OF ASTON IN BIRMINGHAM

THE FATIGUE PROPERTIES OF PRESSURE DIECAST ZINC - ALUMINIUM BASED ALLOYS

KAMEEL SAWALHA Ph.D. 1991

THESIS SUMMARY

The fatigue behaviour of the cold chamber pressure-die-cast alloys: Mazak3, ZA8, ZA27, M3K, ZA8K, ZA27K, K1, K2 and K3 was investigated at temperature of 20 °C. The alloys M3K, ZA8K and ZA27K were also examined at temperatures of 50 and 100 °C. The ratio between fatigue strength and tensile strength was established at 20 °C at 10^7 cycles. The fatigue life prediction of the alloys M3K, ZA8K and ZA27K was formulated at 20, 50 and 100 °C. The prediction formulae were found to be reasonably accurate. All of the experimental alloys were heterogeneous and contained large but varying amounts of pores. These pores were a major contribution and dominated the alloys fatigue failure. Their effect, however, on tensile failure was negligible. The ZA27K posessed the highest tensile strength but the lowest fatigue strength. The relationship between the fracture topography and the microstructure was also determined by the use of a mixed signal of a secondary electron and a back-scattered electron on the SEM. The tensile strength of the experimental alloys was directly proportional to the aluminium content within the alloys. The effect of copper content was also investigated within the alloys K1, K2, ZA8K and K3 which contained 0%, 0.5%, 1.0% and 2.0% respectively. It was determined that the fatigue and tensile strengths improved with higher copper contents. Upon ageing the alloys Mazak3, ZA8 and ZA27 at an ambient temperature for 5 years, copper was also found to influence and maintain the metastable Zn-Al (α'_m)phase. The copper free Mazak3 upon ageing lost this metastable phase. The 1.0% copper ZA8 alloy had lost almost 50% of its metastable phase. Finally the 2.0% copper ZA27 had merely lost 10% of its metastable phase. The cph zinc contained a limited number of slip systems, therefore twinning deformation was unavoidable in both fatigue and tensile testing.

Key words: Fatigue, Metallography, Fractography, Pressure Die-casting, Zinc-Aluminium Alloys.

DEDICATION

To my mother Nijmeh and to my childhood friend Awni Sawalha, may his beloved soul rest in peace.

ACKNOWLEDGEMENTS

I am indebted to my supervisor Dr.Sam Murphy, not only for his expert guidance and continual encouragement, but also for his financial support throughout my research. I thank him.

I wish to thank the academic and technical staff of the Mechanical and Production Engineering Department of Aston University, for advice and active help. In particular my thanks are due to the members of the technical staf: Messrs. D.Farmer, J.Foden, R.Howell, M.J.Scattergood, J.Jeff, A.G.Evitts and P.A.Pizer.

I also wish to thank my family, especially my brothers Facker and Hazim Sawalha for their support and encouragement.

Particular thanks are due to my colleages Dr.M.Durman, Mr.R.Balanza, Mr.Y.Sahin and Mr.S.Taibi.and Miss F.Carter for thir good company, fruitful discussions and willing assistance on many occasions during my time at Aston.

Last, but not least, I am grateful to my wife Helen for her valuable support and understanding throughout the period of research, without whom this work would not have been possible.

LISTS OF CONTENTS

LIST OF TABLES

LIST OF FIGURES

CHAPTER 1

1.0 INTRODUCTION

In the industrial world today zinc aluminium based alloys are considered to be of the utmost importance. Zinc aluminium die cast components can be seen in a multitude of applications ranging from the very simple to the very complex. These alloys possess numerous advantages to the manufacturer; mainly a low melting point, high strength, corrosion resistance, and above all excellent castability. Indeed the fluidity of the zinc alloys is very high and this important property assures that with correct die design there is almost no limit to the complexity of shape or intricacy of surface detail which can be faithfully reproduced in castings with a full degree of soundness. Most research to date has concentrated on the casting of these alloys; the mechanical properties and structure/properties relationships have recieved very little attention. Surprisingly, little or no research has been carried out on their fatigue properties. It is important to study the fatigue properties of zinc-aluminum alloys in order to enable designers to design against fatigue. The past has demonstrated how fatigue failure can give rise to unfortunate situations and even disasters. Furthermore, with increasing dependance today upon modes of transport, machinery and structural design, it is vital to ensure that the risk of fatigue failure is reduced, or ideally, eliminated. This investigation has focused upon the structures and properties of zinc-aluminum alloys with an emphasis on their fatigue properties. Ultimately, this research may be useful in helping to develop better fatigue-resisting zinc-aluminum alloys.

CHAPTER 2

2.0 Development of Zinc-Aluminium Die-Casting Alloys.

Zinc diecasting became recognised in 1929 as a reliable manufacturing method. Today this method is widely used in industry. Before 1929 all attempts at zinc diecasting failed. These castings appeared at first to be satisfactory, but in many cases, rapid deterioration set in after a few months of service and the results were disasterous. The history of the present zinc diecasting alloys and the struggle to prove their suitability was observed and recorded by Evans(1). The cause of failure in these early alloys was traced by Brauer and Price(2). They discovered that the failure was due to intercrystalline corrosion caused by the presence of impurities such as lead, tin and cadmium. Consequently, Brauer and Price(2) stressed the use of a high grade zinc as a basis for the die casting alloys. The highest grade of zinc available commercially had a purity little above 99.90% and contained about 0.05% lead and 0.02% cadmium.When 99.99% pure zinc became commercially available a new alloy was put forward.This alloy contained 3.5-4.3% Al, up to 3.5% Cu and 0.03-0.08% Mg (Zamak2) and the danger of intercrystalline corrosion had been eliminated .The presence of copper in this alloy bestowed strength and helped to restrain intercrystalline corrosion. Later, the alloy suffered from ageing changes resulting in the loss of strength and dimensional changes. Copper was found to be the cause of the ageing problems. In the year 1930 a new copper-free alloy was introduced called Zamak 3.This alloy contained 4% Al and 0.04% Mg .Copper was no longer needed to prevent intercrystalline corrosion and the alloy offered more reproducibility with respect to mechanical properties and dimensional stability. Another very important commercial alloy was introduced.This alloy compromised between the initially stronger and harder Zamak 2 and the more stable Zamak 3.The alloy contained 1% Cu, 4% Al and 0.03% Mg and was named Zamak 5. Of these afore-mentioned alloys (3), Zamak 2 has now lost its popularity and only Zamak 3 and Zamak 5 alloys are of importance today. It was in 1942 when the British

Standards Institution produced a specification (B.S.1004) covering Mazak 3 and Mazak 5 (Alloys A & B). Alloys 3 and 5 have now been used for decades in a multitude of engineering applications.They show a unique combination of properties which permits the rapid economic casting of strong, durable, accurate parts. The advantages of Alloy 3 and 5 over other die casting materials (e.g Aluminium and Magnesium alloys) lie in their castability, their strength and their durability.This means that they require less finishing, that is the dimensions can be held to lower tolerances, and that the die life for zinc die castings far exceeds that of other die casting materials. Furthermore, their production rate is much higher (4).

Table 1 (5,6) shows the nominal compositions of these alloys. Their properties and performance are excellent,with one exception ; resistance to deformation (creep) in applications involving sustained load at temperatures above 100 °C(7). The International Lead Zinc Research Organization, ILZRO(4) concentrated their research upon the development of a pressure die casting alloy that would have high creep resistance, without sacrificing the other excellent properties of Alloy 3 and 5. In the mid-1960s, ILZRO developed an alloy (ILZRO 14) which was then further developed into a superior alloy (ILZRO 16), the composition of which is shown in Table 1. In terms of creep resistance, ILZRO 14 and 16 are superior(8) to the alloys 3 and 5, due to their alloying constituents of Ti and Cr. These elements with high melting points form a fine eutectic intergrowth of intermetallic $TiZn_{15}$ compound particles with zinc (9-11). The presence of such particles created an effective barrier to grain growth and increased the structural stability and creep resistance by eliminating substantial numbers of high energy, mobile grain boundaries (10,11). The room temperature mechanical properties of alloys ILZRO 14 and 16 are inferior to those of Mazak 3 and 5 (4,8) and their low aluminum contents only allow them to be cast by means of cold chamber die casting techniques. The reason for adopting such techniques is that, unlike alloys 3 and 5 (which are cast in a hot chamber die casting machine), ILZRO 14 &16,with their low aluminum contents, would slowly dissolve iron, if left in contact with the steel plunger sleeve and cast iron gooseneck

Alloy	Zn %	Al %	Cu %	Mg %	Ti %	Cr %
Alloy 3	Balance	3.9-4.3	---	0.04-0.06	---	---
Alloy 5	////	3.9-4.3	0.75-1.25	0.04-0.06	---	---
ILZR0.16	////	0.01-0.04	1.0-1.5	0.02	0.15-0.25	0.1-0.2
ZA.8	////	8.0-8.8	0.8-1.3	0.015-0.03	---	---
ZA.12	////	10.5-11.5	0.5-1.25	0.015-0.03	---	---
ZA.27	////	25.0-28.0	2.0-2.5	0.01-0.02	---	---

Table 1 : Chemical Composition of Commercial Pressure Die-cast Alloys(14).

of a hot chamber machine, and continuously immersed in molten zinc in the furnace.In a cold chamber machine, the furnace pot holding the molten metal is not an integral part of the machine. This drawback to ILZRO 14 & 16 is the reason why they are not widely used.

In 1962(12) a new alloy ILZRO 12 was developed. This alloy was introduced as a high strength alloy and contained 12% Al. The alloy was then modified to improve its non-sparking properties by reducing the Al content to 11%. The Noranda corporation(13) then continued the development of further new alloys for ILZRO and in the late 1970s introduced ZA8 and ZA27. These new alloys, along with ZA12, offer exceptional high strength and versatility. They can be made into components which can withstand high stress.Previously, such components were made from iron , aluminum or brass castings.The suitability of ZA8 and ZA12 for pressing and fabricating and their non-sparking properties, make them suitable for applications in hazardous environments such as coal mining and petroleum plants. Table 1(14) shows the compositional ranges of these alloys according to the ASTM and the B669-82 ingot specification. Table 2 shows the mechanical and physical properties of these new alloys in comparison with brass, aluminum and cast iron.

Although these new alloys were first introduced as sand and gravity cast alloys, they were also produced by the cold-chamber pressure diecasting process. In fact the properties of these alloys were found to be at their best when they were produced by the pressure die casting technique later it was found that the low melting point and the low aluminum content of alloy ZA8 allowed it to be produced by the conventional hot chamber die casting technique thus greatly impurity its commercial acceptance(14,15).

Within the new family of ZA alloys, ZA27 possesses the highest strength and hardness, followed by ZA12 and ZA8 respectively (Table 2). Table 2 also reveals that the tensile strength of ZA27 is not significantly affected by the casting method, but in the case of ZA8 and ZA12 it appears that their tensile strength and hardness are higher when produced by pressure die-casting.There is a 50% improvement in the

Properties at 20°C	ZA.8			ZA.12			ZA.27			Zinc (BS 1004)		Brass	Aluminium	Cast Iron	
	Sand Cast	Gravity Cast	Pressure Diecast	Sand Cast	Gravity Cast	Pressure Diecast	Sand Cast	Gravity Cast	Pressure Diecast	M.3	M.5	BS1004 SCB3	LM6M	Blackheart Malleable	Grey
Tensile Strength (MPa)	248-276	221-255	365-386	275-317	310-345	392-414	400-440	424	407-441	283	324	185-240	160-185	290-345	160-345
Yield Strength 0.2% offset (MPa)	—	207	286-294	207	214	312-328	365	—	363-378	195*	—	—	—	—	—
Elongation (%)	1-2	1-2	6-10	1-2	1-2	4-7	3-6	1	1	15	9	15-30	5-7	6-12	<0.5
Hardness (BHN)	82-89	85-90	99-107	90-110	85-95	95-105	110-120	110-120	116-122	83	92	45-65	55-60	110-149	200-250
Modulus of Elasticity (GPa)	—	85	90*	83	—	—	75	—	76*	83*	—	83	71	169	75-145

Table 2 Typical mechanical properties of the commercial zinc-aluminium alloys and other engineering materials

tensile properties of the pressure die cast ZA8 and ZA12, compared with the gravity cast ZA8 and ZA12. This improvement is due to a microstructural refinement, resulting from the rapid cooling rate characteristics of the diecasting process (14).

Murphy, Hill and Durman (16) have investigated the effect of temperatures in the range 20 to 260°C on the tensile properties of pressure-diecast Alloy 3, ZA8 and ZA27, as shown in Figure 1, 2 and 3 .

Figures 1 and 2 show that the ultimate tensile strength and the proof stress of these alloys decreased with an increase in temperature.The rate of decrease was found to be proportional to the aluminum content. At 160 °C and 165 °C, the properties of the alloys were virtually equal. Figure 3 shows the elongation properties of these alloys with different temperatures. The rate of increase in the elongation of ZA27 alloy was very slow below 100 °C but at higher temperatures, the rate of increase exhibited the expected characteristics of the superplasticity of the alloy (ZA27).

Alloy 3 exhibited a different behaviour to the ZA27.There was a rapid initial rise in elongation, but this increase peaked between 150-200 °C and decreased thereafter. ZA8's elongation behaviour exhibited an elongation range between those of ZA27 and MAZAK 3. It elongated in a very similar manner to that of ZA27 up to a temperature of 150 °C, and then peaked at about 200 °C. Then it decreased in a similar manner to that of Mazak 3.

Loong(17) carried out tensile tests on Mazak 3, Mazak 5, ZA8, ZA12 and ZA27.His results,referring to alloys Mazak 3, ZA8 and ZA27, match those of Murphy, Hill and Durman. In the case of Mazak 5 and ZA12, Loong found that their tensile strengths lie between those of Mazak 3 and ZA8 and ZA8 and ZA27 respectively, as expected.The elongation behaviour of ZA12 was similar to that of ZA8. On the other hand, the elongation behaviour of Mazak 5 was similar to that of ZA27.

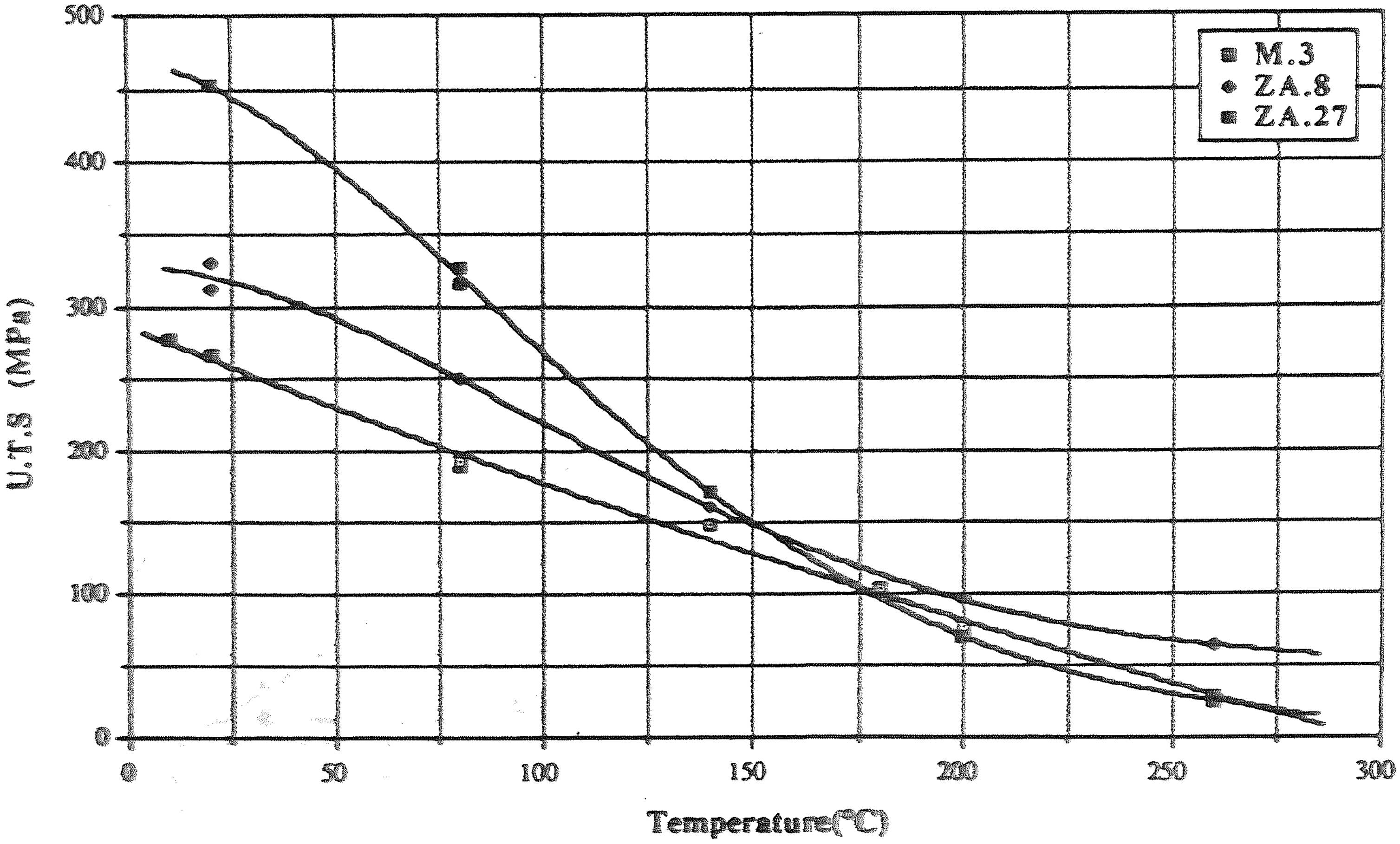

Figure 1 Variation of the U.T.S of the Alloys Mazak.3, ZA8 and ZA27 With Temperature.

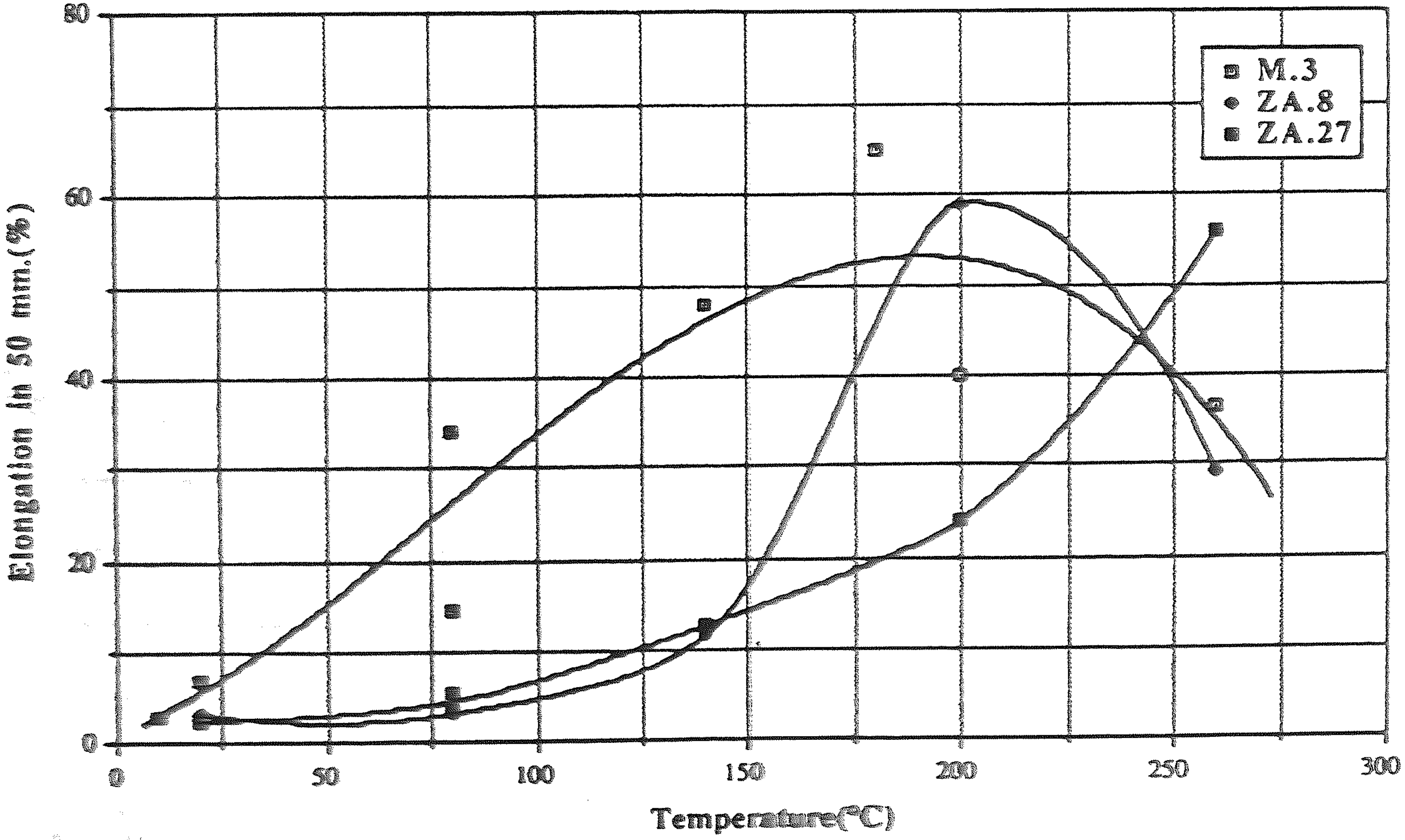

Figure 2 Variation of the 0.2% Proof Stress of the Alloys Mazak 3, ZA.8 and ZA27 With Temperature.

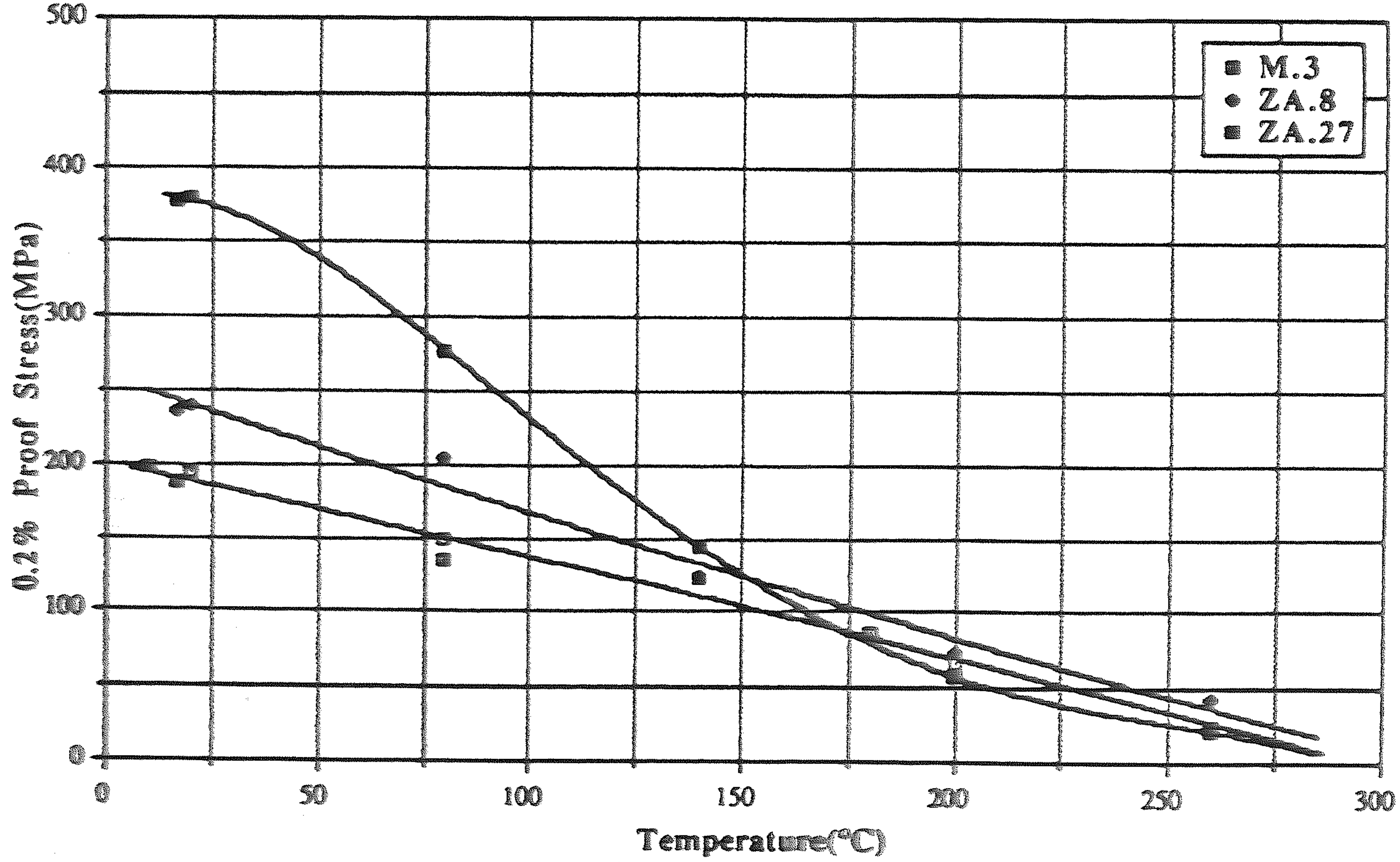

Figure 3 Variation of the % Elongation of the Alloys Mazak.3, ZA.8 and ZA27 With Temperature.

2.2 The Effect of Copper & Magnesium additions to the Zn-Al Alloys

Investigations have been carried out on the effect of Mg and Cu as alloying elements on the Zn-Al alloys.Investigators such as Youdelis & Dallin(18) have reported that magnesium and copper of 0.25% and 3.0% respectively alloyed with zinc containing 30 - 50% Al, can decrease the rate of decomposition of the high temperature phases, therefore affecting the mechanical properties of the zinc alloy after solution heat treatment. They reported a significant increase in strength and hardness, but the alloy suffered a decrease in ductility. The work of Youdelis and Dallin was assisted by a high temperature X-ray diffraction technique to study the decomposition rates in the zinc-aluminum alloy powder, which was annealed in a helium atmosphere at 400 °C in a high temperature diffraction chamber and then cooled on-site to the desired transformation temperature by a helium gas stream directed onto the powder sample. They recorded the progress of the isothermal decomposition and observed the integrated intensities of the [101] diffraction peak of the cph η phase (zinc), and the [200] peak of fcc α phase (aluminium).It was reported(19-22) that, depending on quenching and tempering treatments, the super-saturated solid solution in Al-Zn alloys high zinc content decomposed into two stages with formation of : a) an equilibrium η phase (hcp lattice) and b) quite a stable but strictly metastable α' phase enriched with zinc (fcc ,a = 3.98 Å) It was also reported that(23) a small addition of magnesium to alloy Al +50 Zn delays the formation of the equilibrium η phase .

Toldin, Burykin and Kleshchev investigated the effect of magnesium on Al-Zn alloys containing 60 and 73 wt% Zn both without and with an addition of 1wt% Mg during ageing at 150 and 240 °C. They reported that there are two stages to the decomposition of the supersaturated solid solution in these alloys ; a metastable α'_1 phase is formed in the first and finally decomposed in the second.The magnesium suppresses the development of an equilibrium η phase , as a result of which these stages take longer and the metastable α' phase enjoys a preferred development .

Magnesium has limited solubility in pure zinc (24), less than 0.01% below 375 °C

Furthermore, its solubility in the Zn-Al is limited.For example, its solubility in the Zn-22% Al eutectoid alloy at 275 °C is 0.025% (25) and even at this small percentage it limits the amount of solute strengthening A further increase in the magnesium level results in the formation of β' phase which is based on the intermetallic compound $Zn_{11}Mg_2$ (26) Magnesium is mainly used as an alloying element in the range of 0.02% and 0.1% (27,28) to improve the hardness, U.T.S and creep strength (27,29) as well as to retard intergranular corrosion. The addition of magnesium strongly influences the kinetics of the eutectoid transformation on the TTT diagram. The presence of magnesium and copper in the Zn-22% Al alloy, causes an increase in the temperature of the "nose" of the TTT diagram, but the time for the initiation of the decomposition is virtually unchanged (30). However, the time for the completion of the decomposition is dramatically increased(31) from a few days at room temperature (for Mg free alloys) up to 6 weeks (32). The presence of magnesium modifies the decomposition of a hyper-eutectoid alloy at room temperature because the formation of the zinc rich η phase is depressed initially and the aluminum rich α phase is developed preferentially (33) In the case of alloy No 3 (Zn-4% Al) there is an increase in the transition temperature due to magnesium (34) Magnesium additions reduce the fluidity of Zn-Al alloys, and this could be due to the fact that the magnesium strongly influences the oxidation rate of molten zinc-based alloys (35-39).

The solubility of copper in zinc metal is limited, some indications of the likelihood of precipitation can be inferred from various solubility figures including 1%Cu at 200 °C (40), 1.2%Cu at 275 °C(41), 2.8%Cu at 375 °C(41) and 2.5%Cu at 400 °C (40). Solubility in the α phase of Zn-Al alloy is, however , considerable. Moreover, the addition of copper to the Zn-Al alloys, increases the strength of these alloys and is regularly utilised over a wide range of aluminum levels. The presence of copper in these alloys can only be chosen to a compromised level between possible increase in ultimate tensile strength and hardness and decrease in ductility,while bearing in mind its influence on other properties such as castability, dimensional stability, corrosion resistance, creep resistance and fracture toughness(42,43). It should also be remembered that the effect on the properties is also influenced by the relevant level of magnesium presence. The mode of formation of the α' phase dendrites in the as cast structure for hyper-eutectic Zn-Al alloys can be affected by varying the copper content .A study of the influence of 1wt%Cu and 0.2 wt%Mg on the heat evolution and structural changes of Al-40 and Al 50wt% Zn alloys during isothermal ageing at 30°C and continuous heating up to 400 °C was made by Zahra, Zahra, Dutkiewics and Ciach(44), from their results they reported that at 30 °C, mainly metastable phases appear in Al-40% Zn alloys, at still higher zinc content, the discontinuous precipitation of the equilibrium phase competes with the continuous precipitation mechanism. The amount of metastable phases formed during room temperature ageing increases when the Al-50% Zn alloy contain a small amount of magnesium and copper. They also concluded that magnesium and copper additions limit the extent of discontinuous η precipitates, magnesium being the more efficient. This may be due to the trapping of vacancies and/or the formation of η' precipitates in magnesium containing alloy, or to a copper rich transition phase in copper containing alloys which hinders the discontinuous precipitation front.

2.3 The Effect of Other Alloying Elements and Impurities.

2.3.1 Manganese.

The solubility of manganese in zinc is 0.47wt% at 400 °C (45), this solubility decreases when decreasing the temperature, and at room temperature the solubility is very small, and it gets smaller when the zinc is alloyed with aluminum. It has been reported(46) that in the case of alloy No 3, the solubility of manganese at 390 °C is 0.0013% and 0.0006% at 420 °C. Therefore the use of manganese as alloying element is very limited.

2.3.2 Silicon.

Silicon is virtually insoluble in pure zinc as well as in Zn-Al alloys (47,48). The present of silicon as low as 0.02% increases the ultimate tensile strength, but drastically reduce the elongation and impact properties (49).

2.3.3 Titanium.

Titanium has only a limited solubility in zinc and forms a zinc-rich compound with an eutectic at about 0.11% Ti. However this compound decreases the grain size of cast zinc. The effect of titanium on the ultimate tensile strength and hardness is negligible while it increases the creep resistance, especially with the present of copper (50) in the Zn-Al alloys.

2.3.4 Lead and Tin

Lead and tin are considered to be impurities and should not exceed 0.07% and 0.05% respectively. The solid solubility of lead in zinc is very low and its presence in the Zn-Al alloy result in a massive corrosion which can spread quickly along the grain boundaries. The presence of copper and magnesium in the Zn-Al alloys increases the amount of lead and tin which can be tolerated due to the formation of intermetallics which trap these heavy metals.

2.3.5 Cadmium.

The presence of cadmium exceeding 0.005% can be very harmful, as it affects both the castability and the mechanical properties. It is not clear however as to whether or not cadmium encourages intercrystalline corrosion.

2.3.6 Iron.

The presence of iron to a degree of more than 0.02% can be harmful, as it tends to form a compound with the aluminum with a composition close to $FeAl_3$.

2.3.7 Other impurities.

Arsenic, indium, antimony, bismuth and mercury should all be avoided as they cause intercrystalline corrosion.

2.4 The Equilibrium Phase Diagrams.

2.4.1 The Zinc-Aluminium Binary System.

Aluminium is added to zinc for increasing strength, reducing grain size and decreasing the rate of attack of zinc on iron and steel parts of a diecasting machine or mould. On the other hand aluminium increases the fluidity of the zinc and results in improved mechanical properties (51). Anderson's(52) evaluation indicates at both extremities a constitutional condition favourable for the production of useful alloys; There is far-reaching solid solubility of zinc in aluminum and limited solid solubility of aluminum in zinc. The equilibrium diagram of Figure 4(53) shows a eutectic alloy of composition 95% Zn, 5% Al, melting at 382 °C. At the eutectic temperature there occurs the simultaneous solidification of a solid solution of aluminium in zinc, with the closed-packed hexagonal lattice of zinc, and a zinc-aluminium solid solution of face-centred cubic structure. At the eutectic temperature the solubility of aluminium in zinc is 1.14% falling to 0.05% at 20 °C .

The face centred cubic structure β containing up to 83% zinc at the eutectic temperature is stable only at temperatures above 275 °C. At this temperature β phase containing 78% Zn undergoes an eutectoid transformation into a zinc rich η phase with about 0.7% Al in solid solution and an aluminum rich solid solution of fcc α containing 30% Zn .

The possibility of a peritectic reaction with 78% Zn at 443 °C remains unsettled(54-56). Workers such as Owen, Pickup(57) and Elwood (58,59) failed to settle the argument of such possibility, and other workers such as Fink, Willey (60) and Sutherland (61) later denied the possibility of the peritectic reaction at 443 °C, explaining the phenomenun of thermal arrest as due to a rapid change in composition of the α' solution along the solidus.

Still the Zn-Al binary phase diagram shown in Figure 4 was not satisfactory to workers such as Presnyakov et al (62), Goldak and Parr (63), who disagreed with Sutherland.Presnyakov carried out investigations on the Zn-Al system and came out with certain modifications to the system chiefly a peritectic reaction. Presnyakovs modifications to the Zn-Al system as shown in Figure 5(62) were confirmed by Goldak, Parr and so many others up till now. Presinyakov reported the existence of a peritectic reaction at 443 °C, he also reported that a β phase distinct from the α phase existed, and involved a discontinuity in the high temperature solubility of zinc in aluminium. In 70% Zn, at 340 °C, Presinyakov found a second eutectoid decomposition of the α' phase into α + β. From Figure 5, the alloy is at the liquid state going through different phases as the temperature drops, the symbol α is the aluminum rich phase, α' is the zinc-rich phase in the aluminium side (monotectoid), β is the zinc-rich eutectoid phase, η is the zinc-rich phase in solid solution.

With 70% Zn at 443 °C, both the liquid and the aluminium-rich phase α transform into β (peritectic reaction), while at 95% Zn at 382 °C the liquid transformed into β + η .

Between the temperatures of 443 and 340 °C a narrow gap (63) of α' + β takes place and extends from 69.5% to 70.5% Zn

In 78% Zn at 275 °C (eutectoid temperature) the β phase decomposes into α + η .

Table 3 shows the solid solubility of zinc in aluminium(64).

TEMPERATURE °C	SOLUBILITY (% wt)
77	2.5
127	6.2
177	11.5
227	18.0
275	31.6
327	43.5
340	49.0 - 69.5
351.5	61.3
443	70.0

Table 3. The Solid Solubility of Zinc in Aluminium(64)

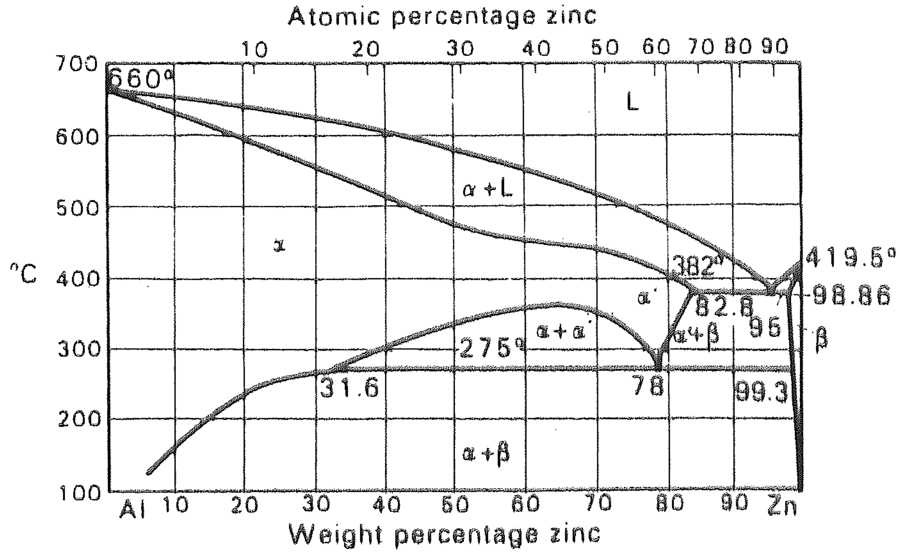

Figure 4 The Zinc-Aluminium Equilibrium Diagram (53).

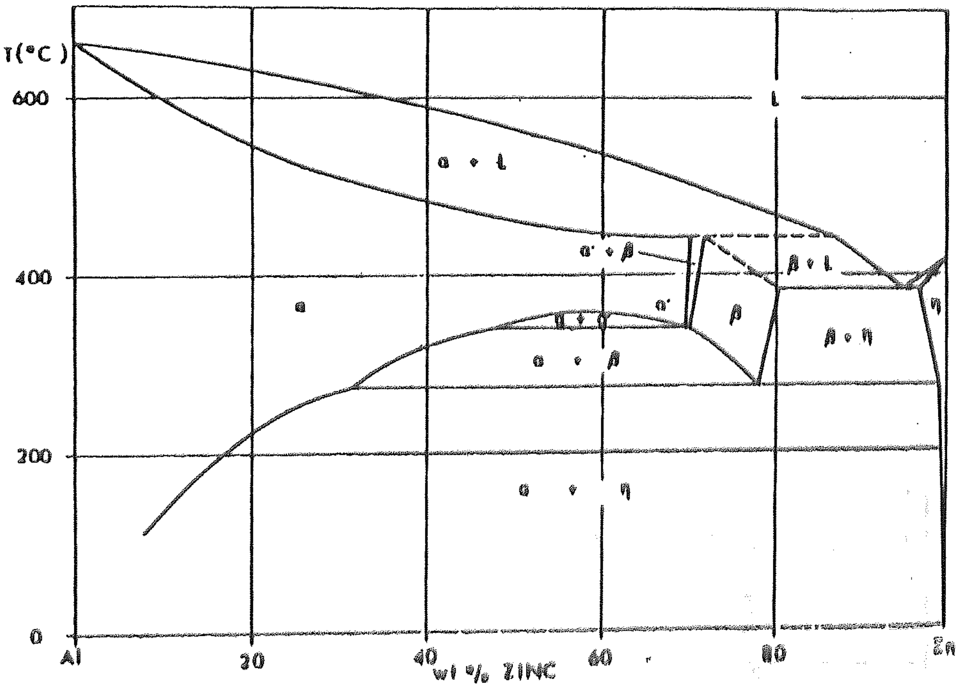

Figure 5 Accepted Phase Diagram of Binary Zinc-Aluminium System(62).

2.4.2 The Binary Zn-Cu System

Alloys of Zn-Cu containing up to 45% Zn are known commercially as brasses. Figure 6 shows the Zn-Cu equilibrium diagram, from this Figure it is seen that as the amount of zinc increases, the solidified and cooled alloy changes from α (fcc) to α + β phases at around 40% Zn, and to β phase (bcc) alone as it approaches 50% Zn. With further increase of zinc beyond the composition of the β phase, there occurs an α phase which is a compound of zinc and copper. The work reported in this thesis is concentrated only on alloys containing up to 2% Cu, therefore only one part of the Zn-Cu diagram is involved, ie the zinc corner is considered in detail. Upon ageing the supersaturated solid solution of η phase precipitate into the ε phase. Both the ε and the η phase have essentially the same crystal structure and the lattice spacing as follows :

ε : a = 2.735 Å c = 4.285Å at 21% at % Cu (65)

η : a =2.668 Å c = 4.870Å at 1.55% at % Cu (41)

The axial ratio of ε decreases from about 1.58 to 1.55, when increasing the zinc concentration from 68 - 88%, while on the other hand, the initial ratio of η increases from about 1.78 near the (ε + η)/ η boundary to 1.856 at pure zinc (41,66).

Table 4 (67) shows the solubility of copper in zinc at different temperatures. From this table it can be seen that the solubility of copper in zinc increases with increasing temperature.

TEMPERATURE °C	SOLUBILITY (wt %)
100	0.3
200	0.9
300	1.65
400	2.5
424	2.7

Table 4. The Solid Solubility of Copper in Zinc(67)

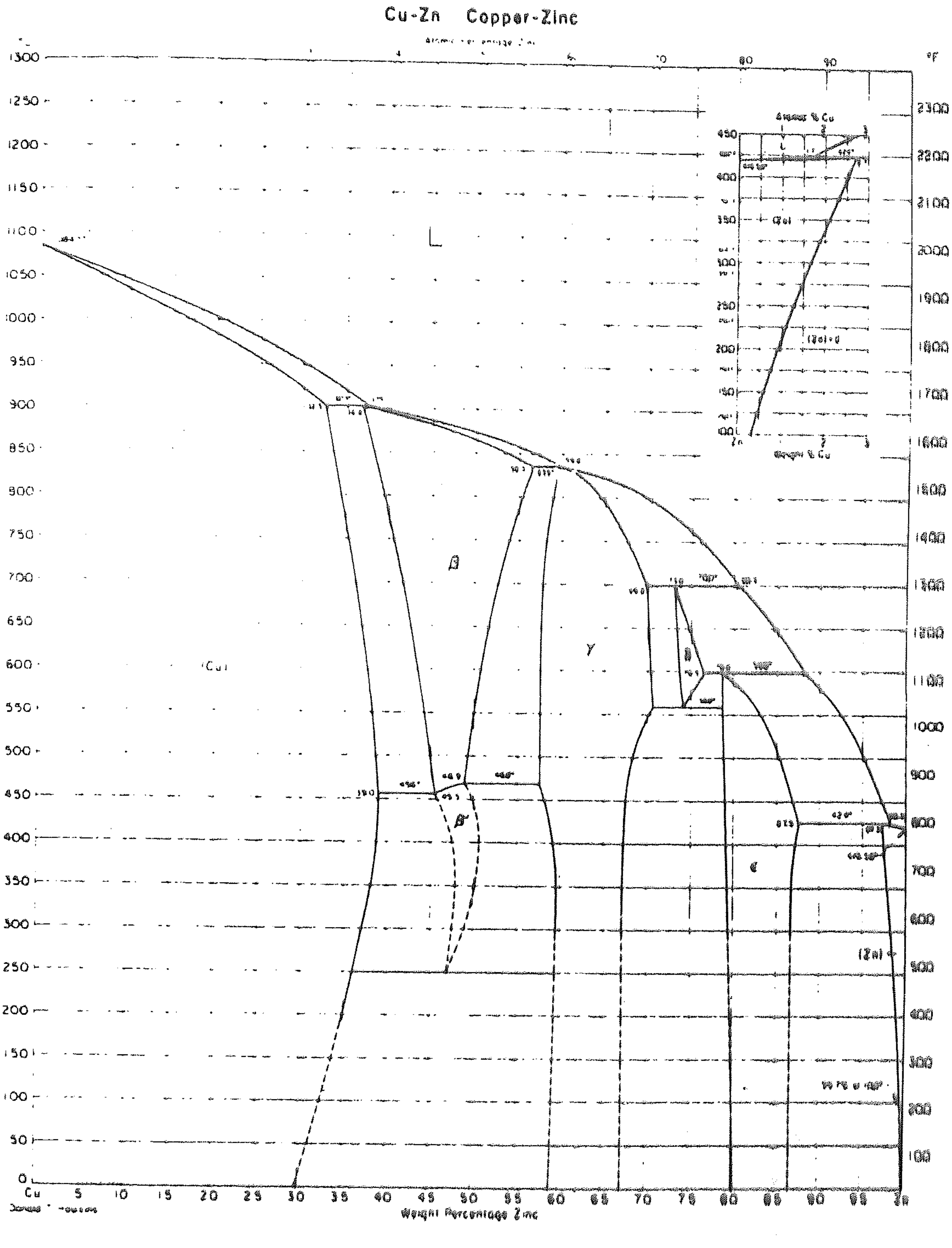

Figure 6 The Equilibrium Phase Digram of the Binary Zn-Cu System.

2.4.3 The Binary Al-Cu Diagram.

The Al-Cu equilibrium diagram is shown in Figure 7(68). When such an alloy say 3% Cu -97% Al, is slowly cooled the initial structure at about 540 °C is an α phase solid solution, but when the temperature falls to below the solvus temperature, the copper-$CuAl_2$ (θ phase) aluminum compound is precipitated. At room temperature the result of this is an α solid solution in equilibrium with Cu Al_2 compound.

The Figure also shows an eutectic between a solid solution containing 5.6% Cu and the intermetallic compound $CuAl_2$.The lever rule indicates that the θ phase is dominant in the eutectic structure, which is therefore brittle. Consequently most of the useful alloys contains less copper than the 5.6% maximum amount soluble in solid aluminium.The solubility of copper in aluminium decreases rapidly with decreasing temperature, from 5.65 to less than 0.1% at room temperature.

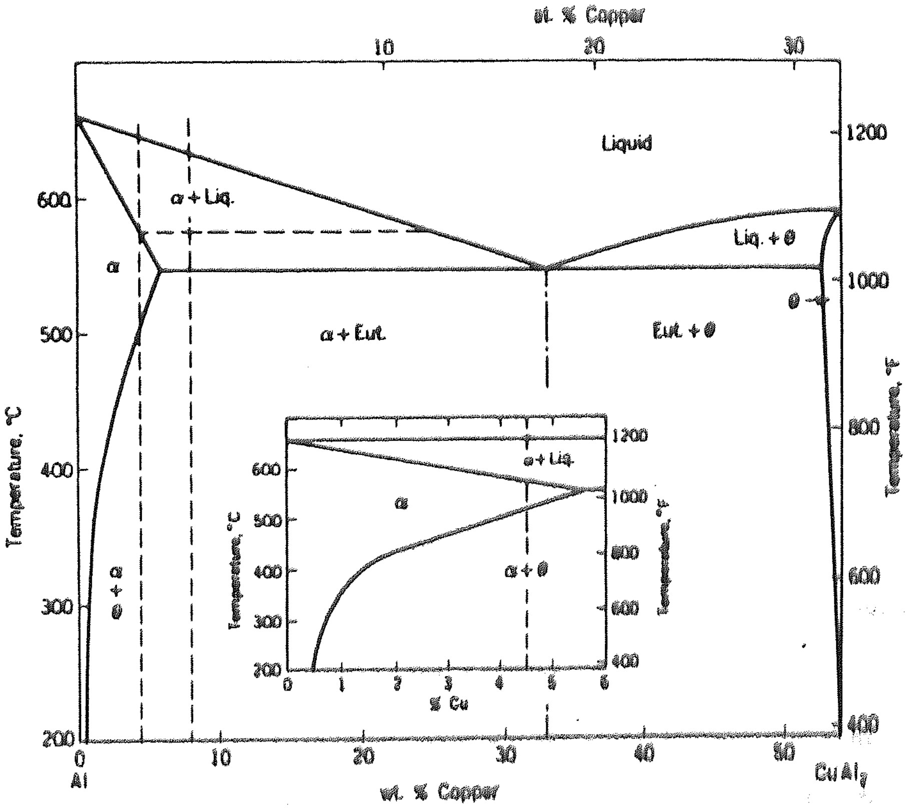

Figure 7 Phase Diagram of the Al-Cu System, from 0 to 54%- Cu (68).

2.4.4 The Ternary Zn-Al-Cu System

When three elements are combined, the equilibrium diagram requires three dimensions, two for composition and one for temperature. It may be noted that small additions of further elements to a binary metallic alloy are frequently made, not to introduce a new phases, but to control the kinetics of reaction and hence the distribution of phases. When aluminum and copper are alloyed with zinc, Burkhardt (69) pointed out that a ternary eutectic at a composition of 7% Al, 4% Cu, 89% Zn and a melting point of 370 °C was formed. He also calculated the solubilities of aluminum and copper in the zinc-rich solid solution to be respectively 1.6 and 3.4% at the eutectic temperature falling to 0.1-0.2% and 0.6-0.8% at room temperature. Then on the basis of his calculations, he pointed out that alloys containing less than about 0.7% Cu should behave as a copper-free alloys .

Koster and Moeller (70-72) investigated the Zn-Al-Cu alloys and their work enabled them to establish the isothermal section of the Zn-Al-Cu system at 350 °C as shown in Figure 8. In addition to the phases present in the binary system Koster and Moeller reported a new phase between 56 to 58% Cu and 10 to 30% Zn. This phase is named ternary " T " phase and can be seen as a narrow strip in Figure 8. The success of Koster and Moellers' work on the Zn-Al-Cu system encouraged them to study these alloys at different temperatures of 400 , 500 , 600 and 700 °C in order to determine the shape of the liquidus surface as shown in Figure 9.Koster studied the eutectic trough which extends from Al-Cu binary edge at 67% Al across to a point near 90% Zn, where it meets a peritectic trough from the Cu-Zn edge and a eutectic trough from the Al-Zn edge to form a ternary eutectic point.

Gebhardt (73) is in agreement with Koster,when he reported that a ternary alloy containing 89.2% Zn , 7% Al and 3.8% Cu would solidify at 377 °C. Further work by Koster and Moeller concluded that the Al-rich end of the single phase field T' (at approximately Al 5 Cu 4 Zn) had a lower crystallographic symmetry at temperatures below 450 °C. The other end of the phase field corresponding to approximately Al

3.5 Cu 5 Zn 2 retained the CsCl structure. Koster denoted the ordered CsCl type structure as T phase and called the lower symmetry structure T'.

Work by Bradley and Lispon (74) based on X-ray diffraction, showed that a similar T phase in the Cu-Ni-Al alloy system had a structure based on a deformed bcc structure cell. The composition of this T phase was given as Al_6Cu_3Ni. Koster and Moeller declared their T phase to be isomorphous with Al_6Cu_3Ni, with an ordered CsCl structure at high temperature. Work was carried out by Willey(75) on the isothermal section of the Zn-Al-Cu system at 700, 550, 350 and 200 °C as shown in Figures 10-13. Willey based his research on Koster and Moellers diagram, and concentrated his work on areas bounded by approximately 60 Al-40 Cu, 15 Al-81 Cu, 40 Cu-60 Zn and 20 Cu-80 Zn.

Arndt and Moeller showed a single phase of γ from about 16-22 % Al when temperatures of 700 and 550 °C were involved. When temperatures of 350 and 200 °C were involved, Arndt and Moeller divided this region into three parts, the Cu rich γ' (16-19% Al), the intermediate γ_1 (19-20.5% Al) and the Al rich γ_2 (20.5-22% Al) .Also they identified the phase field in the binary system between temperatures of 700 to 200°c as γ_2 with aluminum range between 16 - 22%, $\gamma_2 + \delta$ (20-21% Al) and δ (21-22% Al). In addition to that, Arndt and Moeller(76,77) showed a single phase ζ_1 at 700 °C and ζ_2 at 550 °C within the aluminum composition range between 22-26% .

Extensive investigations by Murphy(78) based on electron and X-ray diffraction and electron-probe microanalysis, have determined the structure of the T' phase in equilibrium with α and η of the Al-Cu-Zn system. Murphy concluded that T' has a rhombohedral structure with $a = 8.676$ Å and $\alpha = 27.41°$. The structure was a superlattice based on the assembly of five CsCl type cells, joined corner to corner along the {111} direction. Murphy(79) also studied the isothermal section of the Zn-Al-Cu system at temperatures of 350, 290, 280, 270 and 250 °C as shown in Figures 14-18. Murphy's results on the phase boundaries agree with that of Gebhardt, but disagree in the amount of soluble Cu in the α and $(\varepsilon + \beta)$. Part of

Murphy's work was concentrated on the changes of the β phase as he observed that β phase field was large at 350 °C, but changed considerably on cooling as shown in Figure 19, at three different temperatures (350, 290, 280 °C). On the other hand the copper rich β in equilibrium with ε and η was reduced rapidly in zinc content at lower temperatures .

Clearly the rapid changes in zinc content of β phase with copper content at 0 to 2% level have significantly altered the relative proportions of β and η phases. Further work was made by Murphy on the Zn-Al-Cu system with a low copper content, and resulted in a well established series of solid state phase changes during cooling, and his work is in agreement with Koster and Gebhardt(71,81-84).

The 350 °C isothermal section was characterised by broad two-phase fields, but the β + T' field was very narrow, and it was difficult to differentiate the α, α' and β phases from each other when the compositions were similar, while on the other hand the extent of the α phase in equilibrium with θ and T' increased considerably with the amount of copper in the solid solution.

It was also found that the relationships of the phases at 290 °C were similar to those of 350°C. It was difficult to analyse and determine the composition of the T phase formed in (α + β +T') due to its size, which was found to be very small, but the β composition was measured and found to be very close to that in (β + T' + ε) phase field .

The (β + T') region was found to be very narrow, while the (ε + β) region was still relatively wide .

Clearly a phase reaction (β + T' <==> α + ε) was indicated by these observations. This reaction is a Class II four-phase reaction, and produced a two phase field (α + ε) which appeared instead of the two-phase field (β + T')

Two three-phase fields (α + ε + T') and (α + β + ε) were found to be separated by a narrow two-phase field (α + ε) at 280°c as shown in Figure 16 .

At 270 °C shown in Figure 17, the (α + T' + ε) phase field was present but the β phase had disappeared and was taken over by the (α + ε + η) phase field. That means that another Class II four-phase reaction is going to occur just below 270 °C.

$\alpha + \varepsilon \Longleftrightarrow T' + \eta$

Murphy found that all four phases co-existed in some of his samples, and concluded that the transformation temperature must be at 269 or 268 °C. Figure 18 at 250 °C, shows the phase field ($\alpha + T' + \eta$) which had resulted from the reaction just below 270 °C (269 or 268 °C). Murphy found that the first and third four phase reaction hypothesised by Gebhardt did in fact occur. The first :

$\beta + T' \Longleftrightarrow \alpha + \varepsilon$ (at 288 °C) and the

$\alpha + \varepsilon \Longleftrightarrow T' + \varepsilon$ (at 269 or 268 °C)

The reactions proposed by Arndt and Moeller were denied by Murphy and he stated that such reactions do not take place. The reaction sequences in binary and ternary system, summarized by Murphy are shown in Figure 20 while the formulas of these reactions are shown in Table 5.$^{(79)}$.

Phase	Cu-Al	Cu-Zn	Phase	Cu-Al	Cu-Zn
		Binary Phases			
β	Cu_3Al	CuZn	δ	......	$CuZn_3$
β'	......	CuZn	ζ_1	Cu_4Al_3	......
γ	Cu_9Al_4	Cu_5Al_8	ζ_2	Cu_4Al_3	......
γ'	Cu_9Al_4	......	ε	......	$CuZn_4$
γ_1	$Cu_{32}Al_{19}$	......	η_1 , η_2	CuAl	......
γ_2	Cu_3Al_2	......	γ	$CuAl_2$	......

Ternary Phases

T ....Cu-Zn rich; composition range varies with temperature.

T' ....Cu-Al rich; composition range varies with temperature.

Table 5: The Binary and Ternary Phases of Zn-Al-Cu Ternary System and their Approximate Formulas.

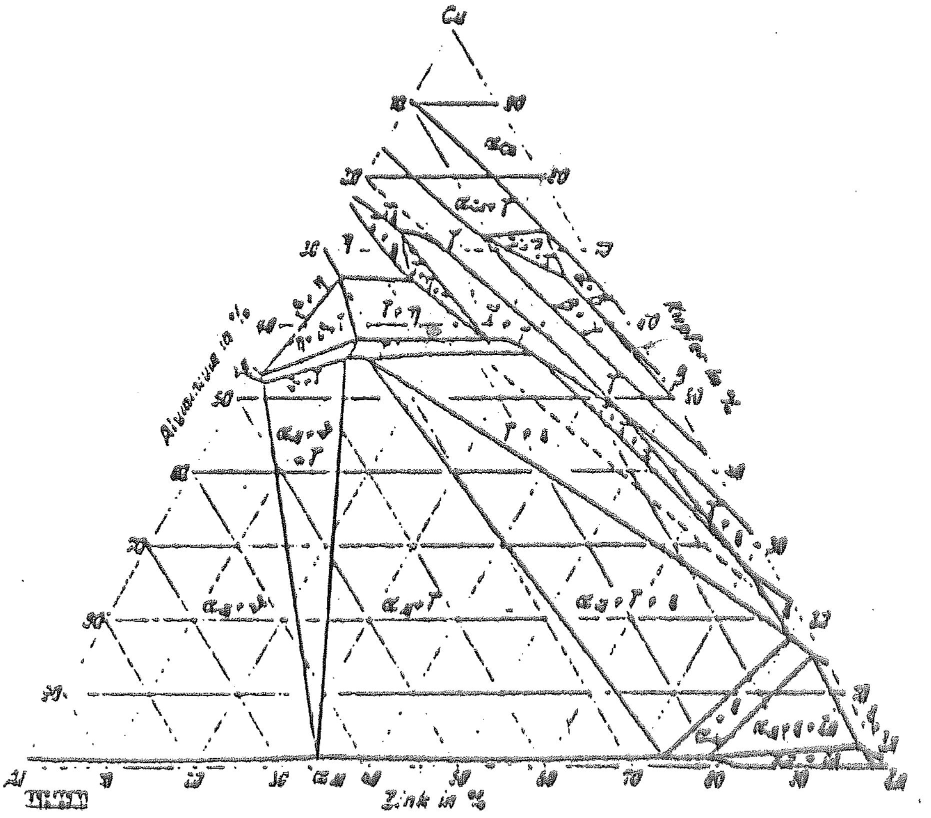

Figure 8 Isothermal Section of Zn-Al-Cu Ternary System at 350°C, according to Koster and Moeller(70-72).

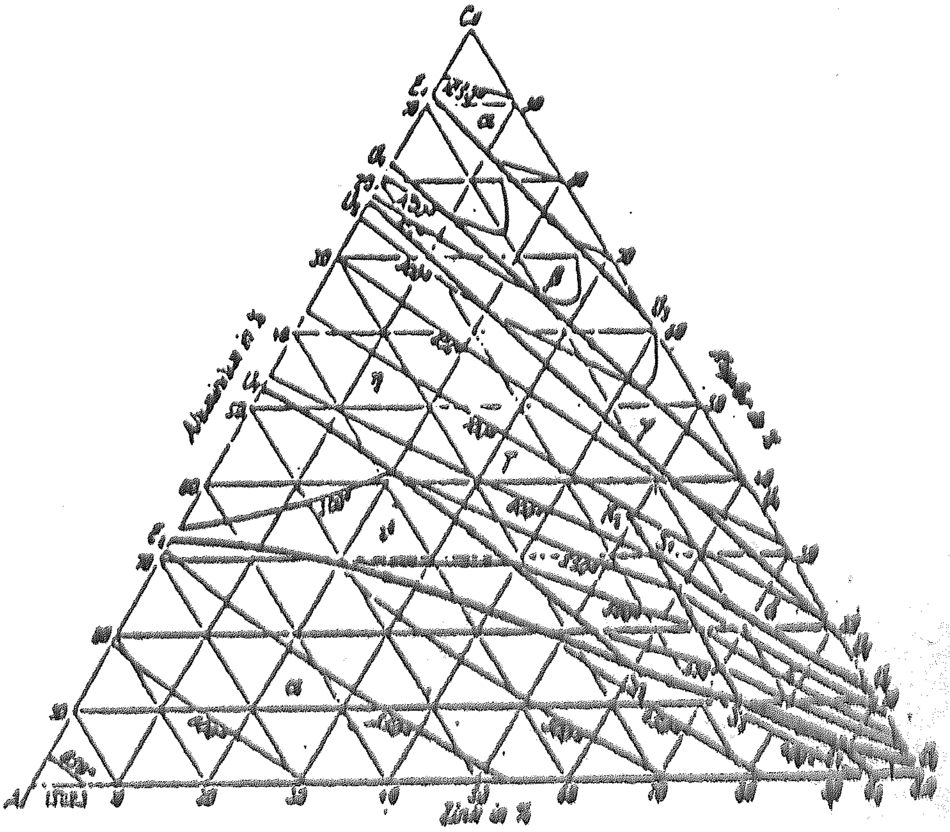

Figure 9 Liquidus Surface of the Zn-Al-Cu System according to Koster(70-72).

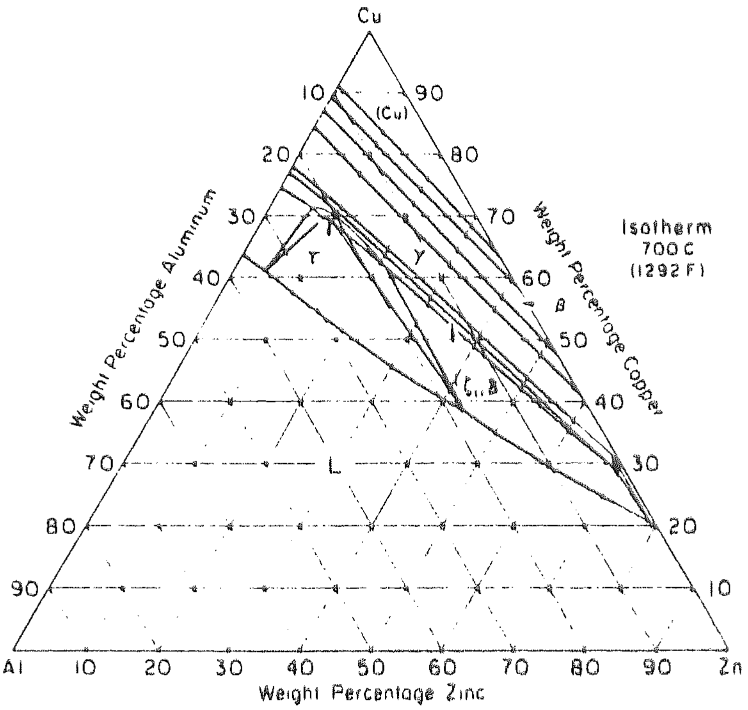

Figure 10 Isothermal Section of Zn-Al-Cu System at 700°C(75)

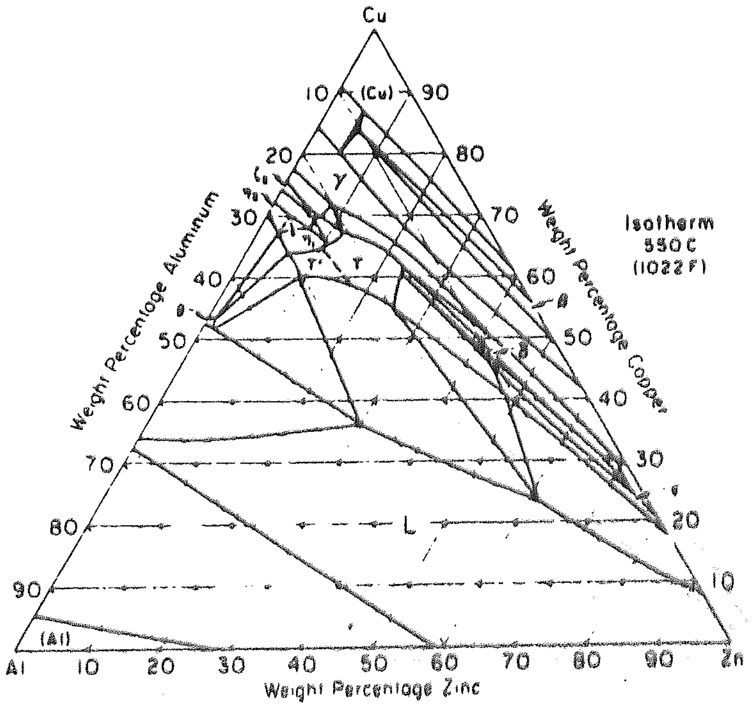

Figure 11 Isothermal Section of Zn-Al-Cu System at 550°C(75)

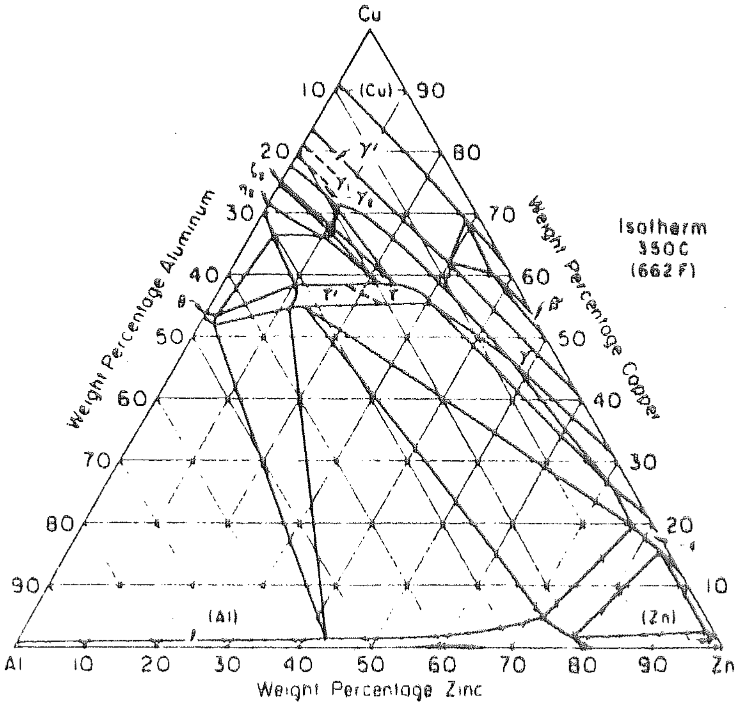

Figure 12 Isothermal Section of Zn-Al-Cu System at 350°C(75).

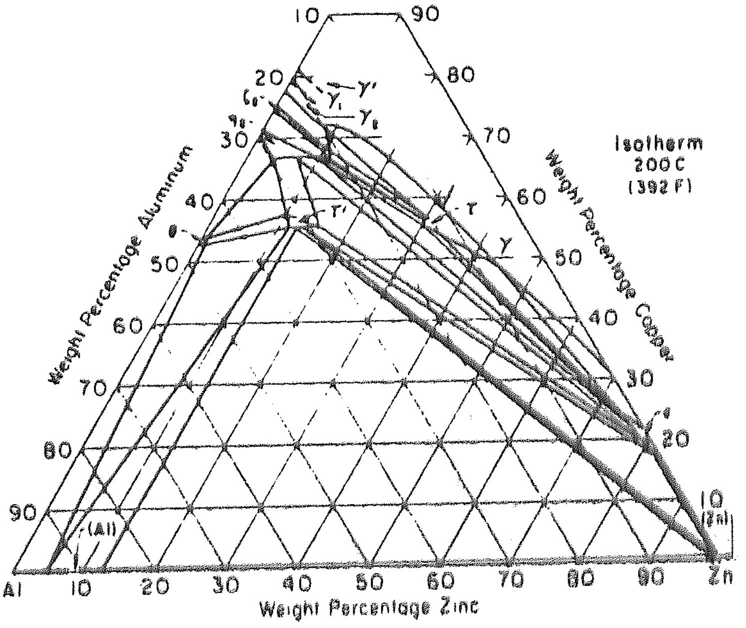

Figure 13 Isothermal Section of Zn-Al-Cu System at 200°C(75).

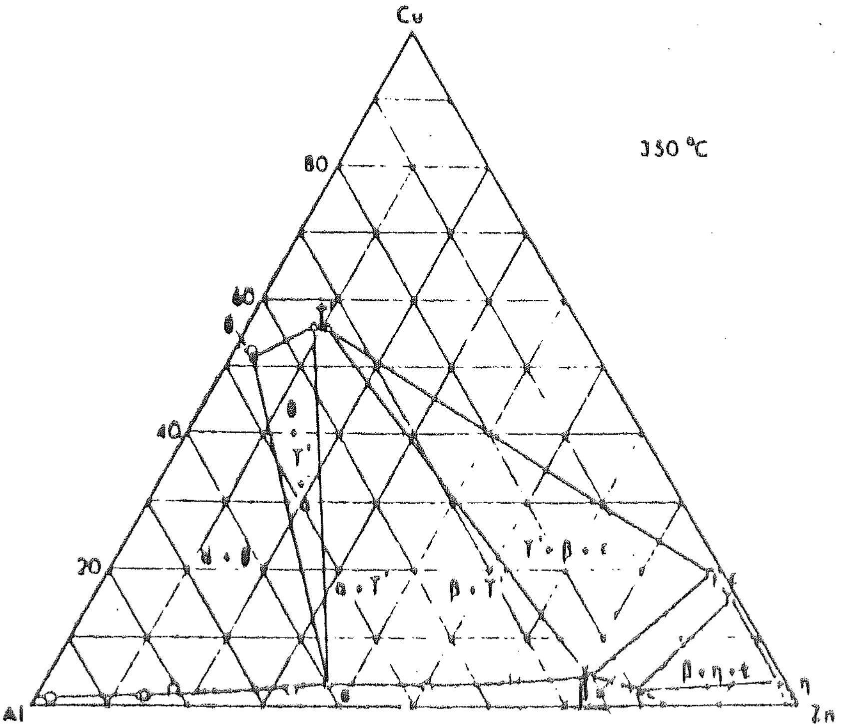

Figure 14 Isothermal Section of Zn-Al-Cu System at 350°C(79).

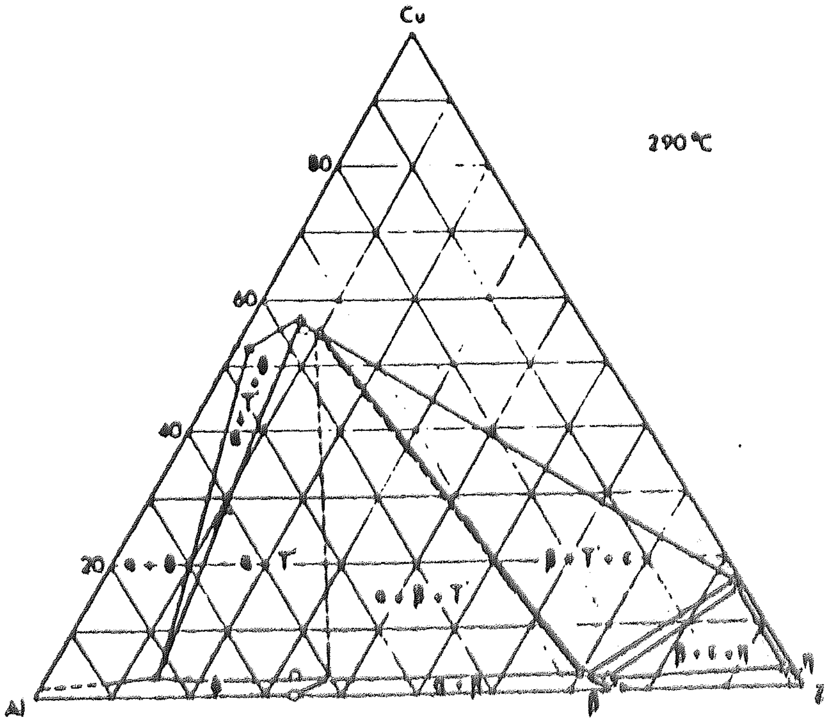

Figure 15 Isothermal Section of Zn-Al-Cu System at 290°C(79).

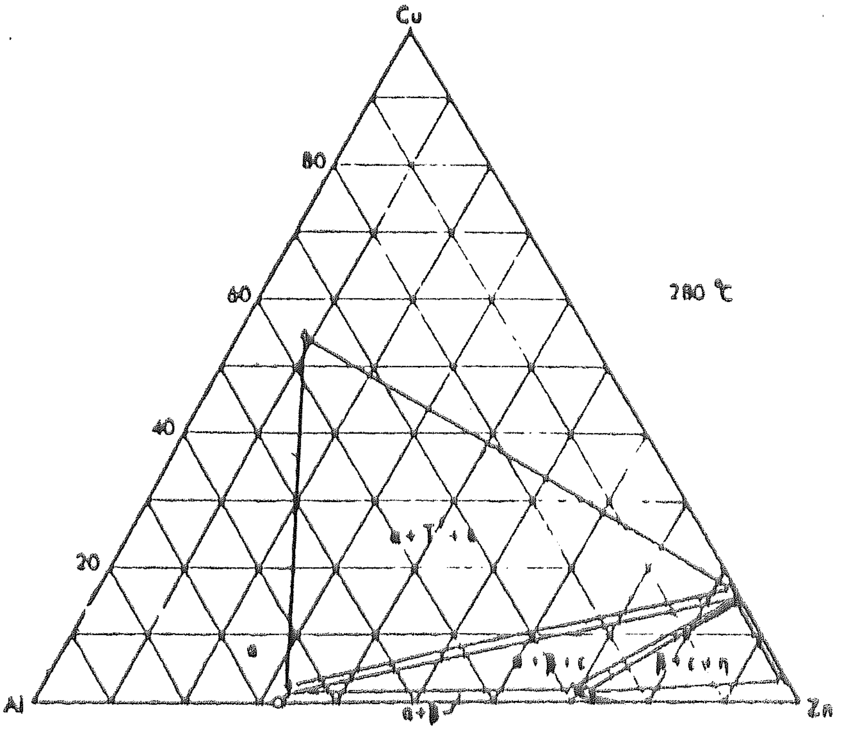

Figure 16 Isothermal Section of Zn-Al-Cu System at 280°C(79).

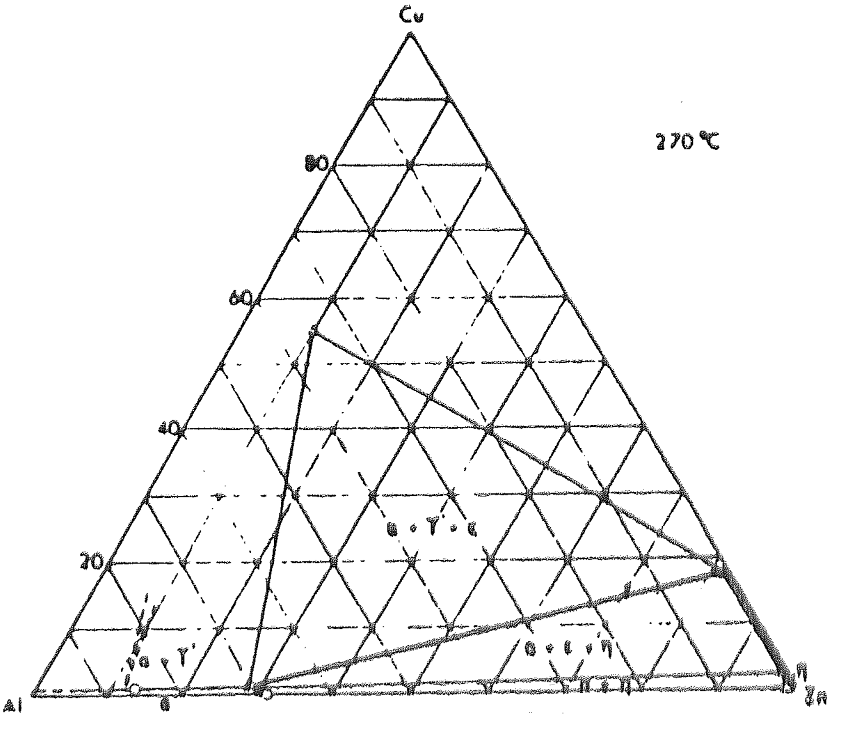

Figure 17 Isothermal Section of Zn-Al-Cu System at 270°C(79).

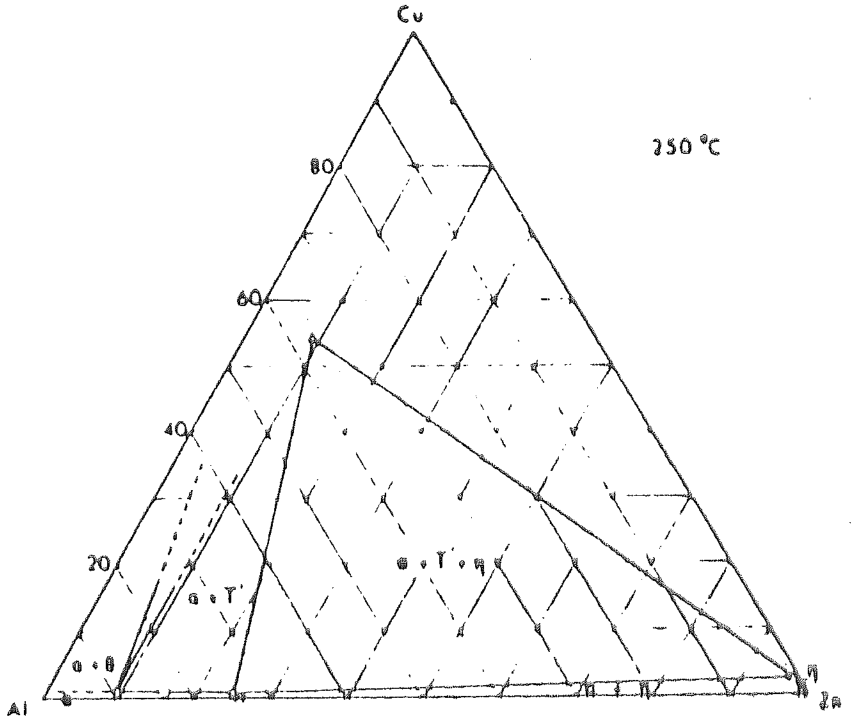

Figure 18 Isothermal Section of Zn-Al-Cu System at 250°C(79).

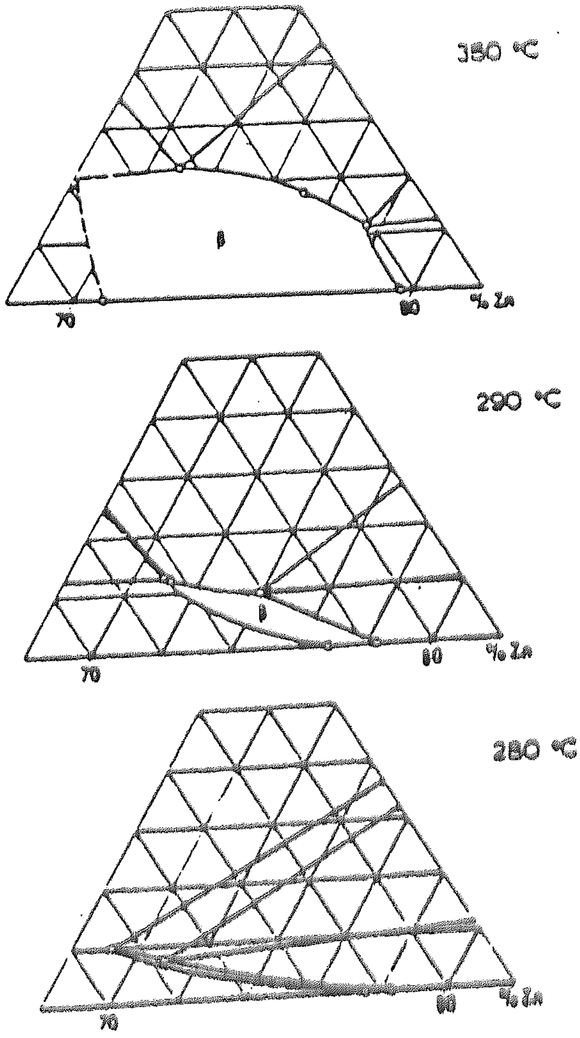

Figure 19 The Shapes of the b-Phase Field at 350, 290 and 280°C (After Murphy (79)).

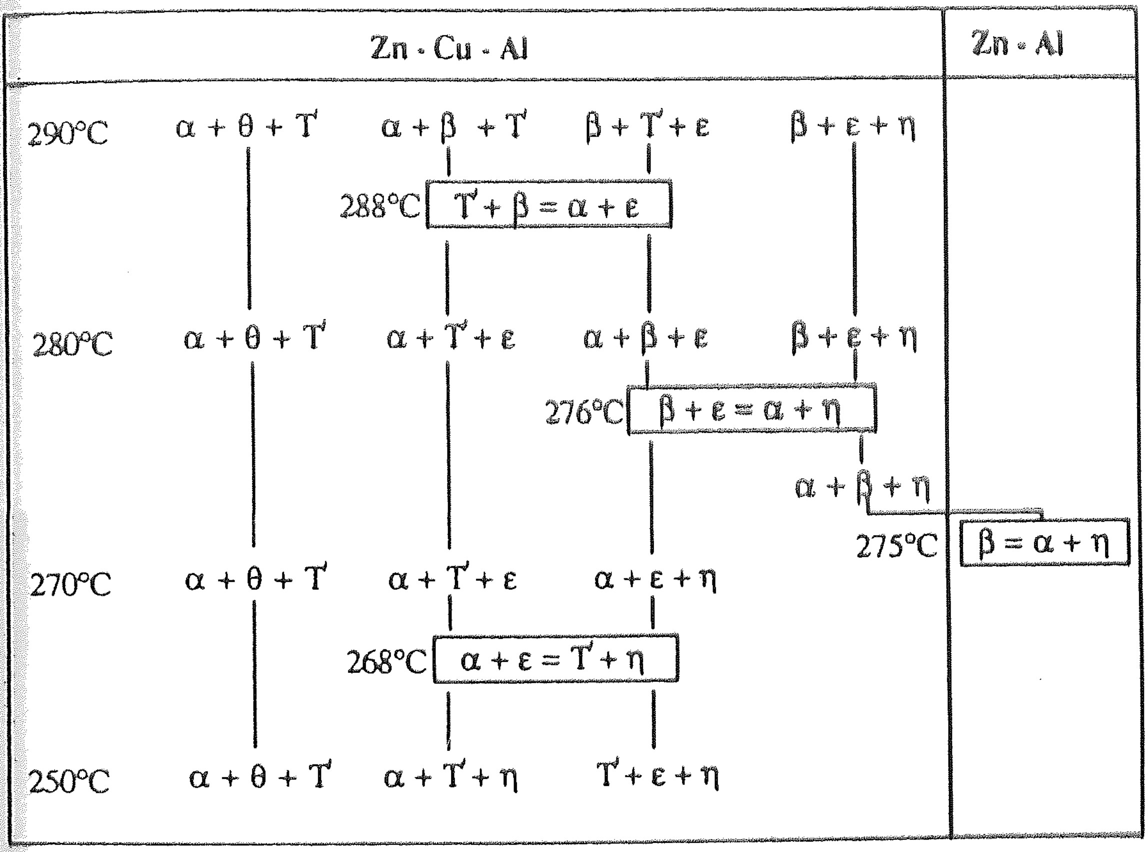

Figure 20 Solid State Reactions in the Low-Copper Part of the Zn-Al-Cu System a ccording to Murphy(79).

2.5 Phase Transformation.

2.5.1 Binary Zn-Al Alloys.

Investigations of the solid solution of zinc in aluminum has been discussed for many years. Based on the Zn-Al phase diagram in Figure 5, four aluminium ranges where possible phase transformation may occur in the Zn-Al system can be classified :

1) Al-rich α phase (60% Al)

2) Monotectoid α /α' phase (40% Al)

3) Eutectoid β phase (22% Al)

4) The region in the ($\beta + \eta$) composition and the Zn-rich η phase ($<$ 20% Al).

These will be considered in turn.

Early investigations were made by Guinier (85) & Borellinus (86), claimed that in quenched aluminium in an α' alloys, small spherical aggregates rich in solute atoms (GP zones) were responsible for the observed rapid hardening at room temperature. These GP zones were the first product of decomposition after quenching the fcc single phase field and ageing at room or sub-zero temperatures. These transformations were studied with the aid of low-angle X-ray scattering, electron microscopy (TEM) and hardness and electrical resistivity measurements.

A large number of workers (87-93) believed that the exact nature of the transformation depends on the zinc content of the quenched alloy. These workers studied low-zinc fcc alloy with up to 30% Zn, and summarised their results as follows :

Spherical GP zones ----> Rhombohedral transition phase α''_m ----> fcc transition phase α'_m ----> Zn -rich stable precipitates.

The rhombohedral α''_m is precipitated in the form of plates and differs only slightly in lattice parameters (a = 3.992 Å, α = 91.36) from the cubic α' phase (a = 3.995 Å) (94)

The early stage of transformation is the rapid segregation of zinc atoms into spherical regions to form GP zones. These zones continue to grow with ageing until up to a certain size of 30 to 35 Å, where these spherical zones become ellipsoidal. The changes of the zone shape have a severe effect on the mechanical properties of the alloy (89,92,95,96). On the other hand, on further ageing at a certain composition, the α''_m phase tends to grow to an extent that coherency is completely lost in the {111} habit planes. Since the rhombohedral distortion is due to coherency, the structure become of non-coherent fcc type once coherency is lost and is called α'_m phase (94).

The stable Zn-rich phase is finally formed mainly on dislocations and grain boundaries (92), and the orientation relationship between the zinc precipitates and the aluminum matrix was determined to be :

[111] Al // [0001] Zn , [$1\bar{1}0$] Al // [$10\bar{1}0$] Zn

At this stage it is worth while to catagorize the decomposition mechanism into two types

1) A conventional cellular (or discontinuous) reaction, mainly resulting in grain boundary nucleated lamellar segregates of $\alpha + \eta$.

2) Spinodal decomposition of the Al rich matrix leading ultimately to the formation of the η.phase.

The conventional cellular decomposition occurs more frequently than the spinodal decomposition in the Zn-Al system. A detailed study of this reaction was made by Ramaswamy et al (97) which involved alloy Al-50% Zn. A more recent investigation was made by Vijayalakshmi et al (98,99), where investigation involved two types of alloys one of 60% Zn and the other with 75% Zn. In all these investigations the monotectoid alloys were subjected to solution treatment. Results by both Ramaswamy and Vijayalakshmi have arrived on the same conclusion, that the cellular reaction started at grain boundaries. The mechanism of such a nucleation stage was explained by Fournelle and Clark (100), in which it attributed the net reduction of the areas of the grain boundary to the migration of a curved grain boundary of the α' matrix. The high diffusivities of the solute atoms across a mobile boundary facilitates the nucleation of stable η precipitates, resulting in the pinning of the boundary. The migrated boundary leaves a narrow region depleted of solute atoms by diffusion to the newly formed allotriomorphs of η, thus a narrow precipitates-free zone is formed. However lamellar structures were observed to have developed from these grain boundary allotriomorphs and tended to grow into the parent grain at later stages of the decomposition. Two mechanisms were involved in achieving and establishing their unique lamellar spacing.

1) A mechanism responsible for branching the existing lamellae (97,99)

2) A mechanism of nucleation of fresh lamellae at an advancing interface (98,99)

Boswell & Chadwick (101) Chatham and Ridley (102) have concluded that the rate of increase of the interlameller spacing is a function of the applied undercooling and thus of the ageing temperature. They observed a decrease in the interlamellar spacing when decreasing the temperature. A relationship between the two was put forward by Cheetham and Ridley (102):

$S \alpha \Delta T^{-0.9}$

where S is the interlamellar spacing, and ΔT is the under cooling in an eutectoid alloy under isothermal transformation conditions.

Boswell and Chadwick (101) on the other hand reported that during the growth of the cells, the lamellae maintained the following orientation relation across their interface

$[111]_{\alpha} // [0001]_{\eta}$ with $(1\bar{1}0)_{\alpha} // (1\bar{2}10)_{\eta}$

Other workers (102-104) carried out their studies on the decomposition of the eutectoid alloy during quench-ageing, isothermal transformation and slow cooling to the transformation temperature. These workers reported that depending on the transformation temperature, more than one type of decomposition product was found on ageing alloys with a composition corresponding to the eutectoid β phase (102,106,107). Decomposition of the eutectoid alloy during slow cooling, or isothermally transforming at high temperature produced a lamellar structure. However decomposition at room temperature after a rapid quench produced a fine (1μm) mixture of equiaxed zinc rich α''_{m} and aluminum rich grains. A possible interpretation of these changes may be due to a spinoidal decomposition which took place at about room temperature (102,104)

A detailed investigation(105) on the processes of decomposition of supersaturated solid solutions in Al-Zn alloys with 40, 50 and 60 wt% Zn (Al Zn II) and in an alloy containing 73wt% Zn (Al Zn III) was also made. The results of these investigations have concluded that (depending on the composition, cooling rate and heat treatment temperature) there were eleven sequences of phase transformations that could occur through metastable phases (R, α'_m) or GP zones as shown in Figure 21.

In Figure 21, positions 6-9 show that the sequences begin with the formation of GP zones after quenching the alloy in iced water , and the (R α''_m) phase is formed preferentially by the mechanism of spinodal decomposition, while the metastable α'_m phase is formed by nucleation.

A recent detailed investigation on the isothermal transformation of the eutectoid alloy was made by Smith and Hare(108), and a fuller TTT diagram was obtained as shown in Figure 22. Smith and Hare regarded the transformation to occur in four stages (Figure 22) .

1) The quenched condition

2) Breakdown of β phase to products of intermediate composition .

3) Adjustment of these products to α and η of equilibrium chemical composition .

4) Adjustment of structure to virtual physical stability .

Further detailed investigations to define phases which might exist in the metastable state in the binary system was made by Toldin, Burykin and Kleshchev (20,109,110) from one and Krupkowski et al(111) on the other side.

The work of all these investigators concluded that two types of metastable state might exist in low temperature ($\alpha + \eta$) region, one being defined by solubility limits of the ($\alpha + \beta$) region which continue to the low temperature ($\alpha + \eta$) region, and the other bounded in the same way of the ($\alpha + \alpha'$) region which continue to the low temperature ($\alpha + \eta$) region as shown in Figure 19 .

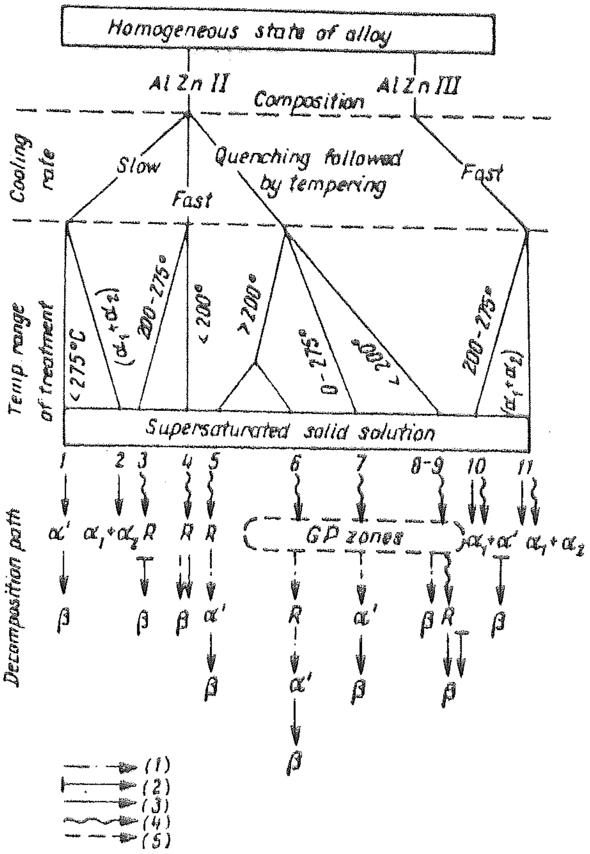

Lines: (1) homogeneous rearrangement, (2) cellular decomposition, (3) nucleation, (4) spinodal decomposition, (5) nucleation at critical defects.

Figure 21 A scheme of Transformation in Al-Zn Alloys according to Toldin (20).

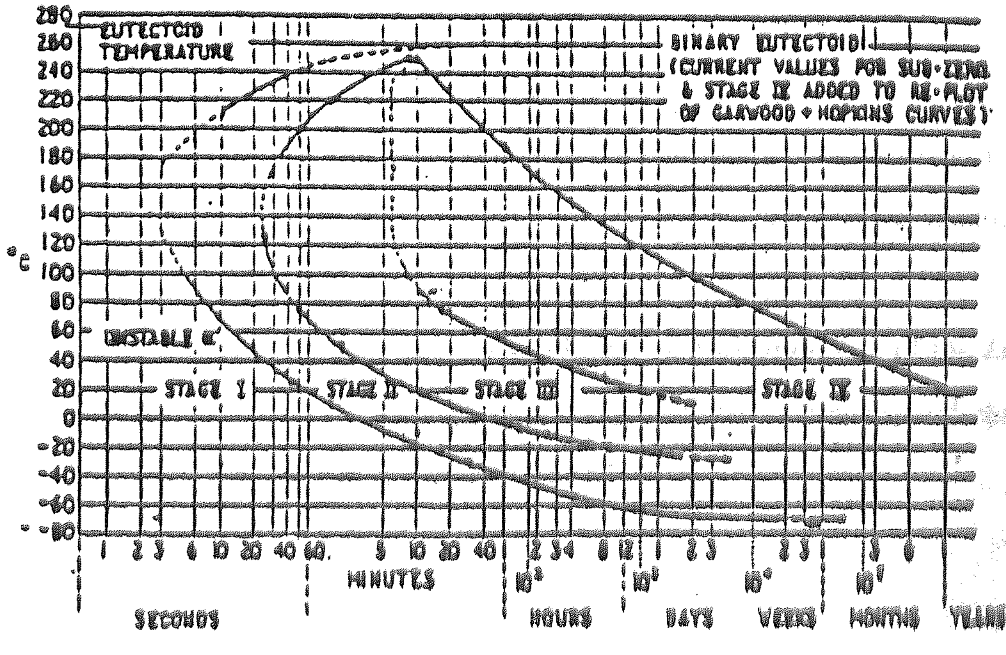

Figure 22 TTT Diagram for Zinc-Aluminium Eutecroid Alloy according to Smith and Hare(108)

2.5.2 Ternary Zn-Al-Cu Alloys.

Although a large number of researchers have investigated the Zn-Al-Cu phase transformation, but still up till now the ternary phase diagram of this system is only partially established in comparison with the Zn-Al binary system. The effect of copper on the mechanism of phase transformation in the Al Zn_{20} Cu_2 alloy was investigated by Truszkowski, Dutkiewicz(112).

Their work involved X ray diffraction, TEM and hardness testing. The decomposition of the supersaturated phase was found and a tetragonal deformation inside the GP zones was observed in the first stage of ageing after quenching (The same as in binary alloys). At the 2% level and upon ageing at room temperature, copper-rich zones are formed. These zones are unstable at room temperature which then transform through intermediate reactions to form a new phase ε :

α (α') or β ===> $\alpha + \eta + \varepsilon$

This reaction is then followed by a four-phase reaction below 273 °C(109).

to form the stable Cu-rich phase T' (72,79,113,114,115).

$\alpha + \varepsilon$ ===> T' + η

This transformation is very slow as it involves the long range diffusion of copper, which requires months or years to be completed at room temperature.

Koster(116) suggested that due to this slow transformation, the sample suffered an increase in the volume of about 4%, while on the other hand Gebhardt reported an increase of 0.53% in the linear dimension of his sample due to the above mentioned reaction, corresponding to a volume increase of 1.6%.

Thus as well as retarding the exceptionally high transformation rate of the Zn-Al binary alloys(115,116,117)copper also causes an undesirable dimensional change when the alloy is subjected to ageing(51,84,115,118)

CHAPTER 3

3.1. Fatigue Definition and Historical Review

The term fatigue has been used throughout history to define a reduction in efficiency of human or animal muscles after prolonged activity. This term is still used today but now, since the advent of machines and technology, it is also used to define the reduction in the ability of metals or components to withstand repeated variations of loads and stresses.Furthermore, fatigue is defined as the tendency of a material to fracture by means of a progressive brittle crack under repeated alternating or cyclic stresses of an intensity considerably below the nominal strength. Although the fracture is of a macroscopically brittle type, it may take some considerable time to propagate, the time depending on both the intensity and frequency of the stress cycle, nevertheless there is very little if any warning before failure, if the crack is not noticed. Probably the majority of engineering failures are of fatigue nature in origin.

3.2 The Appearance and Nature of Fatigue Fractures

The study of the appearance of fatigue fractures can be divided into two objectives :

1)The practical objective of learning to diagnose failure by fatigue.

2)The long range objective of deducing information concerning the basic nature of fatigue by identifying and differentiating between ductile and brittle fractures(119). Figure 23 shows the ductile (A) and brittle (B) fractures of the same material. It must be acknowledged, however, that not every brittle fracture is necessarily a fatigue fracture. Further examinations are necessary to identify the nature of the fracture(120). For example certain cast irons and other materials including zinc alloys reveal brittle fractures in normal tensile loading at room temperature. Steels, which are usually thought of as ductile, can fail in a brittle manner at low temperatures, or under very high-speed loading, or when sharply notched. Although a brittle fracture may be due to fatigue, one can not be absolutely certain and further investigations are required .

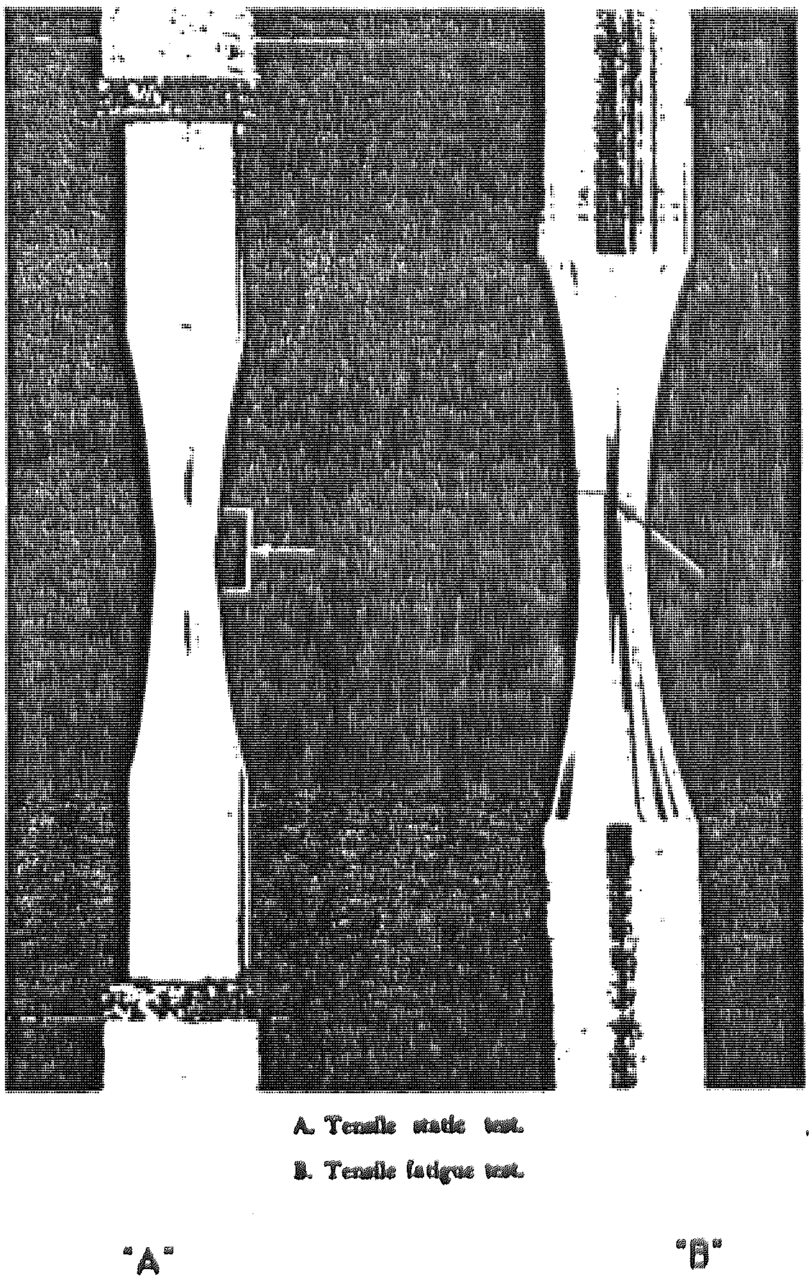

Figure 23 Failure of Steel Bars in Laboratory Tests.

Fatigue cracks start at some nucleus(121) and progress during successive cycles of stressing, without causing large-scale plastic deformation. The fracture may be completed by eventual overstressing after the crack has reduced the cross section of the piece, this latter part of the crack may show evidence of large scale plastic deformation. Examination of fatigue fractures reveals evidence of microscopic deformation, even in the seemingly brittle region of origin and propagation of the crack. Gough and Wood(122) reported that a microscopic slip generally precedes fatigue cracking. However, slip bands have also been observed after repeated stressing below the fatigue limit and without starting a fatigue crack. At any rate, the plastic deformation is usually limited in extent to regions very near the crack.

It seems that when a fatigue crack starts, it follows a path of least resistance(123) through the metal, and very often crosses grain boundaries, whilst in occasional instances, cracks have been observed to branch around grains. Indeed, fatigue cracks tend not only to commence at faults and inclusions in a metal but often they will propagate along lines from one fault or inclusion, to another.

During investigations using X-ray diffraction to study the changes which occur in metallic structures with the progress of fatigue, changes under repeated stresses lower than the fatigue limit of a metal have been found not to be much different in appearance from changes observed under static loading at similar low stress levels. Higher repeated stressing produces severe lattice distortion(124) before fatigue fracture occurs. However continuous and cumulative lattice changes during the whole progress of fatigue are seldom measurable.

3.3 Structural Failure By Fatigue.

Fatigue failure occurs in two main stages:

1) Crack initiation (nucleation), where a crack starts and spreads out from some nucleus.

2) Crack propagation, where the crack continues through the object until final

rupture. The relative proportion(125) of the total cycles to failure that are involved with each stage depends on the test conditions and materials. However, it is well established that a fatigue crack can be formed before 10% of the total life of the specimen has elapsed. There is of course, considerable ambiguity in deciding when a deepened slip band should be called a crack .

3.3.1 Mechanism of Crack Initiation

Fatigue cracks are usually initiated at a free surface(126), while in those rare instances where fatigue cracks initiate in the interior, there is always an interface involved. Fatigue has certain things in common with plastic flow and fracture under static or unidirectional deformation .

Gough(127) showed that a metal deforms under cyclic strain by slip on the same atomic planes and in the same crystallographic directions as in unidirectional strain. However, with unidirectional strain, slip is usually widespread throughout all the grains.In cases of fatigue some grains will show slip lines while other grains will give no evidence of slip .

Slip lines are generally(128) formed during the first few thousand cycles of stress. Successive cycles produce additional slip bands, but the number of slip bands is not directly proportional to the number of cycles of stress.

In many metals the increase in visible slip soon reaches a saturation value, which is observed as distorted regions of heavy slip.

Cracks are usually found to occur in regions of heavy deformation parallel to what was originally a slip band. Slip bands have been observed at stresses below the fatigue limit of ferrous materials. Therefore, the occurance of slip during fatigue does not in itself mean that a crack will form .

A study of crack formation in fatigue can be aided by interrupting the fatigue test to remove the deformed surface by electropolishing.

There will generally be several slip bands which are more persistent than the rest and which will remain visible when the other slip lines have been polished away.

Such slip bands have been observed after only 5% of the total life of the specimen(129). These persistent slip bands(130)are embryonic fatigue cracks, since they open into wide cracks on the application of small tensile stains. Once formed, fatigue cracks tend to propagate initially along slip planes, although they later take a direction normal to the maximum applied tensile stress.

Fatigue crack propagation is ordinarily transgranular (131). An important structural feature which appears to be unique to fatigue deformation is the formation on the surface of ridges and grooves called slip-band extrusions and slip-band intrusions.(132). Extremely careful metallography on tapered sections through the surface of the specimen has shown that fatigue cracks initiate at intrusions and extrusions(133).

Considerable experimental evidence indicates that cross slip is important to the slip-band extrusion process. For example, fatigue failure is difficult to produce in certain ionic crystals which do not easily cross slip,and it is very difficult to produce fatigue failure in zinc crystals which are oriented to deform only in easy glide. Pure aluminum, in which cross slip is extremely easy, does not produce slip-band extrusions (in contrast to most aluminum alloys).

A basic mechanism for producing slip-band extrusions and intrusions was proposed by Wood(134) He determined that microscopic observations of slip produced by fatigue show that the slip bands emanate from a systematic build up of fine slip movements. These movements are of the order of 1 nm, unlike steps of 100 nm to 10 nm observed for static slip bands.

This type of mechanism is believed to allow for the accomodation of the large total strain (summation of microstrain in each cycle) without causing appreciable strain hardening.

Wood's idea (134), showing how continued deformation by fine slip could lead to a fatigue crack, is illustrated in Figure 24. It indicates schematically how the fine structure of a slip band is seen with the electron-microscope. Section (24a) shows that slip from static deformation produces a contour at the metal surface. Conversely, the back and forth fine slip movements of fatigue may create notches (24b) or ridges (24c) at the surface.

The notch would be a stress raiser with a notch root of atomic dimensions.Such a situation might well be the start of a fatigue crack .This mechanism for the initiation of a fatigue crack is in agreement with the facts that fatigue cracks start at surfaces and that cracks have been found to initiate at slip- band intrusions and extrusions .

There is a large similarity between the dislocation structure produced by fatigue and static deformation.The formation of a dislocation cell structure is favoured by a large strain amplitude and a high stacking-fault energy ,both of which are factors favouring cross slip .At low strain amplitudes dislocation loops and dipoles are widespread.There is strong evidence that cell formation is related to the development of slip bands .

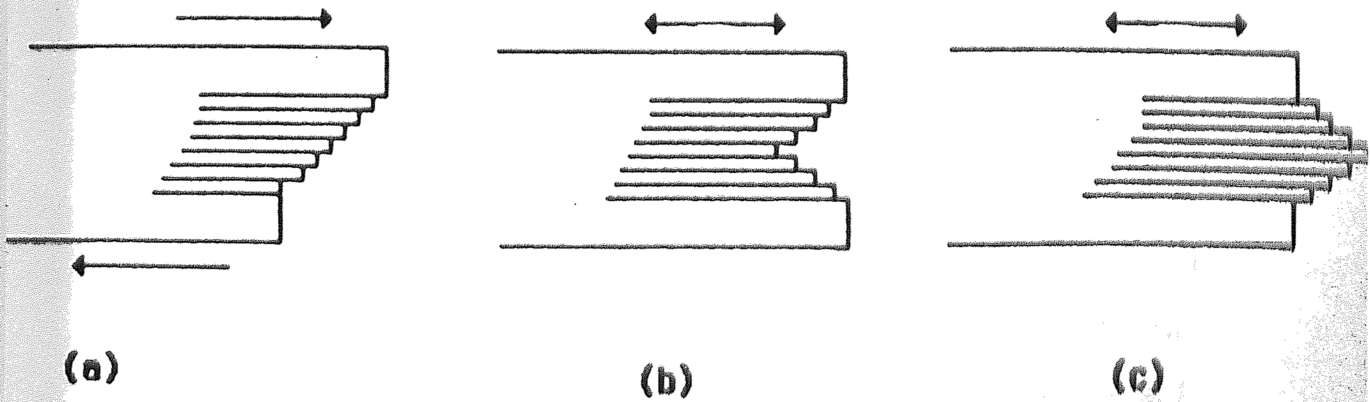

Figure 24 W.A.Wood's Concept of Microdeformation Leading to Formation of Fatigue Crack.

a) Static deformation

b) Fatigue deformation leading to surface notch (intrusion)

c) Fatigue deformation leading to slip-band extrusion.

3.3.2 Mechanism of Crack Propagation.

The crack initiation stage ends in the formation of surface microcracks. These microcracks lie along the active slip planes, in which the shear stress has maximum values. The rate of crack growth depends primarily upon the amplitude of the cyclic stress or strain, the material characteristic and the geometrical configuration of the specimen, and the environmental test conditions. As the number of slip systems in most metals is relatively high, those active slips having an orientation near the maximum shear-stress planes, will propagate thus the planes of microcracks are always inclined approximately 45°(135) to the of the applied stress vector In the course of further cyclic loading, the microcracks grow and link together. A great majority of these microcracks stop propagating quite early and only some achieve a length (or rather depth) greater than a few tens of microns. With increasing length the growing microcracks tend to propagate perpendicular to the stress axis. This transition of the crack plane from the active slip plane to a non-crystallographic plane perpendicular to the stress axis is often called the transition from stage I (crystallographic propagation) to stage II (non crystallographic propagation). In stage II of fatigue crack propagation only one crack is usually propagating, all others stop well within stageI.

Both stages are shown in Figure 25. Sometimes stage II does not occur at all, and the whole propagation right through the fracture is of the stage I type(136). The lower the stress amplitude, the higher the crack length corresponding to the stage I-stage II transition. As the crack propagation rate in stage I is generally much lower than that in stage II, the number of loading cycles spent in stage I propagation may be much higher than that spent in stage II propagation (this case occurs when unnotched specimens are used)

The number of cycles necessary for stage I propagation in sharply notched specimens becomes negligible and the whole fatigue crack is of the stage II propagation. The rate of crack propagation is normally expressed as da/dn, where da is the increment of crack length, dn is the increment of number of cycles.

An early attempt to relate da/dn to the range of applied stress, $\Delta\sigma$ was made by Frost and Dugdale (137) :

$da/dn = (\Delta\sigma)^3 a/c$

Where c is a material constant

Furthermore modifications to this relationship were made by Liu (138,139)

giving : $da/dn = A (\Delta\sigma)^2 a$

Where A is the material constant

The stage I crack propagates initially along the persistent slip bands.

In a polycrystalline metal the crack may extend for only a few grain diameters before it advances into stage II. The rate of crack propagation in the first stage is generally very low, of the order of nm per cycle, in comparison with crack propagation rates of µm per cycle in the second stage .

By marked contrast the fracture surface in the second stage of crack's, shows a pattern of ripples or fatigue fracture striations (Fig.26). Each striation represents the successive position of an advancing crack front that is normal to the biggest tensile stress. Each striation was made by a single cycle of stress. The presence of these striations(140,141) unambiguously defines that failure was produced by fatigue, but their absence does not preclude the possibility of fatigue fracture. Failure to observe striations on a fatigue surface may be due to a very small spacing that cannot be resolved with the observational method used, insufficient ductility at the crack tip to yield a ripple by plastic deformation that is large enough to be observed, or obliteration of the striations by some kind of damage to the surface.

In the experimental ZA alloys, stage I must have gone very quickly to stage II due to the improbability of finding a suitable slip system.

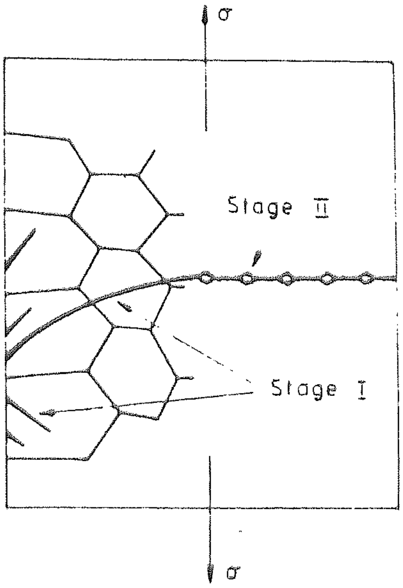

Figure 25 Stages of Fatigue-Crack Propagation.

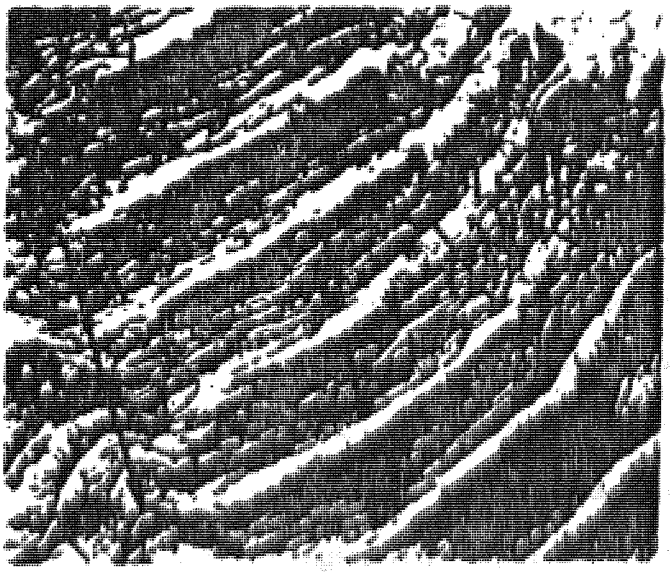

Figure 26 Fatigue Striations in Cold-Worked Copper.

3.4 Means of Approaching the Fatigue Problem.

The fatigue life of a component can be estimated or determined either by using the conventional S/N curve or by the fracture mechanics approach.

3.4.1 The S/N Curve Approach.

For evaluation of the basic fatigue strength of materials, machine parts or a whole structure, the Wohler curve (S/N curve) is useful, here the fatigue behaviour of a metal is determined by taking a number of carefully prepared samples and subjecting them to endurance tests under a particular system of stresses. When a specimen breaks the range of applied stress and reversals to failure are noted. The next specimen is tested at a lower range and so on.Finally, a stress range is reached at which fracture does not occur within 10^7 to 10^8 reversals. The curve obtained by plotting the range of stress S against the number of cycles N, tends to become parallel to the N axis. The degree to which this tendency is found in any particular metal has sometimes been ascribed to resistance to atmospheric corrosion within the usual range of speeds of stress reversals.It takes a number of weeks to reach 10^7 - 10^8 reversals.

However increasing demands on machines$^{(142)}$, regarding both performance and weight, lead to the need to design structural components not only in the classical way for infinite life, but some of them also for finite life. In this case the S/N curve fails. While in the case of a high number of cycles to fracture, the resistance of material against the cyclic stress might be considered of primary importance, in a low number of cycles to fracture (say $10^2 < N < 10^5$) the resistance against the cyclic plastic strain is much more important. Thus another fatigue life curve, based on the plastic strain amplitude,became a necessity for engineering purposes. For notched parts, especially those designed for finite life, the fatigue life predection requires both the stress and plastic strain based material characteristic.

The calculation of the fatigue life of parts containing crack-like defects can best be performed by the application of fracture mechanics. Criteria of material resistance against fatigue which are generally valid can only follow from a deeper understanding of the nature of cyclic deformation processes. The relationships(135) between cumulative damage, the intensity of the cyclic plastic strain and irreversible absorbed energy made it possible to formulate both deformation and energy criteria for fatigue failure. Their particular aim is to offer a basis for evaluating methods for fatigue life calculations in real, complex service conditions.

Further examples of tendencies in fatigue behaviour may, however, be presented if the time-dependent ageing characteristics of metals are considered. On this basis we may consider metals and alloys in three groups: firstly metals which can undergo considerable strain ageing at the temperature of the endurance test, secondly metals in which no prominent ageing effects is found, and finally alloys, which have their useful strength properties conferred upon them by precipitation hardening treatments and whose ageing characteristics extend to an over-aged state with a fall in hardness and tensile strength.

Extensive and comparable data for iron and mild steels, copper and brass and precipitation-hardened aluminum alloys may be drawn upon to illustrate details of fatigue characteristics for each group. It has long been known that iron and mild steel give a very sharp endurance limit and Figure 27 shows typical curves for 0.93%C steel after different heat treatments(143).While the limiting range of stress is well marked for each heat treatment, it can be observed that, apart from the hardened troostitic structure, there is a complete absence of fracture points between values of N from a few million to one hundred milion. This remarkable failure was most apparent with the simple steels used by the earliest workers, thus the classical concept of an endurance limit implied that only a relatively brief period of stressing was needed in order that it may be developed .

The S-N relation for copper shows, by contrast, a failure point throughout the range of N that can be conveniently investigated. An appreciable scatter in the S-N experimental points exists for mild steel and copper, this factor is apparent to such a degree for the precipitation-hardened alloys as to be their distinctive feature.

Figure 28 shows the S-N relation for 24S-T aluminum alloys for different grain sizes It can be seen that breakages are found throughout the range of N and there is no endurance limit.(144)

However, only one type of the S/N curve can be considered as characteristic of the material- the case of homogeneous stress loading (push- pull loading) of smooth specimens. All other S/N curves, such as those obtained in cyclic bending or those obtained on notched bodies, reflect other factors as well as material properties. Figure 29 shows two curves depicted schematically. Curve (a) is typical in that it shows an asymptotic approach to a limiting value, the fatigue limit σ_c, below which fatigue fracture is excluded, irrespective of the number of loading cycles. Such behaviour is typical mainly for steels and other interstitial alloys. In the case of curve (b) the stress amplitude decreases steadily with increasing number of cycles to fracture in such a way that the rate of decrease is lower for a higher number of cycles, but there is no clear fatigue limit as in the preceding case. Instead the endurance limit is usually defined as the stress amplitude corresponding to a number of cycles to fracture of $5x10^7$. The curve (b) behaviour is most often exhibited by aluminum alloys .For cyclic loading with controlled stress amplitude, the S/N curve can be determined for different values of mean stress and is presented for symmetrical cycling ($\sigma_m = 0$) and for pulsating cycling ($\sigma_m = \sigma_a$, σ_a being the fatigue-life curve). On these two curves the conventional division into different regions according to both the number of cycles and stress can be shown .The region of the number of cycles lower than N_c, where N_c represents the "Knee" on the curve ,or the region $N_f < N_c$, is sometimes called the finite-life region, contrary to the infinte-life region for $N_f > N_c$. Very high amplitude loading, in the case of symmetrical cycling, results in quasistatic fracture, and in the case of pulsating cycle, in dynamic creep. The low cycle fatigue region is usually understood to be the region $10^2 < N_f < 10^5$, and the high -cycle fatigue to be the region $N_f > 10^5$.

The Wohler curves are most frequently determined from stress amplitude controlled tests. The other possibility is strain controlled tests.

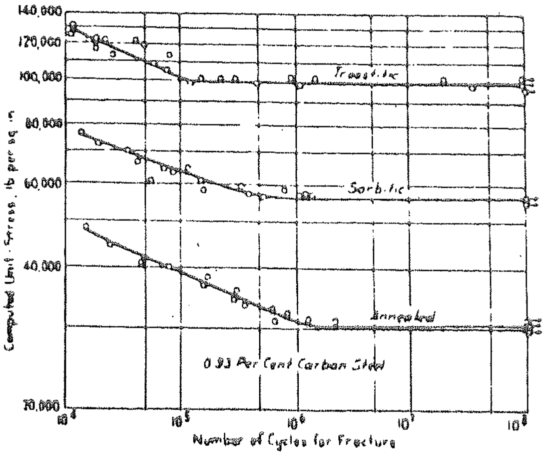

Figure 27 S-N Relation for Steel according to Moore$^{(143)}$.

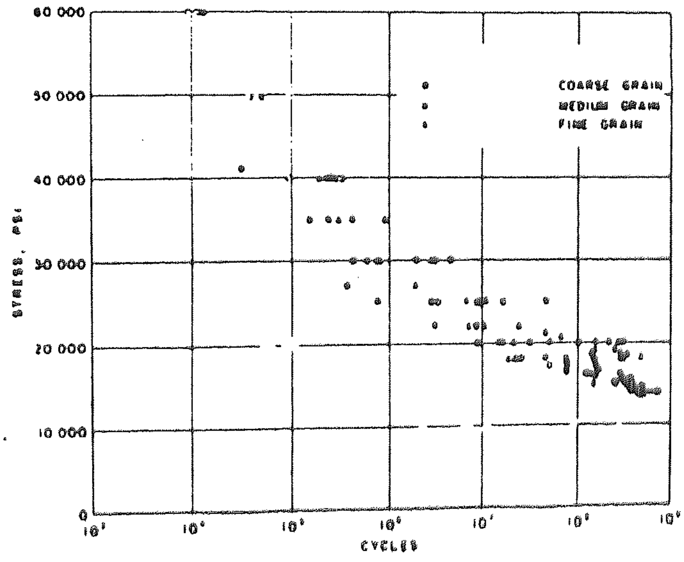

Figure 28 S-N Relation for Aluminium Alloy according to Templin$^{(191}$

The stress amplitude for construction of the S/N curve then follows from the simultaneous measurement of the cyclic stress-strain response, or rather, the cyclic stress-strain curve.

Many attempts have been made to formulate mathematical equations for S/N curves Some types of equations are necessary to develop experimental methods . One of the most useful equations was suggested by Weibull (145) These equations are based on the statistical theory of hyperbolic form :

$(\sigma - \sigma_c)^m N = K$ (for $\sigma > \sigma_e$)

where m and K are material constants, σe is the fatigue limit and σ and N are the variables .

This equation is mainly suitable for the long-life range and implies the existance of a fatigue limit .When taking logarithms of both sides the equation becomes

$m \log (\sigma - \sigma_e) = \log K - \log N$.

which indicates a linear relation between $\log (\sigma - \sigma_e)$ and $\log N$.

3.4.2 The Fracture Mechanics Approach

A crack represents a very effective stress raiser(146). The stress-strain response of the material surrounding the crack tip and the microstructural parameters of the material determine the behaviour of the crack under the action of external forces. The fracture mechanics approach is a study of the parameter $\Delta K/\rho^{0.5}$, where ΔK is the stress intensity amplitude calculated by taking the notch as a crack of the same length and ρ is the notch root radius.

To enable the prediction of fatigue life and performance of a cracked material it is important to consider fracture toughness, the analysis of stress state for the loading conditions, the nature of crack growth, and fracture criterion. Stress analysis and particularly stress intensity factors, are evaluated generally by either analytical and / or numerical methods(147).

3.4.2.1 Linear Elastic Fracture Mechanics.

The fracture toughness approach involves a quantitive study of the stress intensity ahead of a crack tip.Linear elastic fracture mechanics are based on the stress field magnitude and distribution in the vicinity of a crack tip in relation to the nominal stress applied to the structure and to the size, shape and orientation of a crack or defect and to the material properties.

Westergaard(148) proposed two equations, shown in Figure 30, to describe a body subjected to tensile stresses normal to the plane of the crack in relation to the crack tip. Figure.31 shows the three crack displacement modes: the opening mode (I), the sliding mode (II), and the tearing mode (III)(149).

3.4.2.2 Griffith's Theory

Griffith(150) acknowledged the fact that defects give rise to and promote cracks in any component subjected to stresses. Fracture mechanics is a method of stress analysis which allow the determination of the stress field ahead of a sharp crack in terms of the stress intensity factor K, which relates to both the nominal stress level and the size of crack present in the structure to be evaluated.

Griffith's analysis was based on energy conditions. If an infinite plate of unit thickness, containing a through thickness crack of length 2a, is subjected to a uniform tensile stress σ, applied at infinity, then the potential energy of the system U may be written as

$U = U_0 - U_a + U_\gamma$..........(1)

where U_o = elastic energy of the unnotched plate

U_a = decrease in elastic energy caused by introducing the crack in the plate.

U_γ = increase in the surface energy caused by the formation of the crack surfaces.

Applying the stress analysis developed by Inglis (151), it can be shown that.

$Ua = \pi\sigma^2 a^2 / E$.........(2)

and $U\gamma = 2 (2a \gamma_e)$............... (3) where γ_e = elastic surface energy of the material per unit area

and a = crack length.

The total elastic energy, U is thus:

$U = U_o - \pi \sigma^2 a^2/E + 4a\gamma_e$............(4)

If the first derivative of U is made zero with respect to a then

$\sigma a^{0.5} = (2 \gamma_e E / \pi)^{0.5}$................(5)

As E and γe are material constants then the critical value $\sigma a^{0.5}$ must be exceeded before crack extension occurs.

Rewriting equation 5.

$\pi\sigma^2 a/E = 2\gamma_e$............(6)

where the left hand side of the equation is equal to the energy release rate G and the right hand side represents the materials' resistance to crack extension.

3.4.2.3 Stress Intensity Factor.

The work of Irwin (152) and Orowan (153) suggests that Griffiths achievements can be improved for brittle materials and metals exhibiting plastic deformation. By incorporating the plastic strain work γ_p into equation (6) the materials' resistance to crack extension can be equated to the sum of the elastic surface energy and the plastic strain work accompanying the crack extension.Hence,

$\pi\sigma^2 a/E = 2 (\gamma_e + \gamma_p)$...........(7).

Irwin(154) defined Gc as a material property, this being the total energy absorbed during cracking per unit increase in crack length per unit thickness. This is equivalent to $2\gamma_p$, as γ_e can be ignored as it is two to three orders of magnitude less, so equation (7) becomes

$Gc = \pi\sigma^2 a/E$...........(8).

Irwin further suggested that Gc was equivalent to Kc, the critical stress intensity factor. The stress intensity factor is related to the magnitude of the elastic stress field in the vicinity of the crack tip, hence Kc is the level of stress distribution necessary to permit fracture.

Irwin later suggested a relation ship between Gc and Kc which is

$Kc = (E' Gc)^{0.5}$ ....(9)

where $E' = E$ for plane stress conditions (thin section)

$E' = E/(1- \nu^2)$ for plane strain conditions (thick section)

and ν = Poissons ratio

Then for a through thickness crack of length 2a

$Kc = \sigma (\pi a)^{0.5}$.............(10).

And the Griffith equation can be modified to become

$\sigma f = (E\ Gc/\pi a)^{0.5} = Kc/(\pi a)^{0.5}$............(11)

where σf = gross fracture stress.

Hence σf is not a material property, since it depends on the absolute size of the crack or defect.There will exist a critical sized defect for a given applied stress, so this favours the use of Kc as opposed to Gc. Consequently, by using Kc, the comparison of fracture resistance of different materials at equivalent stress levels does not necessitate a knowledge of Young's Modulus.

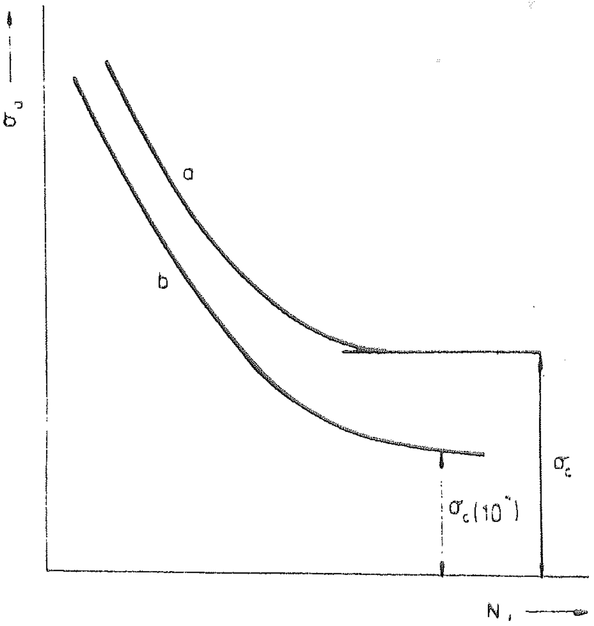

Figure 29 Schematic Drawing of Fatigue-Life Curve σa vs Nf.

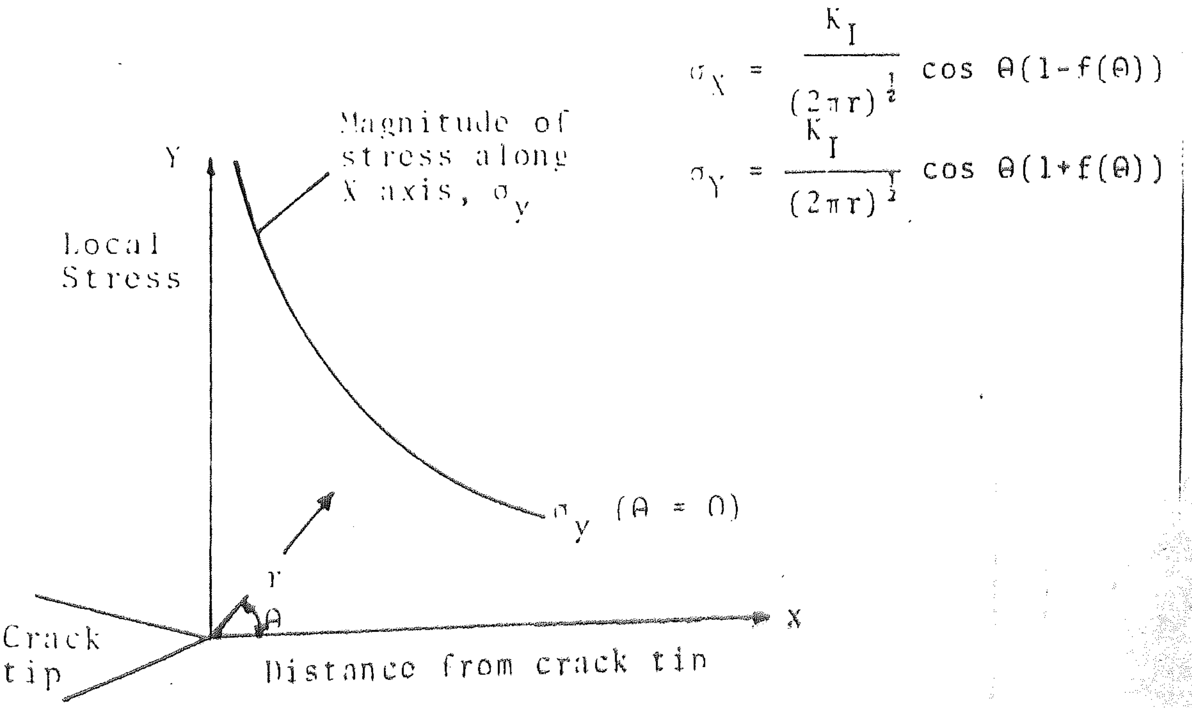

$$\sigma_X = \frac{K_I}{(2\pi r)^{\frac{1}{2}}} \cos \theta(1-f(\theta))$$

$$\sigma_Y = \frac{K_I}{(2\pi r)^{\frac{1}{2}}} \cos \theta(1+f(\theta))$$

Figure 30 Elastic Stress-Field Distribution Ahead of a Crack.

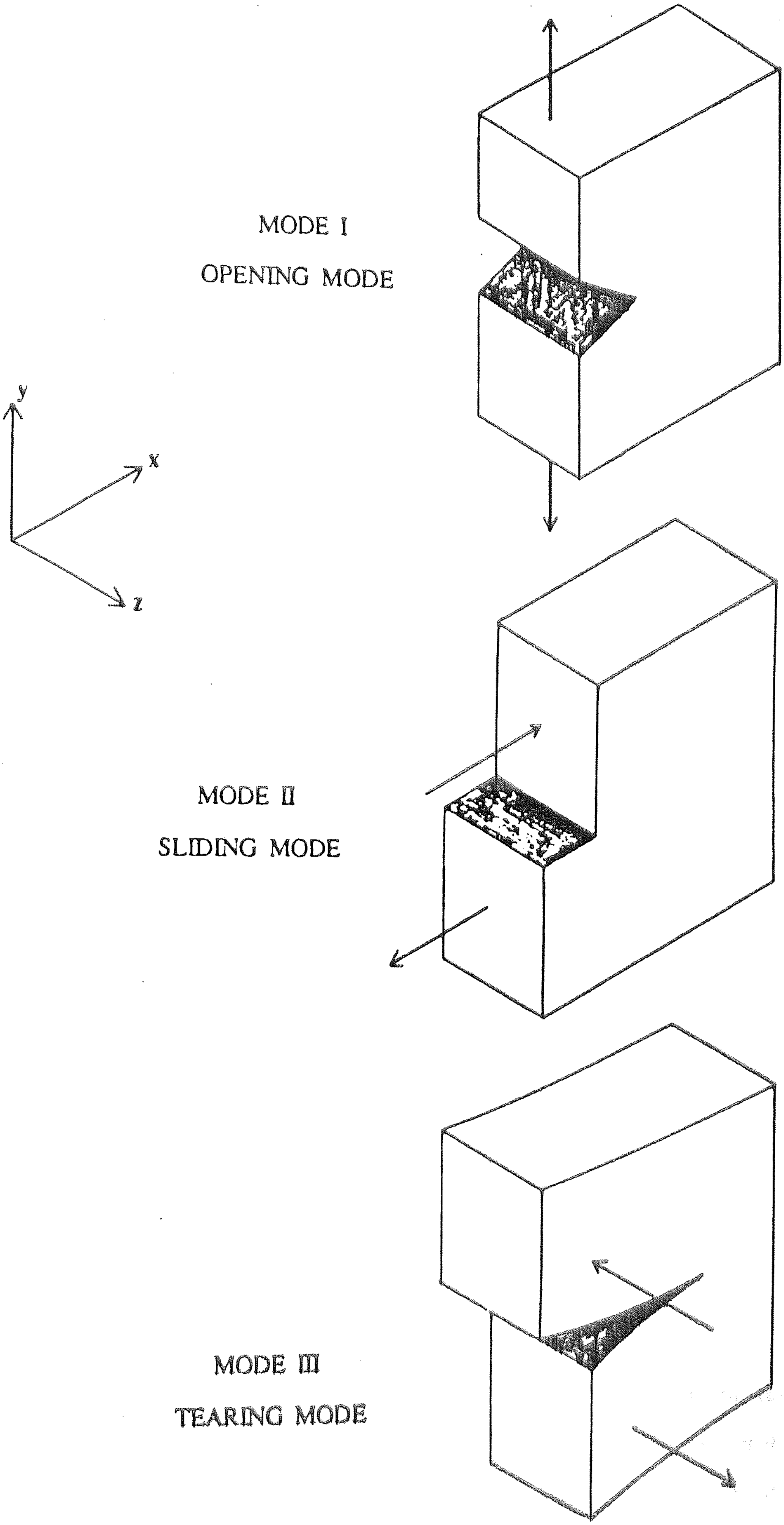

Figure 31 Three Modes of Crack Surface Displacements.

3.5 Fatigue Life Prediction.

No progress can be achieved at this stage unless the fatigue life under random loading is to be theoretically predicted under the assumption that :

1) Material parameters, including cyclic-strain relation, are known.

2) The real spectrum has already been replaced by a full cycle spectrum using a proper cycle counting method. A problem arises at this stage, concerning how to relate these data to the resulting fatigue life, or in other words, seeking a law for summation of damage,knowing that fatigue damage is a very poorly defined term except for damage in the stage of crack propagation, where it is proportional to the crack length. Then it is not possible to derive a general summations rule from the knowledge of the nature of the fatigue process. Thus, in nearly all cases, we must rely on empirical formulae.

3.5.1 Linear Summation of Cycle Ratios (Miner's Rule).

Miner's(155) hypothesis is propably the oldest cumulative damage hypothesis, which assumes that damage D for N cycles at the ith stress or strain level is given by

$D = N_i/Nf_i = (N/N_f)_i$

where Nf is the number of cycles to fracture at this level.

The ratio (N/N_f) is often denoted as cycle ratio $R_i = (N/N_f)_i$.

Fatigue life under the loading condition at further stress or strain levels is then given by the relation :

$\sum R_i = \sum (N/N_f)_i = 1$

3.5.2 Double Linear Summation.

Minor's rule for the crack propagation stage can be arranged so that the resulting equation includes the number of cycles(N_0) of nucleation, assuming that at the begining of the cycling of the specimen with crack length L_0, the counting of cycles starts with values N_o, resulting in

$\sum N/(N_{fi} - N_{oi}) = 1$

The number of cycles No can be understood to be the number of cycles at which the nucleation stage ends and the propagation stage begins. This suggests a double linear summation of cycle ratio, which was proposed by Grover (156) in 1959 in the form :

$\sum N_i/N_{oi} + \sum N_i/(N_{fi} - N_{oi}) = 2$

But the disadvantage of this summation lies in the determination of the end of the nucleation stage N_o. For this reason this method is not widely used.

3.5.3 Other Procedures

Attempts have been made to improve Minor's rule by proposing more complicated cumulative damage hypotheses.In Minor's hypothesis the damage is defined as a cycle ratio N/Nf =R and assumes that failure occurs for some ratios equal to 1.Other hypotheses proposed the preservation of the second condition (sum of damage equal to 1 at failure), but express the damage differently.Such hypotheses came from Cort and Dolan (157) .They state that;

$D = R^{\psi(\sigma_a)}$.

While Manson, Nachtigal and Freche (158) state :

$D = 1 - (1 - R)^{\psi(\sigma_a)}$ where ψ is a coefficient depending on the material strength

Other modifications were made (159-161), but none of these proposed the cumulative damage hypothesis, although the different stages of fatigue were taken into account they probably do not give better results than Minor's hypothesis.A further and more recent development on fatigue life prediction was made by, A. Buch, T. Seeger and M. Vormwald(162). Their work was based on improving the Miner's damage calculation, which is also called notch analysis(163,164). They stated that for damage calculation, according to the nominal stress approach (NSA), numerous constant stress amplitude test data (S/N/M lines for notched specimens) are required and cannot be found in hand books. The NSA does not allow for the loading sequence but does take into account the effect of specimen size, surface quality and fretting, all of which affect the S/N/M lines. Furthermore, for notch analysis, according to the local strain approach (LSA), only cyclic σ/ε and P/N lines for small, unnotched specimens are needed (P is the damage parameter). This type of analysis can allow for the effect of loading sequence on the crack initiation life, while it does not consider the surface quality, the fretting and the stress gradient. Both life prediction methods failed to give accurate evaluations of small frequent stress cycles which lie below the fatigue limit of the notched component. Therefore, the authors (162) have introduced the use of a method called "The Relative Miners Rule", to improve the NSA estimates. The basic assumption of this method is that, for sufficiently similar loading programmes, the deviations from

Miner's failure criterion have the same direction and similar realistic magnitudes.This means that when a test result for a suffeciently similar loading frequency distribution is available and the ratio N'expiremental/N'calculated may be estimated, it is possible to predict the fatigue life N" for the considered case from the equation N"/N"calc = N'exp/N'calc N" = N"calc N'exp/N'calc = N"calc C where C is a correction factor established from tests and calculation results for the related loading spectrum .In the case of these predictions it is important to consider that experience is needed to decide which two loading distributions are close enough to result in the successful application of a correction factor .It should also be noted that damage calculations in the case of NSA are mostly performed by various authors in quite a similar way .In contrast, the application of the LSA is characterised by numerous variants (165,166), and results from different sources can not be compared. Virtually no information is available for zinc-based alloys, therefore, for the purposes of this thesis, it was decided to determine the fatigue life of the zinc alloys by using the S/N curve for unnotched specimens as it is important to know this before going into the prediction techniques.

3.6 Factors Influencing the Fatigue Life of a Component.

3.6.1 The Effect of Notches on Fatigue.

The fatigue behaviour of a material depends on many variables associated with specimen preparation, environmental conditions, testing procedures and techniques ie; it is difficult to describe an absolute property in the fatigue context(167). In other words only a set of properties determined under closely specified and controlled conditions can be stated.

The basic and fundamental fatigue properties of a material, whether in the form of bar, sheet, casting or forging, are usually determined using carefully prepared, longitudinally polished, un-notched specimens tested in a normal laboratory environment. The precise size and shape of the specimen depends on the type of fatigue machines, the method of gripping employed, and the form and type of material being tested. All specimens must have a test section free of any intentional defects and stress raisers. There must be a gradual increase in section from the test section to the gripping portion of the specimen,and the proportions should be such that premature failure in the grips does not occur.

If a test piece of the same material contains a geometrical discontinuity, such as a notch, this discontinuity will give rise to a stress concentration(168). If the elastic stress concentration factor is known, then under ideal conditions the fatigue strength of the notched specimen would be defined as :

$$fn = \frac{fu}{Kt} \text{............} (1)$$

where fn =fatigue strength of notched test pieces

fu = fatigue strength of un-notched test pieces

Kt = elastic stress concentration factor.

Figure 32 shows the variation of the fatigue limit with specimens size of three steels using un-notched and notched specimens (169).

The notched test pieces were geometrically similar. In all cases the curves show appreciable variation of strength with size up to a certain diameter, above which it remains constant. This behaviour is not universal, but indicates a number of points that have to be explained.

Another noticeable fact is that the ratio between the fatigue strengths in the un-notched and notched conditions (fatigue strength reduction factor)

in no case equals the theoretical (elastic) stress concentration factor for the notch. The notch gives a theoretical factor of 2, while the specimens give fatigue strength ratios respectively for the three steels of 1.6, 1.7 and 1.8. This means that these results do not conform to the equation (1)

This deviation from equation is measured by the notch sensitivity of the material in an equation of the form

$$q = \frac{fn}{Kt - 1} \ldots\ldots\ldots\ldots (2)$$

where q is the notch sensitivity .

Notch sensitivity has a value of zero for the case in which the notched test piece has a fatigue strength as high as the un-notched one, and a figure of unity where the ratio of fatigue strengths is equal to the stress concentration factor.

An early paper (170) by R.E.Peterson shows the notch sensitivity for two steels plotted against the number of grains within 5% of the maximum nominal stress. These curves (Fig.33) suggest that by control of the ratio between the grain size and the volume of the material under a high stress, it is possible to get almost any value for notch sensitivity, even with similar materials. This does not mean that notch sensitivity is necessarily associated with grain size. It may be that in the case of Peterson's illustration, the grain size is merely indicative of some other factors in the structure of the material It is enough to show that the structure of the material is of great importance, and that it is not possible to state a single figure for notch sensitivity for any material. The diagram also confirms that there is a definite size effect for notch sensitivity as well as for the basic fatigue properties, and suggests

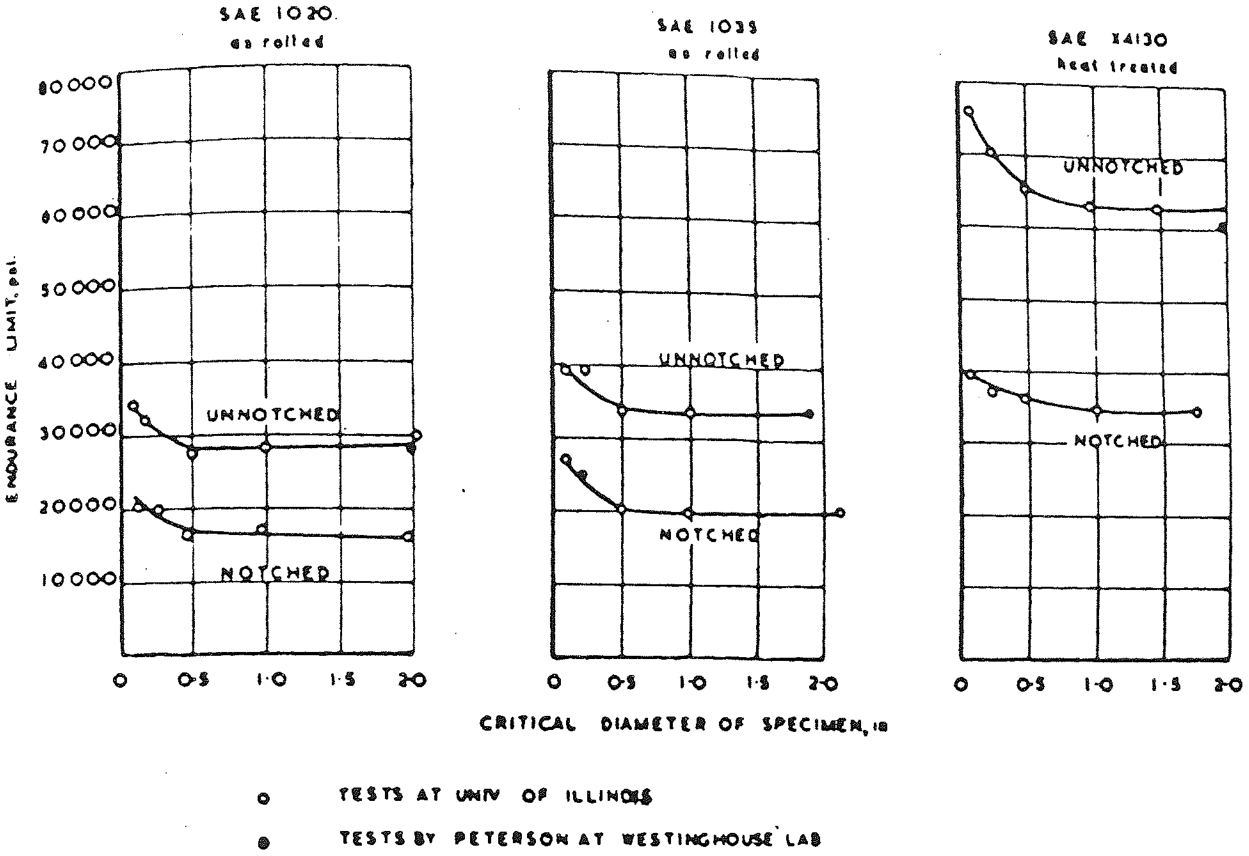

Figure 32 Effect of Size of Specimen on Endurance Limit of Unnotched and of Notched Rotating Cantilever Specimens According to Morkovin & Moore (169).

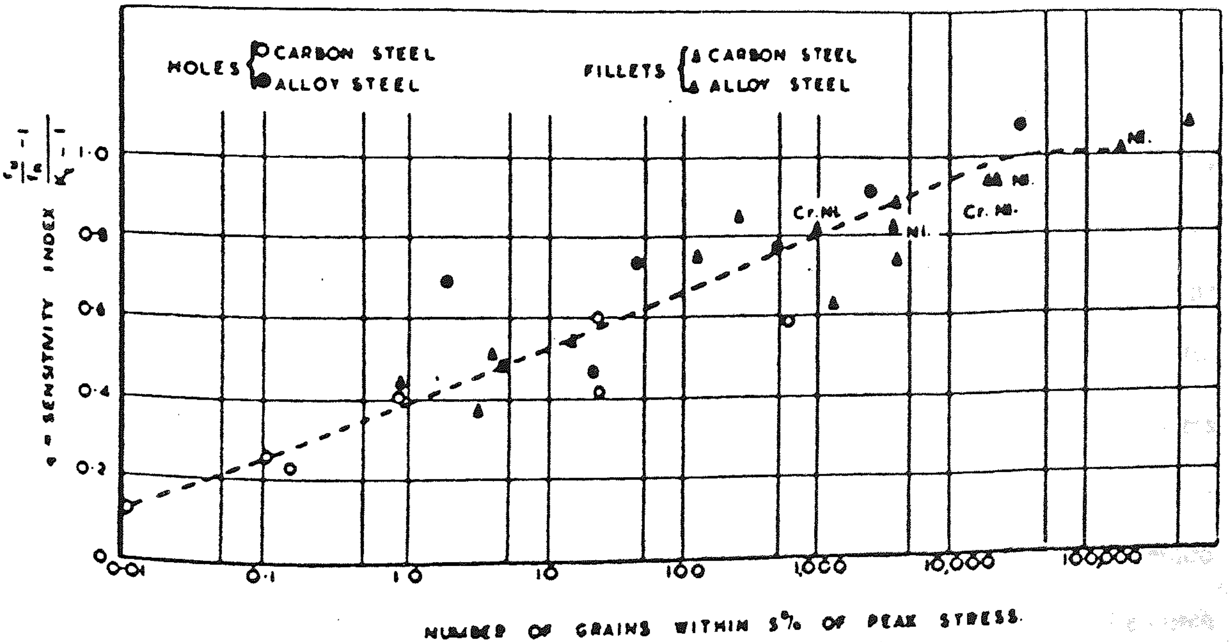

Figure 33 Correlation of Fatigue Tests of Stress Concentration Specimens By R.E.Peterson (170)

that for a given material, if a notched specimen is made large enough with respect to the metallurgical structure of the material (particularly when the root radius of the notch is large), a notch sensitivity of unity should be reached, which means that the notch reduces the strength of the specimen by a factor equal to the theoretical stress concentration factor.

Petersons' results also suggest that, if the specimen is made small enough (and the notch radius is small enough), a notch sensitivity of zero will be obtained. The inference that q shall tend to unity for large pieces seems quite acceptable because if a considerable volume of material is subjected to the high stress, it is reasonable to expect that volume behaves like an independent test piece. On the other hand, the opposite inference that q tends to zero for very small pieces, is less easy to assimilate because it implies that very high stresses developed only locally should have no effect at all.

Local strain and stress measurements at the notch root can give useful information for more precise fatigue life evaluation. The method generally used(171,172) in the evaluation of fatigue crack initiation life is based on the stress/strain concentration factor at the notch root and the small specimen simulation method. However, when used in cyclic fatigue tests, these methods do not always give an accurate prediction of the crack initiation life. Barson and McNicol (173) have used the fracture mechanics method to evaluate fatigue crack initiation life by using the stress intensity factor with flat notched specimens. However, in the crack initiation process, when the initiated crack (small crack) propagation has been located in the components, the application of the stress intensity factor is not appropriate. Hudak J.R (174) also stated that in crack initiation and small crack propagation, the evaluation by stress intensity factor is difficult.

A new evaluation was put forward by, T. Sato and H. Shimada(175).Their method assumes that measured maximum strain behaviour at the region local to the notch root during fatigue tests could systematically explain the crack initiation mechanism. Their test involved using low cycle fatigue conditions and the real time, fine grid method(175). The local maximum strain under loading must be measured continuously to evaluate the crack initiation life from the notch root. The results confirmed that the strain value at the first cycle of the fatigue test and the measured maximum strain value at crack initiation are nearly equal but the physical and the mechanical meaning of this phenomenon is not yet entirely clear.

3.6.1.1 Theories Explaining Size Effects and Notch Sensitivity Variation.

Notch sensitivity can be explained to some extent by these three hypothesis:

1) **The Elementary Block Concept.**

2) **The Inherent Flow Concept.**

3) **Non-Elastic Behaviour.**

1) The elementary block concept :

This concept has been developed by Newber(176). It is suggested that, although the stresses in a body are similar to those calculated from elastic theory, fatigue failure is governed not by the maximum stress present but by the average stress over an elementary block of finite size. Thus, the average stress over a certain block of material must reach a critical value to cause failure, rather than the maximum stress reaching a critical value.

The elementary block concept implies that the behaviour of the material will be closely linked with the stress gradient .This is demonstrated in Figure 34 where two similar cases of stress concentration over notches varying only in size are shown. The distance (d) is in each case the depth of the elementary block, and it can be seen that the actual stress in the case of the small stress concentration will be much higher than with the other.

This means that the nominal stress at failure of the small specimen will be greater than that of the larger one.

2) The inherent flow concept

This hypothesis was developed basically by Griffith (159) and it states that materials behave as if they contained large numbers of internal stress concentrations. These stress concentrations are referred to as "flaws" for convenience, although this is not meant to imply that the materials concerned are faulty. These inherent flaws are thought to be distributed randomly throughout the material and there are several ways in which they might be expected to behave, accordingly to how large and how numerous they are. Firstly, consider the case where they are small and in abundance. Then again, as in the elementary block theory, the behaviour of the material will be linked with the stress gradient. The reason for this is shown in Figure 35 which also shows the case of an external notch varying only in size. Where the notch islarge, the stress concentration factor for the flaw must be applied to the full stress at the notch root so that the actual stress at the flaw will be (fn x Kt x Kf)

where fn = nominal fatigue strength of notched specimens.

Kt = elastic stress concentration factor of notch.

Kf = effective stress concentration factor of flaw.

The actual stress of the nominally plain (notch-free) specimen will of course also be multiplied by Kf. ie.(fu x Kf), so that the actual reduction of strength fu/fn will be equal to Kt. This means that the notch sensitivity will be unity. In the case of the smaller notch, the stress concentration factor of the flaw is applied to a much lower stress value (see point "a" in Figure 35)and, therefore, the maximum actual stress due to notch and crack is much less than with the large notch.

This indicates that where the flaw is of the same order of size as the notch, the two stress concentration factors do not multiply together and, therefore, the external notch appears to have much less effect. With reference to this the question made by Moore, Lyon and Inglis (177) in 1927 is of interest.

"If the defects are large, then the stress raiser acts merely as one more defect and weakens the metal but little in addition. If a piece of metal has a hundred small holes drilled in it at random, it will not be greatly weakened by another small hole, but it will be appreciably weakened by a hole ten times the diameter of the small holes, even though the larger hole makes a negligible reduction of the area of the cross section of the piece ".

There is another aspect of the inherent flaw hypothesis which concerns flaws of relatively sparse distribution like, for example, some forms of porosity or intermetallic constituents. These may be distributed such that the probability of their occurrance on the surface (or in the volume) of notch-free specimens is very high, whereas the probability of their occurance at the root of a small notch is remote. The influence of such sparse flaws may be expected to be related to their frequency and magnitude.

Upon examinations of the experimental alloys, it was found that all these alloys had various degress of porosity.

3) Non-elastic behaviour .

Some materials can behave non-elastically for an infinite time under fatigue stress. The effect of this is shown in Figure 36 If we take into consideration the case of plain specimens under bending, or of notched specimens. Let AOB be the stress distribution according to elastic theory, and COD be the distribution under non-elastic conditions. In each case, the second moment of areas (for cylindrical specimens) beneath the two parts of the curves must be exactly the same, such that the specimens support the required load. It can be noted that the maximum stress according to elastic theory will be the values PA in each case, whereas the actual stress is equal to PC. This means that, where non-elastic behaviour occurs, the theoretical stress distribution in the specimen due to the assumption of elasticity is wrong. Apparent variations in notch sensitivity can occur which may not be real.

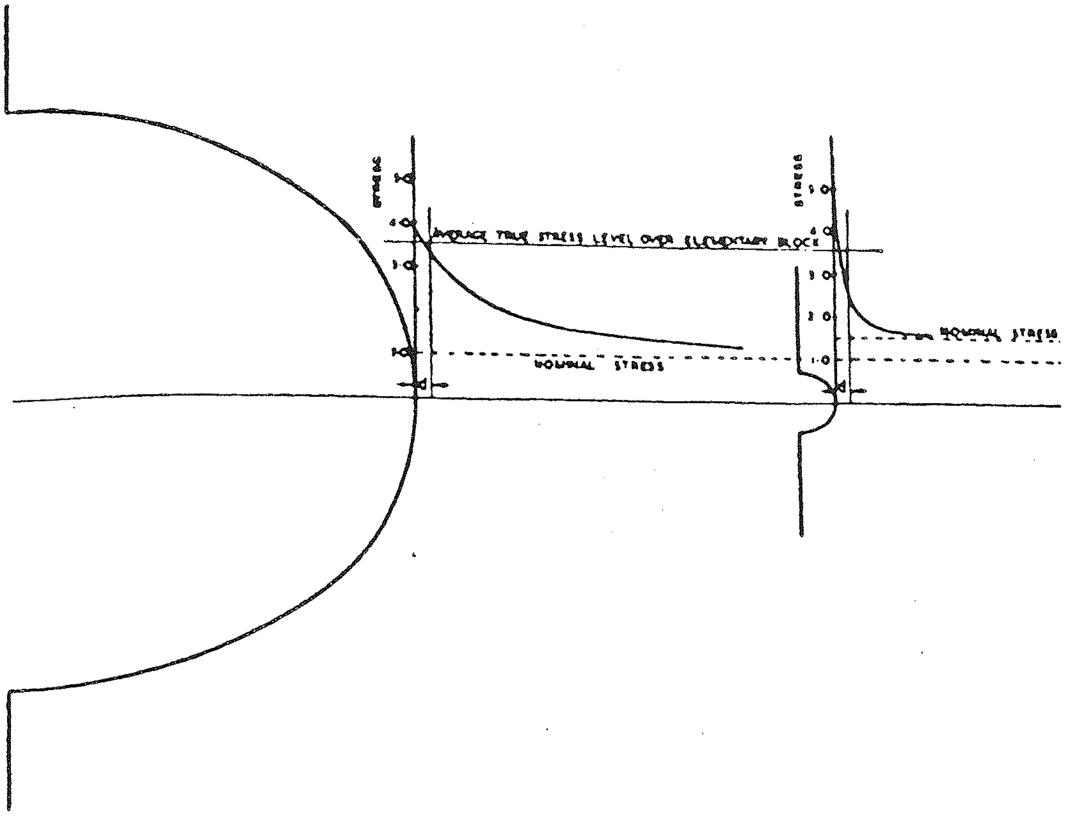

Figure 34 Effect of Notch Size-Elementary Block Theory.

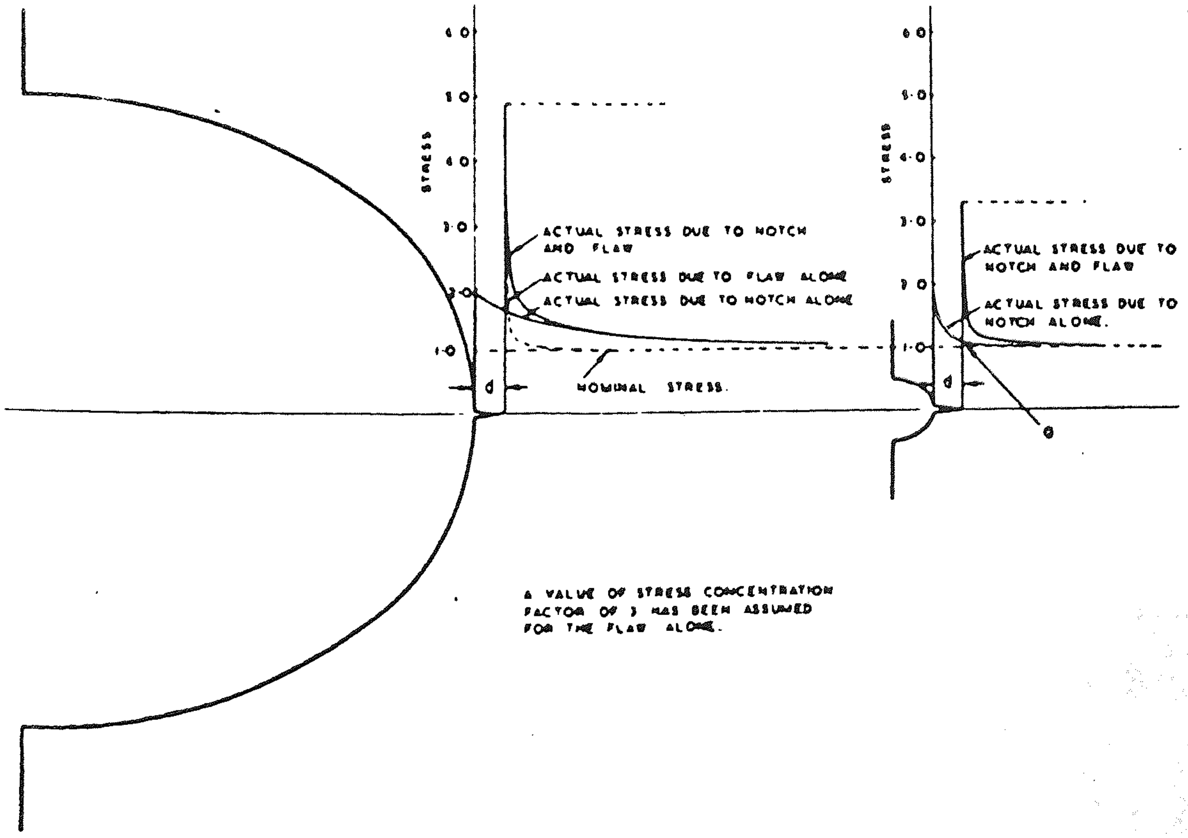

A VALUE OF STRESS CONCENTRATION FACTOR OF 3 HAS BEEN ASSUMED FOR THE FLAW ALONE.

Figure 35 Effect of Notch Size-Inherent Flaw Theory.

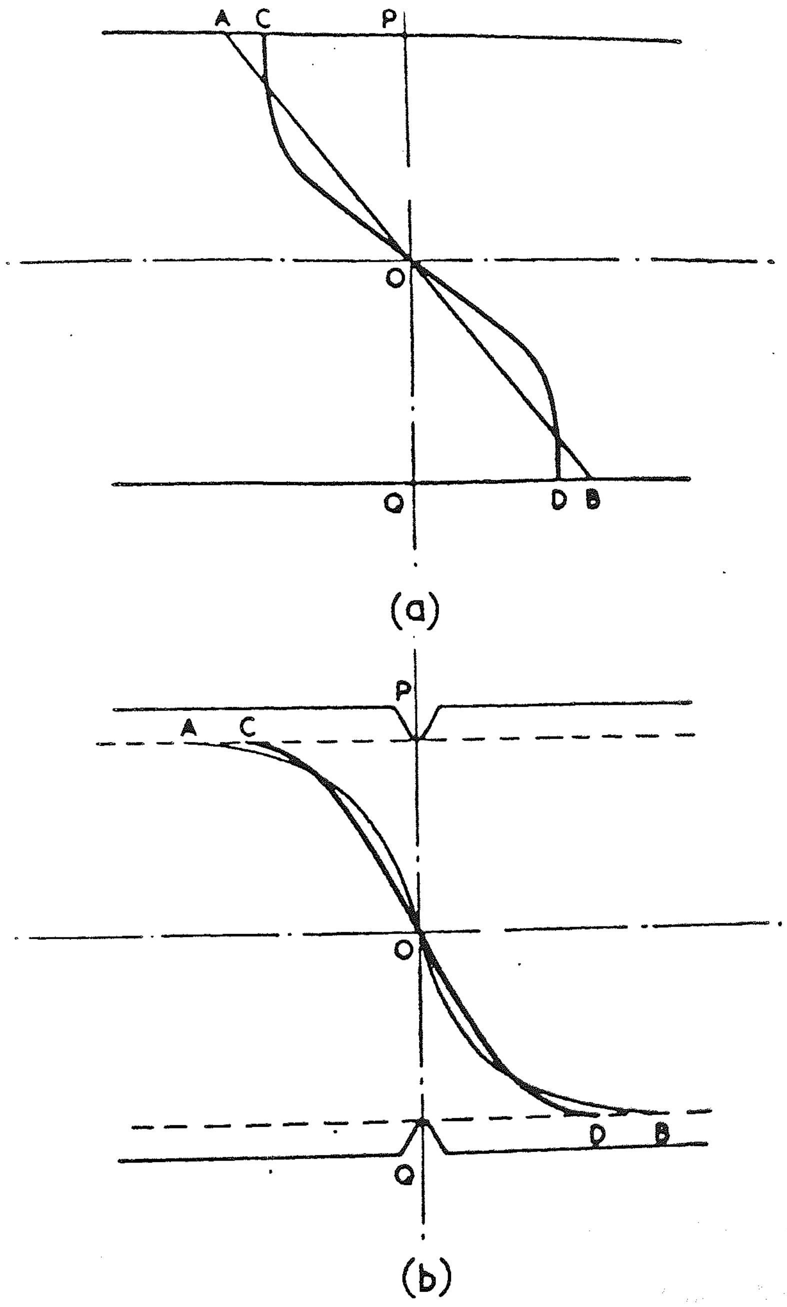

Figure 36 Non-Elastic Behaviour of (a) Plain Specimens under Bending and (b) Notched Specimens.

3.6.2 The Effect of Mean Stress.

Figure 37 shows test results recorded by J.O.Smith (178). In the case of un-notched test pieces the range of stress drops with increasing tensile mean stress as we would expect. However, with compressive mean stresses there is little change on the average up to considerable values, although some materials show a drop and others a rise. In the case of notched test pieces (Fig 38) attention is drawn to the sharp rise in stress range on the compression side of the diagram. It should be noted that Smiths' co-ordinates are not identical for the tension and compression diagrams, and that he regards as notched everything which has not got a smooth polished, surface . Gunn(179), who researched the effect of tensile mean stresses, has explained the shape of the R/M diagram (where R=range of stress, M=mean stress) for notched test pieces as follows (Fig.39). If AB is the R/M diagram for notch-free test pieces, assuming a constant strength reduction factor and elastic conditions, the curve expected for the notched test pieces would be CD, meaning that the intercepts on both axes are divided by the reduction factor. Moving along the curve CD from left to right, at some point the maximum cycle stress will equal the yield point of the material at CH (Fig 39) where the curve CD intersects the line EF which represents the yield point of the material divided by the stress concentration factor. From point H onwards for some distance, as higher mean stresses are applied, the mean stress of the specimen as a whole will be greater, but the mean stress at the root of the notch will stay constant, as a result of the yield. Therefore, the range of stress supported by the specimen will also stay nearly constant, as shown. This indicates that there should be a link in the R/M diagram for notched test pieces at a point not far distant from the zero mean stress axis Gunn (179)has shown that several experimental investigations fit this theory perfectly. With regard to the behaviour under compression ,the test findings by Moore, Lyon and Inglis(177) on cast iron prove interesting since the material in this case is like heavily-notched material (Fig 40), in that the range of stress associated with high compressive mean stress is far greater than those associated with zero or tensile mean stresses. It would be a matter

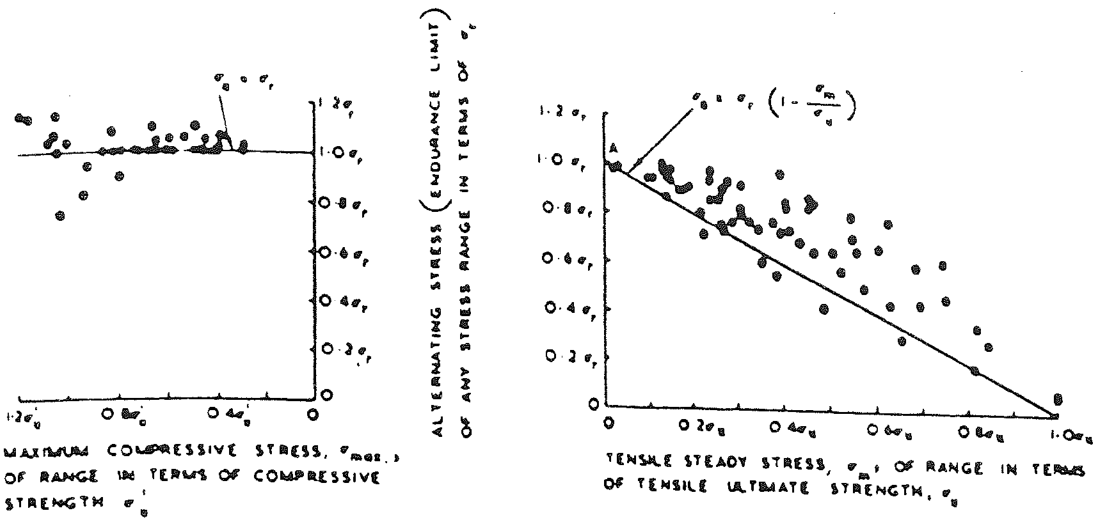

(b) Maximum stress—alternating stress diagram.
The steady stress was compression.

(a) Steady stress—alternating stress diagram.
The steady stress was tension.

Figure 37 Range of Stress Diagrams for Notch-Free Specimens of Thirteen Ductile Metals to Ranges of Repeated Axial Stress Superimposed on A Steady Stress(170).

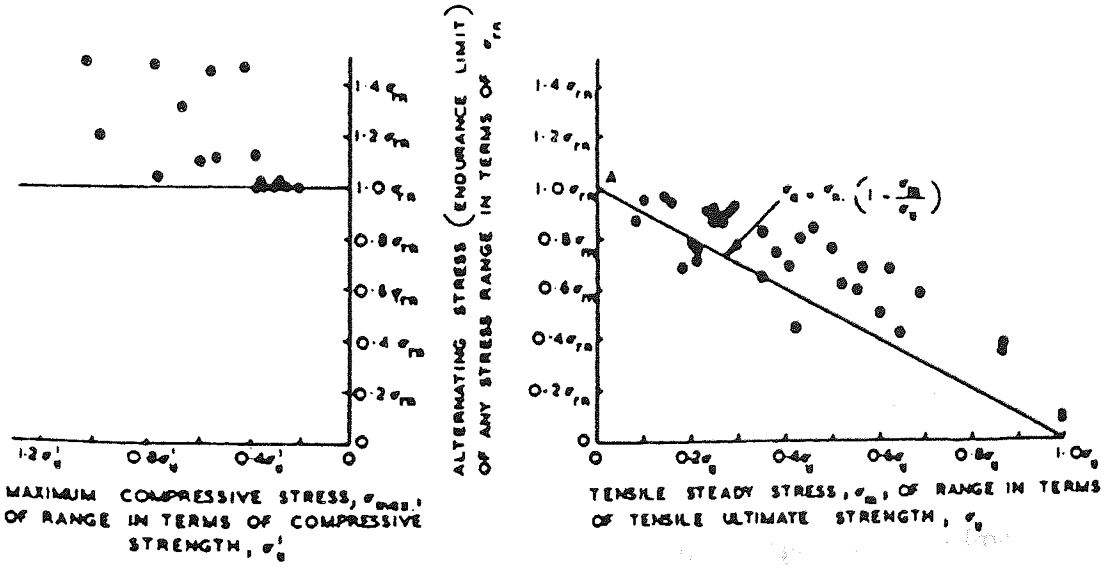

(b) Maximum stress—alternating stress diagram.
The steady stress was compression.
Eight ductile metals.

(a) Steady stress—alternating stress diagram
The steady stress was tension.
Fourteen ductile metals.

Figure 38 Range of Stress Diagrams for Notched Specimens of Ductile Metals Subjected to Ranges of Repeated Axial Stress Superimposed on A steady Stress(170).

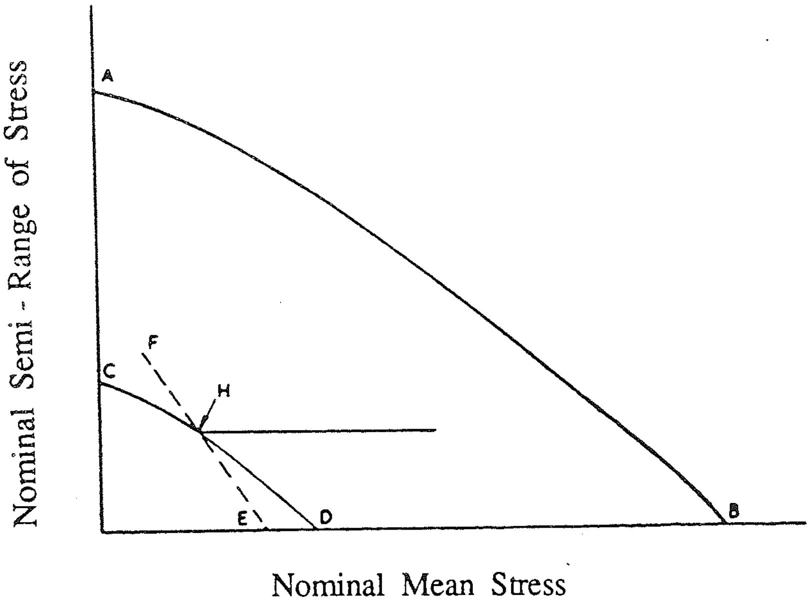

Figure 39 Effect of Mean Stress on Notched Test Pieces (178).

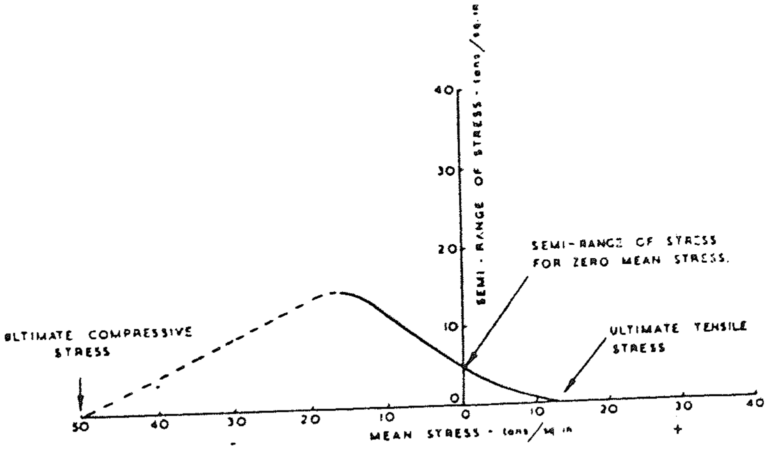

Figure 40 Range of Stress/Mean Stress Diagram for Cast-Iron. After Moore, Lyon and Inglis (177)

of great interest to discover whether tests on notched specimens of cast iron under compressive mean stresses manifest insensitivity to notches ,as in the case of tests with zero mean stress. The effect of compressive mean stresses in augmenting the range of stress associated with the notched test piece has been ascribed to the possibility of cracks forming but not progressing since they do not open and shut under the alternating stress, and can still transmit compression. This is highly important because it lets us see signs of a possible relationship between the shape of the R/M diagram and the structure of the material.

3.6.3 Effect of Residual Stresses.

Up until now notch sensitivity, as related to non-elastic behaviour and the structure of material has been considered, but initial stress conditions have been overlooked. It has been acknowledged of late that it is far from easy to produce fatigue specimens or machined parts in an initially stress-free condition. Residual stress may emanate from non-uniform deformation resulting from heat treatment or mechanical action, eg ; by quenching from a high temperature, stretching of sections with non-uniform properties bending, drawing, rolling or machining. There is no general upper limit to the stresses which may be produced except that which is set by the yield characteristics of the material concerned (180).

In 1936 Becker and Philips(181) examined the effects on a chrome-vanadium steel of residual compressive stresses developed by quenching from the tempering temperature. Their findings are recorded in Table 6 and they reveal that temper-stresses gave an improvement of 8% on notch-free test pieces and of 14% on notched test pieces. Table 7 reveals that improvements up to 44% were achieved by a combination of temper stressing and stressing by mechanical action. Figure 41 shows the effect of residual stresses (182)as a result of quenching after a solution heat treatment on notch-free and notched test pieces of an aluminum alloy. It reveals that for the wrought materials with notch-free test pieces, no difference resulted from the high residual compression resulting from the quenching operation.

The notched test pieces, on the other hand, showed an improvement of up to 80%. Cast material has also shown an improvement with notch-free test pieces. Interestingly, these results show that compressive residual stresses alone can alter the apparent notch sensitivity of material from a reasonably high value to a very low one. Where the residual stresses are tensile they can give apparent notch sensitivity values greater than unity .

The effects of residual stresses must be related to the effects of external mean stresses and the relaxation of residual stress under the fatigue action .

The effects of an externally applied mean stress have been described above. Relaxation of stress during the fatigue test can occur in some materials with low limits of proportionality or non-elastic behaviour under fatigue. Rosenthal and Sines (182) showed an example of this behaviour on an annealed aluminum alloy, which revealed zero effect of residual stresses in the annealed state but a large effect in the heat treated condition .

3.6.4 The Effect of Surface Finish.

Surface finish can have a substantial effect on the fatigue strength of nominally notch-free specimens. Many examples of this can be found in the literature concerning the subject. Typical of these is an early example quoted by Gough(183) and first published by Moore and Kommers(184)(Table 8). This phenomenon can also be considered in terms of surface geometry, the variation of material properties and the applied stress system. Even a polished surface contains notches, albeit they are only of shallow depth. Due to this fact, the general assumptions which have been applied to notched test pieces can also be applied to surface finish. On the other hand, the size of the notch is very small and the notch sensitivity of most materials would be expected to be relatively low.

A further point to be considered is the effect of the manufacturing process in work hardening and surface stressing the material. Several workers (e.g Frommer and Lloyd(185)) have stressed that many machining operations result in residual compression of the surface of the material, but that grinding operations (or, in fact, operations which heat a thin layer on the surface to a very high temperature) can cause high residual tensions.

3.6.5 The Effect of Temperature.

Fatigue strength is affected by temperature and is generally reduced by raising the temperature. At high temperature there is a correlation between the fatigue strength of several metals and their creep rupture strength(186). Lowering the temperature towards absolute zero has been found to raise the fatigue strength in approximately the same proprtion as the U.T.S(187).

Tests on a number of aluminum and steel alloys ranging down to 50 °C, and lower in some cases, have shown that the fatigue strength is as good as and often better than at normal ambient temperature. However, fatigue tests at higher temperatures show little or no effect up to about 300 °C, but in the case of steel at 400 °C there is an increase in fatigue strength to a maximum value, followed by a rapid fall to values well below that at +20 °C. Above a certain temperature there is an interaction between fatigue and creep effects. It is found that up to say 700 °C for heat-resistant alloy steel, fatigue is the criterion of failure, whereas at higher temperatures, creep becomes the cause of failure.

At higher temperatures plastic flow tends to become predominantly a grain boundary sliding mechanism, so that creep rather than fatigue failure becomes increasingly probable. A good high-temperature fatigue strength would be expected from a material able to retain a high resistance to cyclic slip within a grain (initiation resistance) to sliding at grain boundaries (creep resistance) and to atmospheric attack. Because high creep-resisting materials possess those properties, they usually have correspondingly good high temperature fatigue strength (188). Figure 42 shows the variation with temperature of tensile strength, fatigue strength and creep strength of a low carbon steel (Tweedale (189)).

TEST SERIES No	HEAT TREATMENT	CONDITION	ENDURANCE FATIGUE LIMIT tons / sq. in
2	850 °C (Cyanide), O. Q; T 700 °C (Nitrates), A. C	Un-Notched, Un-stressed	± 38.2
3	850 °C (Cyanide), O. Q; T 700 °C (Nitrates), W. Q	Un-Notched; Temper-Stressed	± 41.4
4	850 °C (Cyanide), O. Q; T 700 °C (Nitrates), A. C	Notched; Un-Stressed	± 18.1
5	850 °C (Cyanide), O. Q; T 700 °C (Nitrates), W. Q	Notched Temper-Stressed	± 20.6

Material. Chromium-Vanadium Steel; Machined Surfaces.

Table.6 : Results of Rotating Cantilever Fatigue Tests (Becker & Phillips)(181)

TEST SERIES No	TREATMENT	CONDITION	LIMITING SAFE RANGE OF STRESS tons / sq. in
11	800 °C (Muffle), O.Q; T 600 °C (Nitrate), A.C	As-Rolled,Un-Stressed	0 - 25
15	850-800 °C (Nuffle), O.Q,T 600 °C (Nitrates), A. C, Scragged	As-Rolled,Un-Stressed Scragged	About 0 - 33
16	850-800 °C (Muffle), O.Q.T 600 °C (Nitrates), W. Q, Scragged	As-Rolled,Temper-Stressed. Scragged	0 - 36

Material, Low-Chromium Steel.

Table.7 : Summary of Results of Scragging Tests (Becker & Phillips).

Material	Ultimate Tensile Strength tons/sq.in	Fatigue Range Under Best Conditions tons/sq.in	Relative Fatigue Ranges				
			Particulars of Surface Finish				
			Nos 0 And 0 0 Emery Cloth	Nos 0 And 0 0 Emery Cloth Nos 1, 0 And 0 0 Emery Paper Rouge & Broadcloth	Ground Finish	Smooth Turned Finish	Rough Turned Finish
0.49 % C. Steel	43.2	± 22.0	99	100	89	84	81
0.02 % C. Steel Armco.Im	18.9	± 11.6	100	---	---	92	88

Table. 8 : Effect of Surface Finish on The Fatigue Range (Moore & Kommers)(184)

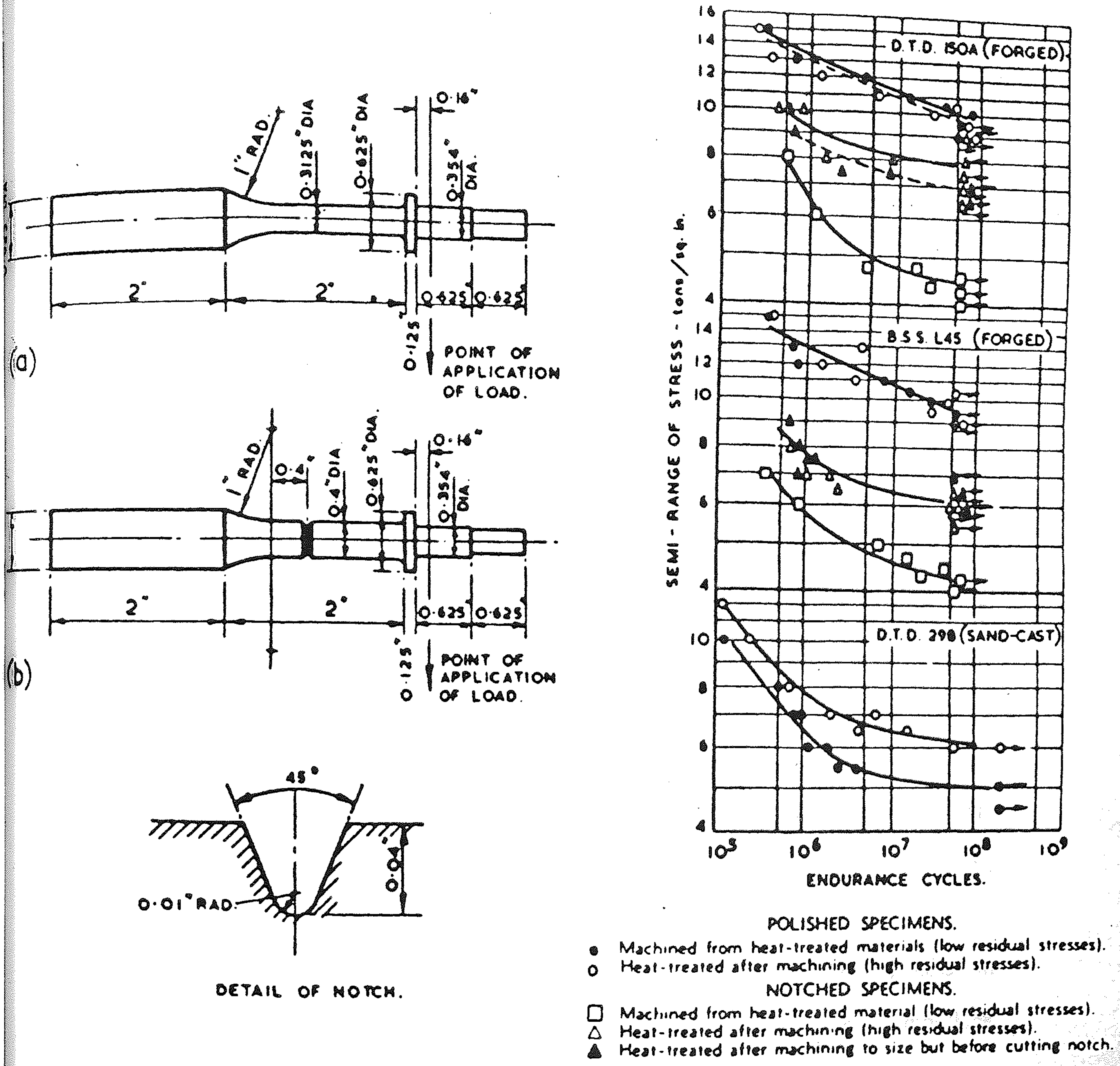

Figure 41 Effect of Quenching Stresses on Fatigue Properties after Forrest(182)

3.7 Fatigue of Zinc Alloys.

Generally fatigue research has been concentrated on ferrous materials and mainly on steel and iron. Later on considerable attention was given to non-ferrous materials such as aluminum because of its importance in the aircraft industry. Workers such as Forrest (190) and Templin (191 have reviewed the fatigue of aluminum alloys and a large amount of data has been collected by Grover, Gordon and Jackson (192).

Alloys containing zinc, as a small addition in aluminum-zinc-magnesium and aluminum-zinc-magnesium-copper alloys, were fatigue tested (193), as shown in Figure 43. Further fatigue work on aluminum-zinc (magnesium or copper) alloys was made by Oberg(194), Waisman(195) and many others. But these fatigue tests were on alloys in which zinc was merely an alloying element. However, some later fatigue work was carried out on zinc-based alloys, as shown in Table 9. From this table it can be seen that fatigue tests were made on both gravity-cast and sand-cast zinc alloys, but not on pressure die-cast zinc alloys.

It was only recently that some work on pressure die-cast zinc alloys was reported and published by C.S Shin and N.A.Fleck(196).They have determined the fatigue properties of the No.3 alloy by the fracture mechanics approach. Compact tension (CT) specimens of 50mm width, by 3.2mm thickness, and a notch length of 15mm were used in their investigation. The No.3 alloy claims a yield stress σy of 210 MPa, an ultimate tensile stress of 285 MPa, an elongation on 50mm of 15%, and a Young's modulus of 73 GPa at a strain rate of 10^{-3} s^{-1}.

Firstly, 3.2mm thick specimens were used to determine the fracture toughness and fatigue crack propagation (F.C.P) response of this alloy. In addition, 1.6 mm thick specimens were also used to study and compare the effect of thickness on fatigue crack propagation behaviour. Due to the invalid size of the specimens, as stated in ASTM E399-81, the K_{1c} measurements had to be abandoned, but the J integral test procedure was found to be appropriate for these specimens, as stated in ASTM E813-81. Therefore, the K1c toughness was measured by using the single specimen technique. The specimens were fatigue pre-cracked using a stress intensity range ΔK

Mechanical Properties	Alloy 8		Alloy 12		Alloy 27	
	Gravity Cast	Sand Cast	Gravity Cast	Sand Cast	[a] Sand Cast and homogenised	Pressure Die-Cast
Ultimate Tensile Strength (MPa)	221-255	275-317	310-345	400-440	310-325	424
Yield Strength (MPa) (0.2% Offset)	208	207	214	365	255	360
Elongation on 51mm (Percent)	1-2	1-3	1-2	3-6	8-11	1-3
[a]Hardness (B.H.N)	85-90	92-96	88-90	110-120	90-100	105-120
Shear Stress (MPa)	241	248-262	N.A	283-297	221-228	N.A
[a] Impact Stress (J) (10mm x 10mm bar unnotched) at 20°C.	N.A	27±3	N.A	48±7	58±12	N.A
Fatigue Strength (MPa)(10^8 cyces)	51.8	103.4	N.A	172.5	103.5	N.A
Creep Strength (MPa)(Stress to produce creep rate of 0.01% / 1000 h at 20°C	59 approx	59 approx	59 approx	69 approx	86 approx	N.A
Creep rate at 138 (MPa) stress (% 1000 h) at 20°C.	0.2	0.2	0.2	0.1	0.07	N.A

[a] Homognised for 3 h at 320°C followed by furnace cooling. N.A. Not available

Table.9 : Mechanical Properties of Zinc-Base Casting Alloys.

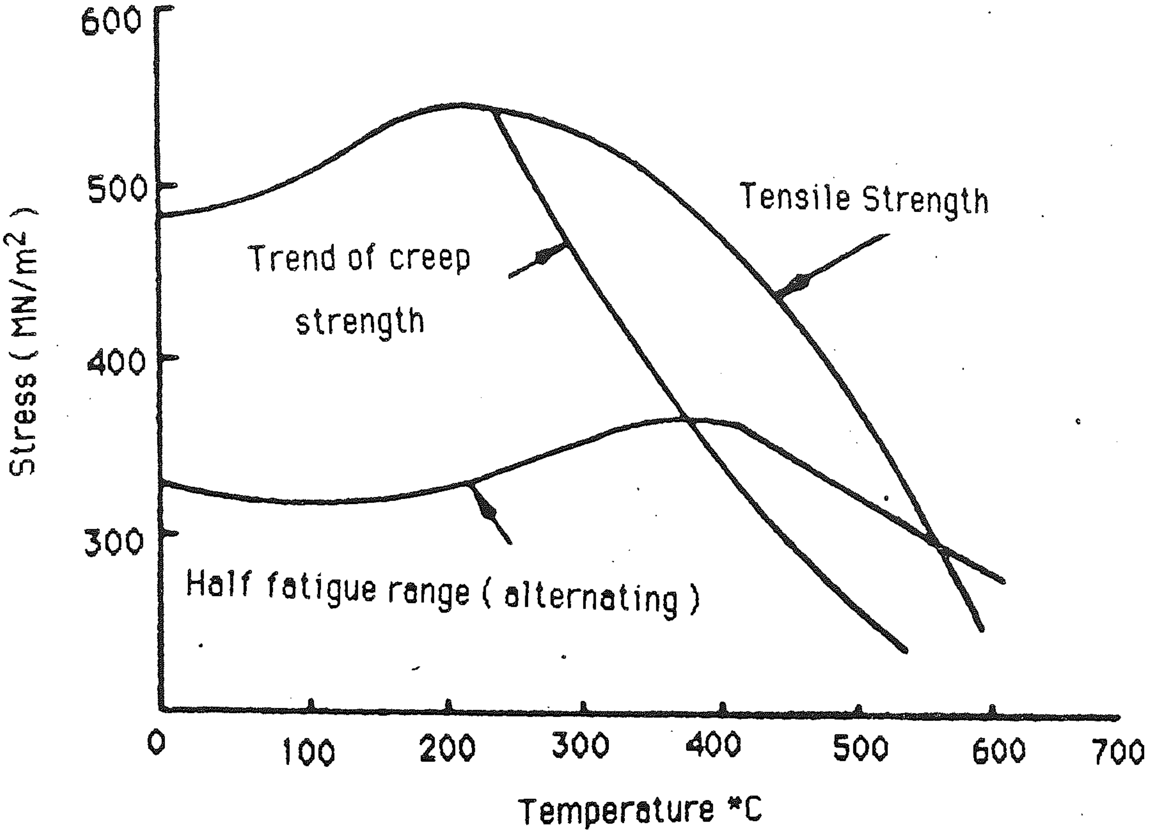

Figure 42 Variation with Temperature of Tensile Strength, Fatigue Strength and Creep Strength of A low-Carbon Steel (According to Tweedale (189)).

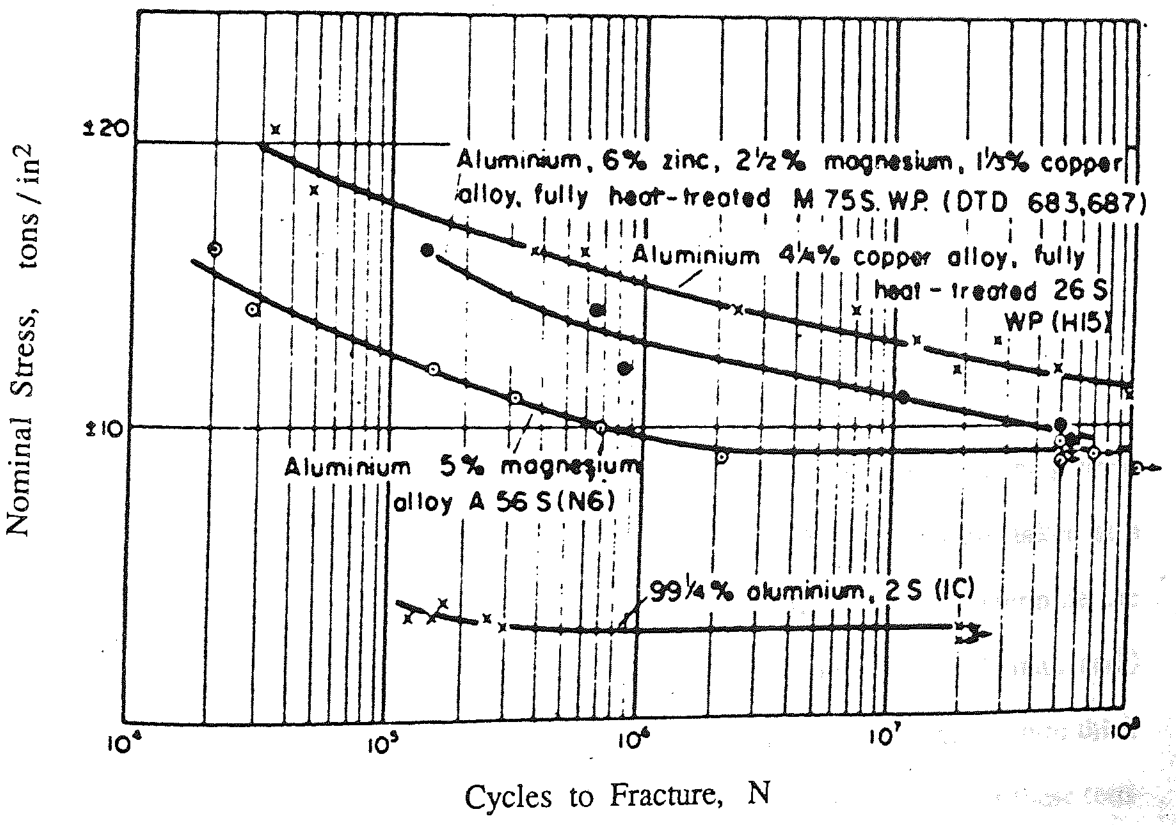

Figure 43 S-N Curves for Aluminium Alloys. (Alum Labs Ltd).

of 8 MPa $m^{1/2}$ and a load ratio R of 0.05. A travelling microscope was used to measure the crack length during the tests and later fractographic examination indicated that the crack front had remained straight throughout the test, thus the surface measurements of crack length were valid. The J-integral versus crack extension, Δa, response was calculated from the load P, versus crack opening displacement v of a specimen. The displacement v is measured along the load line by mounting a slip gauge across the notch on one side face of the specimen. Figure 44 shows the results for initial crack length-to-width ratios ranging from 0.52 to 0.67. From Figure 44 the least squares fit through J-Δa gives a linear regression line which intercepts the blunting line $J = 2\sigma y \Delta a$ at $J_Q = 4.5 \times 10^{-3} MNm^{-1}$. The quantity $25J_Q/\sigma y = 0.56$ mm is less than both the specimen thickness (3.2 mm) and the minimum initial size (16.4 mm). Furthermore, the slope of the regression line is 18 MPa, which is less than the yield stress (210 MPa). Thus, J_Q is a valid measure of the plane strain toughness and can be designated J_{1c}.The scatter in the J - Δa response in Figure 44 is due to the fact that the material contains a random distribution of pores, as shown in Figure 45 .The fatigue crack propagation was also observed by a travelling microscope and the crack closure response was monitored by an offset-compliance technique using a back face strain gauge. Crack closure was quantified by the U value, defined as the fraction of the load cycle for which the crack is open, thus

$$U = \frac{(Kmax - K\,op)}{(Kmax - K\,min)} = \frac{\emptyset keff}{\emptyset K}$$

where Kmax, Kmin and Kop are the maximum, minimum and crack opening stress intensities respectively, both crack length and crack closure were taken at a frequency of 5Hz .Constant amplitude tests were carried out to determine the influence of specimen thickness on crack growth .The ratio R (min load / max load) of 0.05 and 0.5 was used on the 3.2 mm thick specimens, while the 1.6 mm thick specimens were subjected to a load ratio R of 0.05 only. The results of these tests are shown in figure 46. From this figure it can be noticed that there is no significant difference in crack growth rate between thick and thin specimens for the same load ratio of 0.05, to within the experimental scatter which was probably due to the influence of pores in the structure .

Figure 47 shows typical fatigue surfaces of the 3mm thick specimens when R was equal to 0.05 and 0.5. For R values there is a large area fraction of transgranular cleavage of the primary Zn-rich β dendrites and of the eutectoid (α+β) mixture between the dendrites.

When comparing the fatigue crack propagation data of the zinc alloy with other metallic alloys (197), as shown in Figure 48, it was found that crack growth in the zinc alloy is higher than that in other metallic materials under the same $\Delta K/E$. The faster growth in the zinc alloy may be due to the fact that it has an hexagonal close-packed structure with a limited number of slip systems. Shin and Flieck concluded that fatigue crack growth in zinc alloys is accompanied by crack closure when the load ratio equals 0.05, but no closure was observed at a load ratio of 0.5. The zinc alloys display faster crack growth rates than aluminum or two typical steels when compared on the basis of $\Delta K/E$ or $\Delta K_{eff}/E$. Fatigue crack retardation, following an over-load in zinc alloys, is primarily due to crack closure. The apparent discrepancy between measured growth rates and the predicted growth rates from closure measurements is as a result of discontinuous closure.

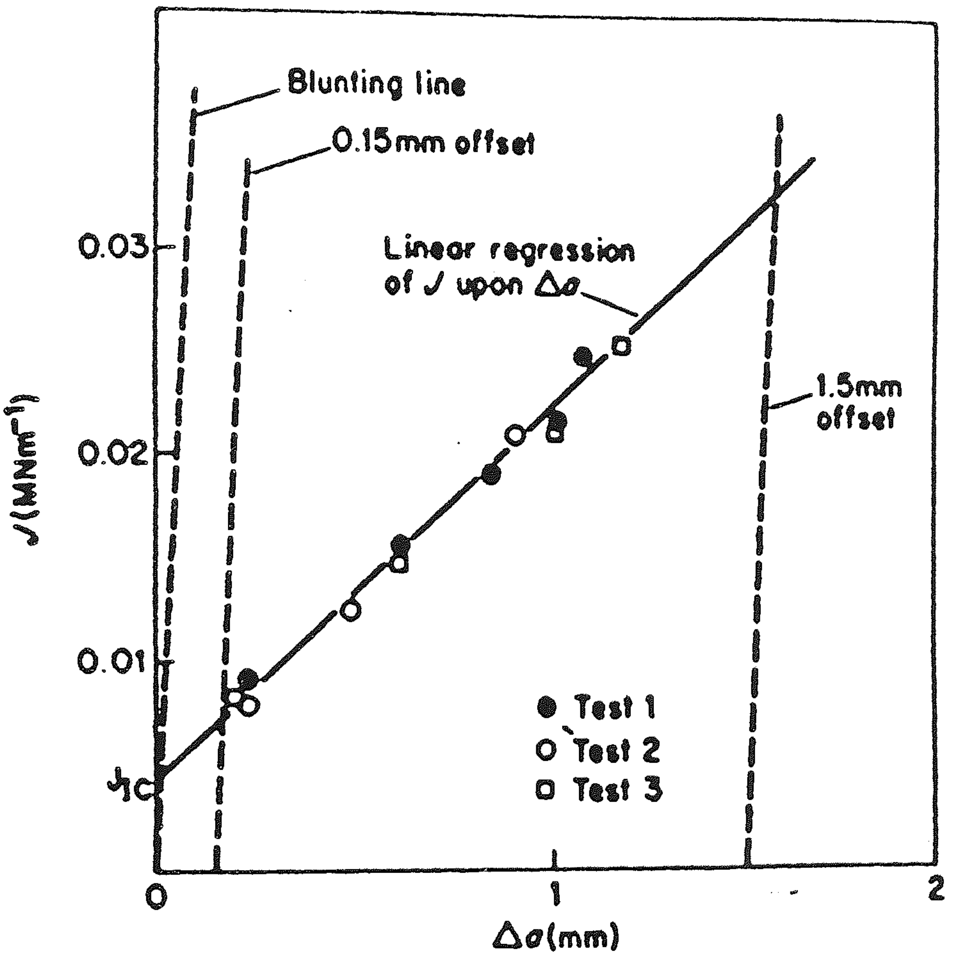

Figure 44 Crack Tearing Response (J-Δa) for a 3.2mm thick Specimens of Zinc-based die-cast Alloy No 3(196).

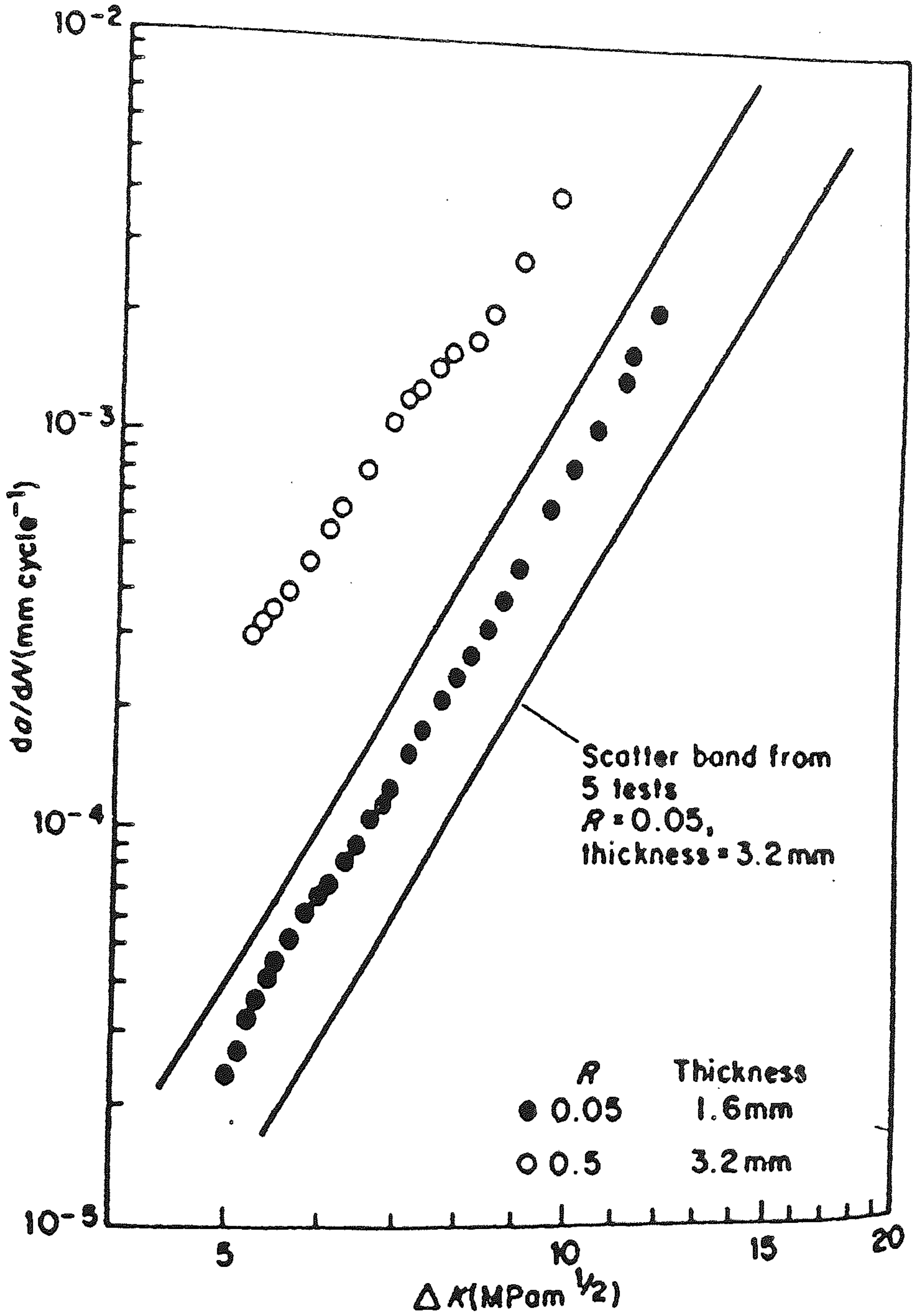

Figure 45 Crack Growth Rate Da/dN Versus Stress Intensity Range ΔK for R = 0.05 and R = 0.5(196).

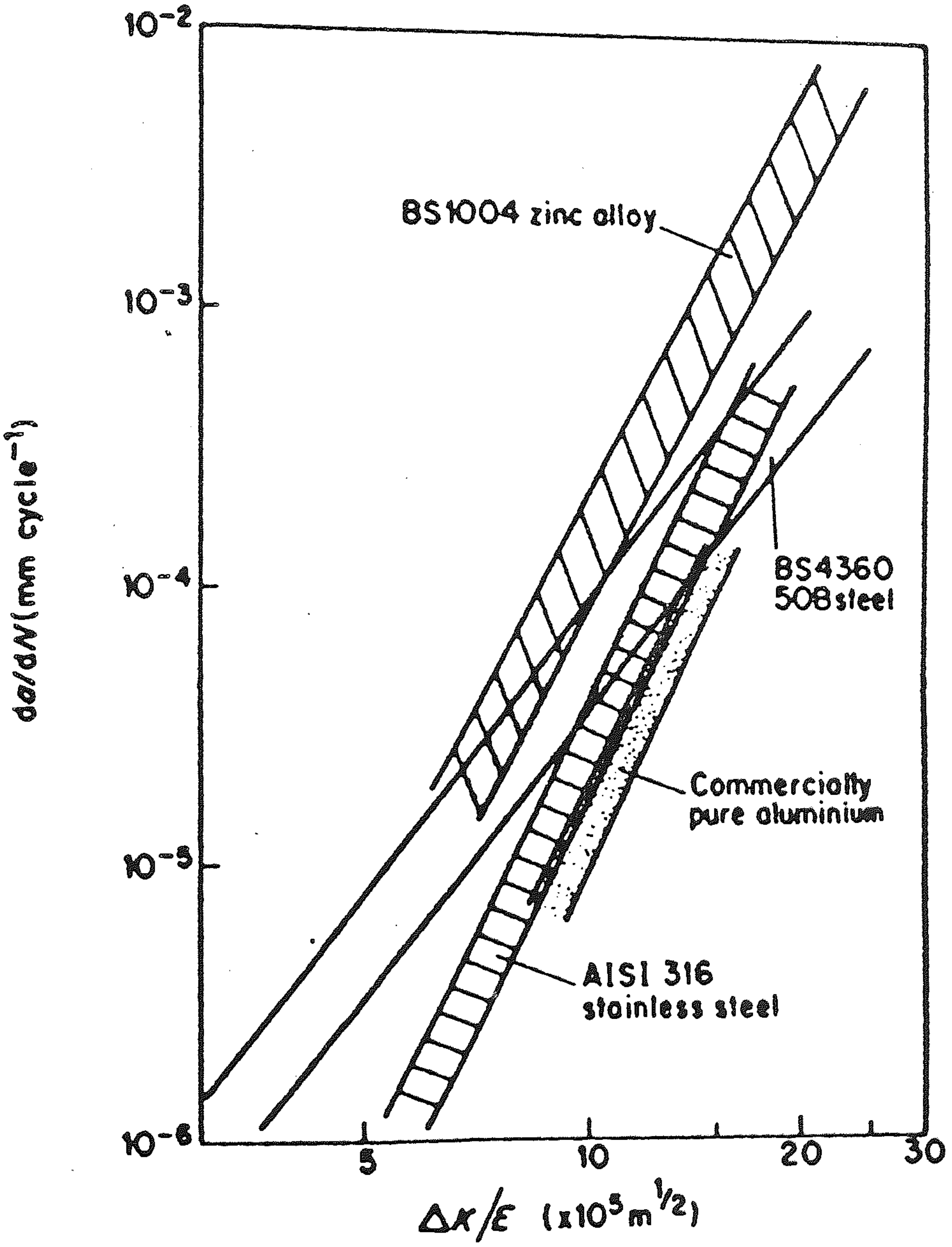

Figure 46 Crack Growth Rate da/dN Versus Maximum Stress Intensity Factor K_{max} for R=0.05 and R=0.5(196).

CHAPTER 4

4.0 EXPERIMENTAL WORK.

4.1 Preparation of the Alloys.

Fatigue tests were carried out on three different batches of alloys

a) Commercial alloys (Mazak 3, ZA8 and ZA27) supplied by Mazak Ltd. These alloys were cast by means of cold-chamber pressure die-casting machines, into plates of 2.18 mm in thickness, 250 mm in length and 50 mm in width with shallow ribs and bosses. Standard fatigue test samples were machined out of these plates. The size specifications of these samples are shown in Figure 47.

b) Ingots of the above-mentioned alloys were also supplied by Mazak. These ingots were melted and pressure die-cast at the Aston foundry. The alloys were then called Mazak 3K, ZA8K and ZA27K .

c) Three alloys called K1 , K2 and K3 were also pressure die-cast at Aston foundry. The compositions of these alloys were based on the standard ZA8 alloy, but with copper contents altered to 0%, 0.5% and 2% respectively. Calculated proportions of zinc and aluminum with commercial purities of 99.99% and 99.985% respectively were used in the charge of these ingots. In the case of alloys containing copper (K2, K3), a calculated amount of the master alloy, containing 50% Cu and 50% Al, was added to the charge and then stirred vigorously. The calculated amounts of magnesium for each alloy were added to the melt at lower temperatures and again stirred vigorously. The melts were then poured into a coated steel mould to form the required ingots. Silicon-carbide pots in an induction furnace were used in the melting procedure.

4.2 The Die Casting Machine and Die Design.

A cold-chamber pressure die-casting machine (EMB10) as shown in Figure 48 with a locking force capacity of 76 tonf was used. This machine is operated in two phases

Phase 1. A fixed low-speed movement of the injection plunger.

Phase 2. The injection plunger was accelerated to high speed the speed was

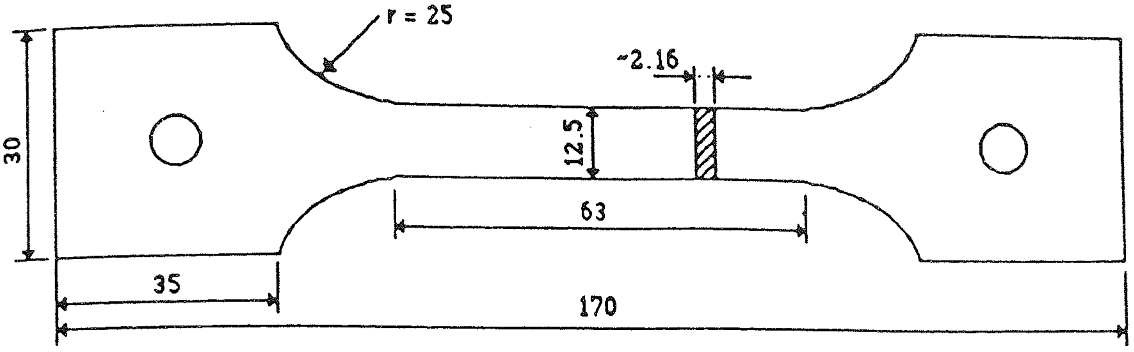

Dimensions in mm.

Figure 47 Flat Sample used for Fatigue and Tensile Tests.

Figure 48 EMB.10, Cold Chamber Pressure Diecasting Machine.

adjustedto suit the required castings. The fixed low-speed of phase 1 is used to draw as much air as possible away from the sleeve and die cavity. When the molten metal reaches the gate of the die cavity, a sudden acceleration (phase 2) takes place to force the metal into the die cavity at the required speed.

An optional third phase can be seen in the more advanced pressure die-casting machines in which a high pressure is applied to the castings during solidification in the die to compensate for shrinkage and minimise porosity. This third phase is not needed with the present alloys. However, to ensure optimum pressure in the second phase of the casting , an extra high pressure reservoir was fitted in series with the present reservoir.

A specific die was designed for these experimental alloys by the author, and co-workers(M Durman). The die was designed in such a way that the castings would be produced in the form of two identical rectangular plates .The designers carefully considered the following factors :

1) The feed systems.

2) Cavity fill time.

3) Gate velocity and fill pattern.

The die design was based on computer data supplied by Mazak Ltd and then translated into a form suitable for the Macintosh computers. The programme basically matches the characteristics of any die casting machine, for example, the maximum pressure capacity of the machine, the maximum dry shot plunger speed, the plunger diameter and line pressure and the volume of the casting. When selecting the afore-mentioned conditions, the computer displays the recommended gate areas, the gate velocities and the cavity fill times. Figure 49 shows a schematical drawing of the die cavity indicated by following the above procedures and it is characterised by the following design parameters :

Machine Calibration Parameters :

Plunger diameter	44.4 mm
Line pressure	1.03 MPa

Maximum pressure on metal	33.73 MPa
Dry shot speed	7.6 m/s

Working Parameters

Plunger diameter	44.4 mm
Line parameter	0.93 MPa

Castings data

Number of components in shot	2
Total component weight	2 X 37.8 = 75.6 g
Total component volume	2(2 X 25 X 120) = 12000 mm^3

Selected casting conditions

Gate area	60 mm^2
Gate velocity	58.1 m/s
Fill time	3.4 ms

Gate dimensions

Gate length	100 mm
Gate thickness	0.30 mm

To aid the selection of design parameters, the programme was designed to display a graph, as shown in Figure 50. When the graph shows a smooth section decrease from the feed system to the gate of the cavity (good hydrodynamic behaviour), it indicates that the parameters are suitable. Moreover, further modifications were made by Durman by machining the gate length down to the levels of the impressions to give a gate length of 110 mm for each gate. Eventually good quality castings were achieved, and an example is shown in Figure 51.

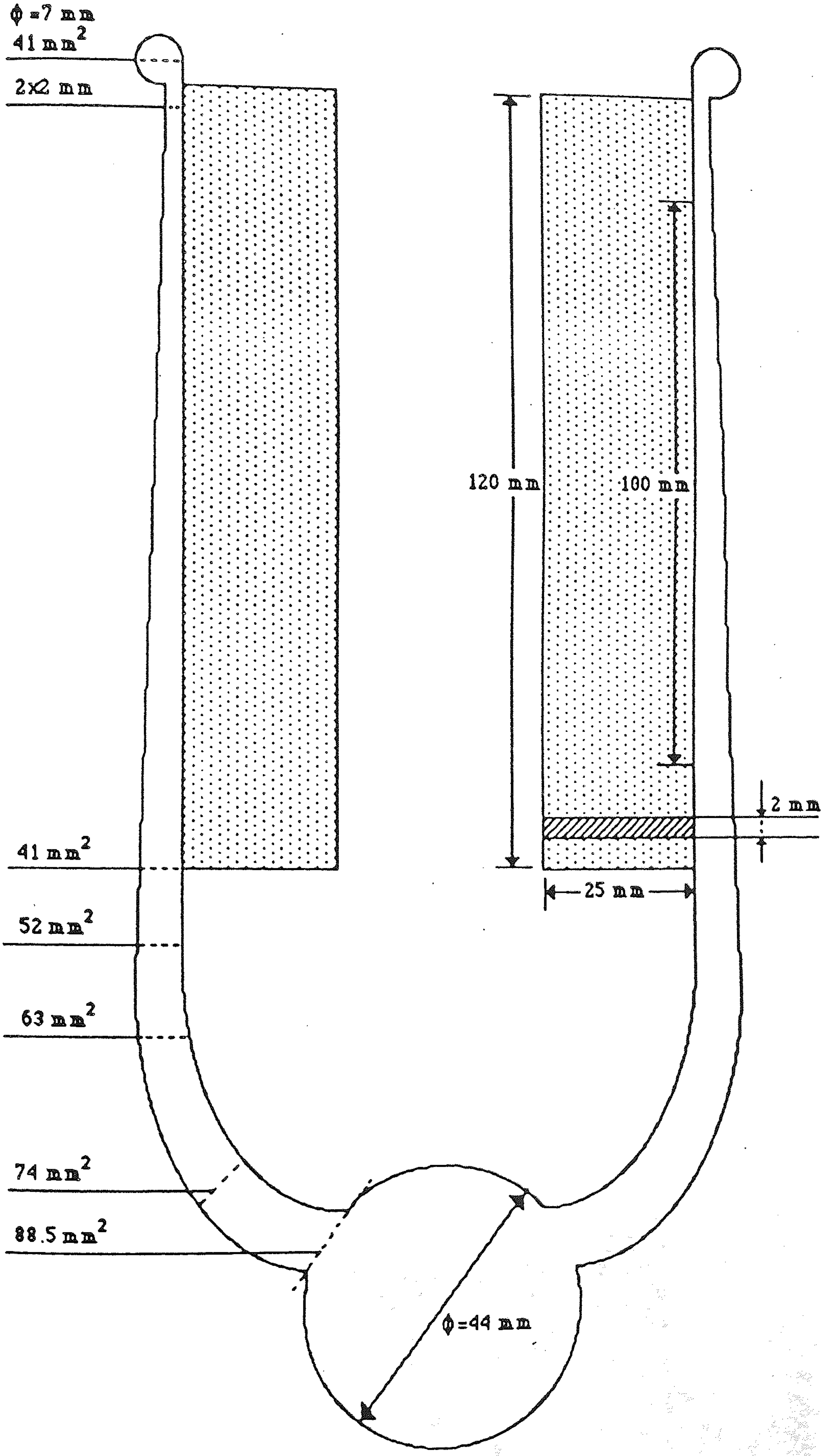

Figure 49 Die Cavity Design for Thin Section Plates.

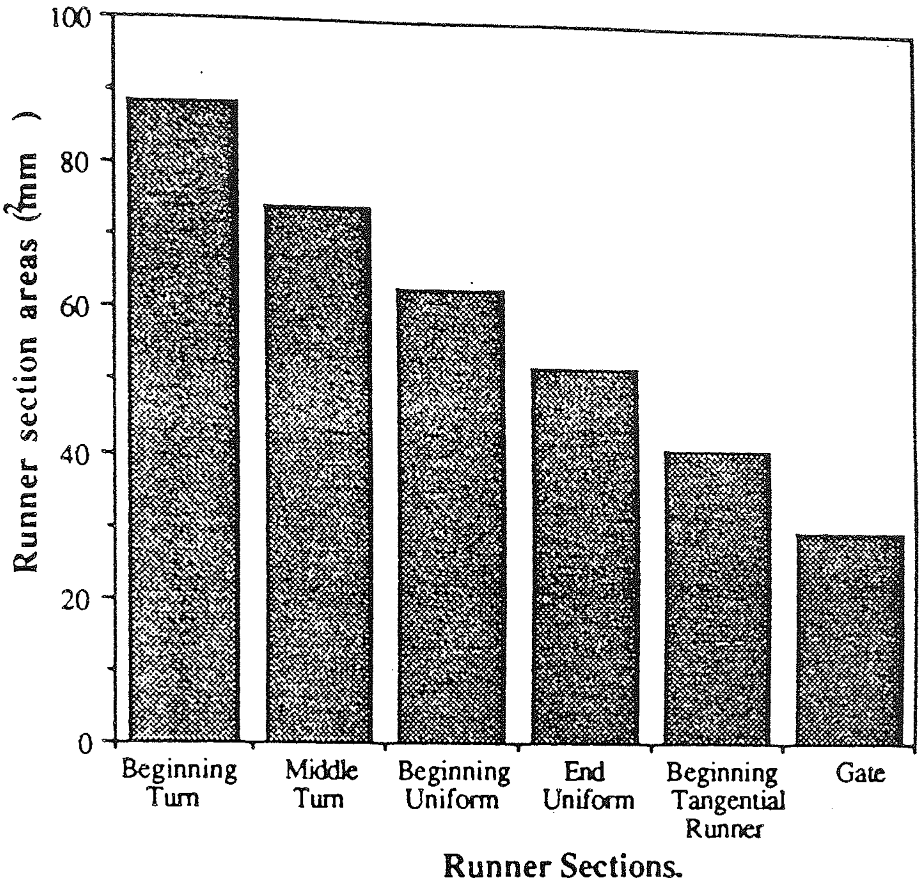

Figure 50 Decrease of the Section along the Flow Path of the Feed System of the Die.

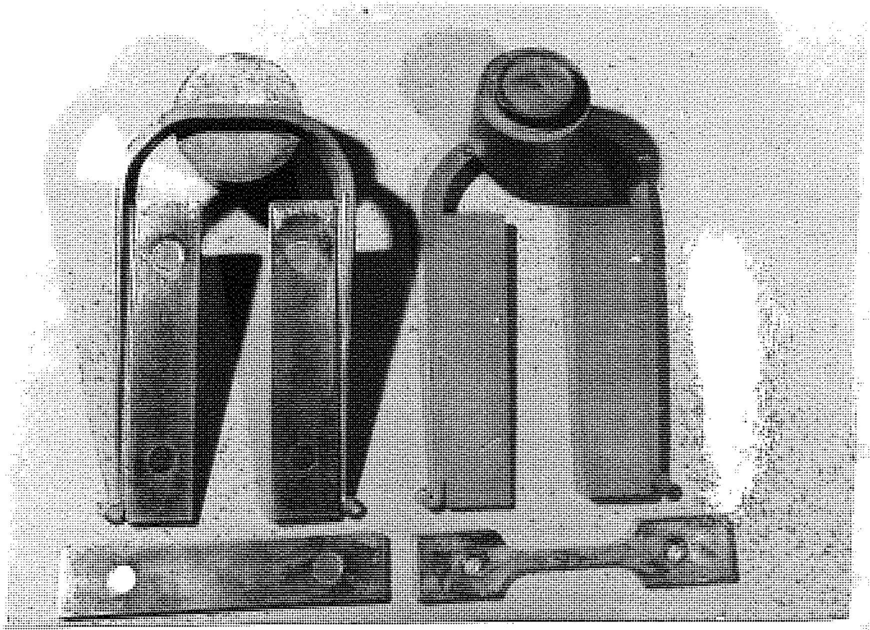

Figure 51 :Photograph of the Castings.

4.3 The Die Casting Procedure.

The ingots were placed in a clay graphite pot with a charge capacity of 30 kg. They were left to melt and stabilise at the required temperature in an electrical resistance furnace. Thermocouples were placed into the melt to monitor the temperature. The molten metal was stirred every few minutes using a coated steel bar to prevent segregation of aluminium from the zinc. Then the melt surface was skimmed to remove any oxides and slags.

The die was preheated and stabilised at a temperature between 180-220°C. Two thermocouples (chromel-alumel) were located in the die block at a distance of 20 mm away from the middle of each impression.

The casting of these alloys then commenced with a variation of injection speed and pressure until the required quality was obtained. The castings were inspected for porosity by X-ray radiography. The best samples were then selected for experimentation. During the casting process the die faces were lubricated sparingly with an oil based lubricant (Dycote-2021).

The best castings were obtained for the low-freezing range alloys M3 and ZA8, when the highest injection pressure and plunger speed were used. The gate velocity at this setting was calculated to be about 53 m/s.

4.4 Fatigue Tests

Fatigue tests were carried out on an ESH 50 KN electrohydraulic machine as shown in Figure 52. The machine was equiped with an electrohydraulic control system. This was regulated by a local cell or a stroke transducer, which controls a servo-valve governing the oil flow. In order to ensure complete thermal and electrical stabilization of the electrical and electronic systems, the machine had to be switched on and run for about 30 minutes before the testing commenced.

A logic box was fitted to the machine to enable the operator to control it by the use of an Apple Macintosh computer programme.

The specimens were mounted on the machine by using Hounsfield clamps.

The work in this thesis is only concerned with tension fatigue tests of flat specimens. Some of these specimens were supplied by Mazak in the form of plates which were then machined into the required size recommended by BS 18 (1970)

The vast majority of the specimens used were produced at the Aston foundry. The fatigue tests were firstly carried out at room temperature and, after establishing the fatigue life curves of these alloys, a decision was made to investigate the effect of elevated temperatures on their fatigue life. Therefore, further sets of tests were carried out at temperatures of 50 and 100 °C. The elevated temperature tests were achieved by the use of a variable resistance electric furnace. A reasonable period of time was given to each sample to ensure that it stabilised at the required temperature before any loads were applied.

The aim of these investigations was to find the fatigue life curve of the alloys involved,. therefore, in every case, the samples were tested to rupture. The number of cycles to failure was recorded with either the use of a digital counter on the machine or from the display on the Macintosh computer screen. The fatigue life curves for the ZA alloys involved in this work were unknown. Hence it was necessary to determine a range of loads to be used on each alloy under differing conditions of stress and temperatures. Therefore, one specimen from each alloy was tested at a high load, then another specimen was tested at a low load. A frequency of 50Hz and a fixed R ratio (min stress/ max stress) of 0.1 were both used throughout the tests.

Nominal stress data, attained from the division of loads into the initial cross-sectional areas, and the number of cycles were collected for each alloy under every condition.Then the computer provided a plot of the S-N curves.

4.5 Tensile Tests

Tensile tests were carried out on the Instron 100 KN Universal Testing Machine as shown in Figure 53. The specimens were mounted on the machine with Hounsfield clamps. The tensile tests were carried out on all the ZA alloys, firstly at room temperature, then at 50 °C and 100 °C. The UTS, the elongation, and the 0.2% proof stress were calculated for each alloy. Furthermore, an electrical strain gauge was fitted on to one sample of each alloy and with the aid of a digital strain counter and a chart recorder, the Young's Modulus was determined for each alloy at room temperature, at 50 °C, and at 100 °C.

4.6 Metallographic Examination.

The as-cast structures of all the alloys involved in this work were examined by the optical microscope and the electron microscope (SEM). Then, for further detailed investigations, the transmission electron microscope (TEM) was used.

4.6.1 Optical and SEM Metallography

Samples were cut from each alloy and mounted in bakelite. These samples were then ground on silicon carbide papers and polished on diamond abrasive to a final finish of 1 µm. In some cases, however, 1/4 µm was needed to obtain a very fine finish .

For the optical metallography, the polished samples had to be etched in 2% Nital for an adequate time, depending on the type of alloy. The optical metallography was then abandoned as the alloys exhibited a very fine structure which could not be revealed by the limited magnification power of the optical microscope. Attention, therefore was then drawn to the SEM in back-scattered electron mode which provided good resolution at higher magnifications. The contrast in back-scatteredelectron mode mainly depends on the average atomic number distribution, therefore the zinc-rich phases appeared light, while the aluminum-rich phases appeared darker. This is due to the fact that zinc has a higher atomic number than aluminum and has more electron scattering power and gives a greater number of back-scattered/electrons.

A Cambridge 120 SEM, fitted with a special large-area back-scattered electron detector, was used for the metallographic examinations of the alloys involved in this work.

4.6.2 Fracture Topography.

The binocular microscope was used with a maximum magnification of 40x to examine the fatigue-fractured surfaces. Secondary electron images in the SEM was used to study the fracture topography in greater detail. A mixture of back-scattered and secondary electron signals was used to show both the fractured surfaces and the microstructure at the same time.

4.6.3 Transmission Electron Microscopy.

It was necessary to use the TEM to investigate the structures in more detail. Unlike the case of the SEM, the TEM samples had to be made in the form of electron-transparent thin foils.

4.6.3.1 Thin Foil Preparation.

The preparation of thin foils involved three stages :

1) Thinning 2mm-thick samples to 150μm by grinding them on silicon carbide papers, starting with a grit size of 120 and finishing at 600 grit .

2) Spark machining the 150μm thick samples to produce discs 3mm in diameter. The discs were then thinned down to about 100μm by holding them in a small jig and grinding them on 1200 grit abrasive papers (wet grinding).

3) The final stage of thinning was carried out by electropolishing, using a commercial Tenupol electropolisher as shown in Figure 54. The machine is a double-jet device which thins both sides of the specimens simultaneously. A pump (in the electrolyte reservior below the polishing cell) circulates electrolytes through the dual jets, which are directed at the centre of the 3mm disc specimen. The specimen is mounted in a removable holder and an anode potential is applied via a metal strip which runs through the centre of the holder. The polishing action is stopped as soon as a hole has formed in the disc specimen, an indication of this is given by a buzzer sound from the light source detector (Photo cell).

Several recipes of electrolytes were given for each material of the Zn, Zn alloys and

Al-Zn alloys. Those electrolytes were based on a mixture of perchloric acid (10-20%) and ethanol. However, the afore-mentioned recipes were not suitable for these present alloys because of chemical attack by the perchloric acid. Trial and error led to the development of a new electrolyte containing 4-5% perchloric acid, 20-25% 2 butoxy ethanol and 65-70% ethanol. Liquid nitrogen was added to cool this electrolyte to about -30 °C during polishing. The specimens were cleaned instantly when polished, firstly with water and secondly with methanol. They were then dried with clean filter papers. Table 10 shows the operating conditions for electropolishing for commercial ZA alloys.

4.6.3.2 Transmission.Electron Microscopy.Work.

Unlike the SEM, the contrast in the TEM is only slightly affected by the atomic number, as it is dominated by the orientation and foil thickness variations.Therefore, the zinc-rich phases appeared darker than the Aluminium-rich phases due to the difference in thickness resulting from the preferential thinning of phases when preparing foils. Four different types of transmission electron microscopes were used in the examination of the thin foils; Jeol JEM 100B, Jeol JEM 100C, Philips EM400T and Jeol 2000FX respectively. These four types of transmission electron microscopy lend themselves to a variety of techniques to suit different purposes.

The conventional TEM mode enabled bright and dark field images of the structures to be studied with the corresponding selected area diffraction patterns (SADP). The tilting technique, using a double-tilt stage, was employed in order to aquire three-dimensional information and to allow selection of particular crystallographic directions to reveal structure and to differentiate the diffraction patterns of small particles with similar lattice parameters for the matrix phase. In order to procure selected crystallographic directions, tilting about the direction determined by the Kikuchi line was followed by using schematic Kikuchi maps as an aid in selecting tilt axes. This was carried out by firstly tilting to the nearest attainable and recognizable pole, then by calculating the angle between the beam direction of this pole and the pole of interest and finally by tilting through this known angle about a defined tilt axis, detemined by the Kikuchi map. This method necessitate tilting through large angles and was seen as a rather difficult job in CTEMs because the small areas of interest moved laterally resulting in the corresponding SADPs of these areas disappearing during tilting. However, the use of a small convergent probe (convergent beam) served to overcome this difficulty. The angle of the beam was controlled by the size of the second condenser lens aperture and the size by the strength of the first condenser aperture. This method focused the second condenser lens aperture onto the specimen, creating diffraction patterns of various disc sizes, depending on the size of the second condenser lens aperture being utilised. With this method, convergent beam diffraction patterns (CBDP) of very small areas were also created.

The STEM mode of the microscope was also used to analyse the chemical composition of the present phases. In order to carry out analyses on a selection of small phases, the smallest probe was achieved by switching off the second condenser lens and enlarging the strength of the first lens, and by using the smallest second condenser lens aperture, and then by focusing the probe onto the area to be analysed ,using the objective lens.

An EDS system was used to make X-ray microanalyses of the phases. In order to prevent any X-ray contamination arising from the standard specimen holders, a special carbon specimen holder was utilized. The analyses were then carried out on the samples' thinnest areas. X-ray intensities were obtained after various times, between 200 and 500 live-seconds.

A computer programme was used to accomplish the background fitting to the elements'characteristic peaks. This programme also enabled the modification of a fitted background in some regions which were clear of the elements' characteristic peaks. When an adequate fit was found, it was subtracted from the characteristic peaks to formulate the elements' real intensities. The intensities were then computed to find the true concentrations with atomic number correction only.

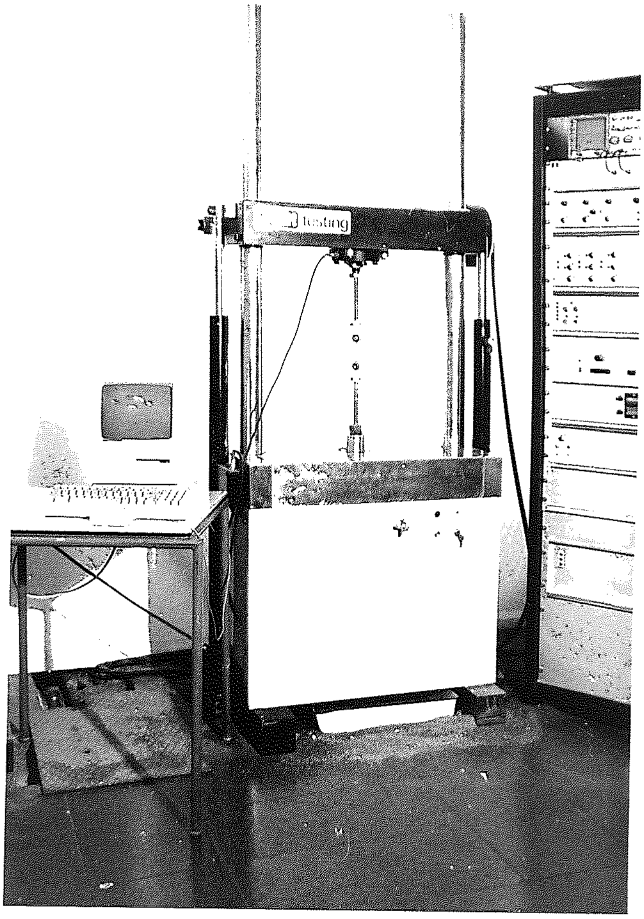

Figure 52 The ESH.50.KN Testing Machine.

Alloy	Voltage (V)	Current Density (A/cm^2)	Flow Rate Setting	Temperature (°C)
M3K	25-35	0.3-0.37	6.5	-15 to -25
ZA8K	25-35	0.28-0.34	6.5	-15 to -25
ZA27K	25-35	0.25-0.28	6.5	-20 to -30

Table.10 : Operating Conditions for Electropoishing Commercial ZA Alloys.

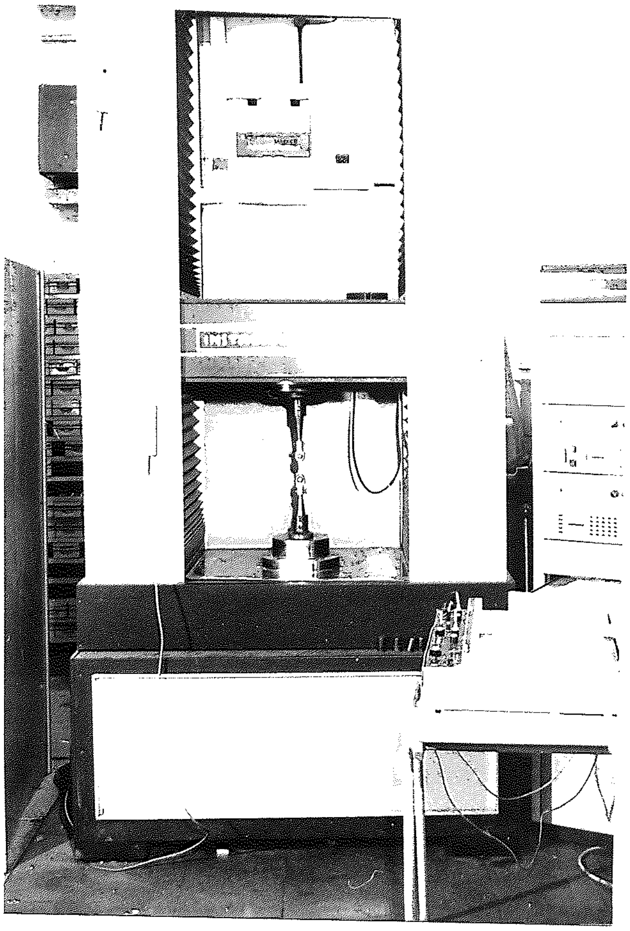

Figure 53 The Instron 100KN Universal Testing Machine.

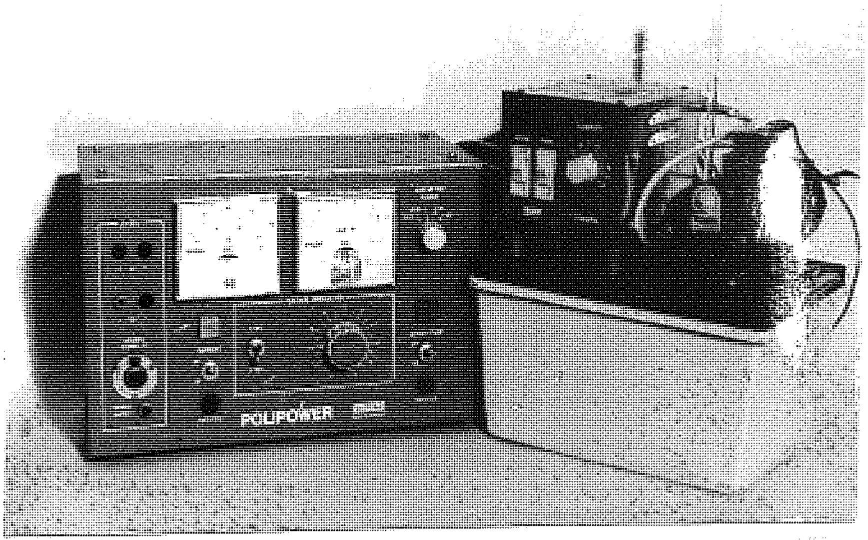

Figure 54 The Electropolisher (Tenupol, Struers Ltd).

CHAPTER 5

5.0 EXPERIMENTAL RESULTS

The experiments were carried out initially on the commercial alloys Mazak 3, ZA8 and ZA27. These alloys had been cold-chamber pressure diecast elsewhere.In order to carry out the required tests for these investigations, hundreds of samples were needed. It was, therefore, decided to pressure die-cast these commercial alloys at the University of Aston's foundry. The required amount of samples was produced and the initial K was appended to each alloy as a means to differentiate them from the above mentioned commercial alloys.

After completing the tests on these alloys (M3, ZA8, ZA27, M3K, ZA8K and ZA27K) three more alloys, based on the standard ZA8, were produced at Aston. The only difference between these alloys and ZA8 lay in their copper contents, which were 0%, 0.5% and 2% for K1, K2 and K3, respectively .

Table 11 shows the chemical compositions of all the alloys involved and investigated in this work.

Alloy	% Al	% Cu	% Mg	% Fe	% Zn
Mazak.3	4.2	< 0.003	0.049	< 0.01	Rem
ZA.8	8.1	1.06	0.024	< 0.01	///
ZA.27	28.5	2.08	0.016	0.01	///
M.3K	4.25	< 0.01	0.041	< 0.01	///
ZA.8K	8.7	1.04	0.026	< 0.01	///
ZA.27K	26.9	2.02	0.014	0.17	///
K.1	8.2	< 0.01	0.024	< 0.01	///
K.2	8.7	0.52	0.024	< 0.01	///
K.3	8.5	1.92	0.024	0.01	///

Table. 11 : Chemical Compositions of The Experimental Alloys.

5.1 Metallography of The Commercial Alloys M3, ZA8 and ZA27

The as-cast structures of the commercial alloys M3, ZA8 and ZA27 have been examined using SEM techniques. The structure of each individual alloy was thoroughly examined in at least three different magnifications, in order to discover further information about the change of phases, as a result of decomposition or transformations on cooling after casting.

5.1.1 Mazak 3 Alloy

The as-cast structure of the alloy M3, shown in Figures 55-57, at different magnifications, exhibits the different phases present in this alloy. The structure of this alloy was very heterogeneous, but was clearly hypoeutectic. The structure shown in Figures 55-56 consisted of a few large (about 20 μm) and many small dendritic particles of the primary zinc-rich η phase, appearing as white areas with different and variable sizes. A small portion of lamellar eutectic pools surrounds the zinc-rich η phase. Many small rounded dark particles, about 1 μm in diameter, were attached to the hypoeutectic η particles. These small dark particles are revealed at high magnification in Figure 57, and believed to be a pseudoprimary aluminium-rich former β phase, as a result of high undercooling during eutectic solidification. They had subsequently decomposed into some aluminium-rich α and zinc-rich η phase mixtures at below the eutectoid temperature of 275 °C. In addition to that, the edges of the primary η dendrites were decorated with thin haloes of the eutectic aluminium-rich α phase. They were thought to have formed due to the process of removing the excess aluminium from the supercooled liquid before normal eutectic solidification took place. This is because the solubility of aluminium in zinc is reduced at low temperatures. The eutectic phase (Figure 57) had formed as plates or lamellae of β phase in a zinc η matrix with an interlamellar spacing of about 0.5 μm, and this β phase had also decomposed on cooling through the eutectoid temperature after solidification. The Figure also showed that the former β plates had apparently decomposed into rows of aluminium-rich α particles or thinner plates of α, the η constituent of the eutectoid reaction presumably joining the matrix.

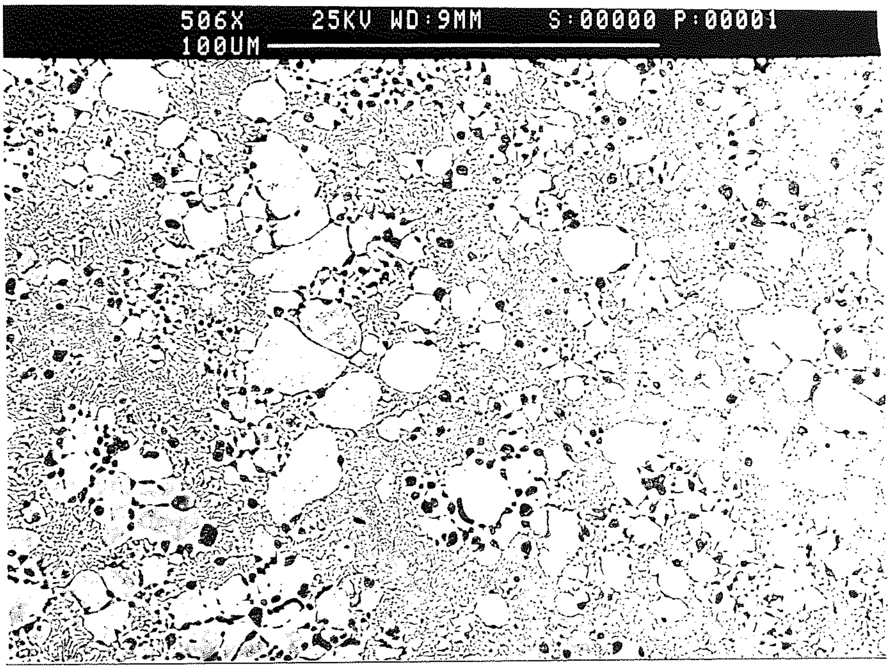

Figure 55. SEM.As-cast structure of Mazak3, showing the primary η of different sizes surrounded by eutectic.

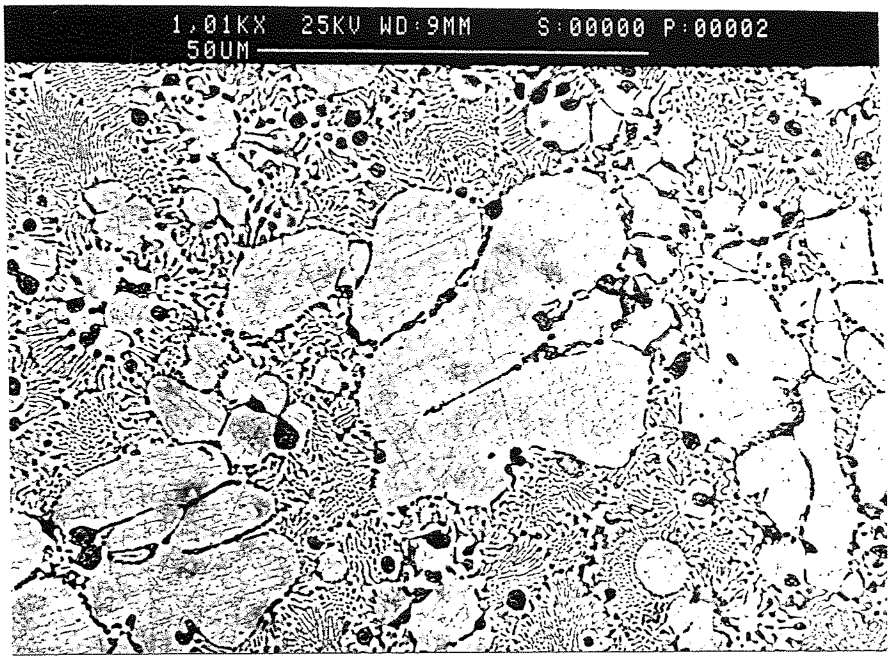

Figure 56. SEM.As-cast structure of Mazak3, showing aluminium-rich former β phase attached to the primary η.

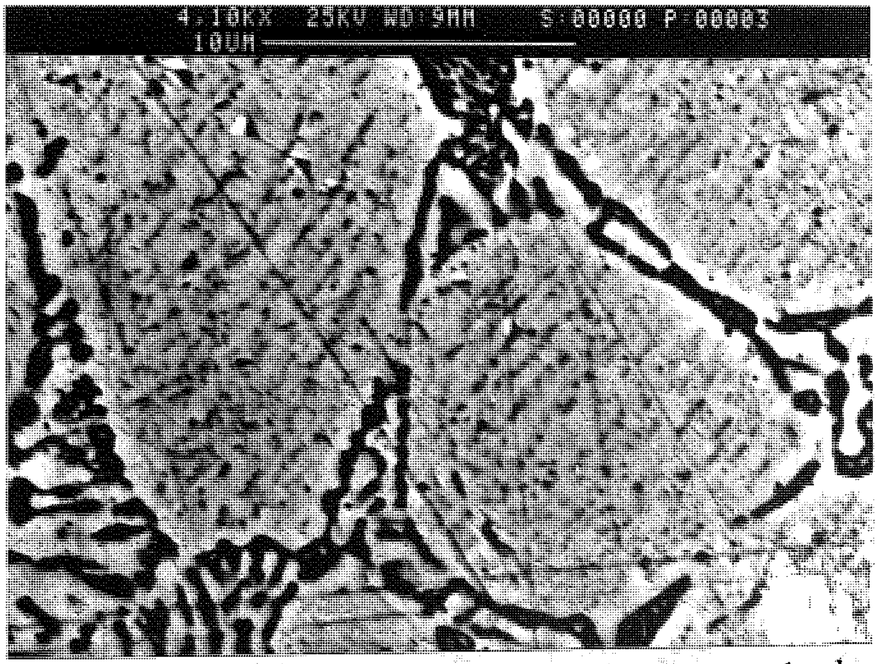

Figure 57. SEM.As-cast structure of Mazak3, showing the border between primary η and the surrounding eutectic, also showing a spot of pseudoprimary β in the middle top of the micrograph.

5.1.2 ZA.8 Alloy

The as-cast structure of ZA8 is shown in Figures 58-60 at three different magnifications. The structure of this alloy (Figure 58) was heterogeneous and clearly hypereutectic, and consisted of uniformly distributed primary β particles of different shapes and sizes, with an average size of 12 μm. The structure also consisted of eutectic pools surrounding the primary β phase. The β had decomposed into two different morphologies, as shown in Figures 59-60, one being a well developed lamellar form, mainly in the central portion of the grains surrounded by a rim of coarser mixture of phases. The second, and less frequent, was only a coarse mixture of phases. Also seen at low magnification in Figure 58 was the presence of zinc-rich η phase. These regular η areas were almost the same size as the primary β phase. These η areas are believed to be pseudoprimary η, or rather they are the eutectic η, resulting from a highly supersaturated zinc-rich liquid subjected to temperatures below the eutectic temperature, during rapid cooling of the castings. Thin haloes of η phase can be seen to have formed around the primary β dendrites and were probably due to high undercooling applied to the castings. The Figures also showed that the majority of the eutectic had formed into lamellar-like shapes, whilst the remaining part had developed into different and peculiar shapes.

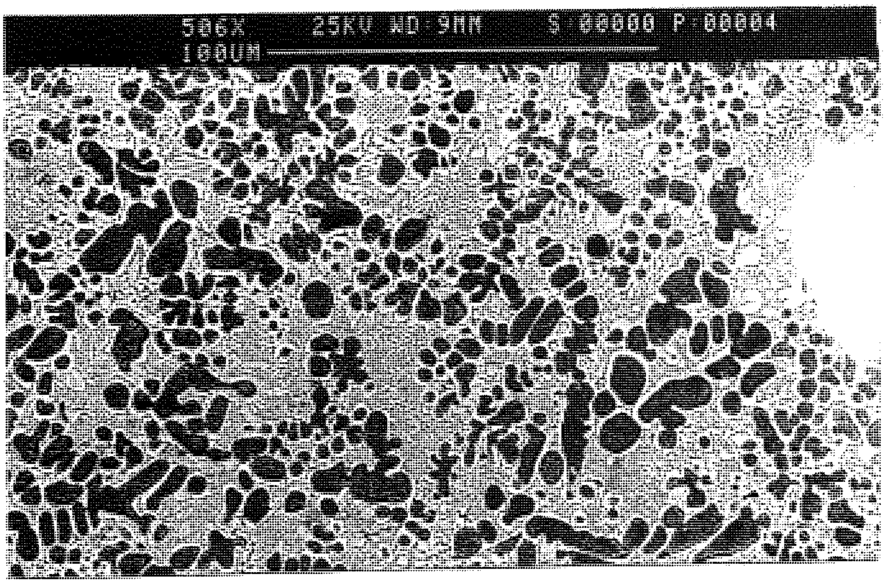

Figure 58. SEM.As-cast structure of ZA8, showing primary β particles surrounded by eutectic, with some pseudo-primary η phase.

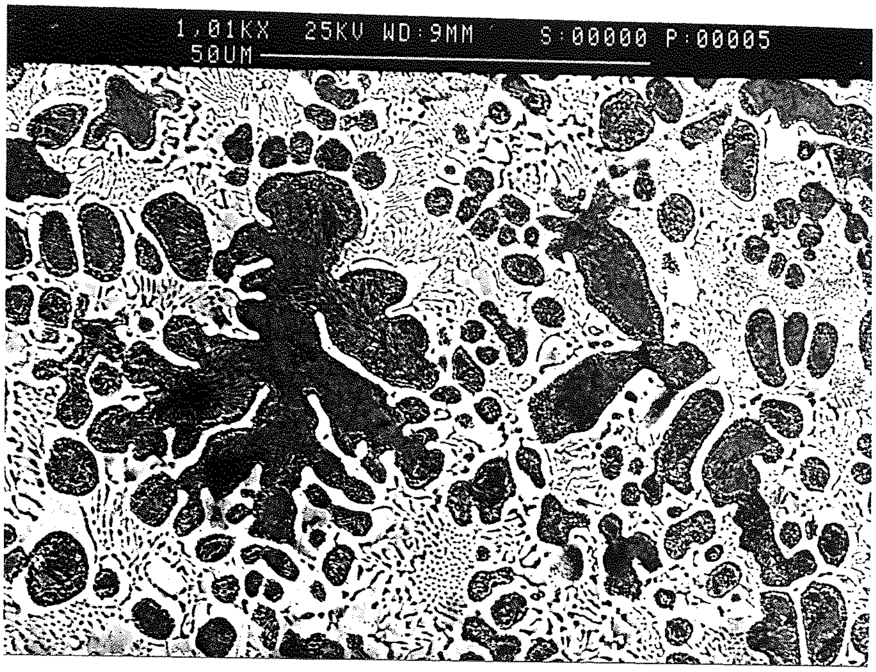

Figure 59. SEM.As-cast structure of ZA8, showing decomposed primary β particles surrounded by a thin film of η, and set in an eutectic matrix.

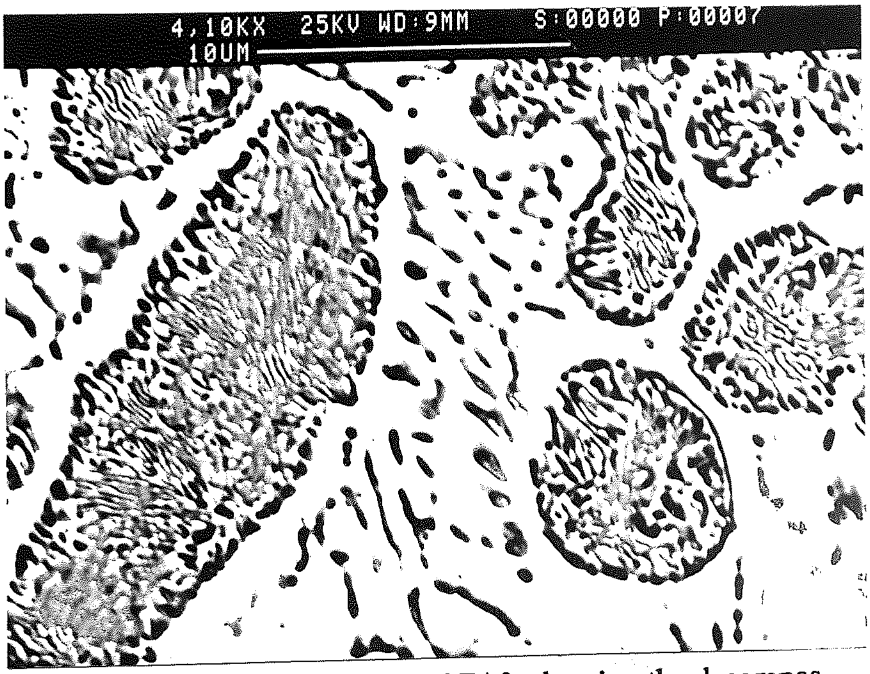

Figure 60. SEM.As-cast structure of ZA8, showing the decomposition of β into nicely formed lamellae and a coarse mixture of phases at the edge.

5.1.3 ZA27 Alloy

The as-cast structure of ZA27 is shown in Figures 61-63, at three different magnifications. The alloy was heterogeneous and consisted of a multi-phase complex structure. Figure 61, at low magnification, showed a fine dendritic α' structure in a mass of much smaller aluminium-rich β, and the interdendritic eutectic zinc η. In other words (η + β). The average size of the primary α' was found to be about 14 μm. Figures 62 and 63, at high magnifications, showed that the solidification of this alloy commenced with the formation of aluminium-rich (α - α') dendrites, and was followed by the precipitation of a further zinc-rich β phase, specifically around the primary dendrites, through a peritectic reaction between the first-formed α-phase and the residual liquid.

The decomposition of β particles resulted in the formation of coarse lamellar cellular products and a fine mixture of a zinc-rich phases in an aluminium matrix. The β subsequently decomposed into lamellae or irregular particles of α and η, with eutectic pools occupying the remaining interdendritic areas.

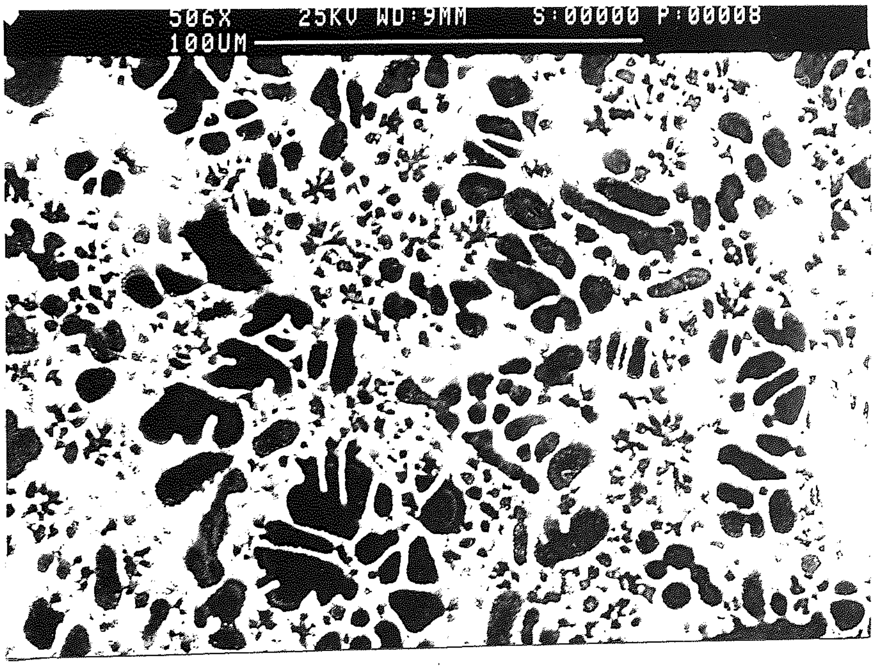

Figure 61. SEM.As-cast structure of ZA27, showing α' dendrites surrounded by β with small amounts of interdendritic η.

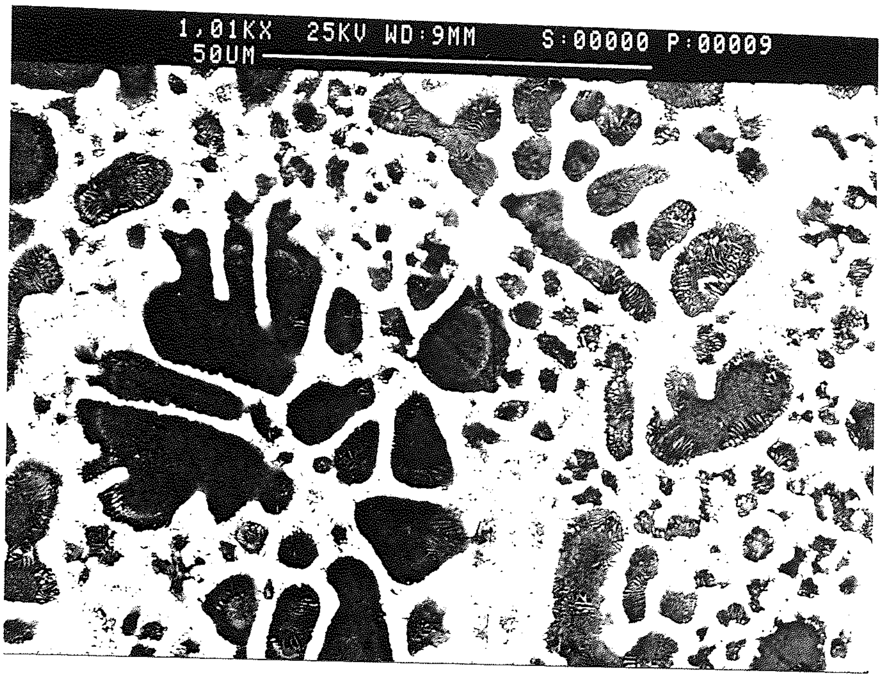

Figure 62. SEM.As-cast structure of ZA27, showing details of the decomposition of primary α' and β phases.

Figure 63. SEM.As-cast structure of ZA27, showing the decomposition of α' into fine particulates or lamellar products.

5.2 The Metallography of Alloys M3K, ZA8K and ZA27K

The as-cast structures of the commercial alloys M3K, ZA8K and ZA27K were firstly examined in the SEM using a back scattered scanning electron microscope, and details of their structures were recorded on micrographs .In order to analyse the structures in greater detail, the Transmission Electron Microscope was used, as it is capable of providing micrographs, quantitive analysis and diffraction patterns analysis.

5.2.1 M3.K Alloy

The as-cast structure of the alloy M3K is displayed in SEM micrographs and is found in Figures 64-67 at four different magnifications. Figure 64 revealed that the structure consisted of a large number of the primary zinc-rich phase η distributed throughout the structure. These primaries consisted of various sizes, ranging from as small as 1 μm up to 20 μm and averaged out at 7 μm.

The structure also consisted of eutectic pools surrounding the primary particles. Two different kinds of tiny dark spots were also associated with the primary η, one being on the edges of the primaries, which is believed to be derived from the pseudoprimary aluminium-rich former β phase, and the other kind was found surrounded by the η grains and is believed to be porosity, developed due to the different magnitude of surface energy between the gas bubbles and the zinc-rich η during solidification. This will be revealed at higher magnification later on in this chapter. The pseudoprimary aluminium-rich former β phase can be seen more clearly in Figures 65-67. Figures 66-67 at high magnification, showed the aluminium-rich α particles at the dendrite edges, and the decomposition of eutectic β and pseudoprimary β. The Figures also showed fine precipitates within the primary η dendrites and radial eutectic cells nucleating on the primary η.

The as-cast structure of the alloy was also examined in detail in the TEM. Figure 68 depicts primary η particles surrounded by eutectic. When these primary particles were examined at higher magnifications (Figures 69-70), tiny white areas were seen scattered on the η particles. These white areas were thought to be aluminium-rich α precipitates resulting from the precipitation of excess aluminium from solidification. Electron diffraction patterns were obtained from the primary η particles (seen in Figure 70). This pattern, shown in Figure 71, revealed the reflections of the zinc matrix with a beam direction of $\langle 1\bar{2}10 \rangle$, but failed to show any reflections from the precipitates.

Thin haloes of the eutectic Al-rich α phase around the η phase can also be seen in Figures 68-69. Figures 72-74, at high magnifications, showed that the eutectic appeared to have taken the form of lamellar shapes and, in some cases, oval shapes. This was due to the fact that on cooling through the β-transformation, the lamellae had broken up into strings of α particles and zinc-rich portions of the eutectoid in the form of η precipitates in the eutectic region. The tiny dark spots that appeared on some parts of the eutectic in Figures 72-74 will be discussed later on in the thesis. Chemical analyses, using a small probe obtained in STEM mode of operation, were carried out on different areas, which have been labelled on the figures. The results of these analyses are shown in Table 12.

Phases Analysed	% Al	% Cu	% Mg	% Zn
Primary η : (area.1 in Figure.69)	0.35	0.5	0.4	Rem
Eutectic Matrix : (area.2 in Figure.72)	0.70	0.6	0.9	////
Eutectic α : (area.3 in Figure 73)	79.0	0.4	0.9	////
α'_m Phase in Eutectic : (area.4 in Figure.73)	12.7	0.5	0.4	////

Table.12 : STEM Analysis of Alloy M3K.

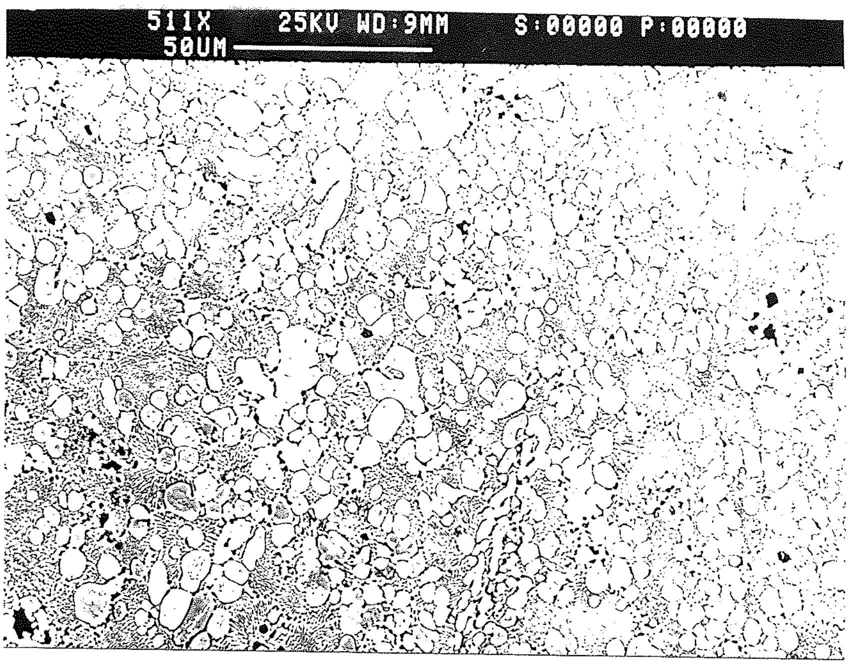

Figure 64. SEM.As-cast structure of M3K, showing primary η of ranging sizes surrounded by eutectic.

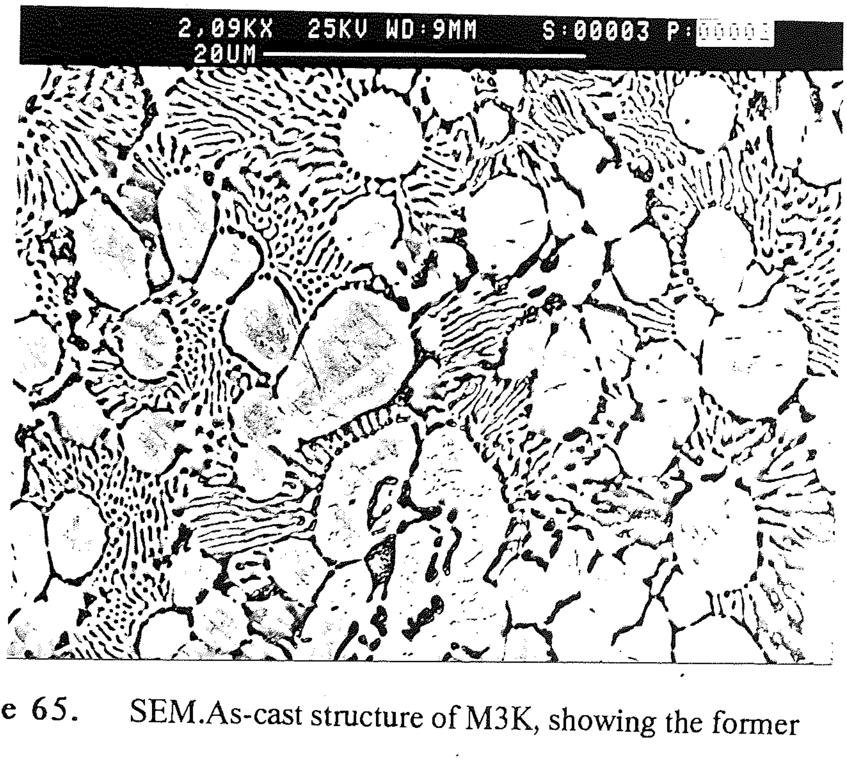

Figure 65. SEM.As-cast structure of M3K, showing the former β particles formed on the primary η.

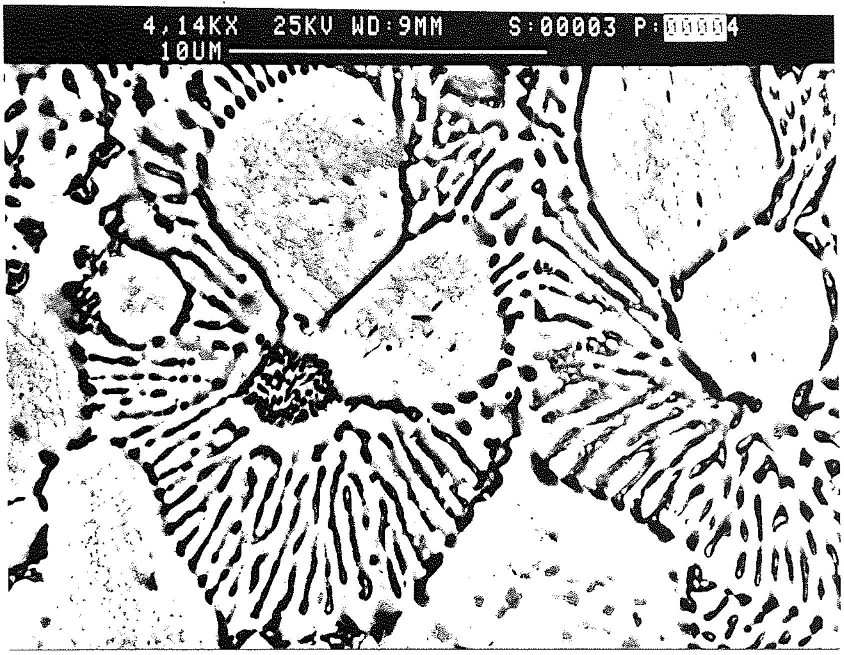

Figure 66. SEM.As-cast structure of M3K, showing nicely formed pattern consisting of primary η, pseudoprimary β and radial eutectic cells nucleated on the primary η.

Figure 67. SEM.As-cast structure of M3K at high magnification, showing the decomposition of a pseudoprimary β particle and fine precipitates within the primary η dendrites.

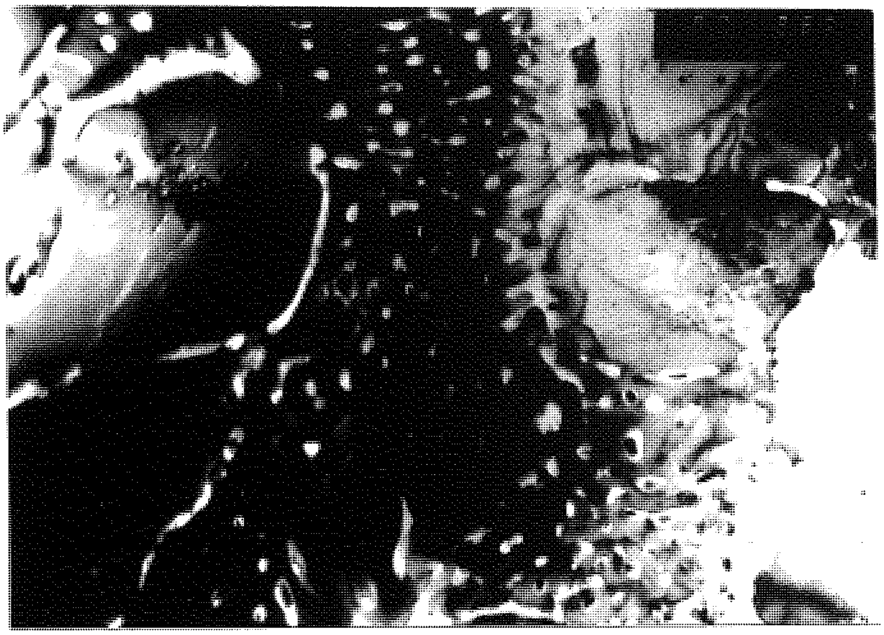

Figure 68. TEM micrograph of M3K, showing primary η surrounded by eutectic. X 8.3k

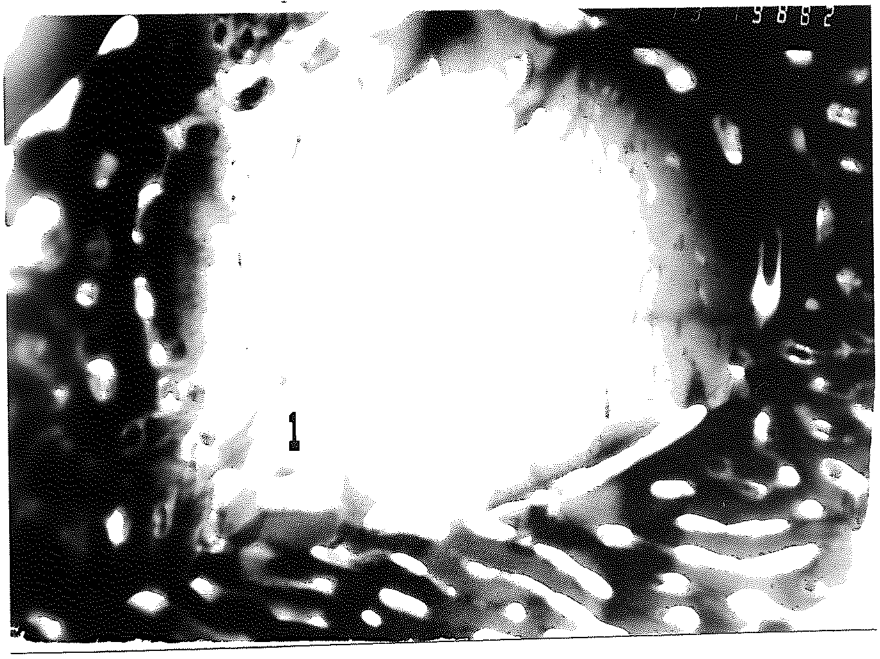

Figure 69. TEM micrograph of M3K, showing primary η grain with internal precipitates. x13k

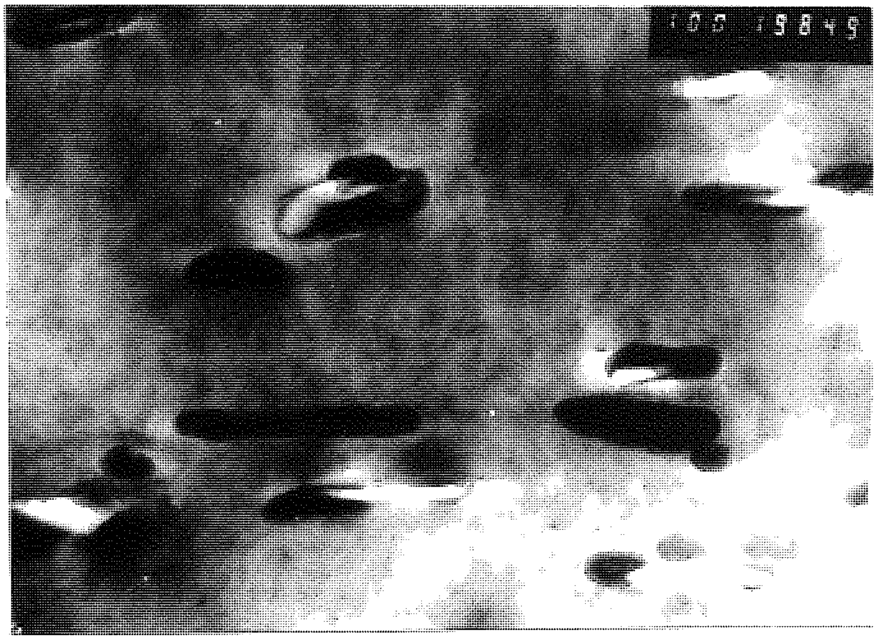

Figure 70. TEM micrograph of M3K, at high magnification of a primary η particle, showing internal precipitates. ×100 K

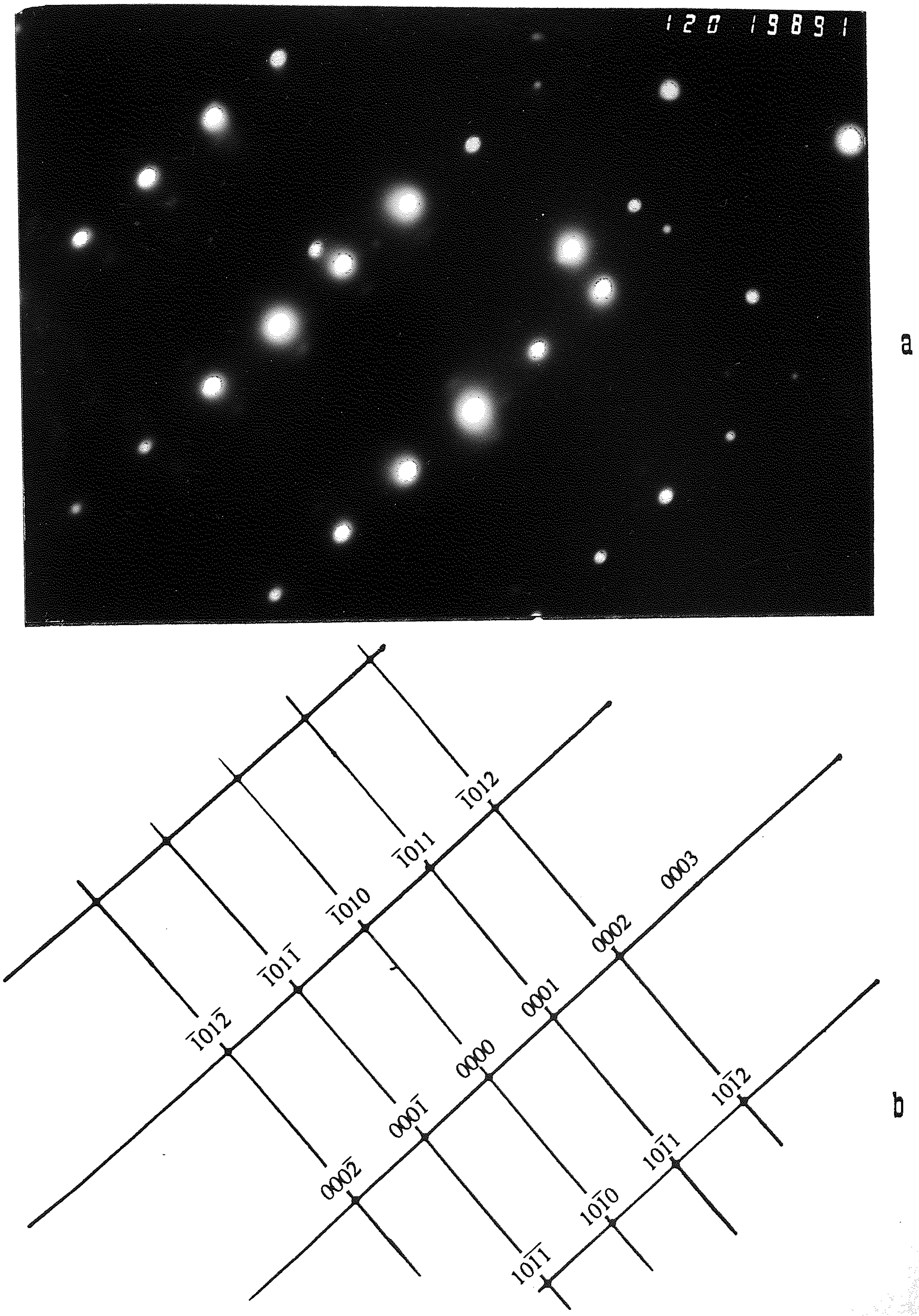

Figure 71. a) SADP's taken from figure 69, showing a diffraction patterns with a beam direction of $[1\bar{2}10]$.

b) Indexing of the above pattern.

Figure 72. TEM micrograph of M3K, showing ribbon-like α-phase in eutectic. X33k

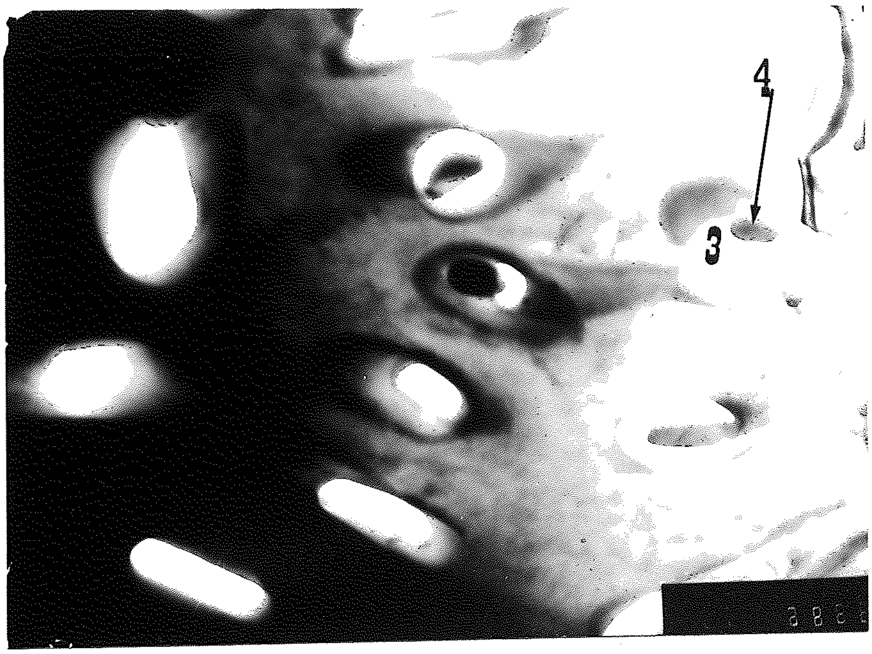

Figure 73. TEM micrograph of M3K, showing dark particles in the eutectic α. X66k

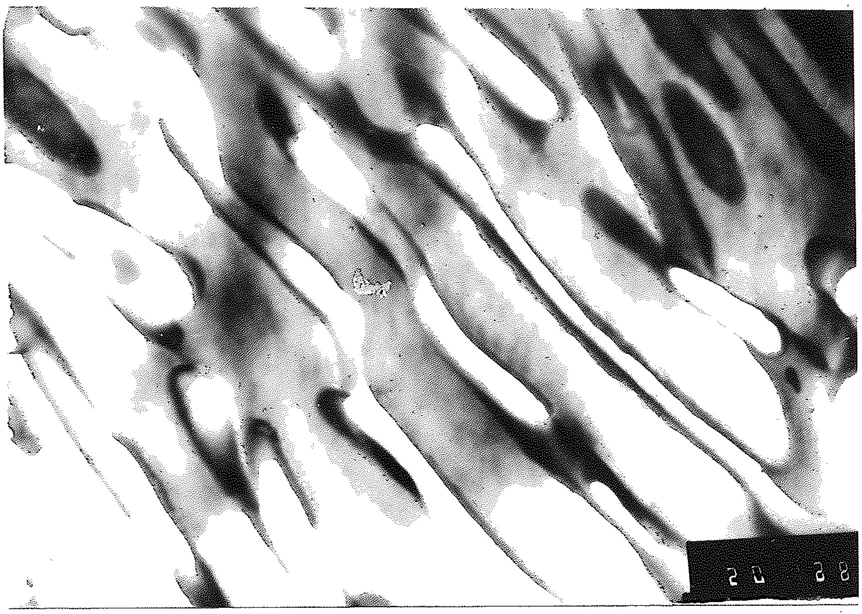

Figure 74 TEM Micrograph of M3K, Showing Eutectic in a Form of α Lamellae with Very Few Internal Phases. ×20k

5.2.2 ZA.8K Alloy

The as-cast structure of the ZA8K alloy, as revealed by SEM micrographs, is shown in Figures 75 to 80 at six different magnifications. The structure consisted of the primary β phase with different shapes and sizes ranging from as small as 3 µm up to 15 µm, and averaging out at about 6 µm (Figure 75). The Figure also showed the eutectic pools surrounding the primary β particles. Figures 75 and 76, at low magnification, showed the presence of zinc-rich η particles with almost the same size as the primary β particles. Pores are also observed in Figures 75 and 76, these pores were surrounded by the η particles, which seemed to have grown around the pores due to the different magnitude of surface energy between the gas and the zinc-rich η phase. The decomposition of the β phase is shown in Figures 77-79, Figure 77 showed a variety of decomposition structures in the former β dendrites surrounded by haloes of η. Figure 78, at high magnification, showed the decomposition of β into well developed lamellae, and a coarse mixture of different phases around the edges. Figure 79 showed the decomposed β, and also focussed on the eutectic matrix, to show a good eutectic lamellar morphology with an interlamellar spacing of 0.5 μm. The eutectic was also formed into nicely-formed particulate pools and is shown in Figure 80 at high magnification.

Further detailed investigations on the as-cast structure were conducted by using the TEM and are shown in Figures 81-87. General structure of this alloy can be seen at low magnification in Figure 81. The structure consisted of the primary β (white) surrounded by polycrystalline eutectic cells. In the eutectic, short and irregular aluminium lamellar arms enclosed a small dark particle of a different phase. These were shown in most of the later Figures at higher magnifications. Also seen in this Figure, thin haloes of η surrounded the β dendrites. The grey areas, seen in the bottom left side of the micrograph, which appeared to be decorated by dark pen points, are the ε-precipitates.

Figure 82, at higher magnification, showed the decomposed β particle surrounded by haloes of zinc-rich η phase. Both this Figure, and more apparently Figure 83, revealed the tiny dark spots on almost every aluminium-rich α particle. These dark spots were either rounded or, less frequently, elongated shapes. The presence of these spots will be discussed in the following chapter. SADP diffraction pattern was taken from the aluminium-rich α phase in the eutectic region from area 1 in Figure 83 and is shown in Figure 84(a). The indexing of this pattern is shown in Figure 84(b), which revealed that the pattern was fcc α with a beam direction of $\langle 110 \rangle$. Another SADP was taken from area 2 in Figure 83 and is shown in Figure 85(a), the indexing of this pattern is shown in Figure 85(b). The pattern revealed an fcc α' with a beam direction of $\langle 110 \rangle$α'. Quantatitive analyses on areas 1 and 2, from Figure 83 of the aluminium-rich α, are shown in Table 13. The results of these analyses did not correspond to any equilibrium phases in the Zn-Al system.

The eutectic and two families of ε-precipitates within the η matrix can be seen in Figures 86 and 87 at higher magnification. The precipitates had nucleated heterogeneously in very large densities covering the eutectic matrix. A number of SADP's were taken from the areas of precipitates in Figure 87. One example is shown in Figure 88(a) and the corresponding indexing is shown in Figure 88(b). Figure

88(b) revealed that these precipitates had a beam direction of $\langle 01\bar{1}1 \rangle$ of cph structure of the η matrix, but failed to show any clear evidence of the presence of a precipitate phase. Further SADP's were taken from the areas of precipitates in Figure 87, and one is shown in Figure 89(a) and indexed in Figure 89(b). The pattern revealed two sets of identical streaks around the matrix reflections, both of which were found to correspond to the cph ε-phase ($CuZn_4$) with the same zone axis of $\langle 1\bar{2}10 \rangle$ as the matrix. STEM analyses were conducted on these areas of precipitates (area 3 / Figure 83), and are shown in Table 13. The analyses revealed that these areas contained 1.2%Al, 3,5%Cu, 0,7%Mg and 94.6%Zn.

Further TEM work was focussed on the decomposed primary β particles, as shown at high magnification in Figure 90. The Figure showed the final products of the decomposed primary β particle to form regular and irregular lamellae.

Phases Anaysed	% Al	% Cu	% Mg	% Zn
α'm Phase in Eutectic (area.1 in Figure.83)	19.0	1.0	0.6	Rem
α Phase in Eutectic (area.2 in Figure.83)	67.0	1.2	0.9	////
Eutectic Matrix (area.3 in Figure.83)	1.2	3.5	0.7	////

Table 13 : STEM Analysis of ZA8K.

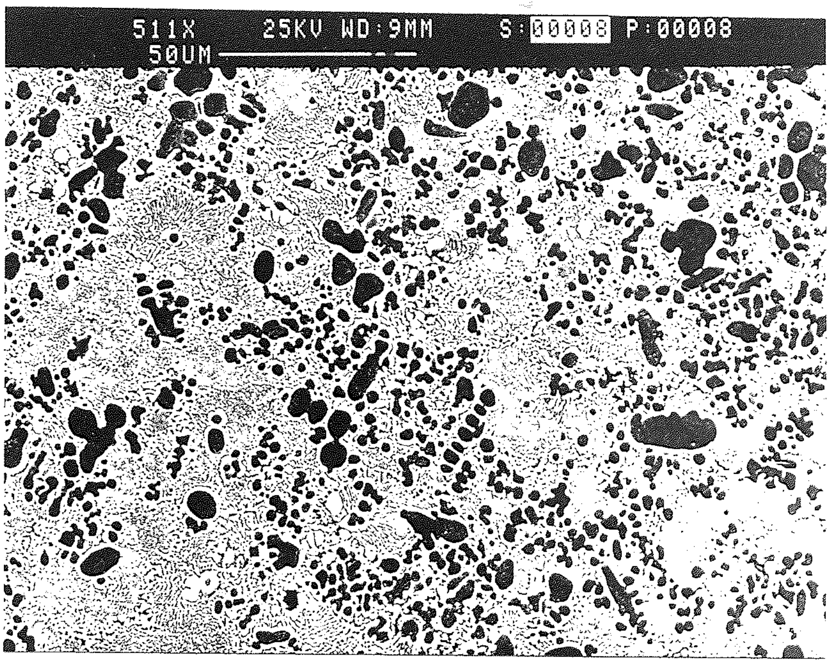

Figure 75. SEM.As-cast structure of ZA8K, showing primary β-pahse surrounded by thin film of η and set in eutectic.

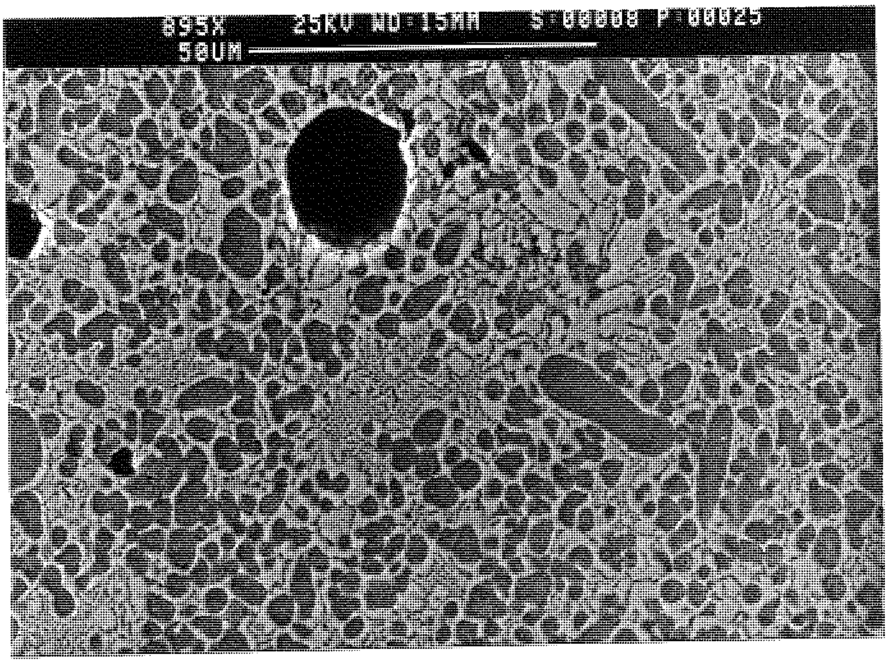

Figure 76. SEM.As-cast structure of ZA8K, showing primary β, η particles. Pores have nucleated on η particles. Eutectic cells have nucleated on the primary β and grown radially.

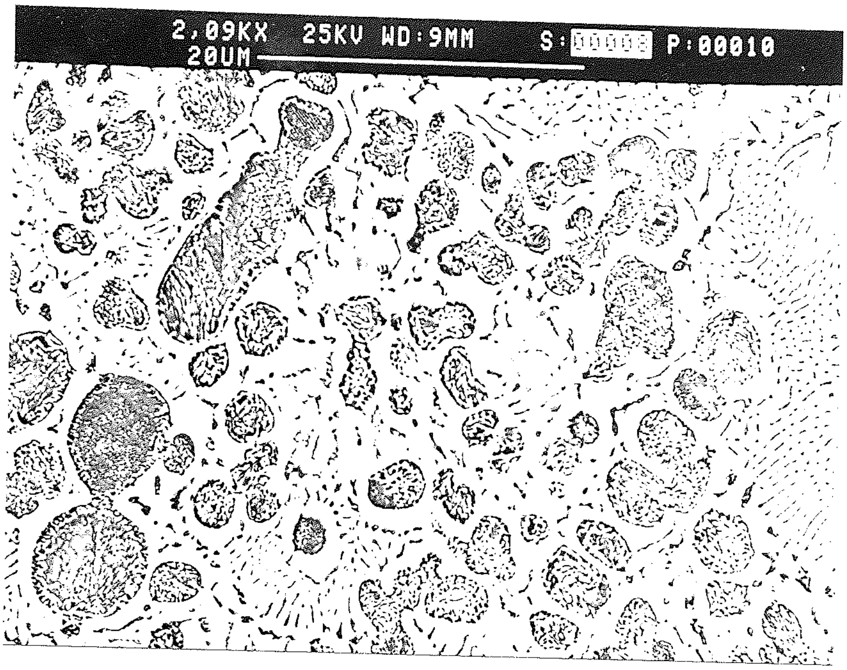

Figure 77. SEM.As-cast structure of ZA8K, showing variety of decomposition structure in the former β dendrites.

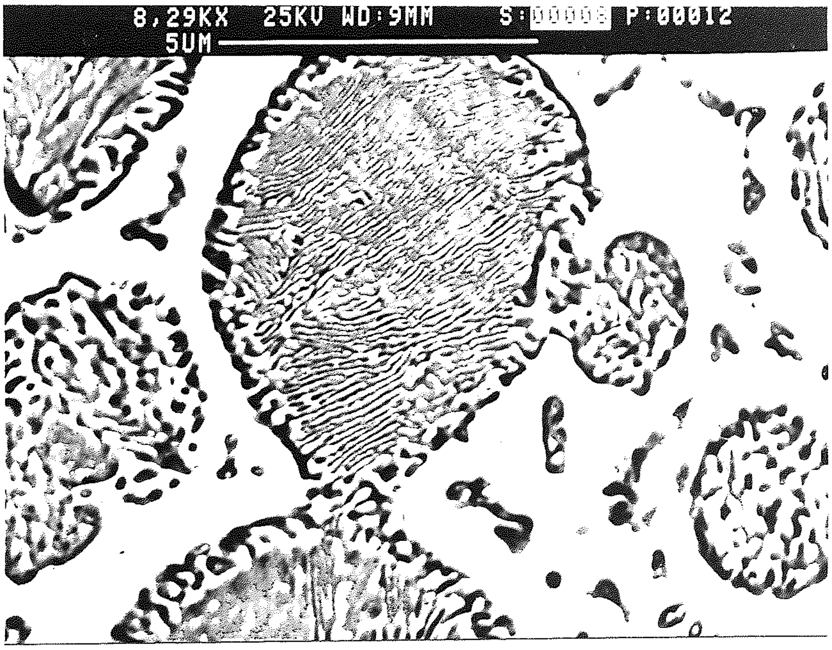

Figure 78. SEM.As-cast structure of ZA8K, showing b decomposed into well-formed lamellae and a mixture of phases.

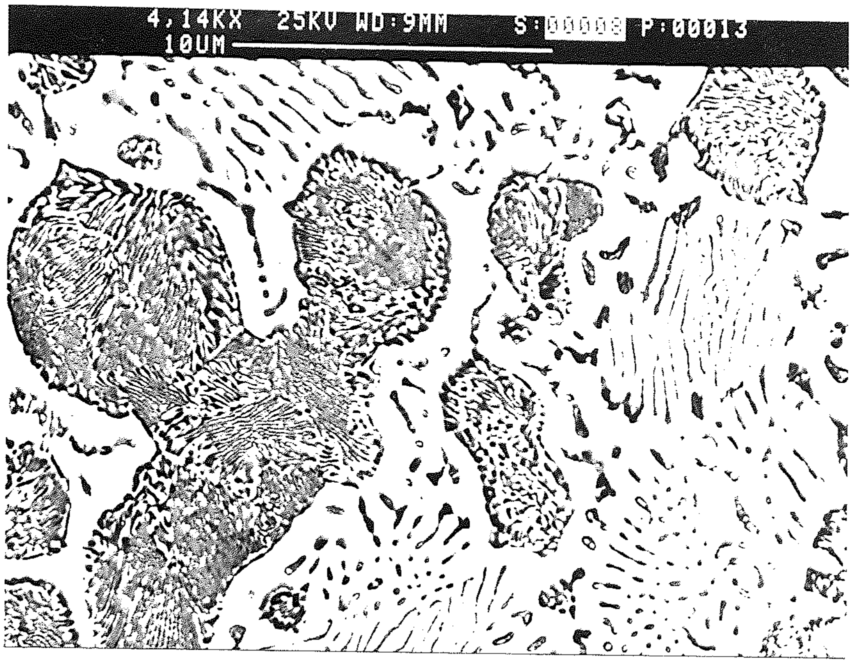

Figure 79. SEM.As-cast structure of ZA8K, showing decomposed β and eutectic matrix with good lamellar morphology.

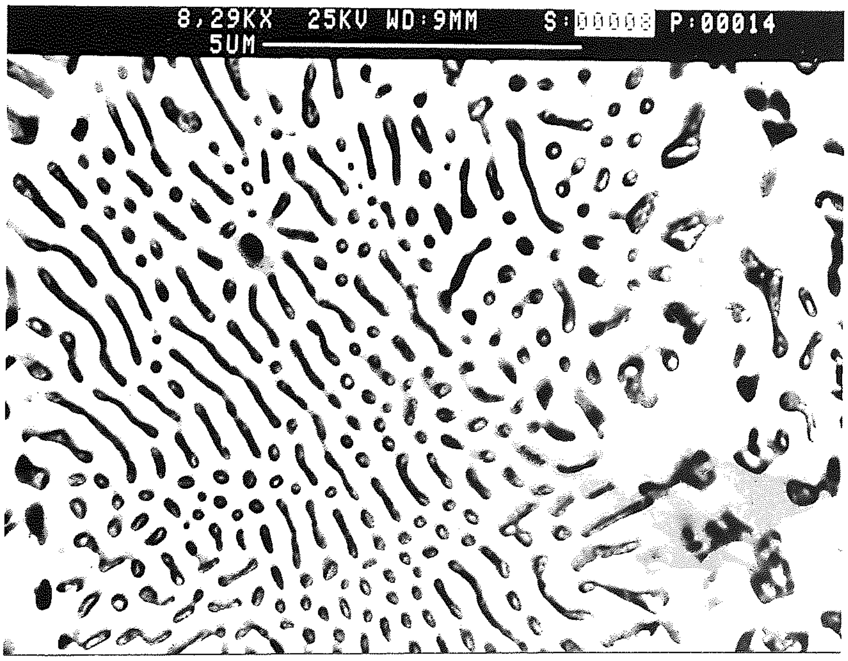

Figure 80. SEM.As-cast structure of ZA8K, showing a nicely-formed particulate eutectic pool.

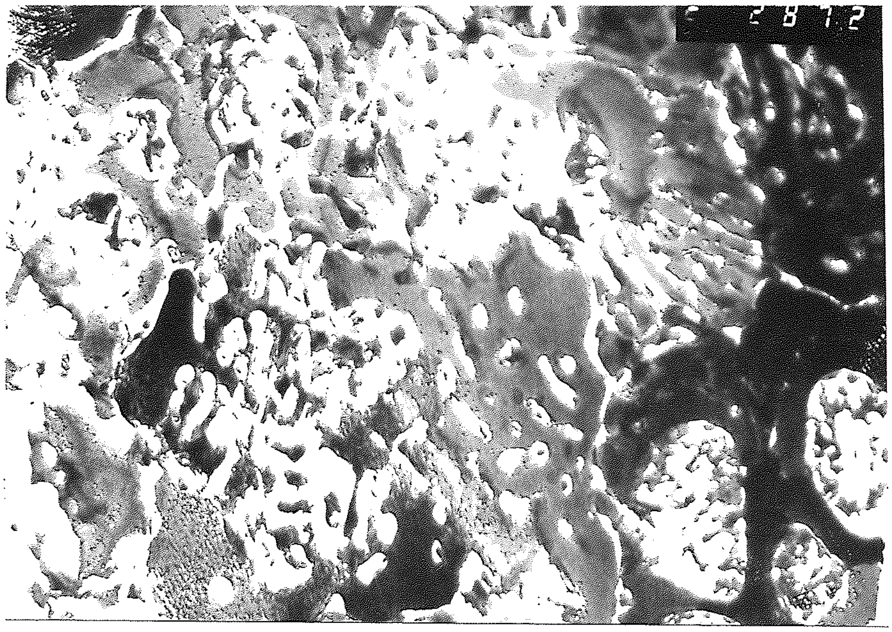

Figure 81. TEM micrograph of ZA8K, showing primary β dendrites (white) surrounded by polycrystalline eutectic cells. ×20 k

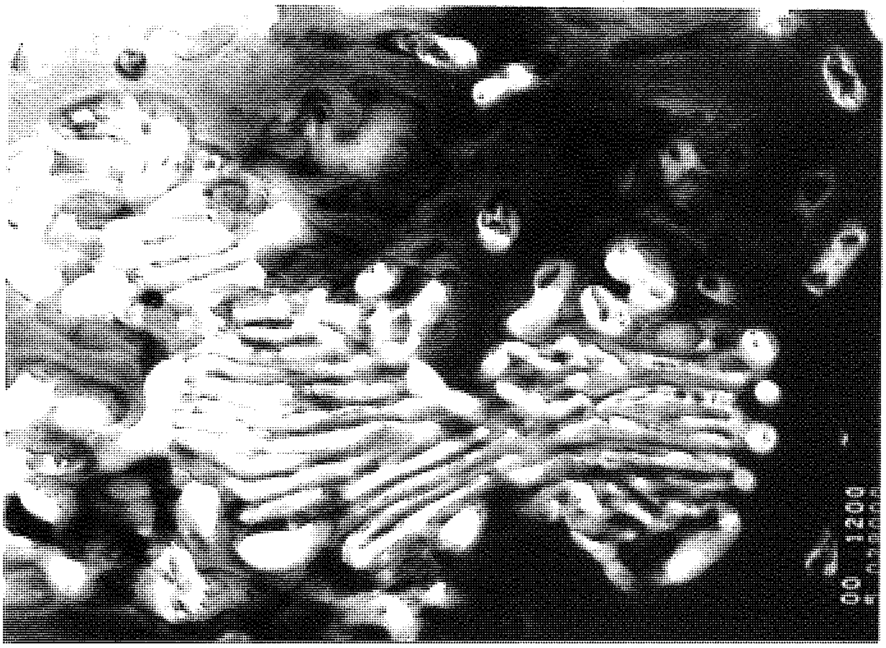

Figure 82. TEM micrograph of ZA8K, showing decomposed β particle at high magnification. x28k

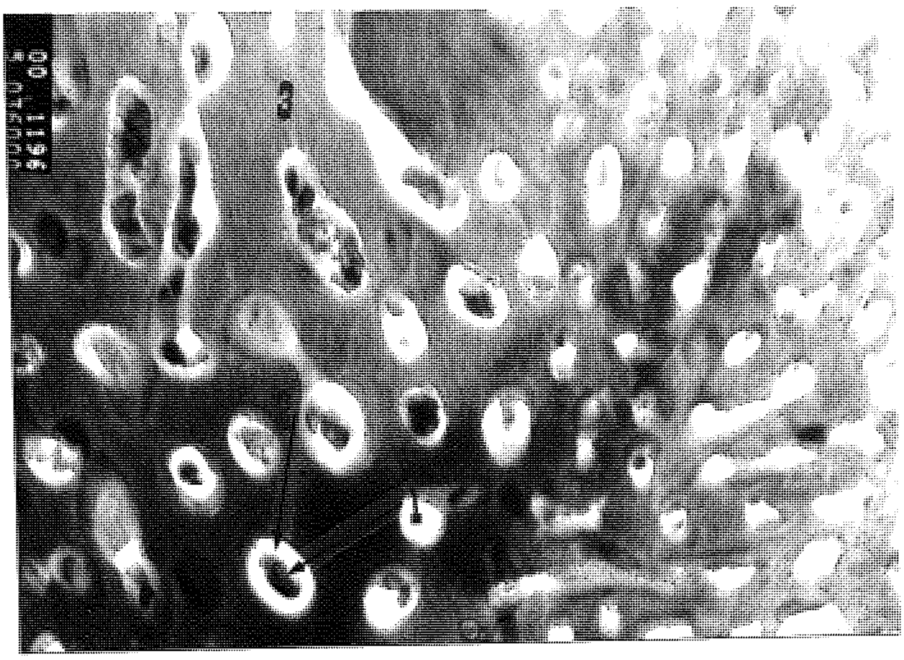

Figure 83. TEM micrograph of ZA8K, showing eutectic area and also revealing dark particles formed within the α part of the (α + η) eutectic. ×36k

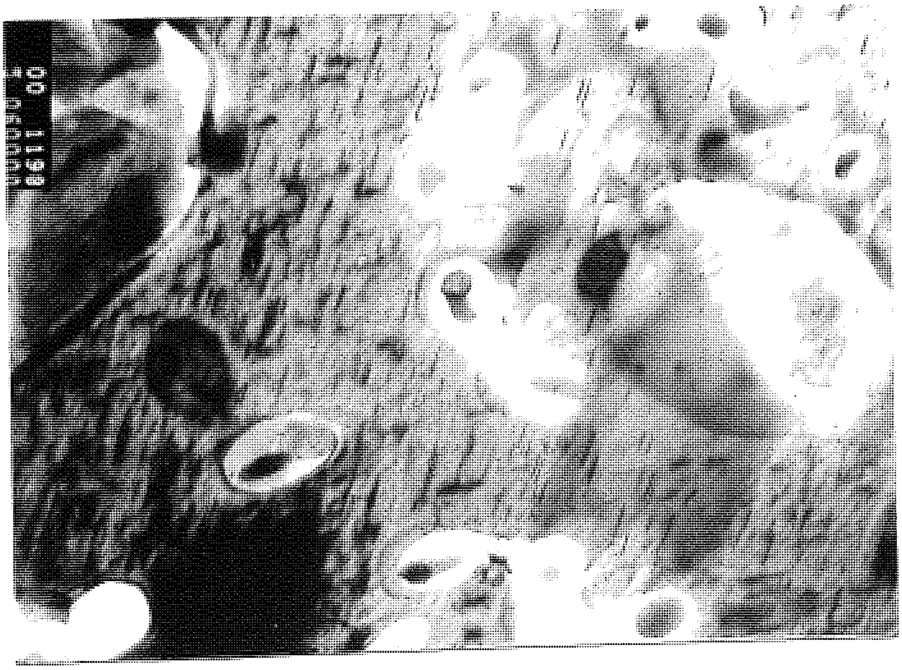

Figure 86. TEM micrograph of eutectic in ZA8K, showing two families of ε-phase precipitates within the η matrix.×60k

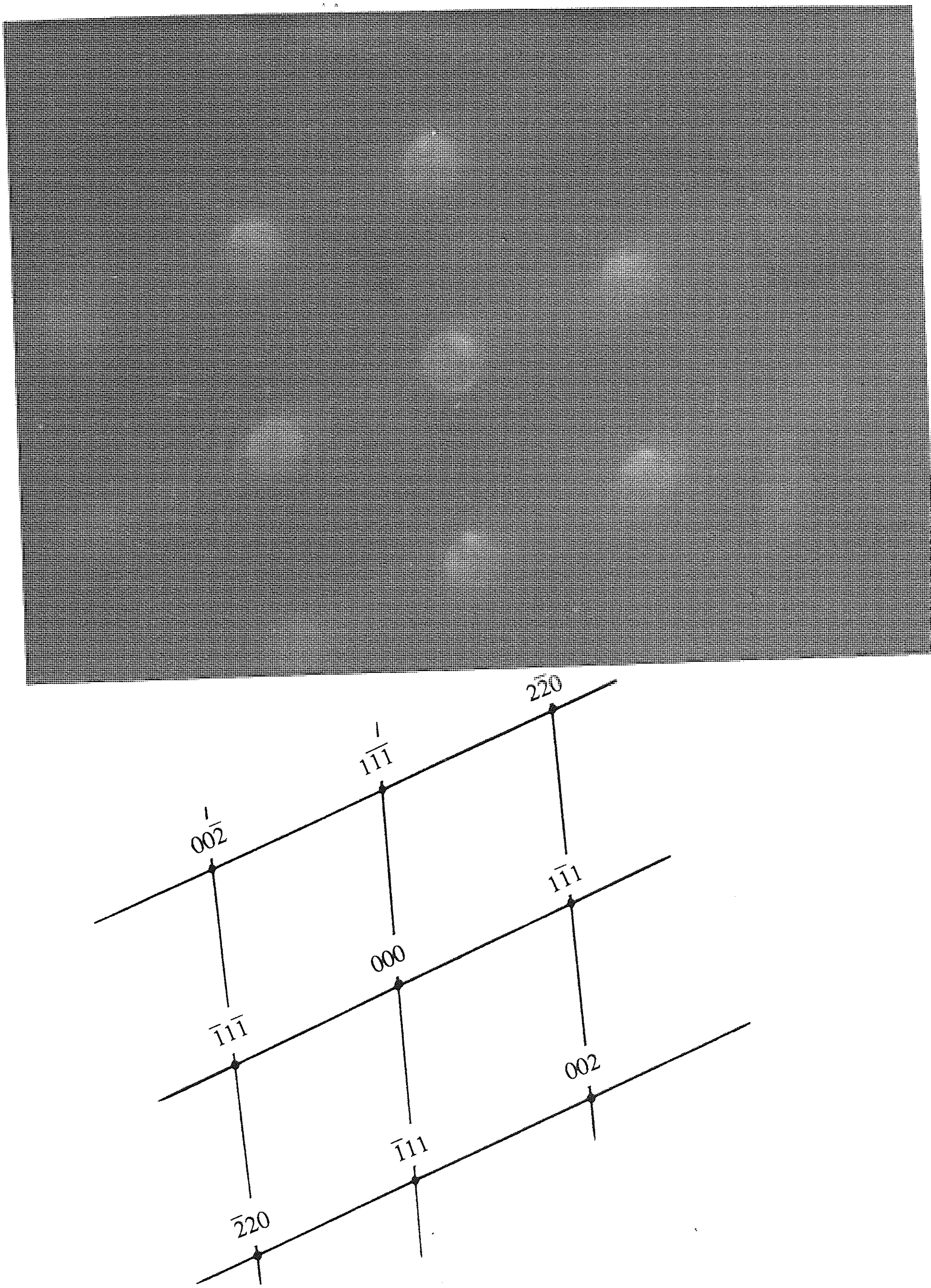

Figure 84. a) SADP's taken from area 1 in Figure 83, showing a diffraction pattern from fcc crystal with abeam direction of [110] α. b) Indexing of the above pattern.

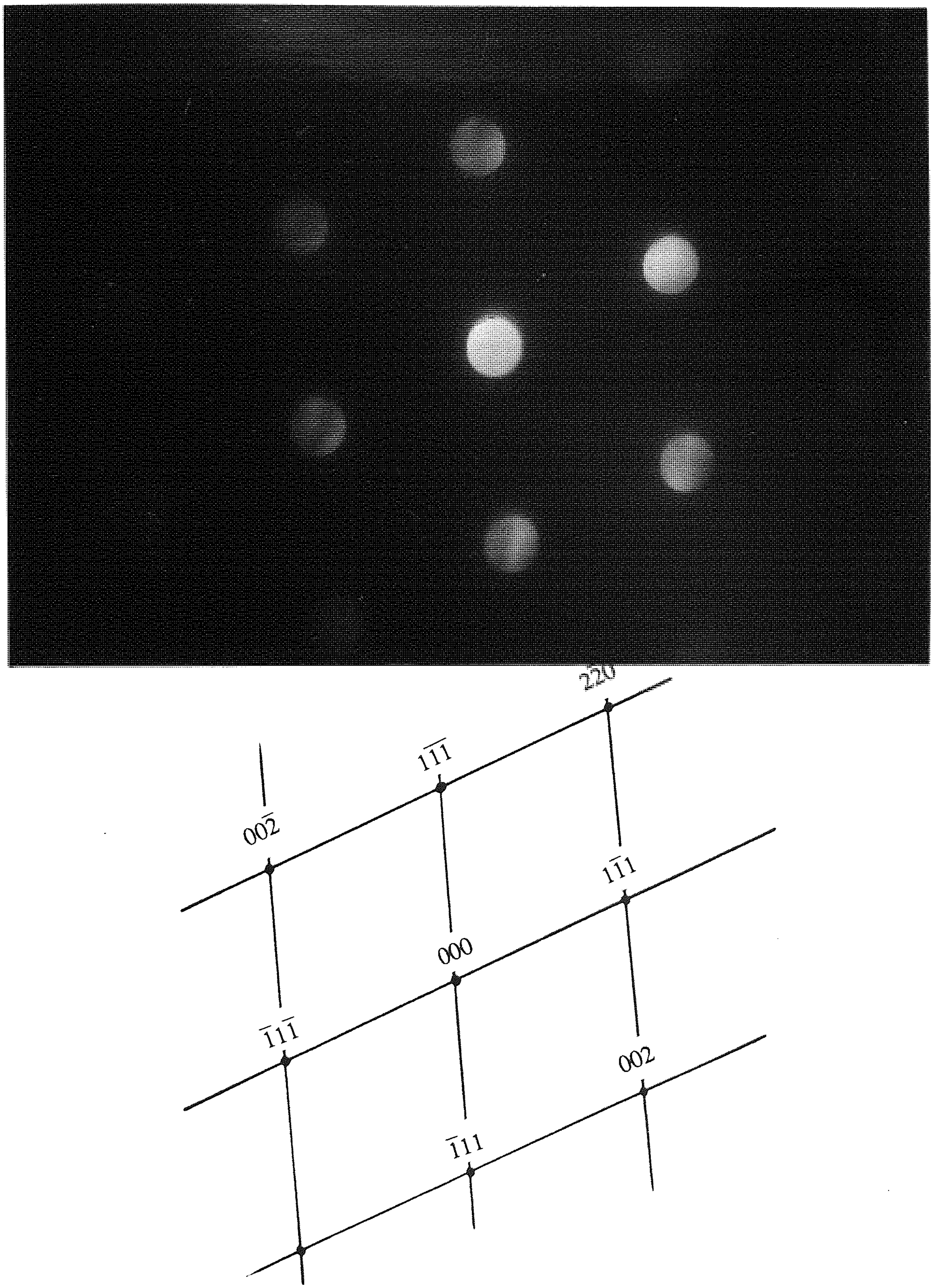

Figure 85. a) SADP's taken from area 2 in Figure 83, showing a diffraction pattern from fcc crystal with a beam direction of [110] α'_m. b) Indexing of the above pattern.

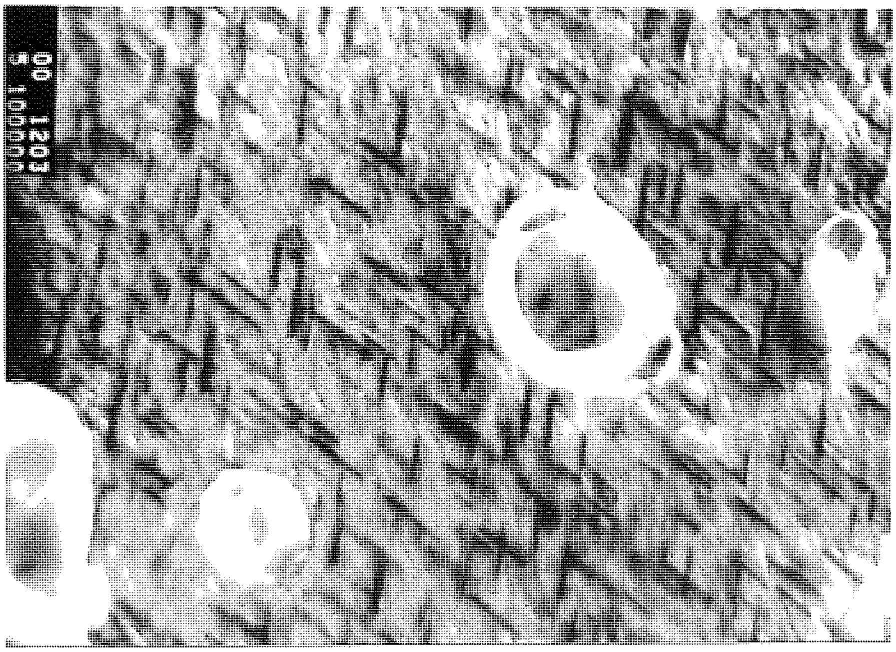

Figure 87. TEM micrograph of eutectic in ZA8K, showing eutectic α with internal phase and two families of precipitates of ε-phase within the η matrix. **x100k**

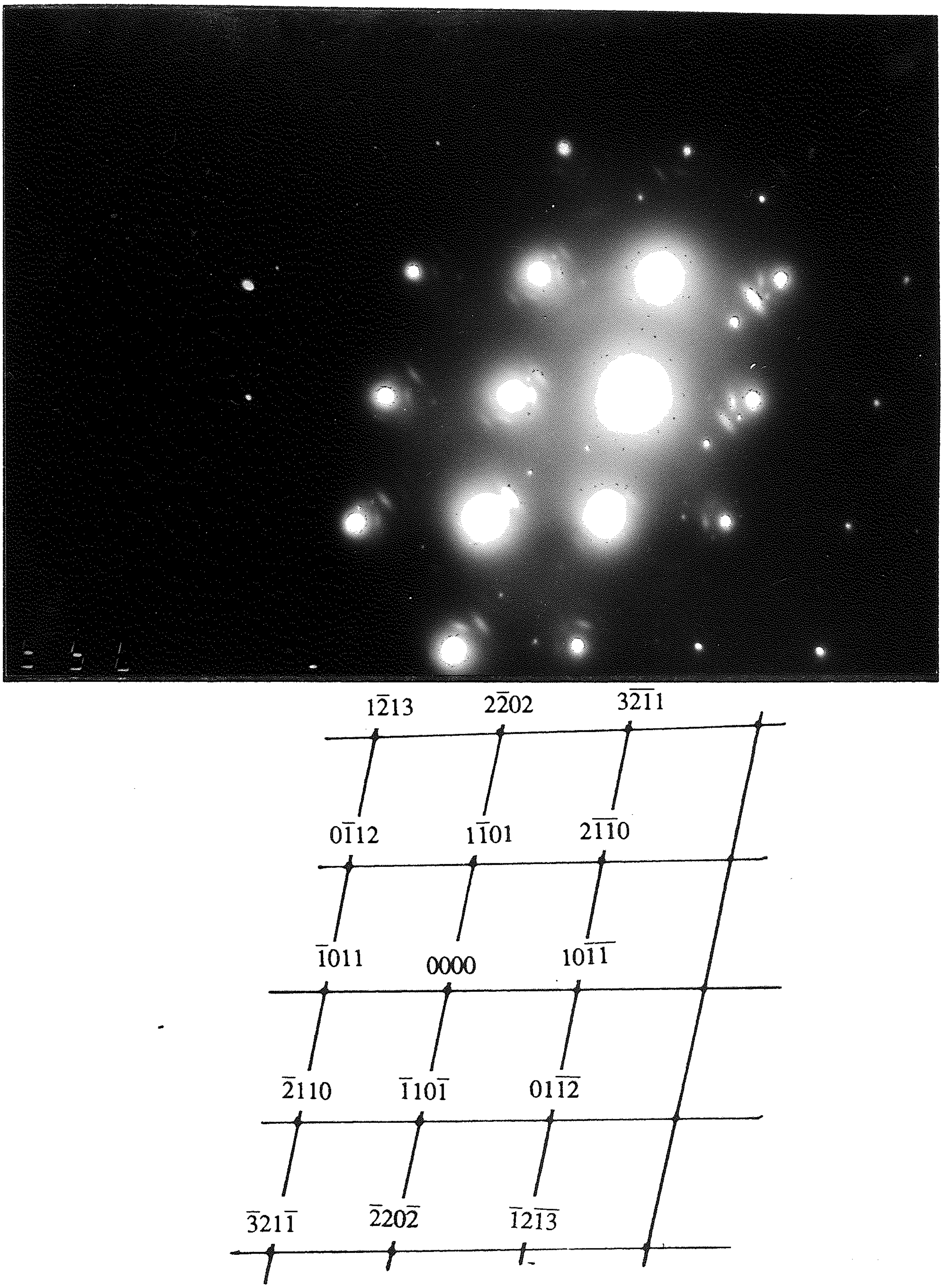

Figure 88. a) SADP's taken from the precipitates in Figure 87, showing a diffraction pattern with a beam direction of $[01\bar{1}1]_{\eta}$. b) Indexing of the above pattern.

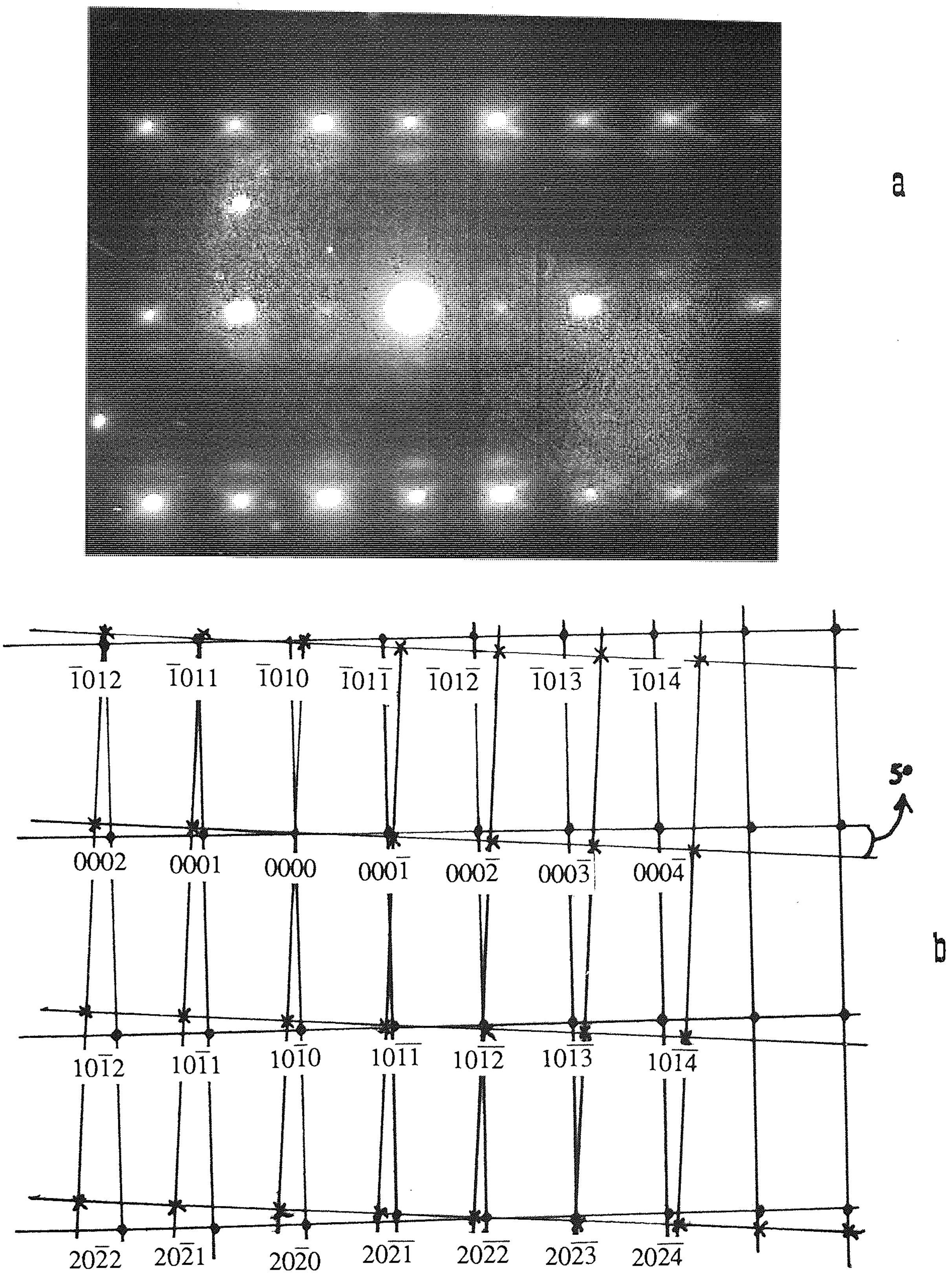

Figure 89. a) SADP's taken from the zinc-rich area 3 on Figure 83, showing a diffraction pattern with a beam direction of $[1\bar{2}10]$ η and $[1\bar{2}10]$ ε. b) Indexing of the above pattern.

● - $[1\bar{2}10]_\eta$
X - $[1\bar{2}10]_\varepsilon$

Figure 90. TEM micrograph of ZA8K at high magnification, showing finally decomposed primary β particle. The precipitates of ε-phase, with Al-rich area in the middle. α lamellae contain internal phase particles and the η contain ε-precipitates like those in the eutectic η surrounding the dendrite. 60k

5.2.3 Alloy ZA27K

The as-cast structure of the alloy ZA27K is shown at four different magnifications in Figures 91 to 94. The alloy exhibits a very complex heterogeneous structure. Figures 91 and 92 showed α' dendrites (seen as dark areas) surrounded by a decomposed β layer with small pockets of interdendritic eutectic η. The average size of the α' particles was found to be about 7 μm. Figures 93-94, at high magnifications, showed the final products resulting from the decomposed β, these were mostly cellular lamellae and fine zinc-rich phases in an aluminium matrix. The Figures also showed lamellar or irregular particles of α' and η, with η occupying the remaining interdendritic areas.

TEM work was also conducted on the as-cast structure of ZA27K alloy and is revealed in Figures 95-99. A fine equiaxed mixture of the decomposed α' structure is shown in Figure 95. The grains shown in this Figure are very small. EDS/STEM analyses were carried out on the area marked 1 in Figure 95, the results are shown in

Table 14. Figure 96 showed another type of discontinuous decomposition of α', producing a lamellar array of final products. Figure 97 showed these lamellae at high magnification, and the numerals label the parts which were chemically analysed by EDS in STEM mode, and the results are shown in Table 14.

An SADP was taken from the aluminium lamella marked 2 in Figure 97, and is shown in Figure 98. The diffraction pattern revealed the fcc structure of the α phase with a zone axis of $\langle 211 \rangle$. The complex structure revealed in Figure 99 is of aluminium and zinc-rich phases resulting from the decomposition of β, which also contained large dark particles. These dark particles are probably metastable epsilon phase. EDS/STEM analyses were conducted on the area marked 4 in Figure 99, and the results shown in Table 14 revealed a high copper content of 15.2%.

Area - Figure	% Zn	% Al	% Cu	% Mg
1 - 95	29.8	65.4	3.7	1.0
2 - 97	76.2	18.1	5.3	0.4
3 - 97	26.1	71.2	1.8	0.8
4 - 99	83.3	0.8	15.2	0.2

Table 14. STEM Analysis of ZA27K.

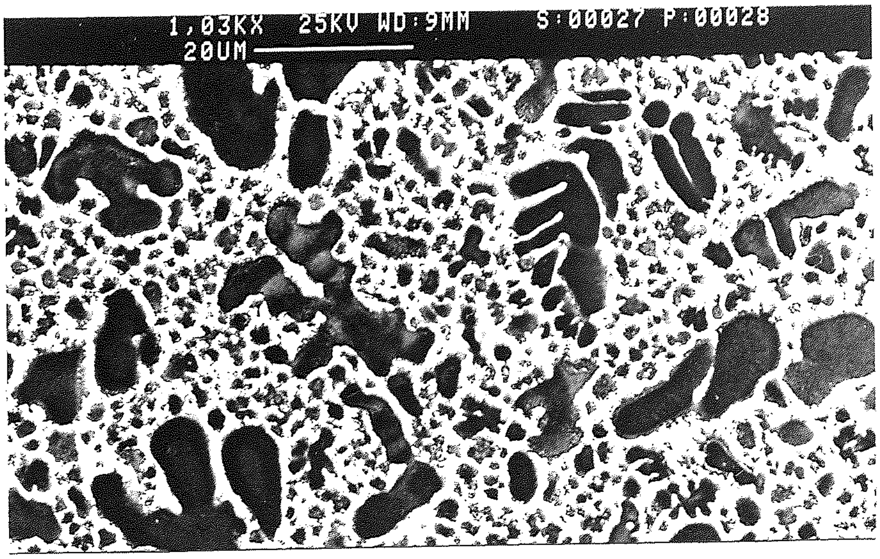

Figure 91. SEM.As-cast structure of ZA27K, showing a fine structure of former α' particles surrounded by β and interdendritic η.

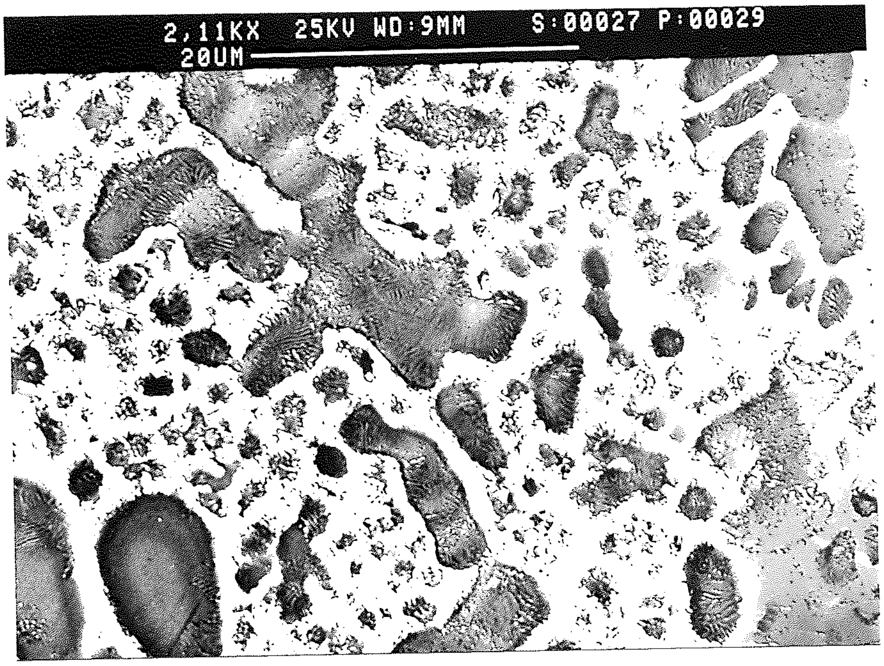

Figure 92. SEM.As-cast structure of ZA27K, showing the decomposed α' and β.

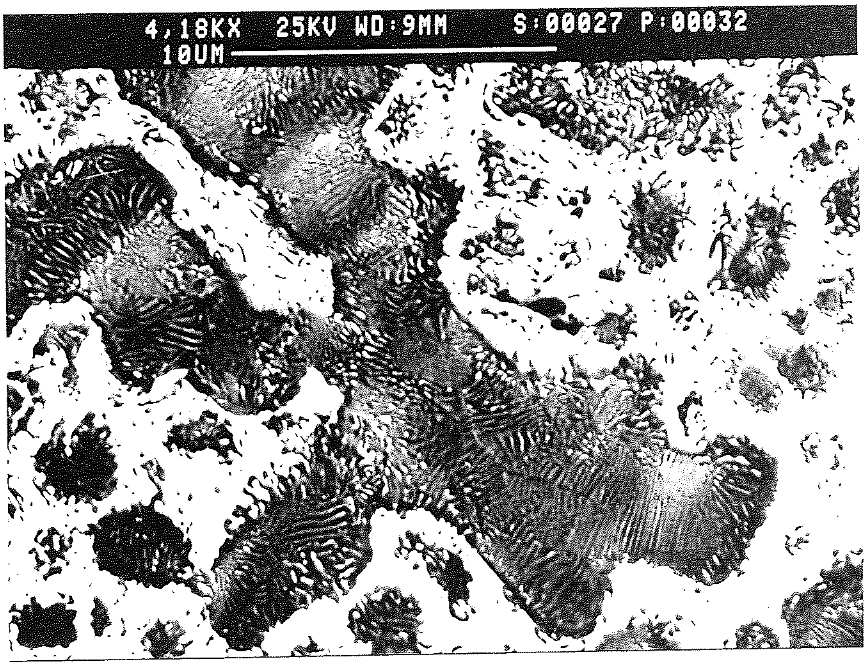

Figure 93. SEM.As-cast structure of ZA27K, showing the decomposition of α' particles.

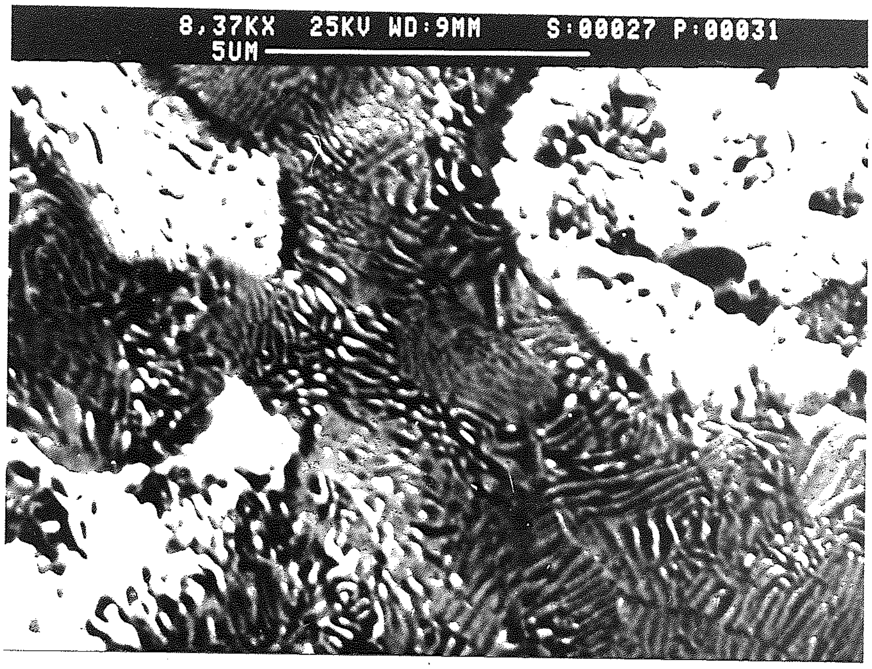

Figure 94. SEM.As-cast structure of ZA27K at high magnification, showing the final product of decomposition of α' and β.

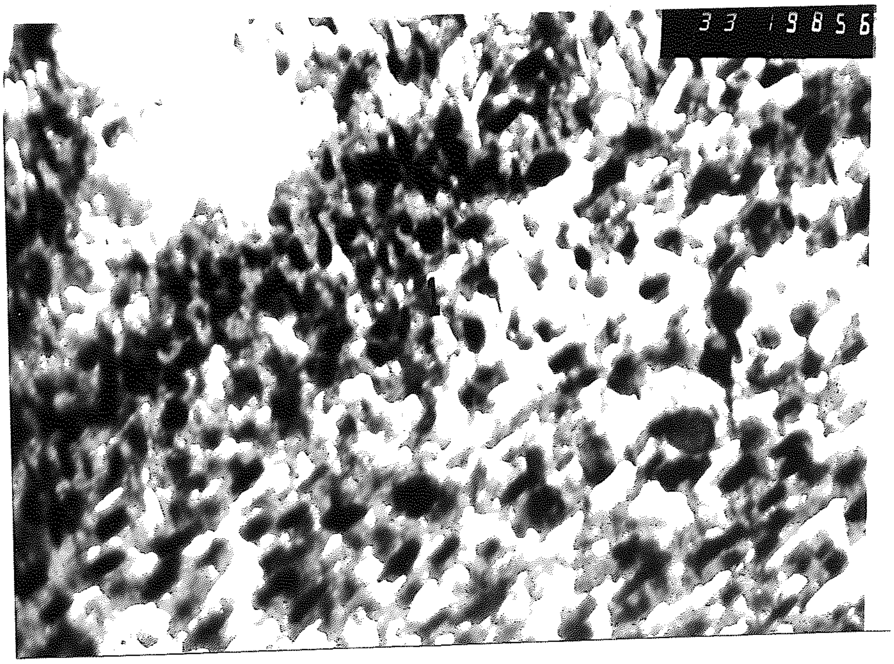

Figure 95. TEM micrograph of ZA27K, showing equiaxed mi of phases within the former α' cores of the dendrit

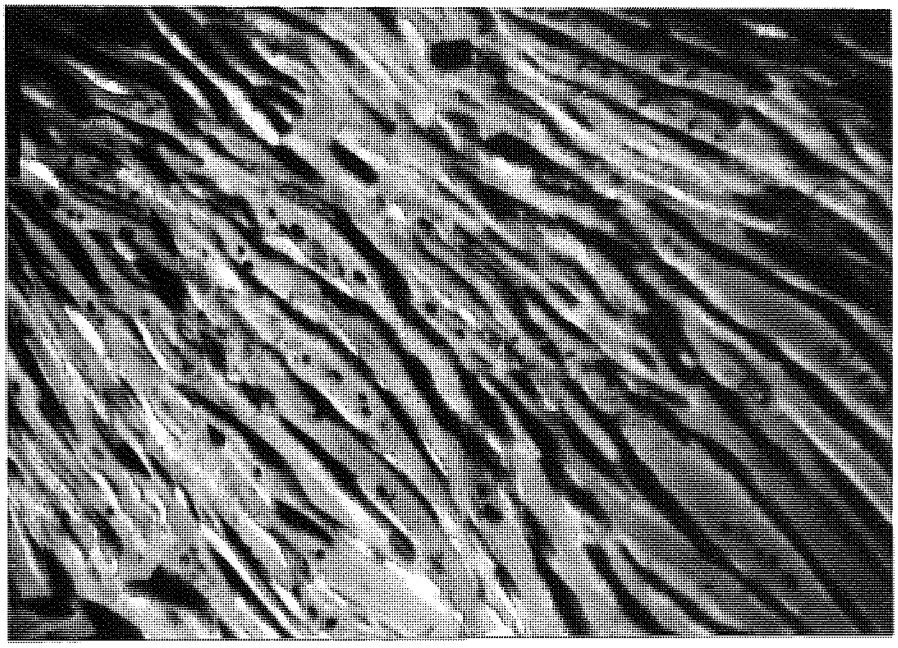

Figure 96. TEM micrograph of ZA27K, showing discontinuous decomposition of α' dendrite cores into a lamellar final product. x28 k

Figure 97. TEM micrograph of ZA27K, showing decomposed α' at high magnification analysed areas marked 2 and 3. x44k

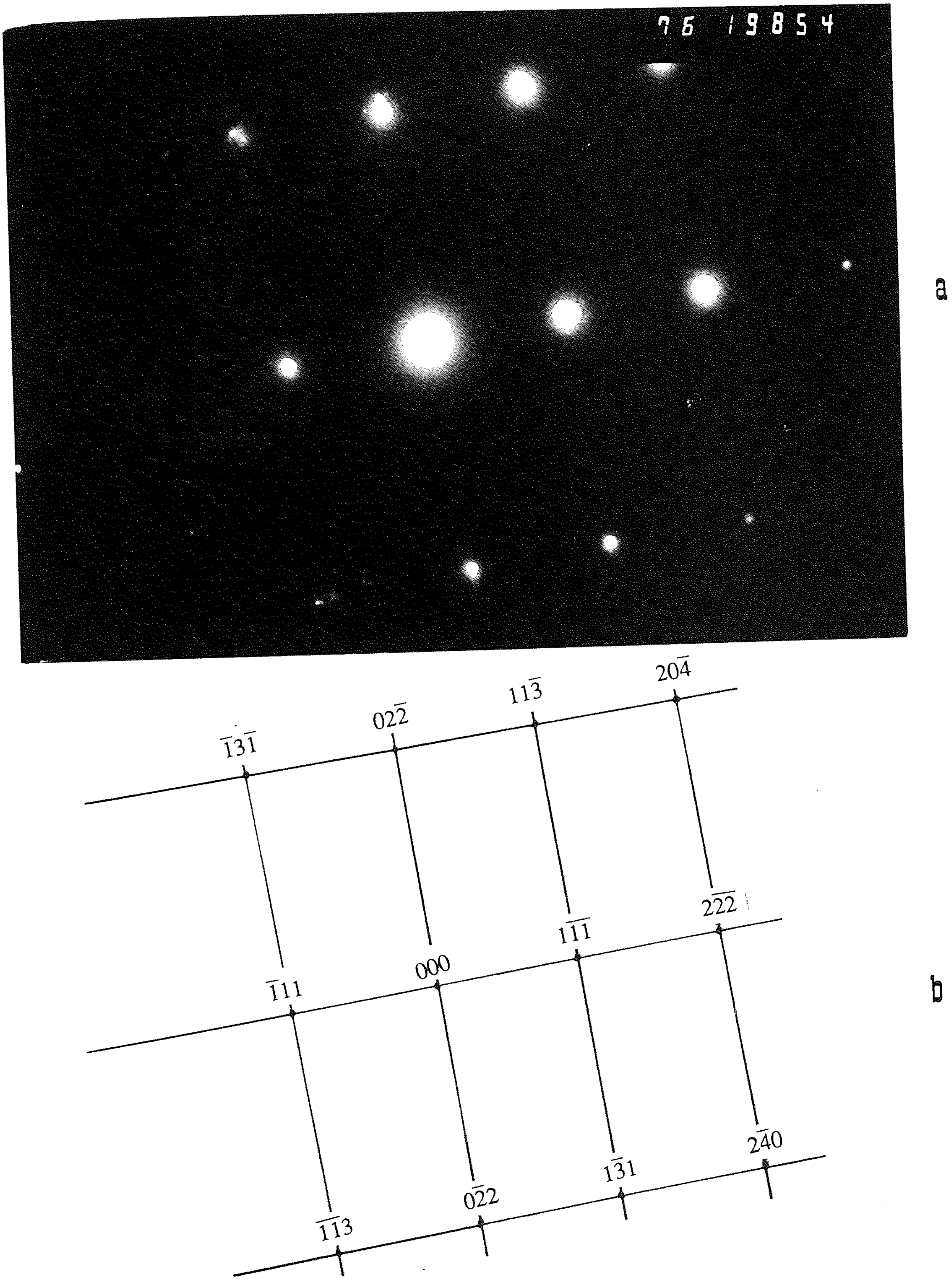

Figure 98. a) SADP's taken from area 2 on Figure 97, showing a diffraction pattern with abeam direction of [211]α.

b) Indexing of the above pattern.

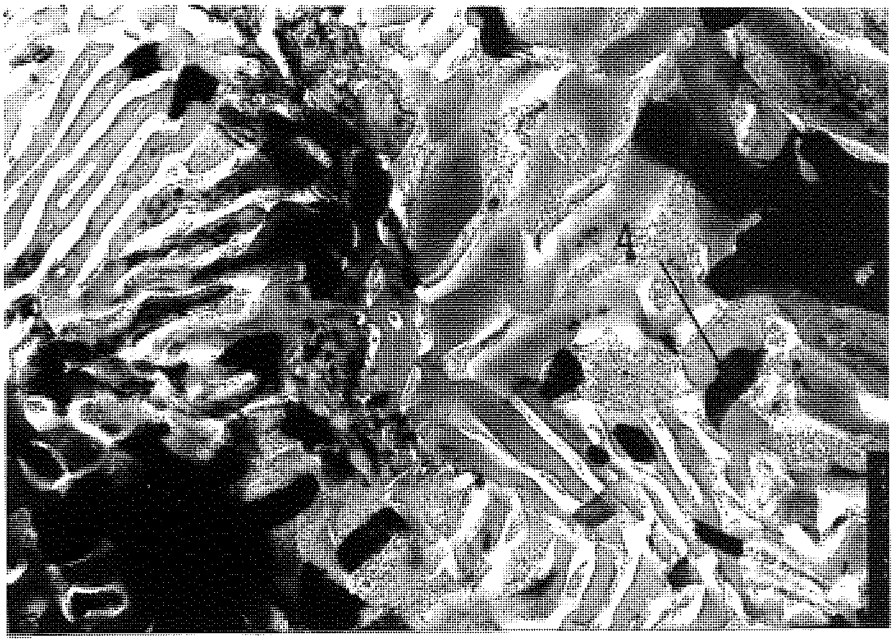

Figure 99. TEM micrograph of ZA27K, showing a complex structure of eutectoidally-decomposed β. Fine surface oxides formed on the η phase during electropolishing. ×17k

5.3 Metallography of the K1, K2 and K3 Alloys

K1, K2 and K3 alloys, which are based on the ZA8 alloy but vary in their copper content, have been examined using the SEM technique. The as-cast structure of these alloys was examined at three different magnifications.

5.3.1 Alloy K1

The as-cast structure of the K1 alloy, shown in Figures 100 and 101 at two different magnifications, shows primary β (black areas) surrounded by eutectic. The figures also show the presence of η particles (the white areas).

Details of the β phase, decomposed into lamellae and a particulate phases, is shown in the higher magnification micrograph of Figure 102.

The average size of the primary β was found to be about 5 μm, whilst the average size of the eutectic pools was about 11 μm.

5.3.2 Alloy K2

The as-cast structure of the alloy K2 is shown in Figures 103, 104 and 105 at three different magnifications. Figures 103 and 104 show primary β surrounded by eutectic, whilst Figure 105, taken at a higher magnification, shows the decomposed β which had formed lamellar and particulate products. The average size of the primary β was about 8 μm, and the average size of the eutectic pools was about 10 μm.

5.3.3 Alloy K3.

The as-cast structure of the alloy K3, shown in Figures 106 to 108 at three different magnifications, shows primary β surrounded by eutectic. Also seen in Figures 106 and 107, is the presence of η particles.

The average size of the primary particles was found to be about 3 μm, whilst the average size of the eutectic was about 11 μm. Figure 108 illustrates the final products of the decomposition of β particles. The Figure also shows large cells of intermetallic particle ($CuZn_4$).

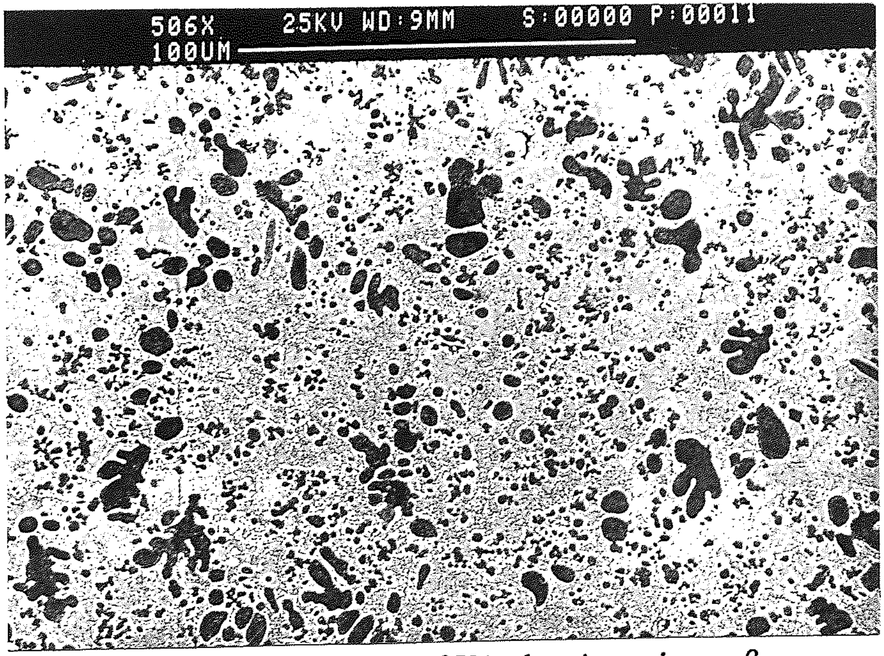

Figure 100. SEM.As-cast structure of K1, showing primary β particles surrounded by eutectic.

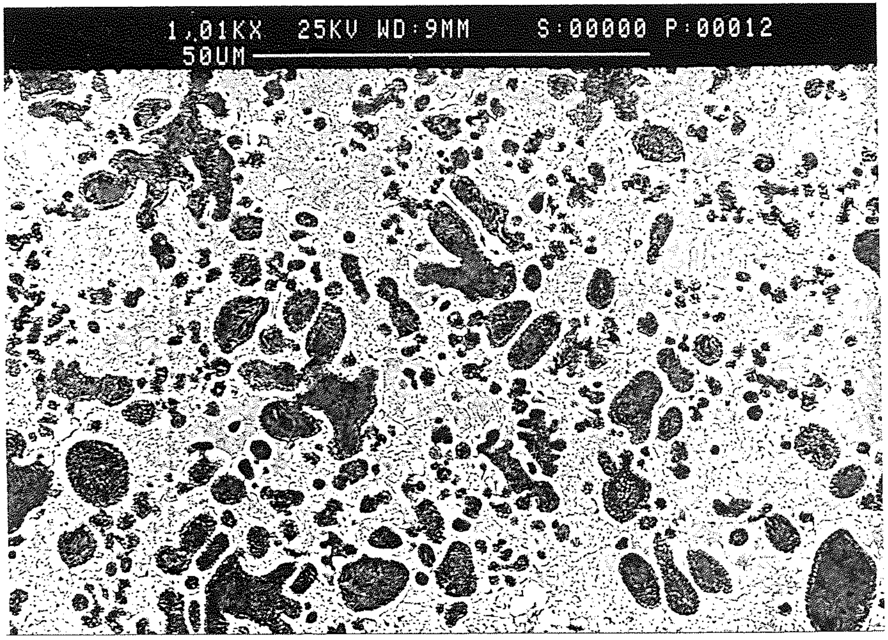

Figure 101. SEM.As-cast structure of K1, showing some pseudo-primary η phase as well as the primary β and eutectic.

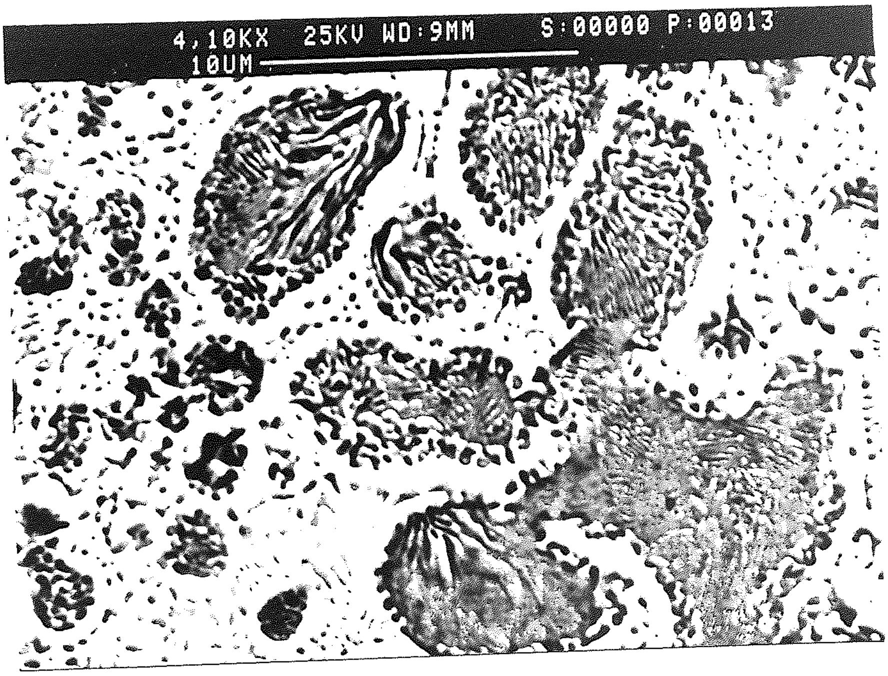

Figure 102. SEM.As-cast structure of K1, showing β particles decomposed into lamellae and a mixture of particulate phases.

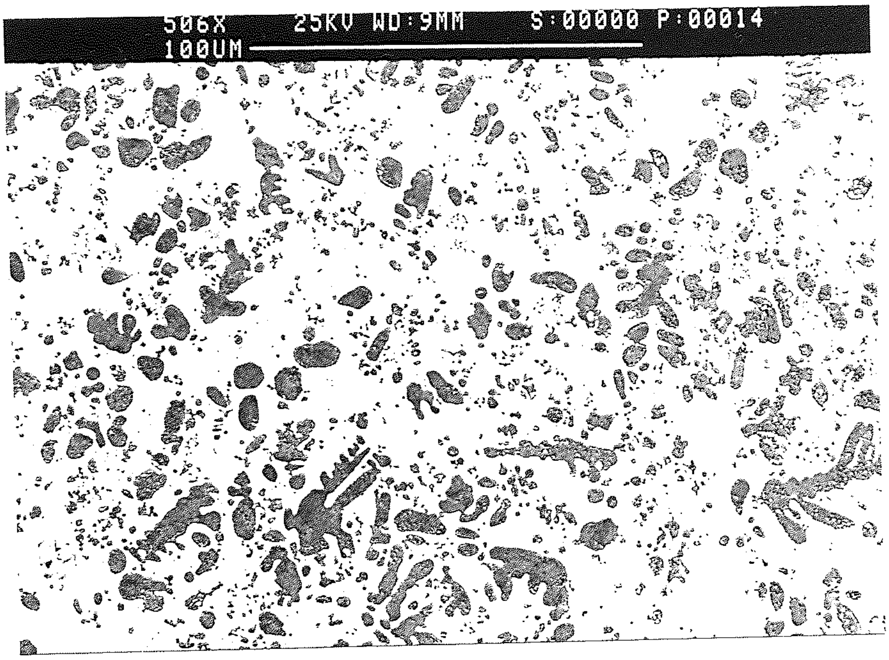

Figure 103. SEM.As-cast structure of K2, showing primary β particles surrounded by eutectic.

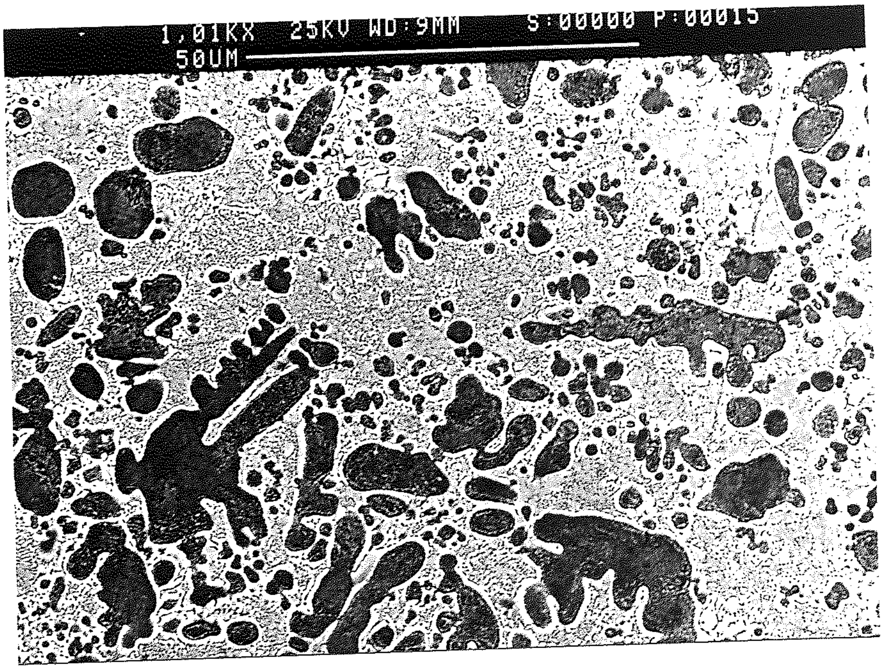

Figure 104. SEM.As-cast structure of K2, showing β, η and eutectic phases.

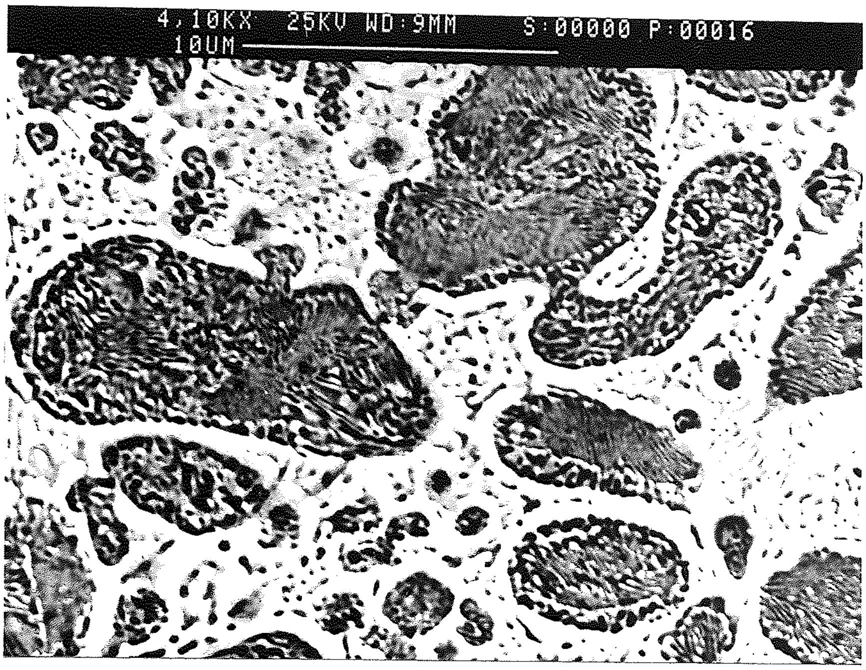

Figure 105. SEM.As-cast structure of K2, at high magnification, showing β primaries decomposed into lamellae and particulate mixture of phases.

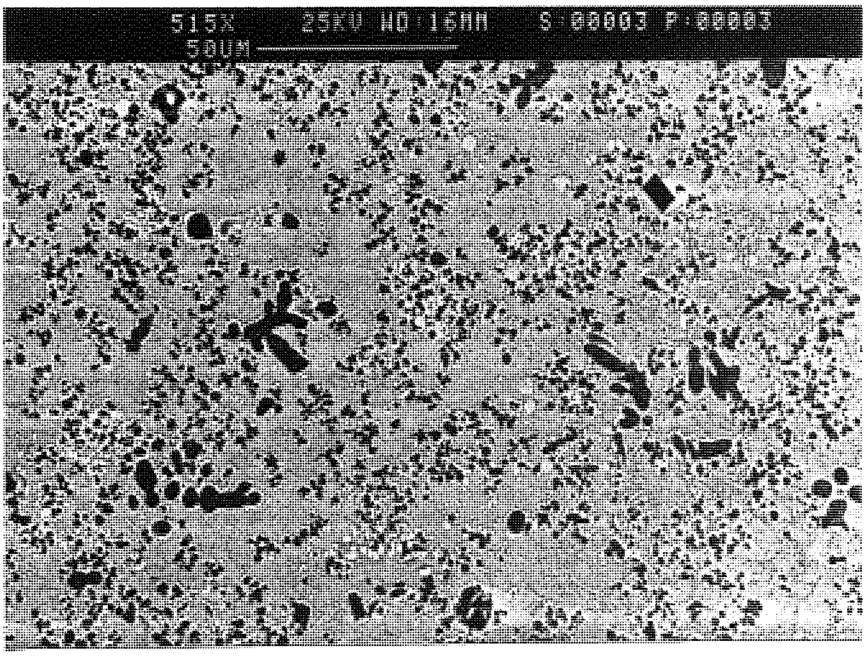

Figure 106 SEM.As-cast structure of K3, showing primary β surrounded by eutectic.

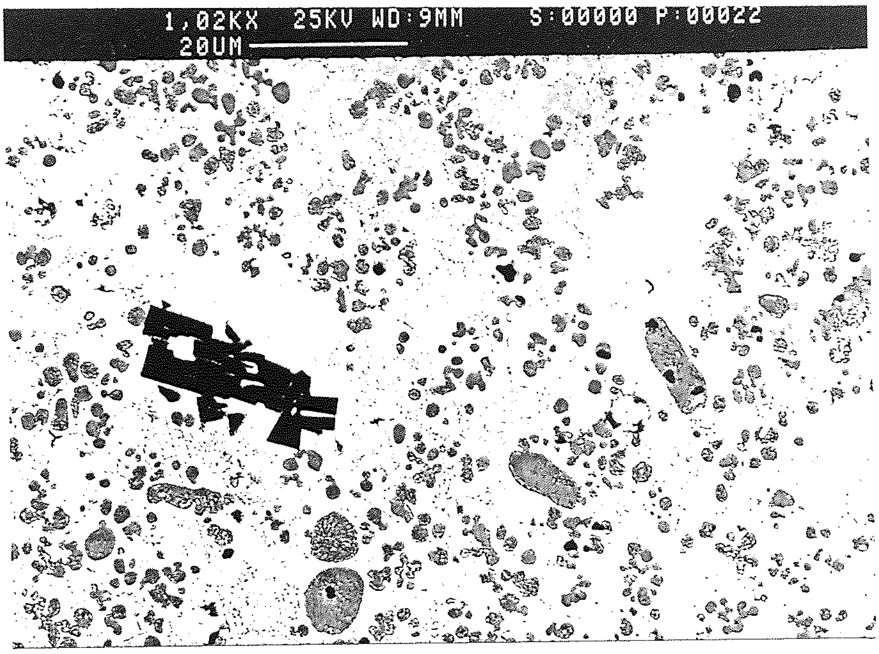

Figure 107. SEM.As-cast structure of K3, showing primary β and pseudoprimary η particles surrounded by eutectic. Also showing intermetallic particles.

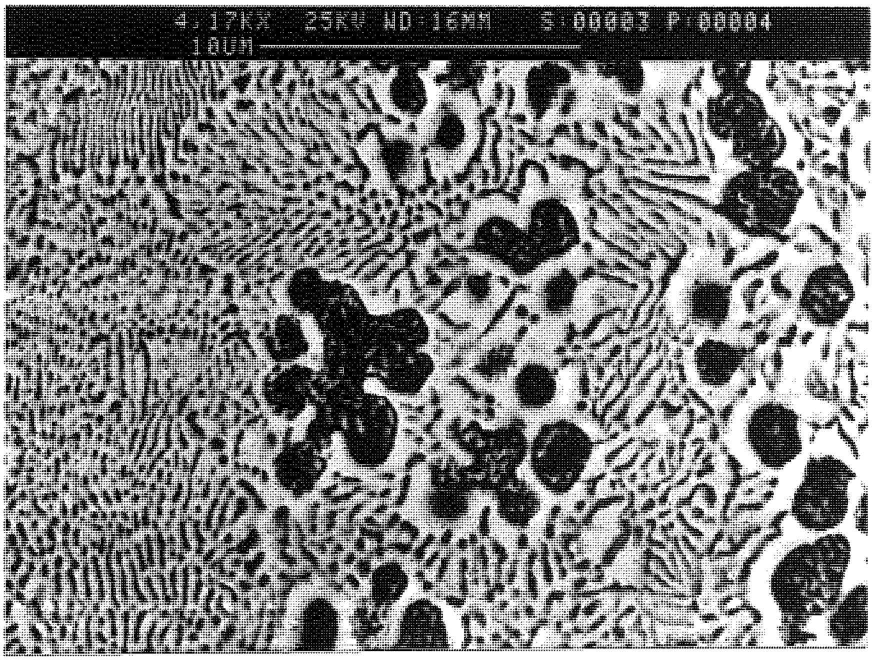

Figure 108. SEM.As-cast structure of K3, showing internal structure of primary β.

5.4 Fatigue Results

Fatigue tests were carried out on the commercial alloys, M3, ZA8, ZA27, M3K, ZA8K and ZA27K. Tests on M3, ZA8 and ZA27 were carried out at room temperature. Furthermore, the alloys M3K, ZA8K and ZA27K were tested at room temperature, but samples of these alloys were also fatigue tested at 50 °C and 100 °C. Alloys K1, K2 and K3 were fatigue tested only at room temperature.

In order to obtain a direct comparison of the fatigue life of these alloys, all the fatigue tests were carried out under standard conditions. A direct uniaxial pull-pull test was used, so that the stress at any given moment was constant across the whole cross-section. The frequency was chosen to be 50 Hz, however, in each case throughout the fatigue tests. The ratio R between the minimum and the maximum stresses was chosen to be 0.1. In addition, the same range of loads and stresses was also applied throughout the tests because the cross sectional area of all the samples was 14±0.2 mm^2. All the samples were tested to failure to establish the S/N curve for each alloy individually, and also to try to discover the fatigue limits of these alloys, if indeed there were any.

After the tests had been completed the S/N curve for each alloy was drawn and these are shown in Figures 109 to 121. Figure 121 shows the 20 °C results for the alloys with different copper contents K1, K2, ZA8K and K3 plotted on the same graph.

5.5 Tensile Test Results

Room temperature tensile tests were carried out initially on the commercial alloys M3, ZA8 and ZA27. The U.T.S, 0.2% proof stress and % elongation to failure values for each individual alloy were calculated. The results of these tests are shown on Table 15.

In the case of alloys M3K, ZA8K and ZA27K, the tensile tests took place at room temperature, 50 °C, and 100 °C, respectively. The results of these tests are shown in Figures 122 to 124. These figures show the effect of temperature, respectively, on the U.T.S, 0.2% proof stress and % elongation of these alloys. Furthermore, the

Young's moduli of these alloys were also determined at each of the above-mentioned temperatures and are shown in Table 16. Subsequently, the K1, K2 and K3 alloys were also tensile tested at room temperature. Their U.T.S, 0.2% proof stress and % elongation values were also calculated, and the results, together with those for the 1% copper alloy ZA8K, are plotted respectively as a function of copper content in Figures 125 to 127.

Alloy	U.T.S (MPa)	0.2 % P.S (MPa)	% Elongation
Mazak.3	270	213	7.0
ZA.8	315	264	4.0
ZA.27	420	371	2.0

Table.15 Tensile Test Results from the Commercial Alloys Mazak3, ZA8 and ZA27

Alloy	Young's Modulus (GPa)		
	20 °C	50 °C	100 °C
M.3K	82.0	75.0	67.0
ZA.8.K	88.0	84.0	65.0
ZA.27.K	75.0	66.0	50.0

Table.16 : Young's Modulus Values of the Commercial Alloys M.3K, ZA.8K and ZA.27Kat Different Temperatures.

Squeeze-cast samples from the ZA27 and the ZA8 alloys were fatigue and tensile tested at 20 °C. The results are shown in Table 17

The fatigue lives of these queeze cast alloys is similar to the pressure die-cast ZA27K and ZA8K at 20 °C. UTS similar for ZA8K but higher for ZA27K.

Alloy	Fatigue Life at 110 MPa	U.T.S / MPa
ZA 27	13 M Cycles	480
ZA 8	9 M Cycles	320

Table 17. Fatigue and Tensile Results of Squeeze-Cast ZA27 and ZA8 at 20 °C.

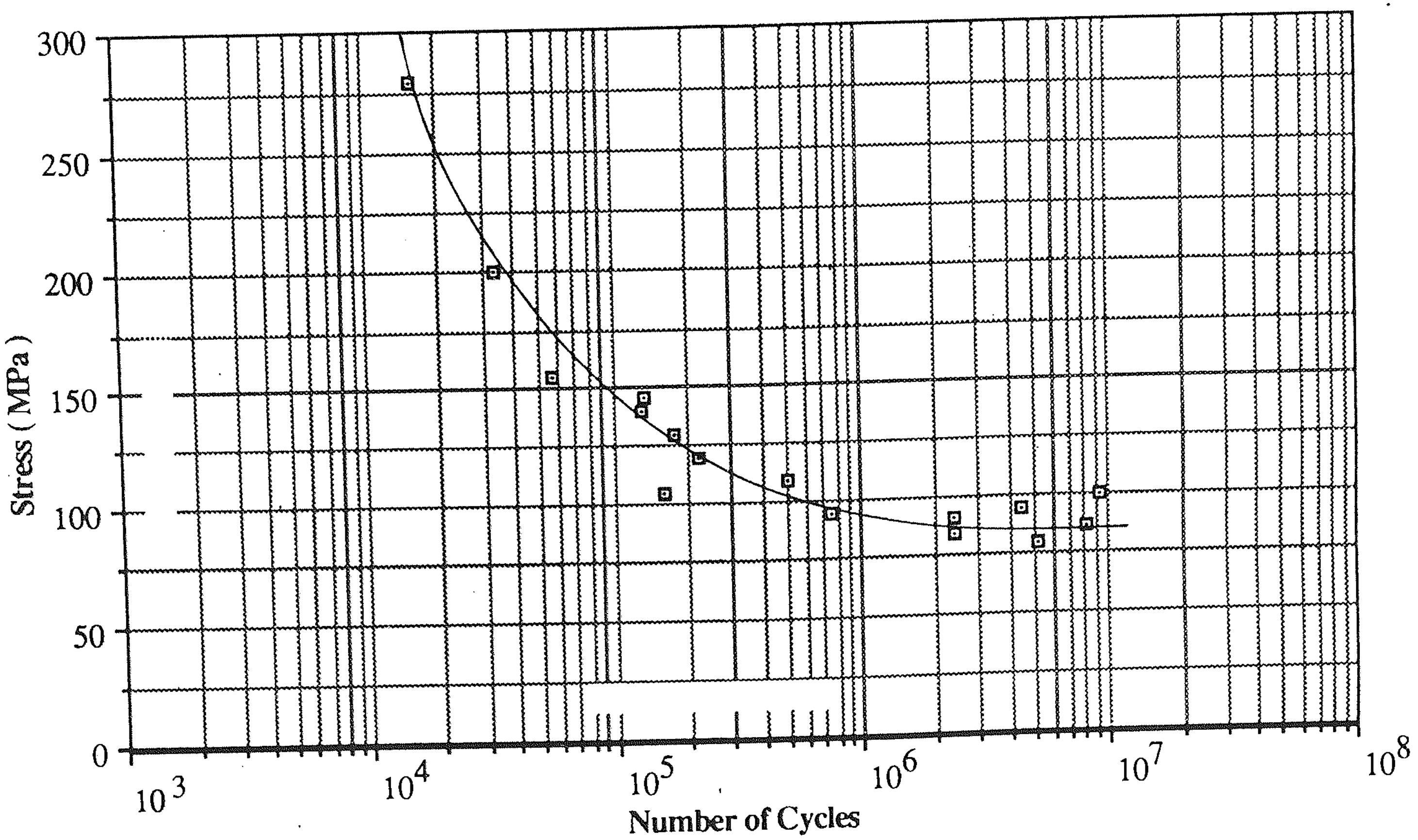

Figure.109 : S/N Curve For Mazak.3 Alloy, at 20°C .

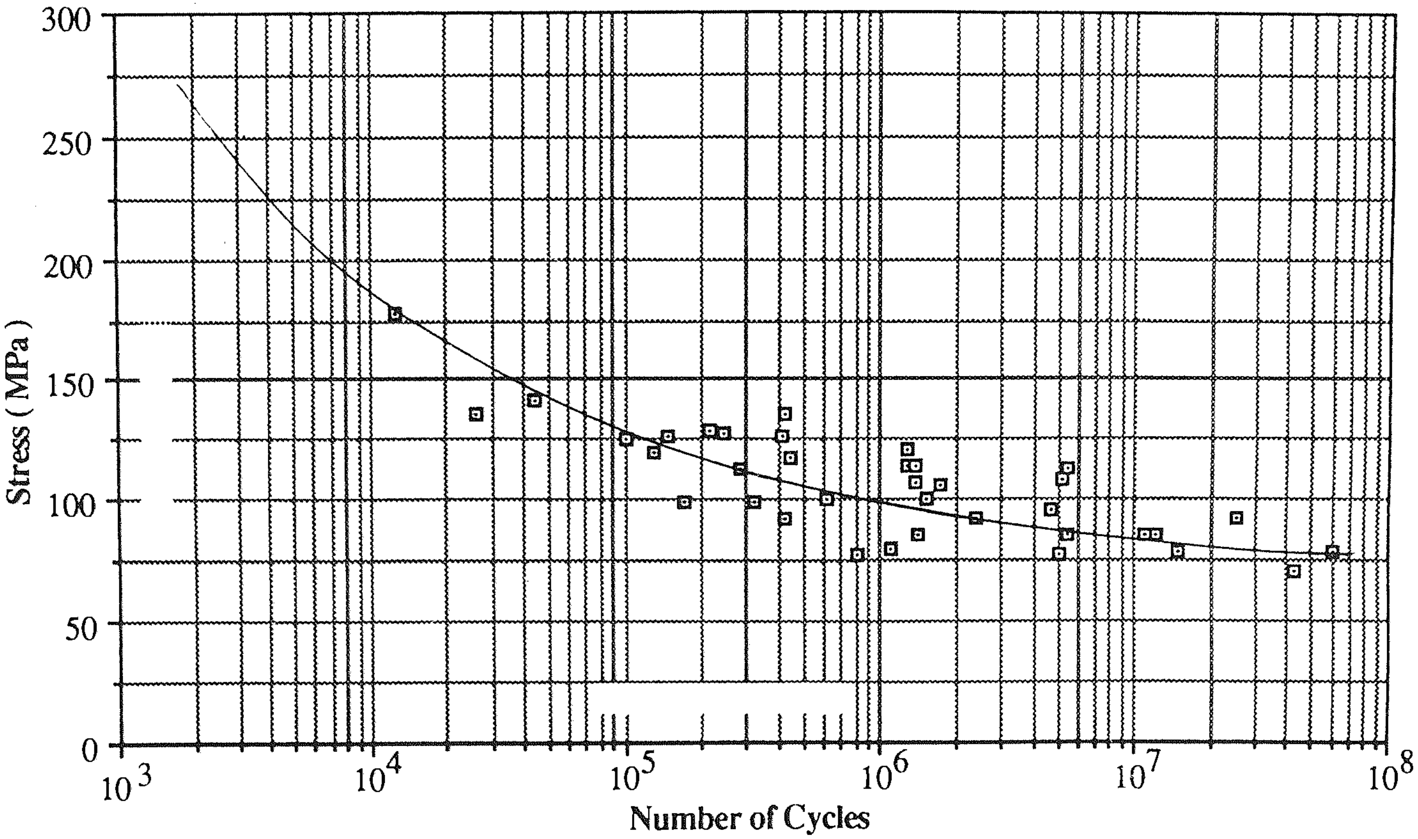

Figure.110 : S/N Curve For M.3K Alloy, at 20 °C.

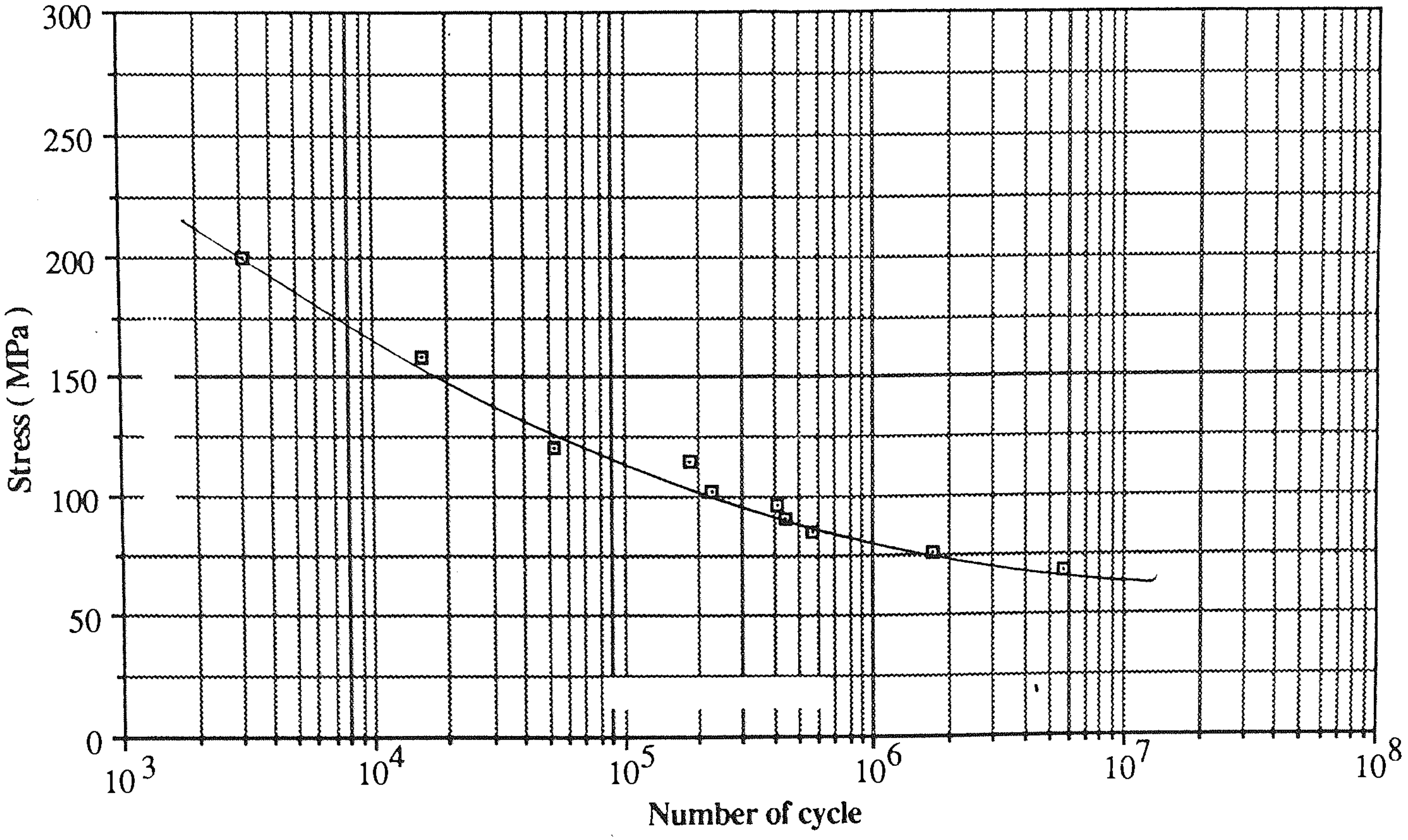

Figure.111 : S/N CurveFor M.3K Alloy at 50 °C.

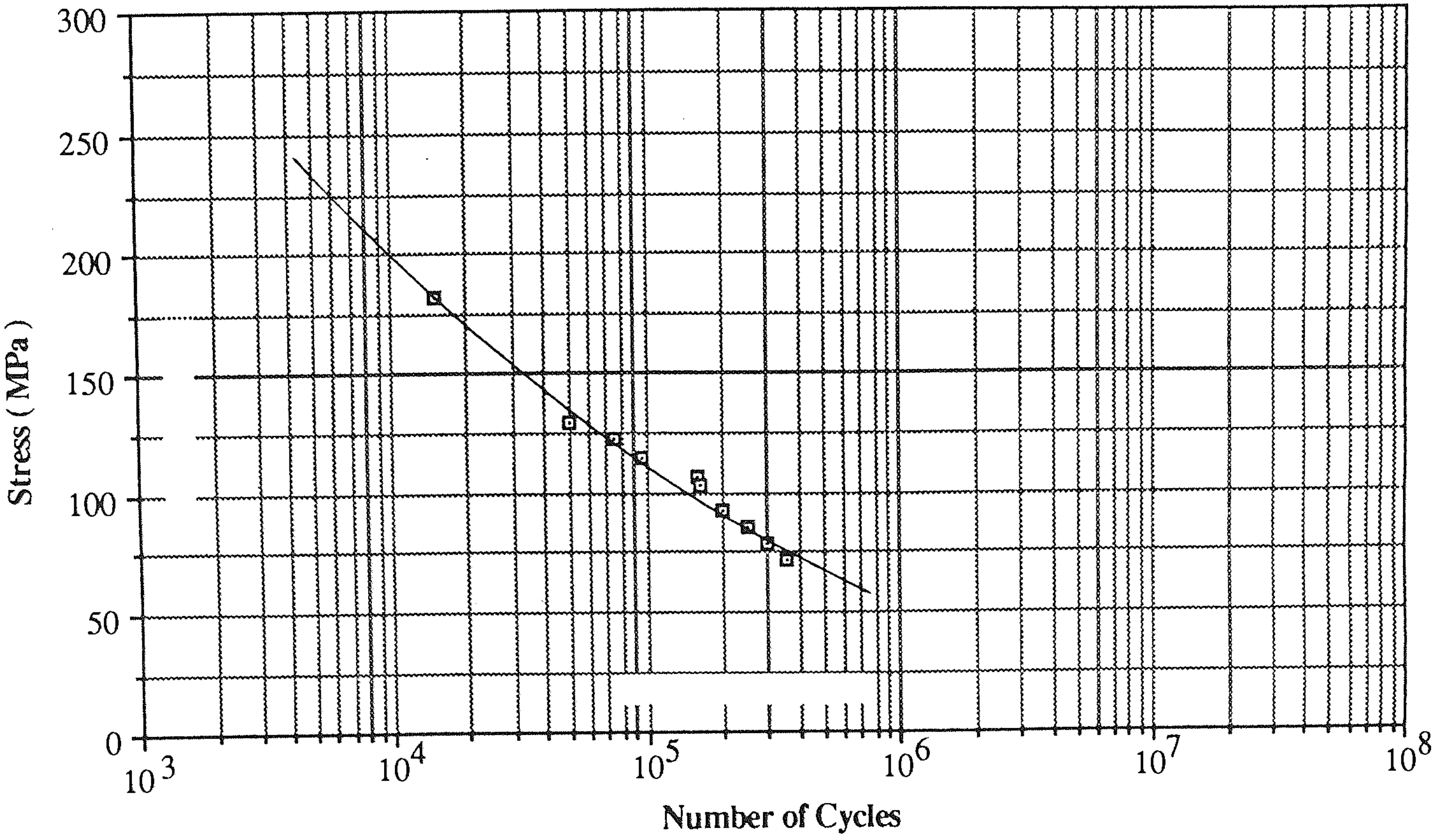

Figure.112 : S/N Curve For M.3K Alloy, at 100 °C.

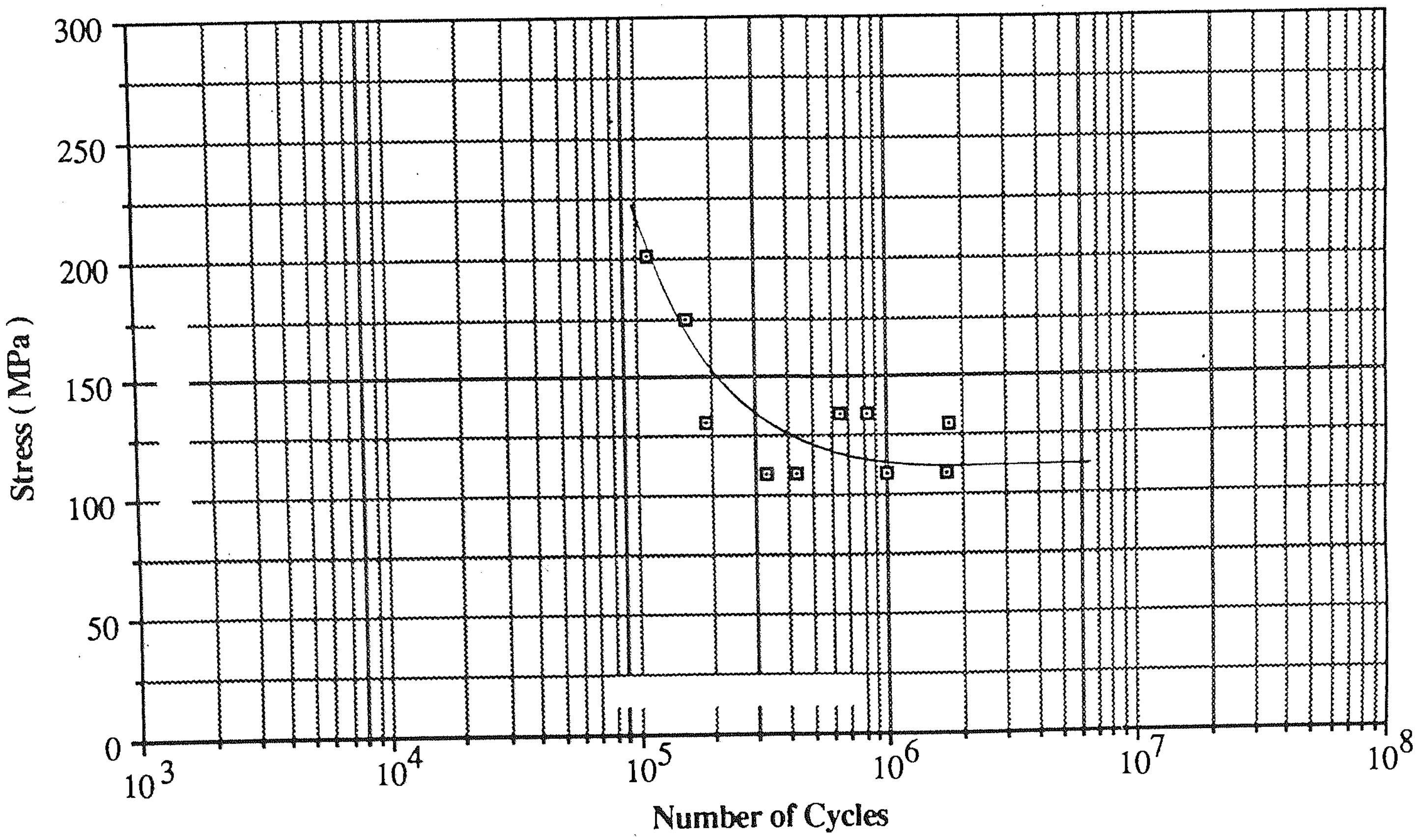

Figure.113 : S/N Curve For ZA.8 Alloy, at 20 °C.

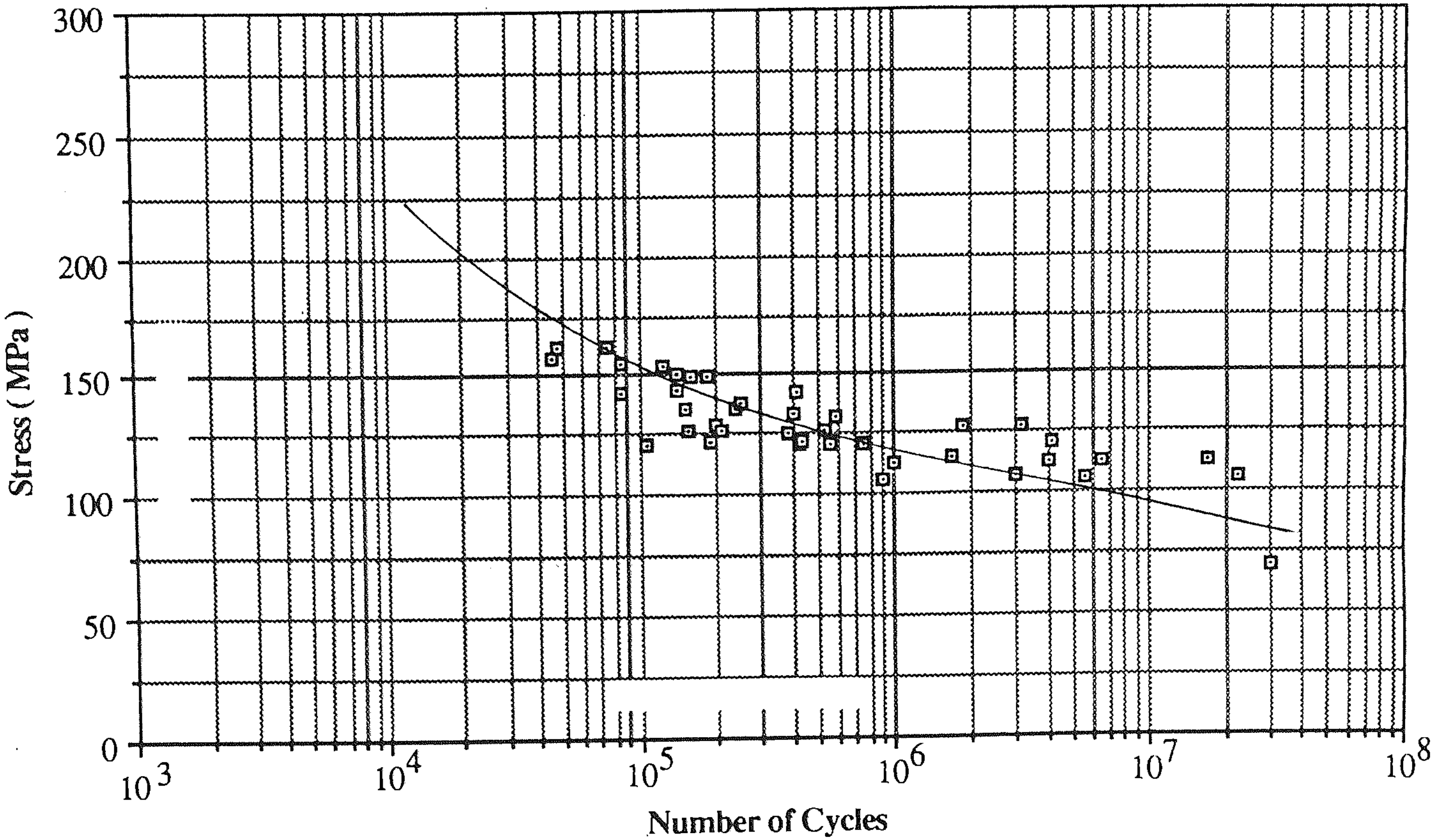

Figure.114 : S/N Curve For ZA.8K Alloy, at 20 °C.

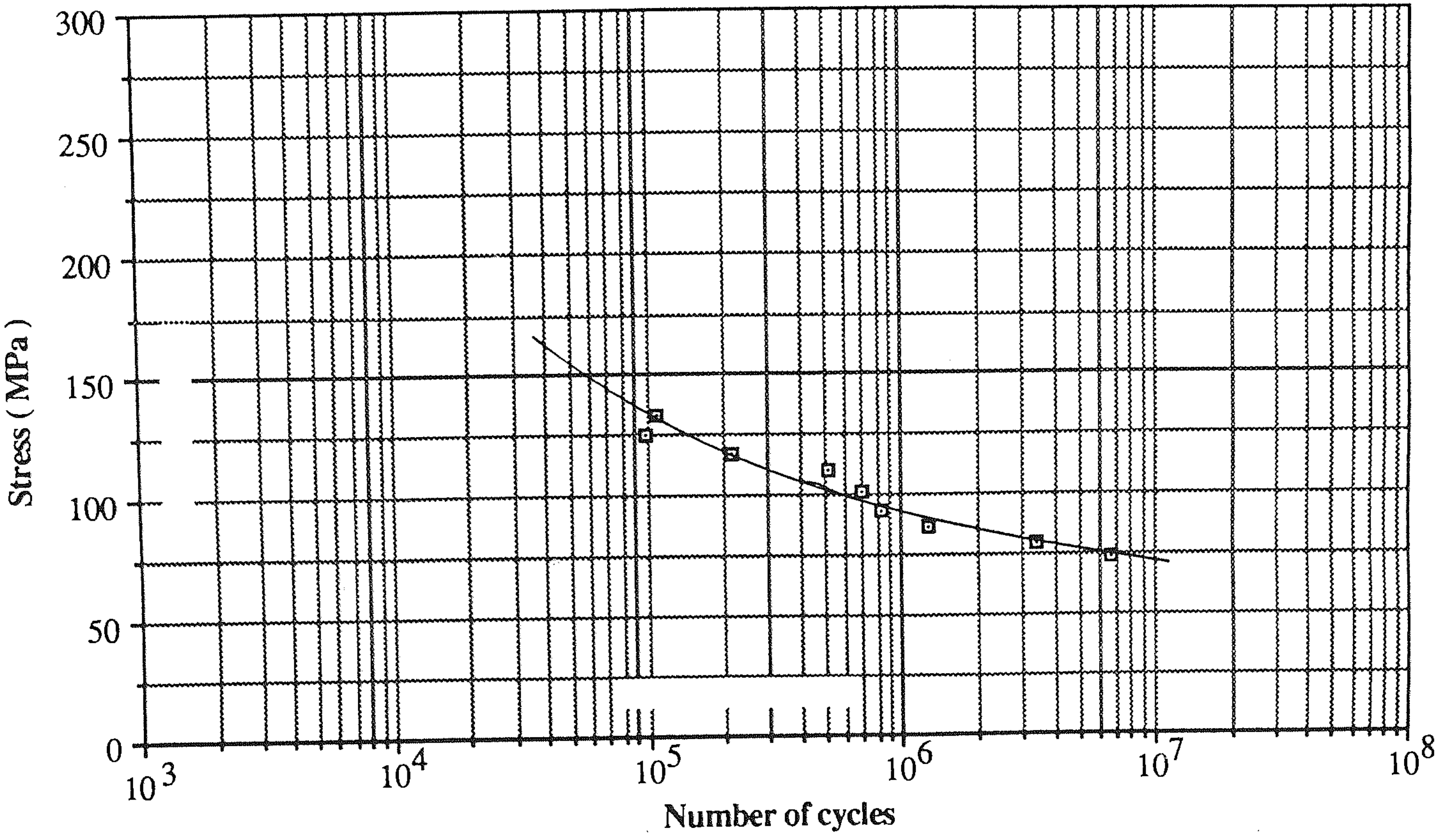

Figure.115 : S/N Curve For ZA.8K, at 50 °C.

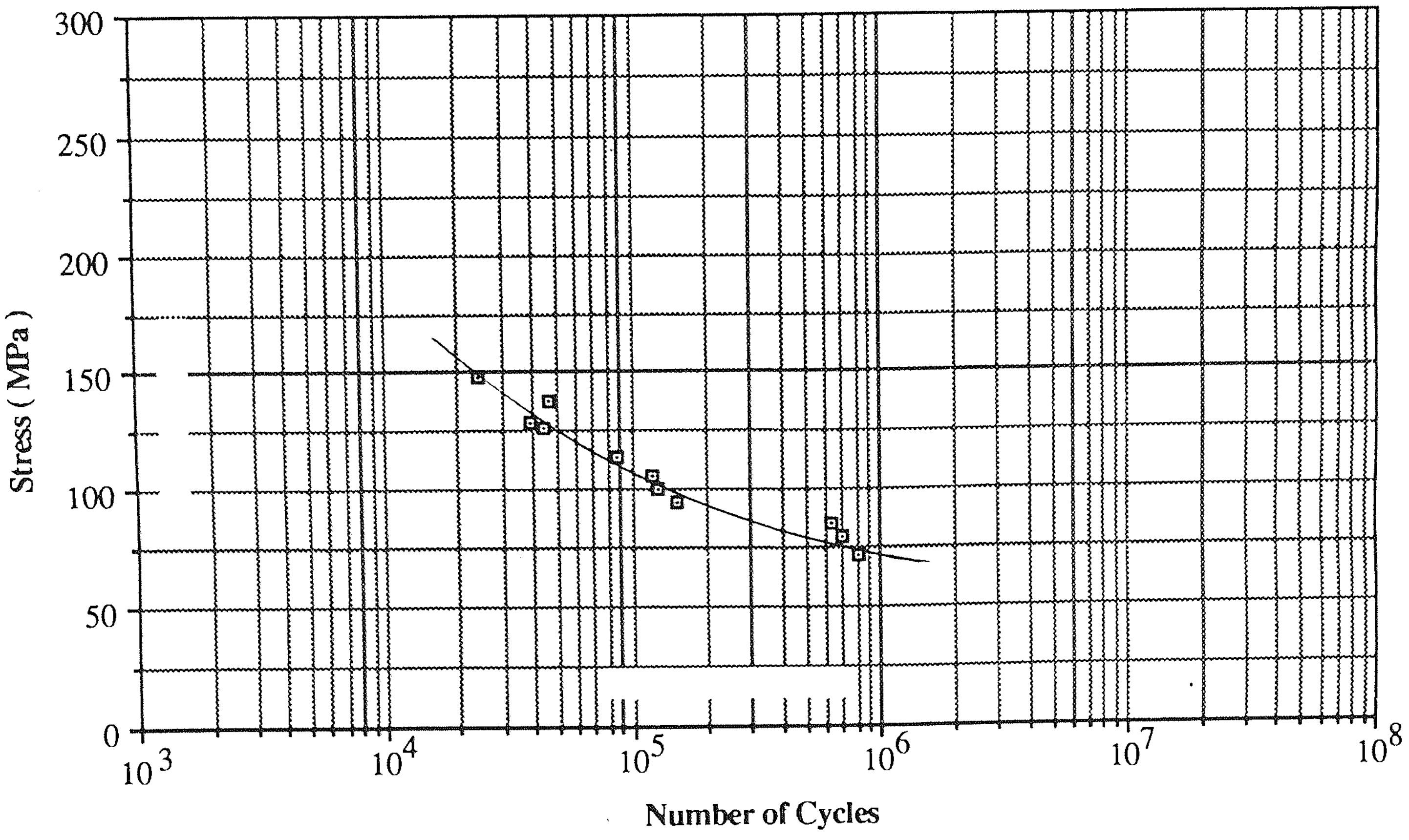

Figure.116 : S/N Curve For ZA.8K, at 100 °C.

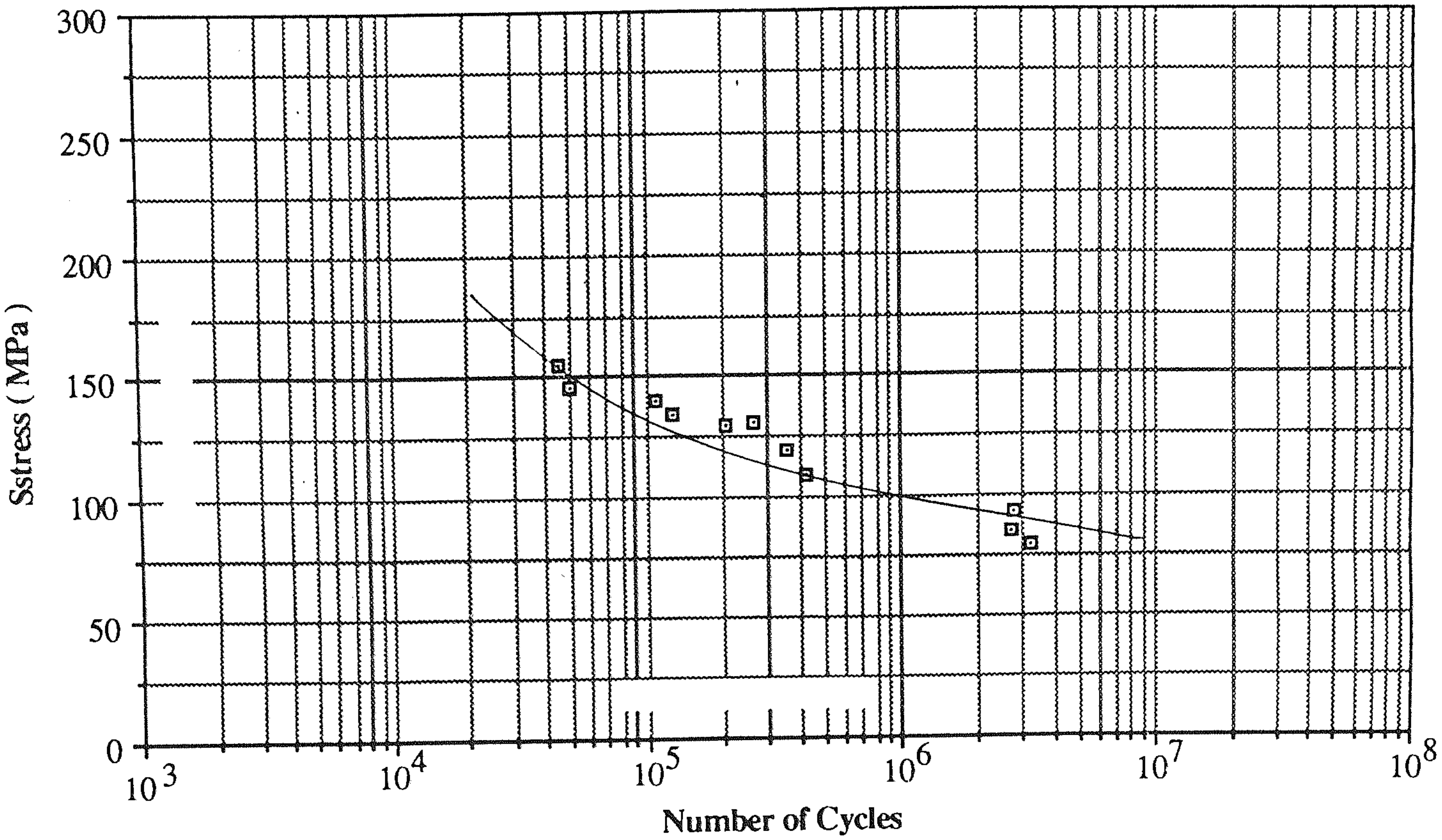

Figure.117 : S/N Curve For ZA27 Alloy, at 20 °Ç.

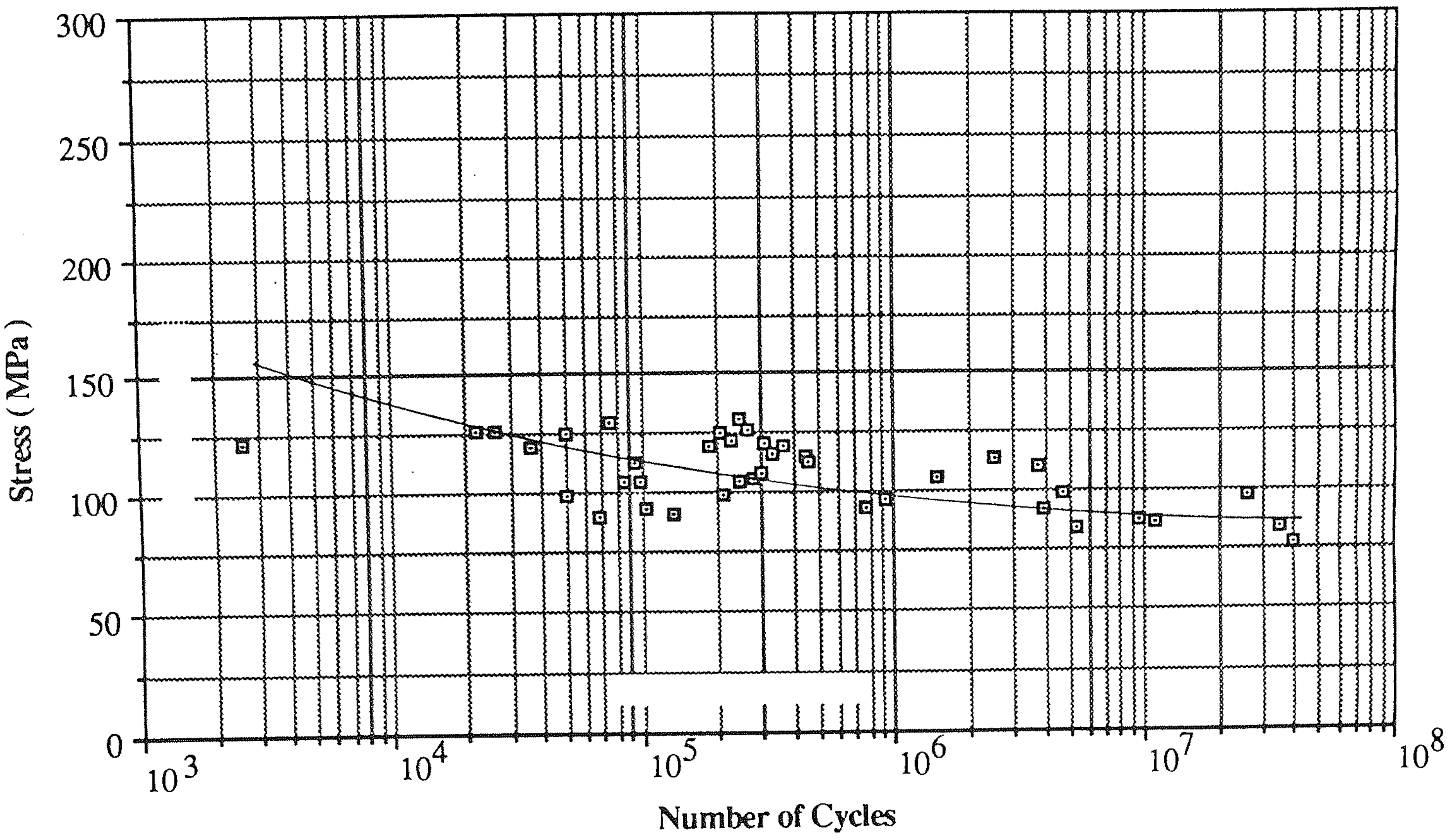

Figure.118 : S/N Curve For ZA.27K Alloy, at 20 °C.

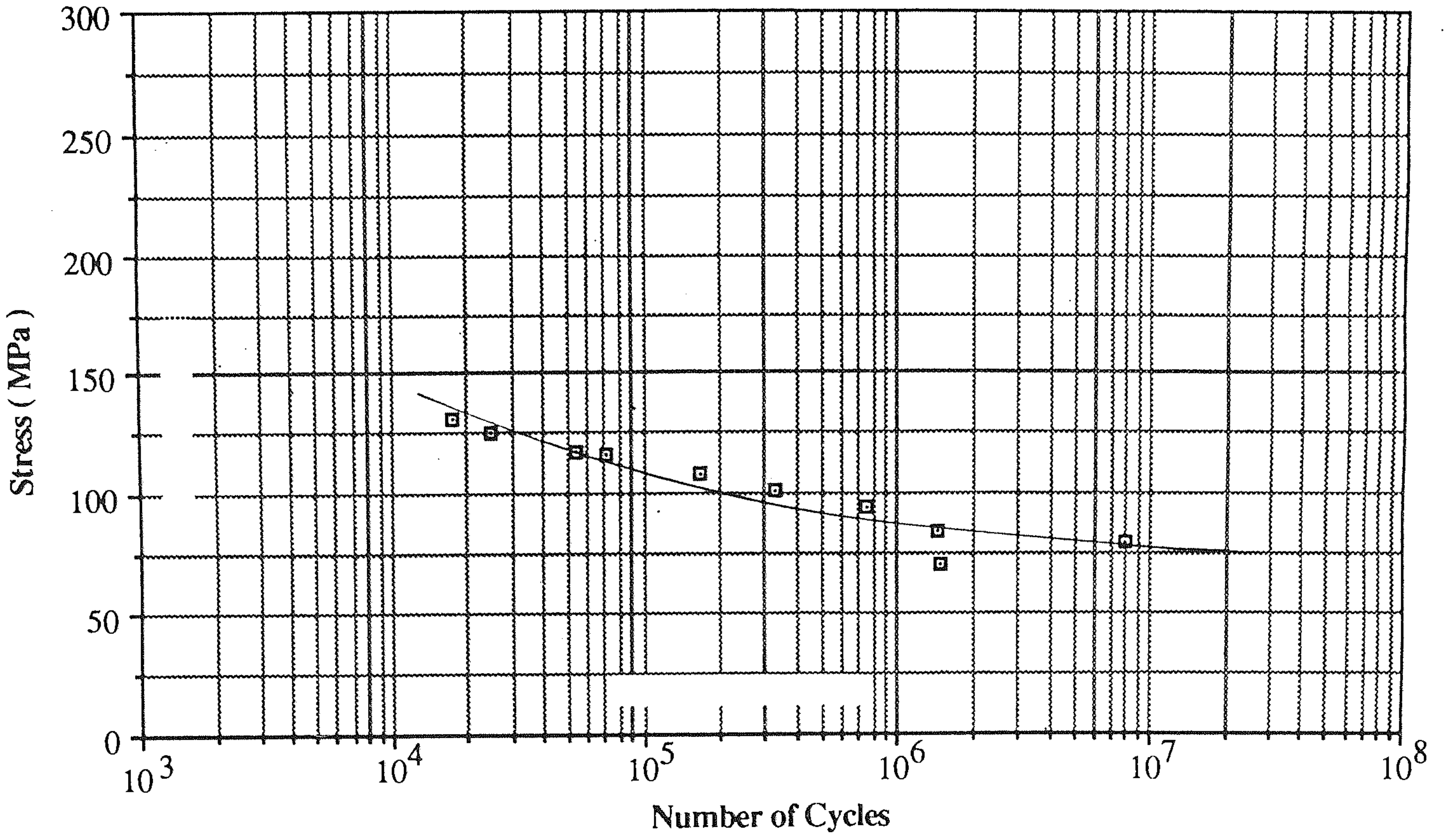

Figure.119 : S/N Curve For ZA.27K Alloy, at 50 °C.

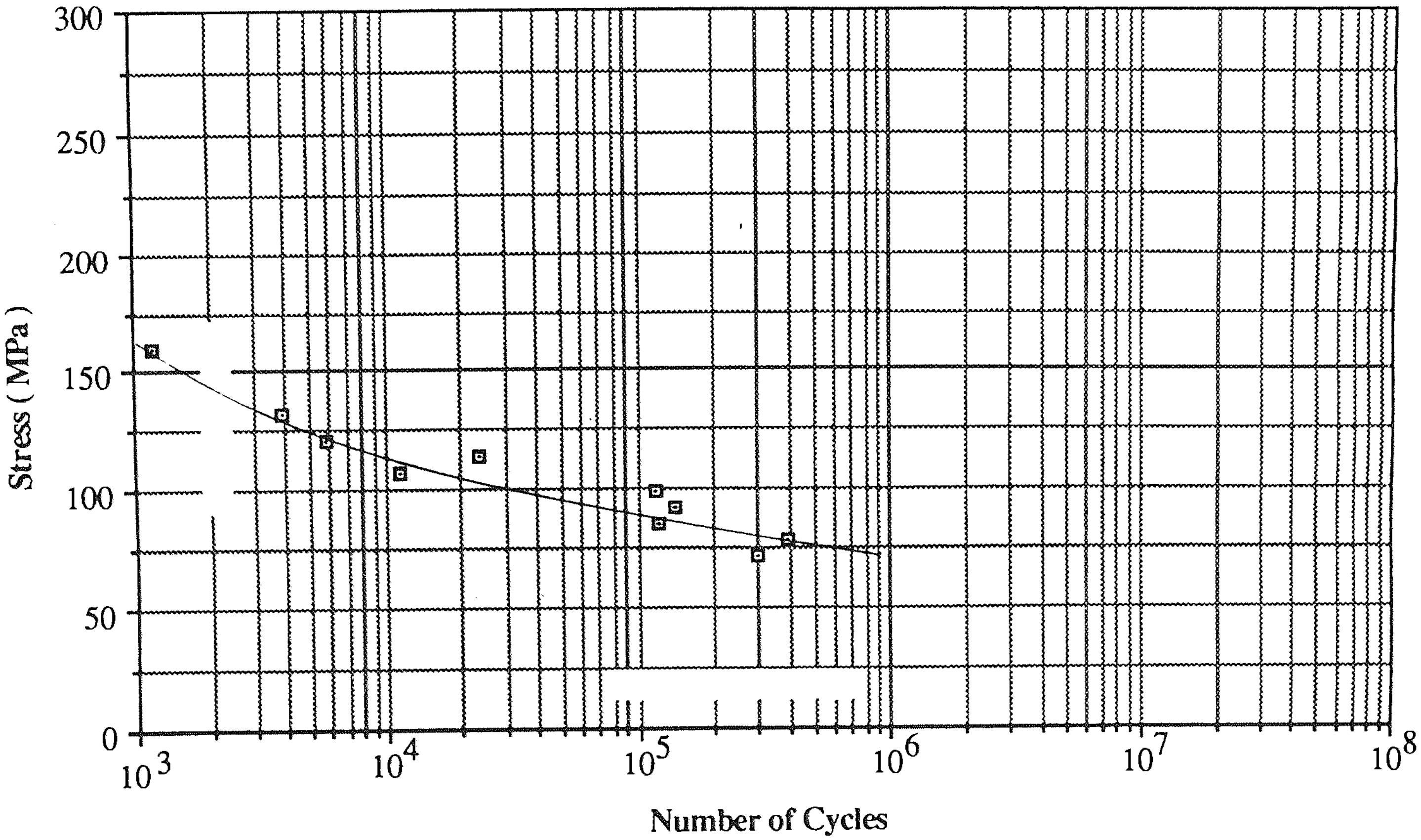

Figure.120 : S/N Curve For ZA.27K Alloy, at 100 °C.

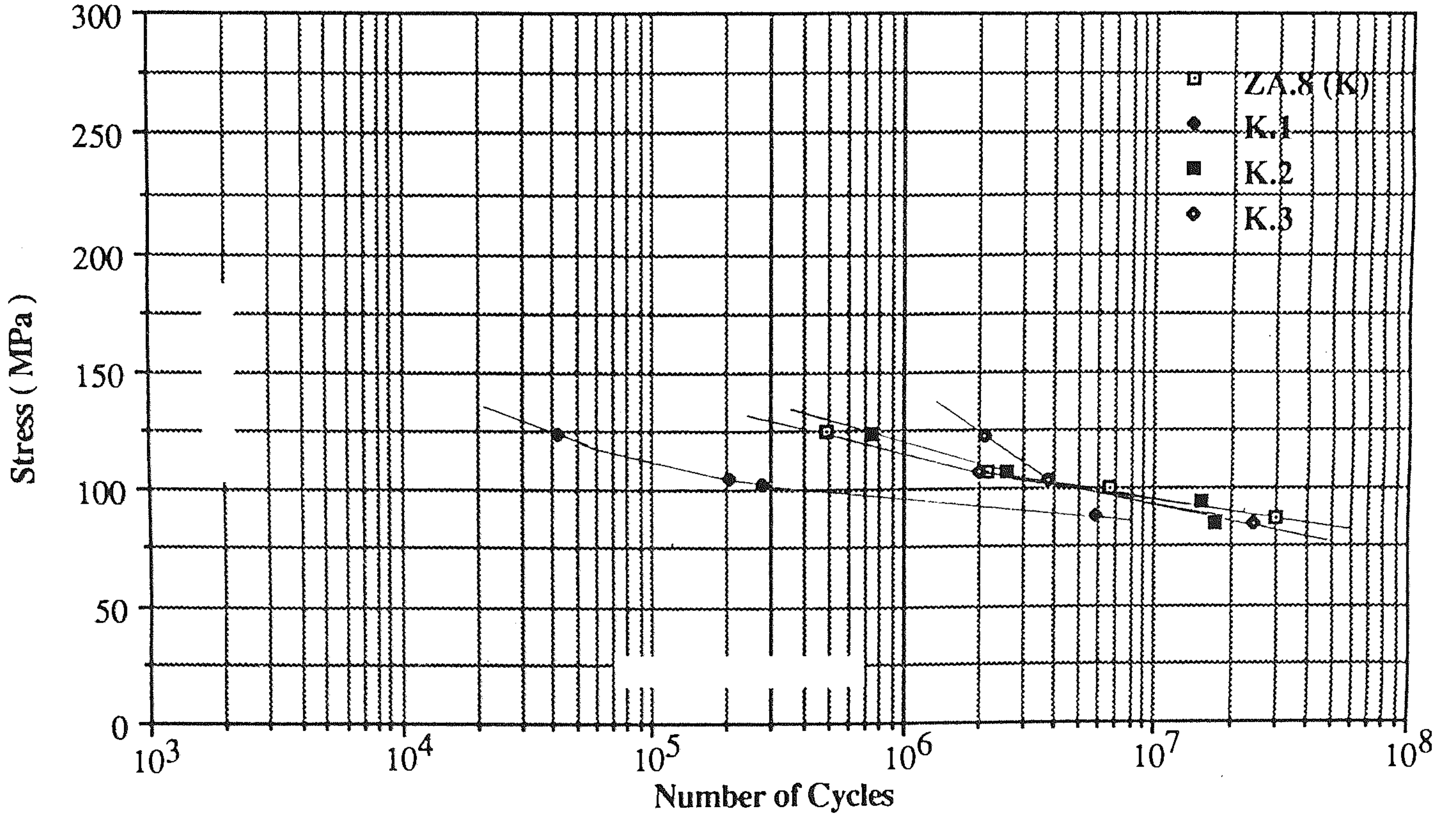

Figure.121: S/N curves of Alloys K1, K2, K3 and ZA.8K, at 20 °C.

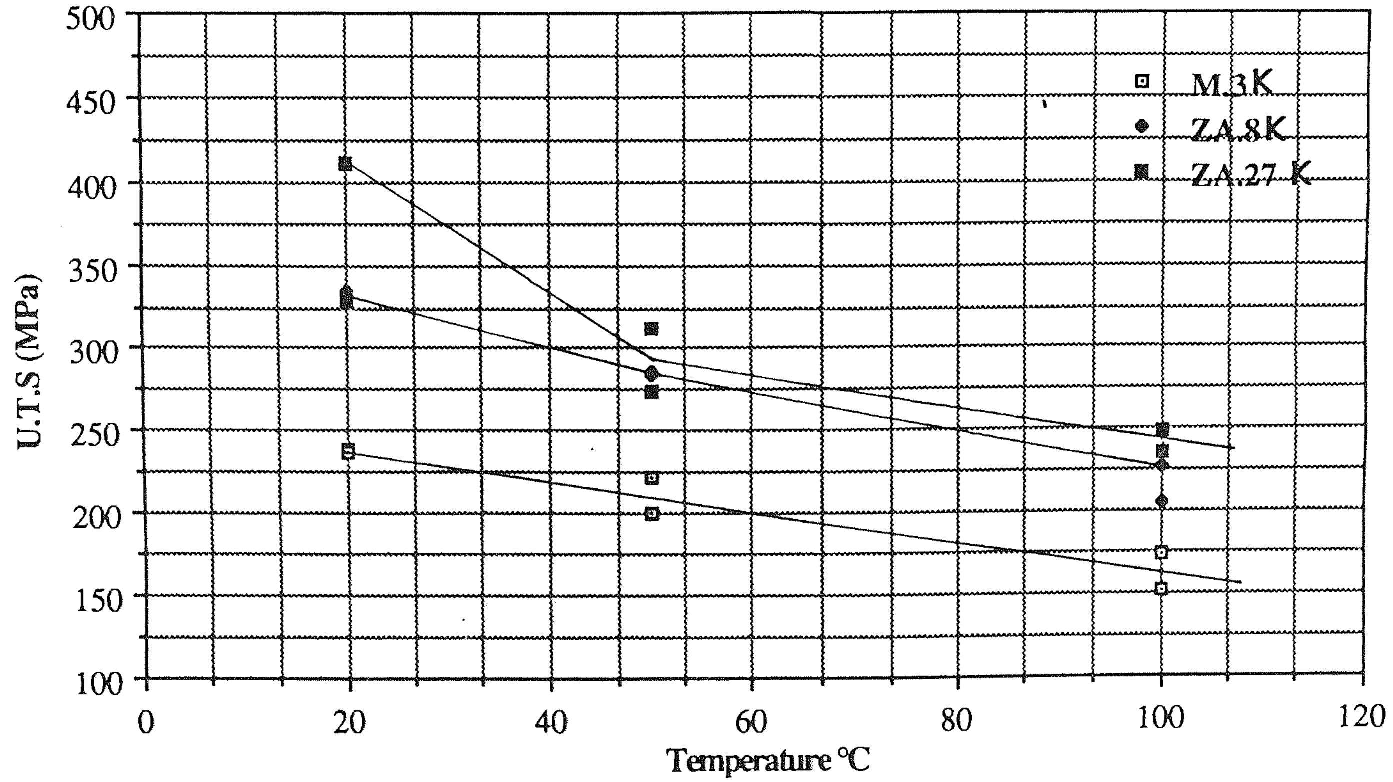

Figure.122 : Ultimate.Tensile.Strength For Alloys M.3K, ZA.8K and ZA.27K at Variable Temperature.

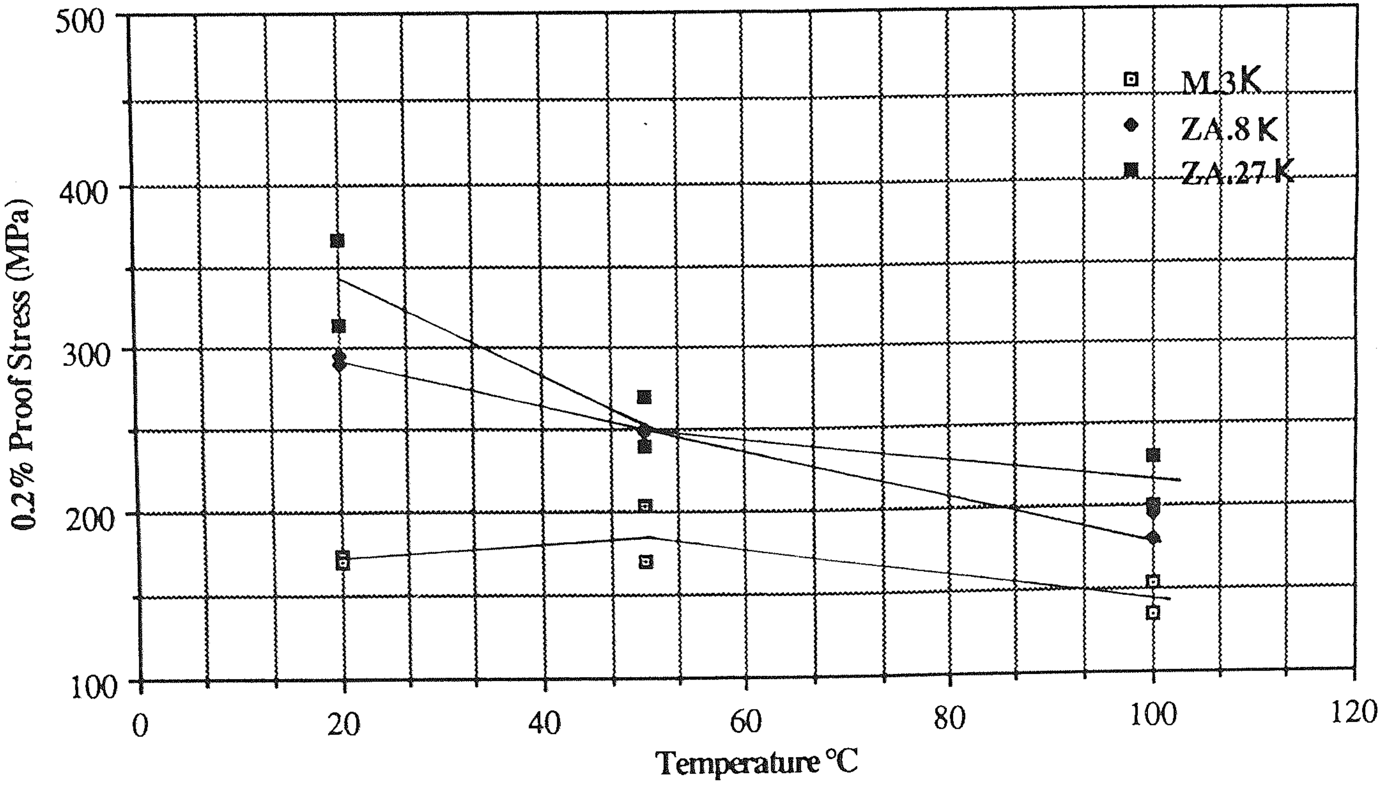

Figure.123 : 0.2% Proof Stress For Alloys M.3K, ZA.8K and ZA.27K at Variable Temperature.

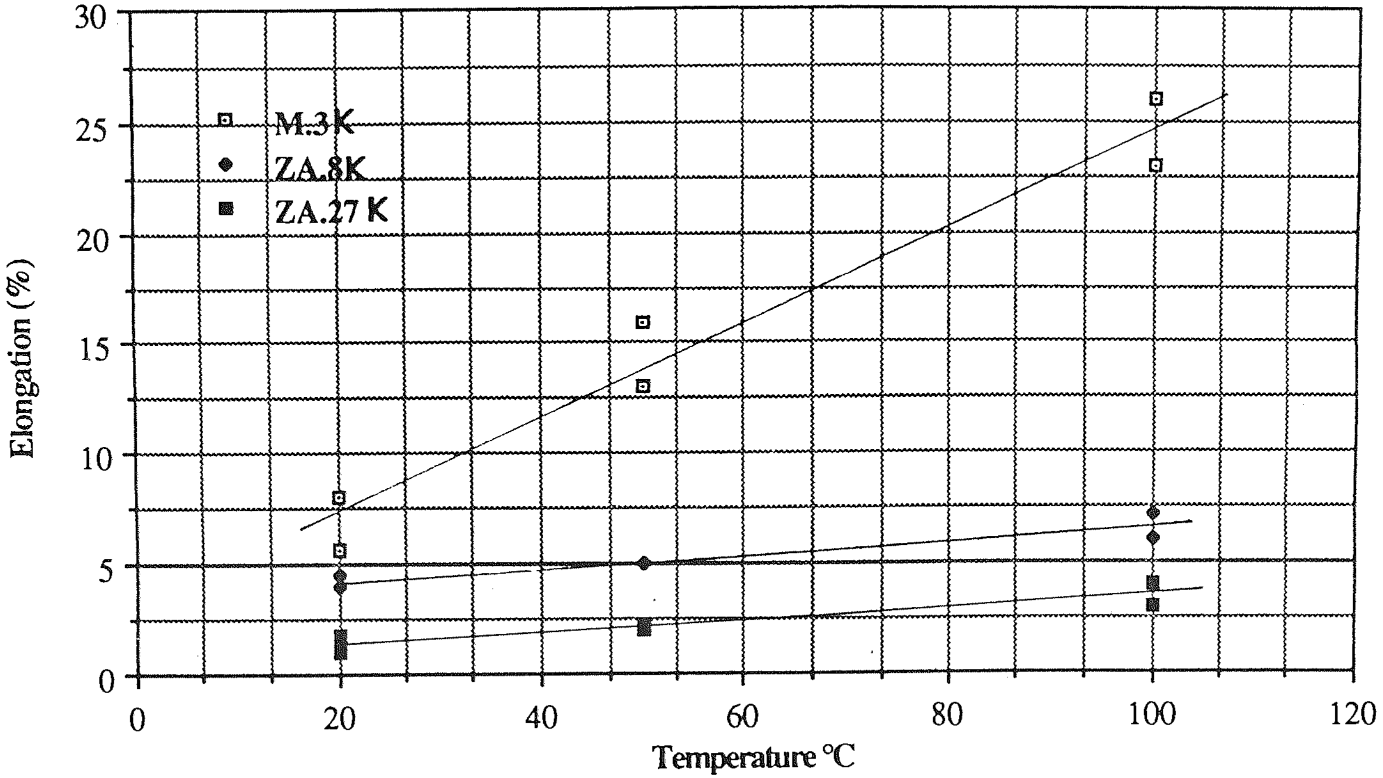

Figure.124 : % Elongations For Alloys M.3K, ZA8K and ZA27K at Variable Temperature.

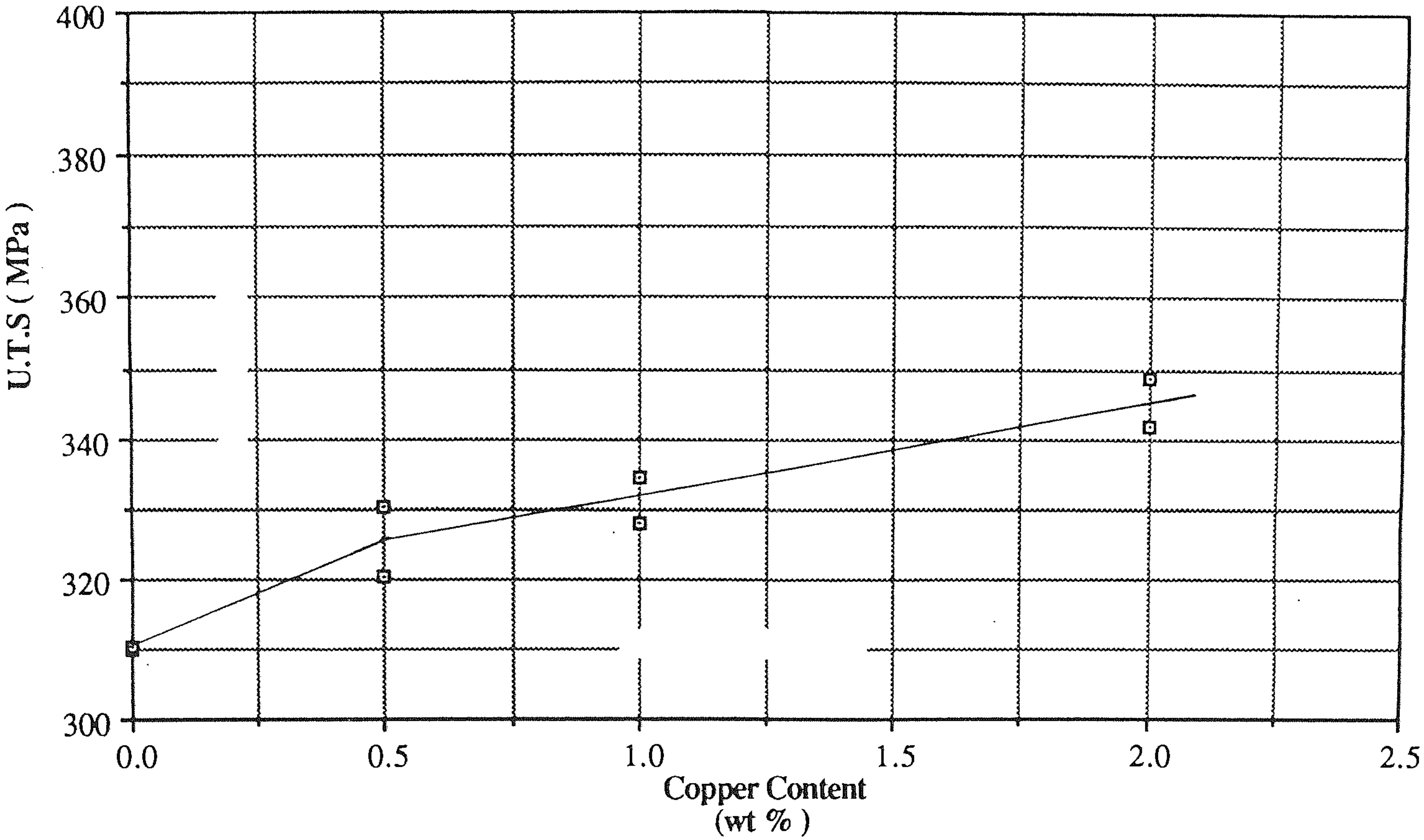

Figure.125 : Ultimate Tensile Strength For Alloys K1, K2, ZA8K and K3.
(0.0%,.0.5%, 1.0% and 2.0% Cu Respectively)

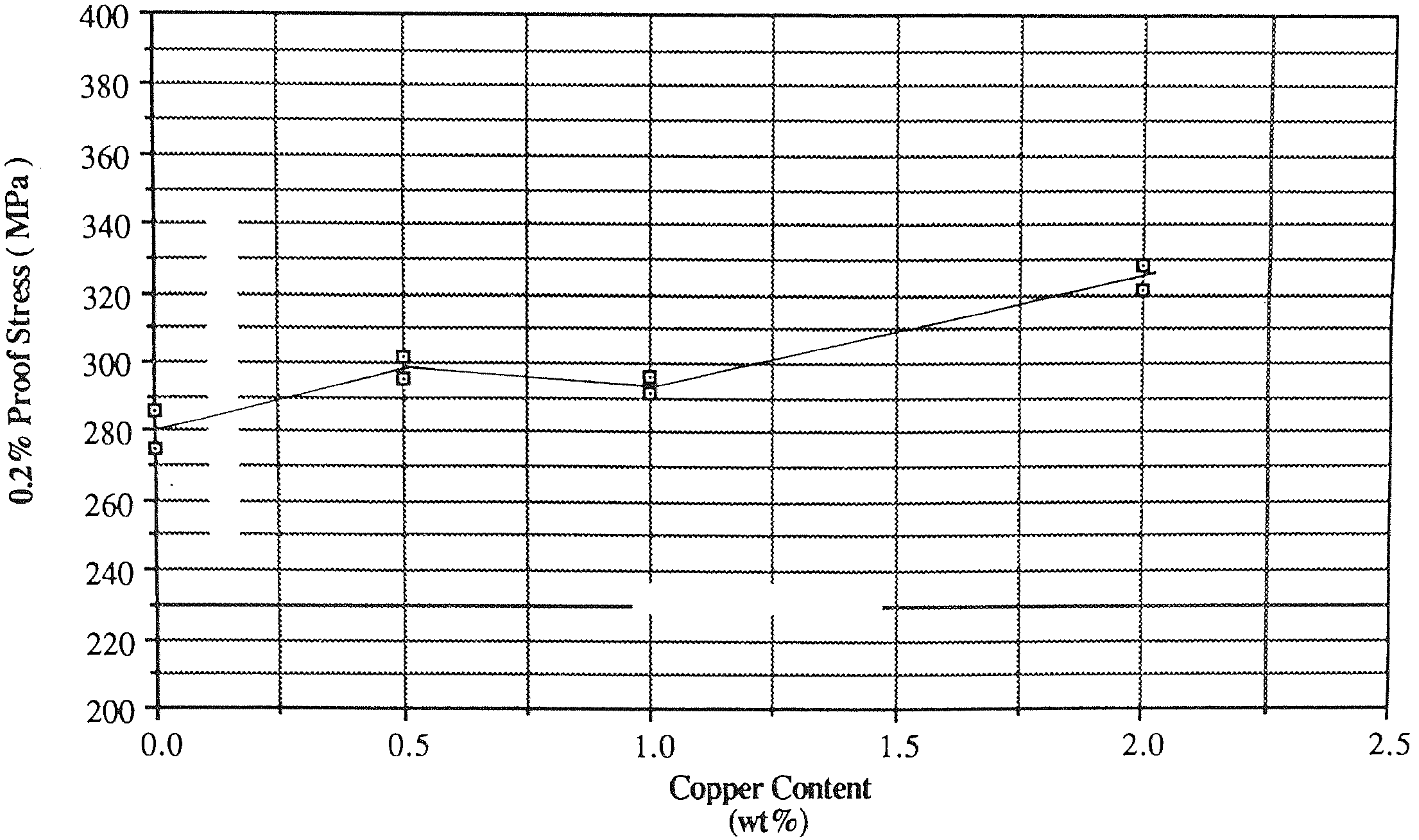

Figure. 126 : 0.2% Proof Stress For Alloys K1, K2, ZA8K and K3.
(0.0%, 0.5%, 1.0% and 2.0% Cu Respectively)

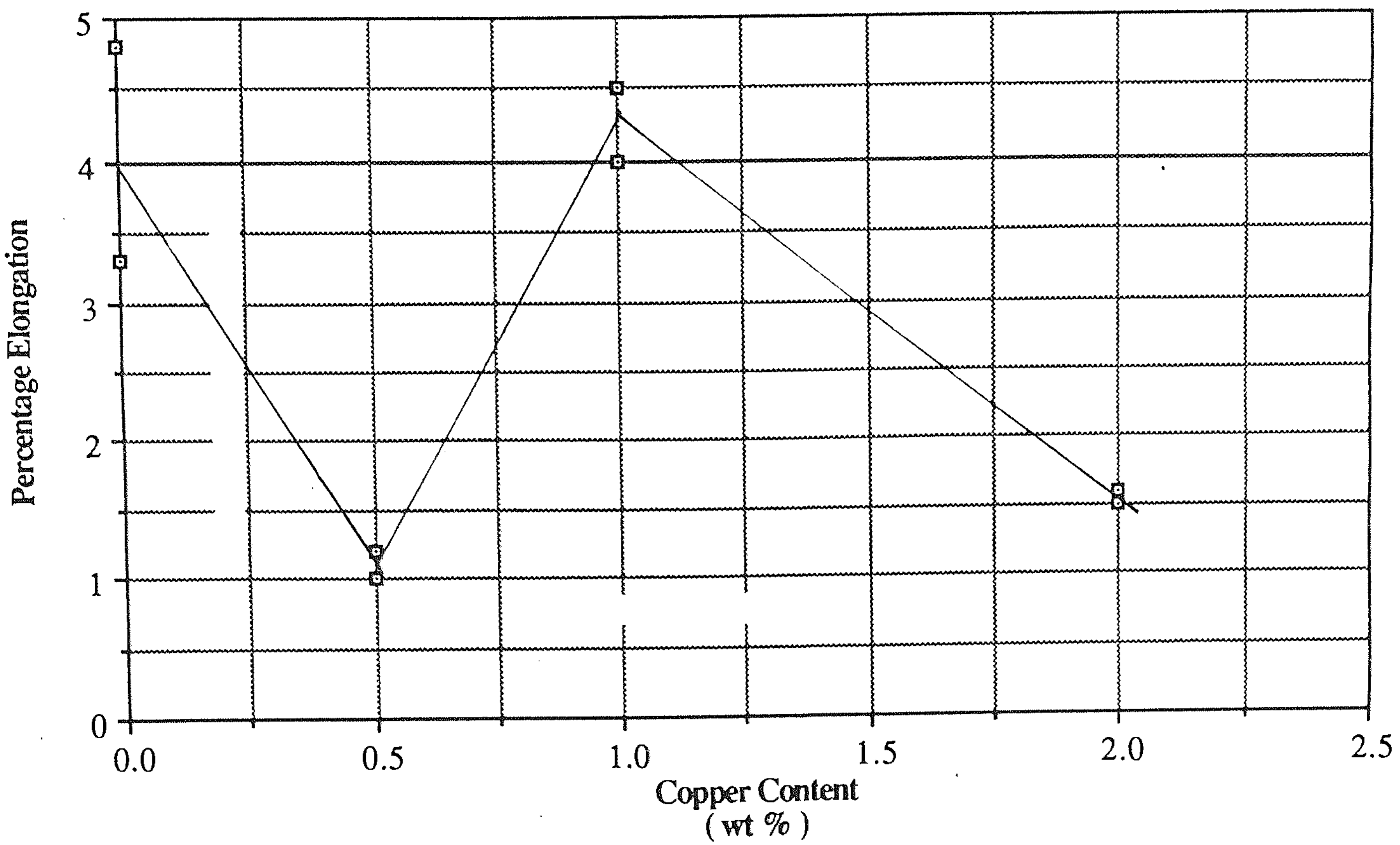

Figure.127 : % Elongation For Alloys K1, K2, ZA8.K and K3
(0.0%, 0.5%, 1.0% and 2.0% Cu Respectively)

5.6 Fracture Morphology of Alloys M3K, ZA8K and ZA27K.

The fractured surfaces of these alloys were examined using the binocular optical microscope and the SEM technique of both secondary electron and back-scattered imaging. Furthermore, metallographical studies were made on the cross-sections of the fractured samples using back-scattered imaging. The aim of these studies was to determine where the cracks initiated and to observe their propagation. Because of the uniform applied stress, there was no preferred point for crack initiation, and this was thus controlled by the local microstructure.

From each alloy fractured samples were selected from those which had been subjected to high, medium or low stresses, ie from samples which ranged from short to long fatigue lives. The stress direction is indicated by an arrow on the side of the micrographs.

5.6.1 The Fracture Morphology of Alloy M3K.

The fractured surfaces of the M3K alloy were examined and topographs of the fractured surfaces were taken using the SEM utilities, to show both the fractured surface and the microstructural damages to that surface. Figure 128 shows what appears to be a crack initiation starting on the surface of the sample subjected to a stress of 78 MPa and lasting for 14.9 M cycles at 20°C. Figure 129 shows a similar sample subjected to a stress of 92 MPa at 20 °C and lasting for 24.9 M cycles. These two figures are believed to indicate that pores have acted as stress raisers and are responsible for the initiations of cracks. It is also observed from these figures that cracks had propagated for a short distance only, before the sample failed under tension. In the beginning it was difficult however to decide which structural phases are targeted by the crack progress. The use of back-scattered imaging on the fractured surface made it possible to see the cracks' starting point and the relationship between the plane of cracking and microstructure.

Figure 130(a) shows a SE micrograph of a fractured sample subjected to a stress of 80 MPa at 20 °C which lasted for 5.6 M cycles, while Figure 130(b) shows the microstructure of the fractured area in terms of atomic number contrasts (B.S.E.). In this figure (130(b)) cracks have developed from the various sized pores. The stress is concentrated more on the larger pores, as can be seen from this figure. Large pores have contributed to establish wider and deeper cracks. The figure also shows a scatter in the crack propagation due to random porosity. In the centre of Figure 130(a) a large cleaved area is observed. Figure 130(b) identified that area to be a concentrate of zinc-rich primary η phase. The nature of cph zinc is that it contains insufficient slip system to accommodate plastic flow, therefore, it deformed by twinning. Figures 131(a) and (b) show the cleavage and possibly twinning of Figure 130 at higher magnification. It is clear that the cleaved area was a concentrated colony of primary η dendrites with some eutectic pools.

Figure 132 shows BSE of a fractured sample subjected to a stress of 60 MPa at 20°C lasting for 24 M cycles. Various sizes of randomly distributed cracks emerged from the pores. Cleavage is also observed in this figure at three different locations, just before the ductile failure.

Figure 133 (SE/BSE) showed a fractured surface of a sample subjected to a high stress of 120 MPa at 20°C, and this sample lasted for 368 k cycles. The figure showed cleavages and ductile fracture area.

Figure 134 showed a cross section of a fatigued sample subjected to a stress of 70 MPa at 20°C, which lasted for 19 M cycles. The figure shows a crack, which initiated from a concentrated area of micropores, grew parallel to the fractured surface, advanced through the eutectoid and reached the primary η, splitting it in half before continuing its course. In some cases this crack went under the η particles and continued to advance through the structure. Similar investigation was carried out on a fractured sample, subjected to a stress of 110 MPa at 20°C, which lasted for 687 k cycles, as shown in Figure 135. From this figure a cluster of pores is seen to be responsible for the development of a non-planar crack parallel to the fractured surface, with subsiduary cracks elsewhere.

Fatigue tests were also conducted at 100°C, the relevant samples of which are shown in Figures 136 and 137, at the two different magnifications. These figures were obtained from a cross-section of a fatigued sample subjected to a stress of 60 MPa which lasted for 700 k cycles. Figure 136, taken at low magnification, presents the badly damaged sample caused by tension. It also indicates the beginning of crack developments parallel to the fractured surface. Figure 137 shows elongated η particles caused by tensile plastic deformation at a high temperature. Samples fractured in simple tension were also studied.

Figure 138 shows a general area of a tensile fractured sample, obtained by using a mixture of secondary electrons and back-scattered imaging. From this figure it appears that cracks spread through the sample in a triangular manner.

Figure 139, at high magnification, depicts cleavage cracks going through and more extensive plastic deformation with eutectic regions. A cross section was taken from a tensile sample to show that microcracks had developed from the opening of a pore lying parallel to the fracture surface, as shown in Figure 140. The micrograph also shows elongated primary η dendrites indicating extensive plastic deformation under the fracture surface.

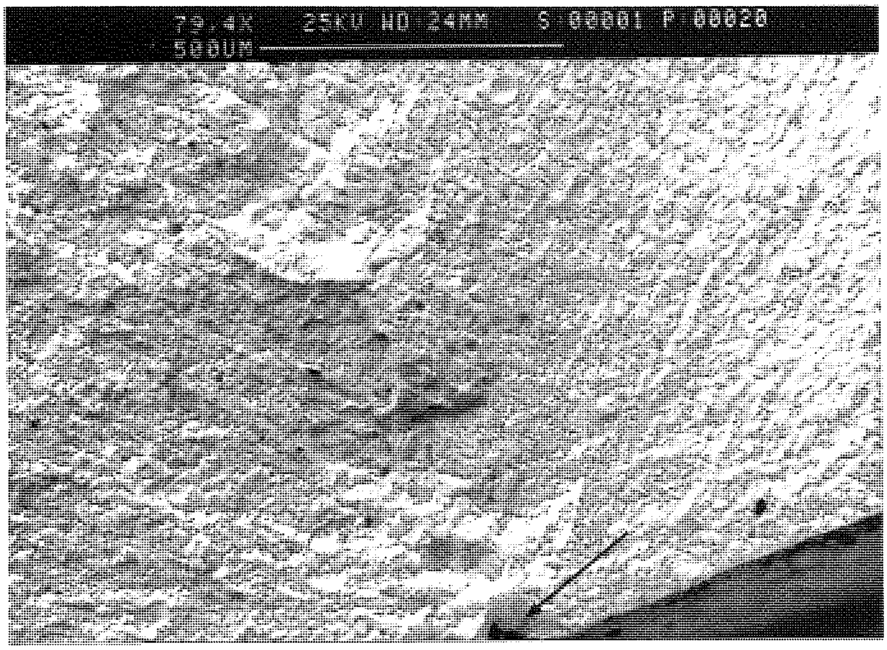

Figure 128. SEM. M3K, 78 MPa at 20 °C / 14.9 M cycles. Defect and initiation point (arrowed).

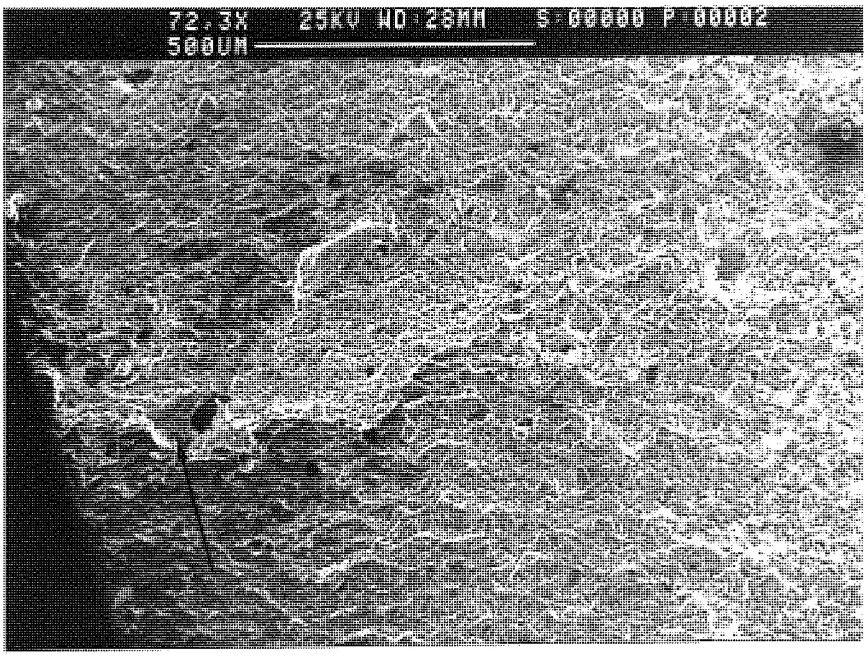

Figure 129. SEM. M3K, 92 MPa at 20 °C / 24.5 M cycles. Defect and initiation point (arrowd).

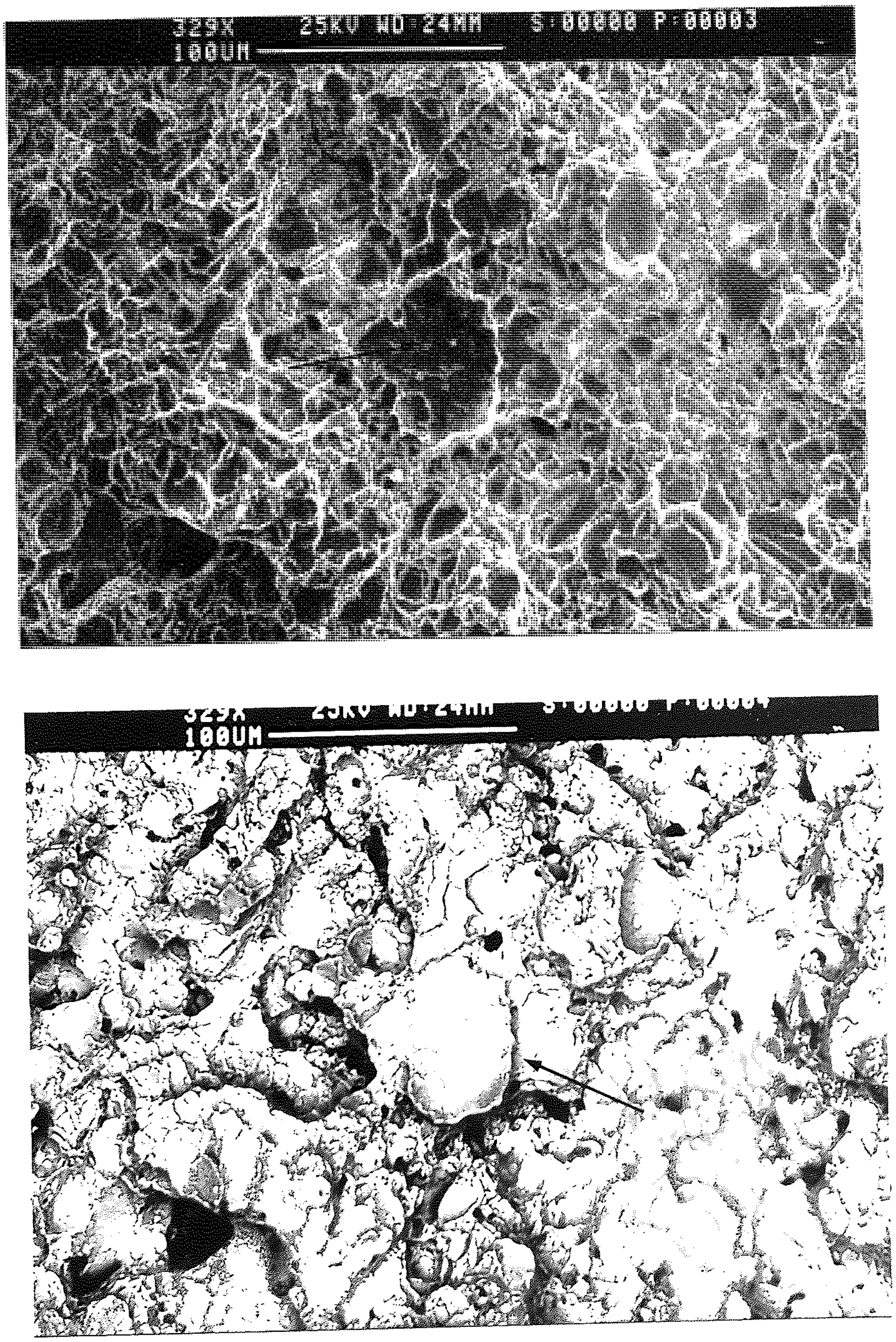

Figure 130. a) SEM. Secondary electron. M3K, 80 MPa at 20 °C / 14.9 M cycles. Cleavage and crack (arrowd).

b) Back-scattered Image of (a).

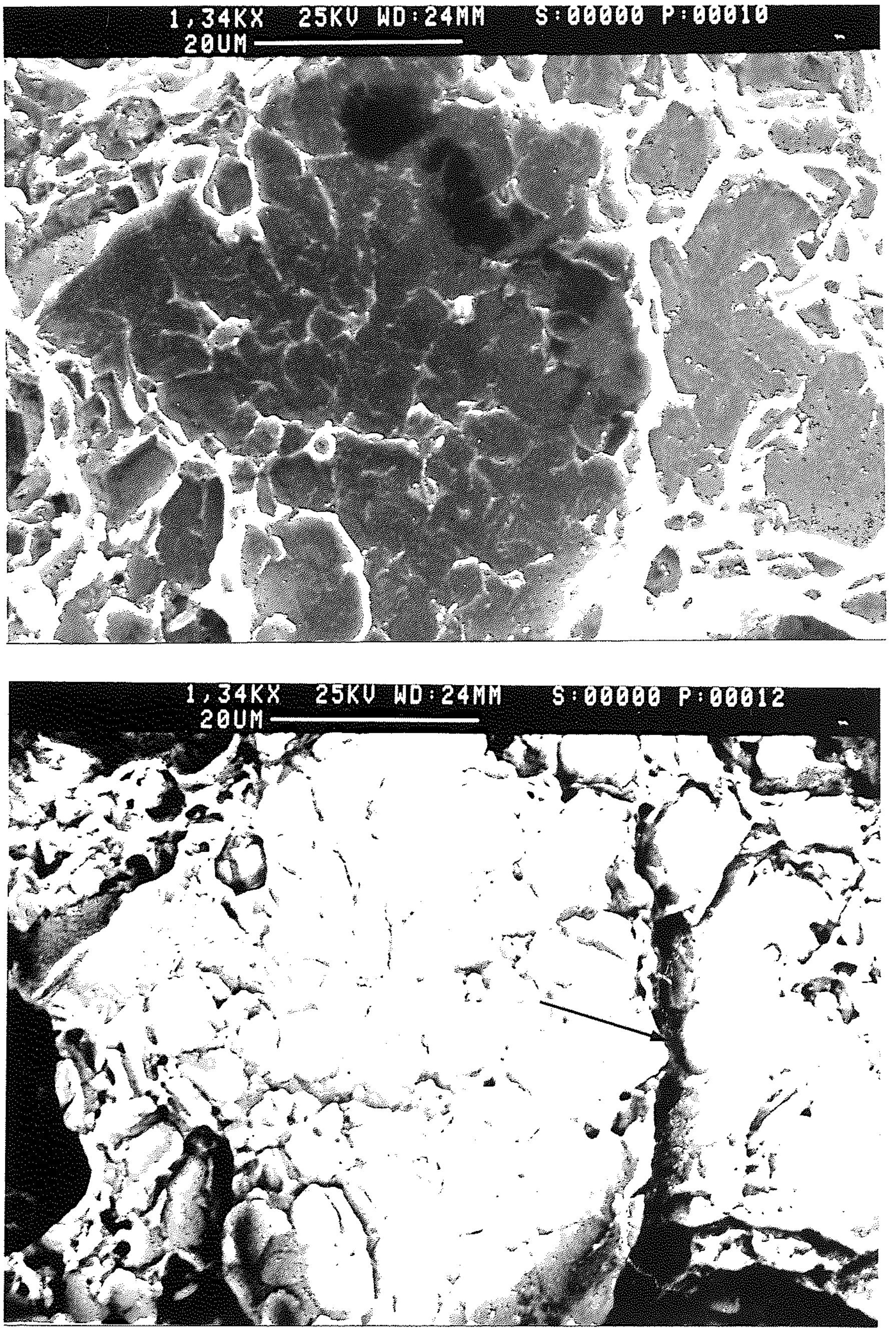

Figure 131. High magnification of Figure 130, showing the large cleaved area. cleavage edge (arrowed).

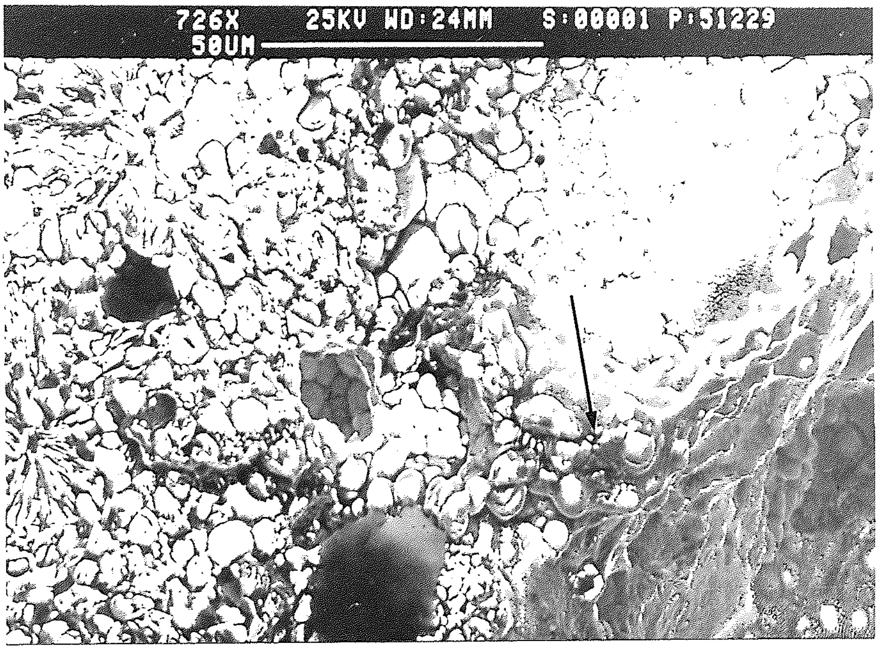

Figure 132. SEM. Secondary electron. M3K, 60 MPa at 20 °C / 24 M cycles. Cracks leading to ductile fracture (arrowed).

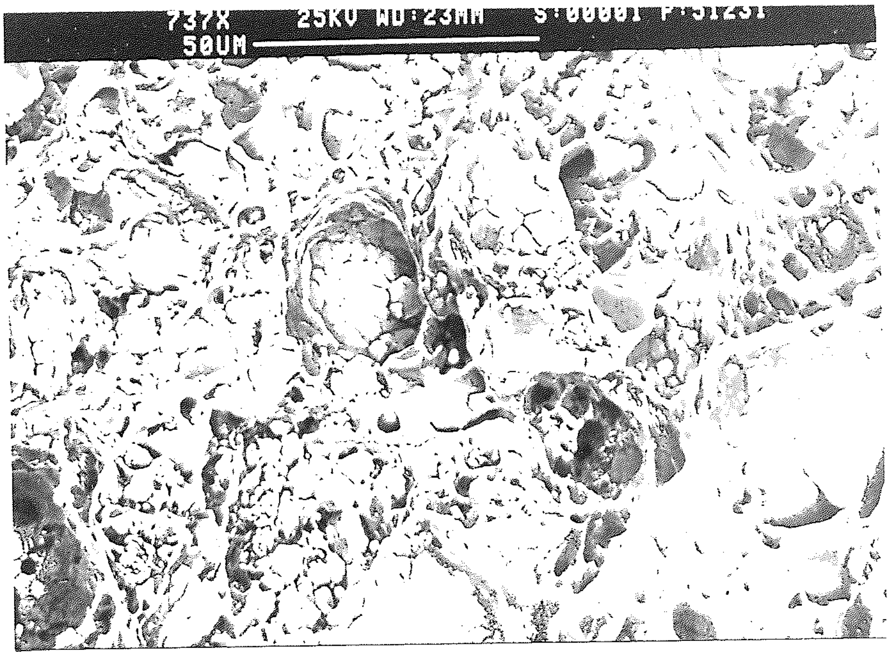

Figure 133. SEM. Secondary electron. M3K, 120 MPa at 20 °C /368 k cycles. Large cleavages resulted from the severe tensile force.

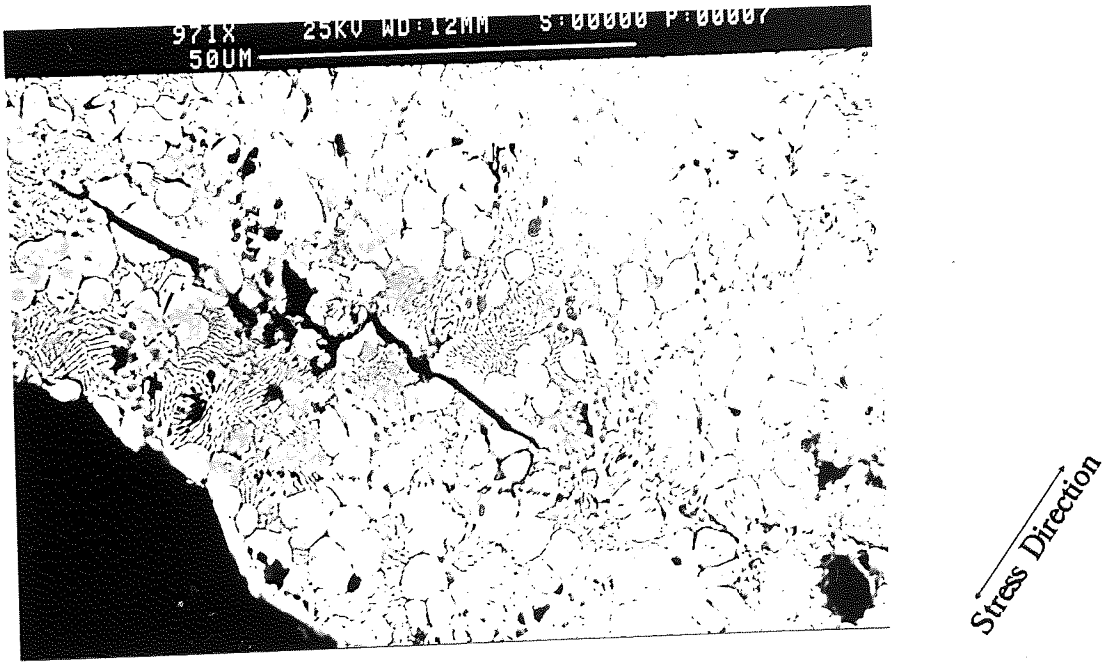

Figure 134. SEM. Cross-section. M3K, 70 MPa at 20 °C/14 M cycles. Subsidiary cracks developed from pores and propagted 90° to the applied stress.

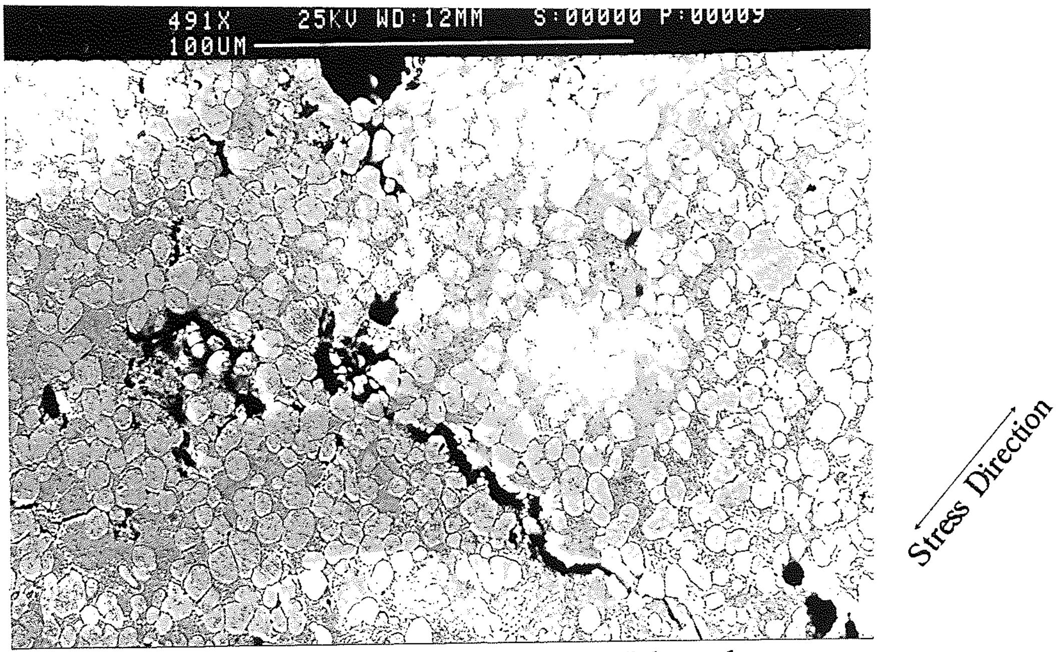

Figure 135. SEM. Cross-section. M3K, 110 MPa at 20 °C/687 k cycles. Subsidiary cracks developed from stress concentrated areas (pores).

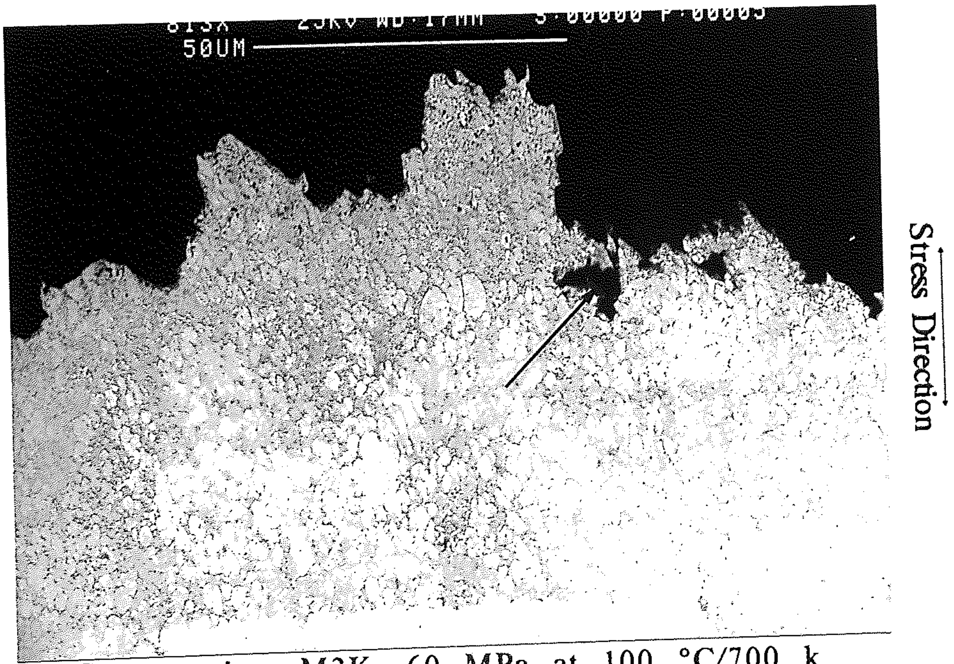

Figure 136. SEM. Cross-section. M3K, 60 MPa at 100 °C/700 k cycles. Severe damage (ductile) due to high temperature. Opening of pores towards the stress direction .

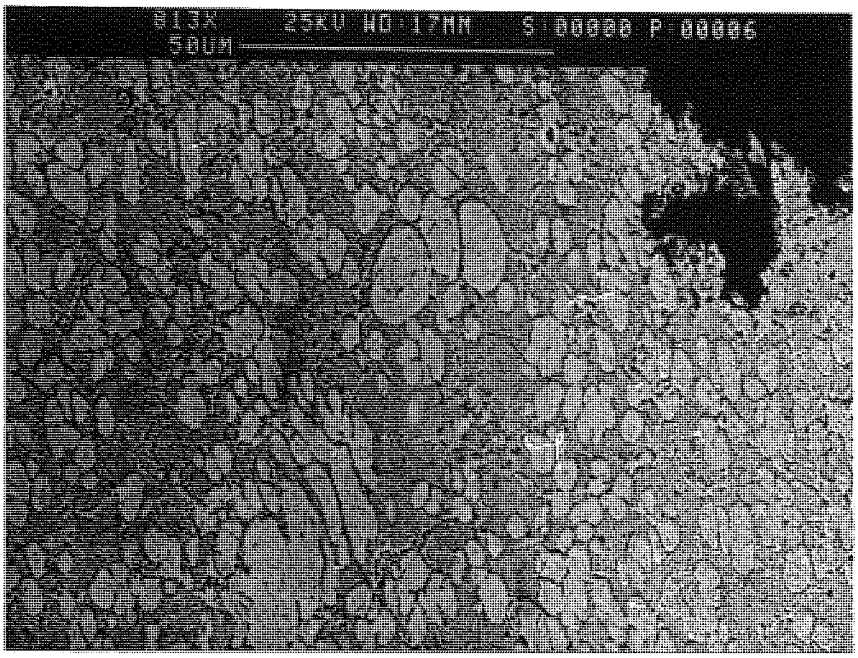

Figure 137. High magnification of Figure 136. Elongated primary η due to elevated temperature.

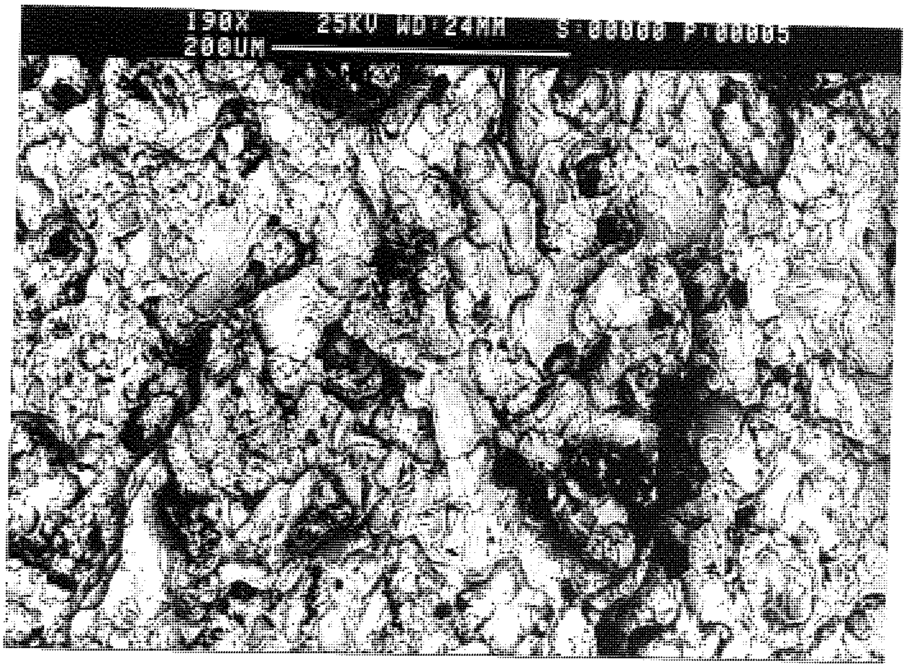

Figure 138. SEM. Mixed signals of Secondary/back-scattered electrons. M3K, tensile fracture. Large number of cleavages as a result of tension.

Figure 139. High magnification of Figure 138. Complex and multi directional in a transgranular manner.

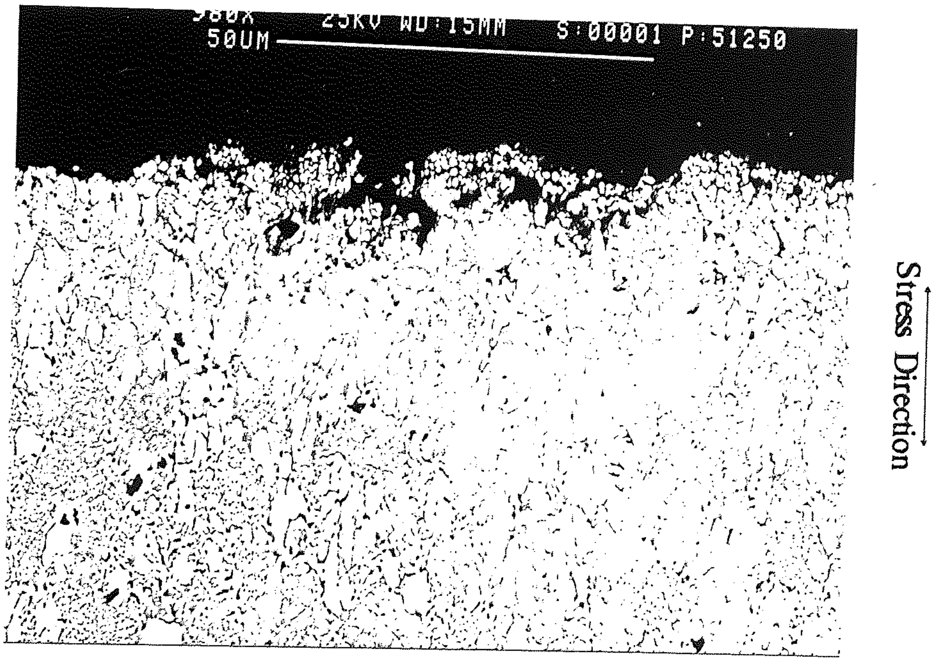

Figure 140. SEM. Cross-section. M3K. Tensile fractured sample. Badly elongated η particles (worse near the fracture) and severe opening of pores in towards the direction of stress.

5.6.2 ZA8K Fracture Morphology

The fracture morphology of ZA8K was examined initially by the optical binocular microscope and then by the SEM using both techniques of secondary electron and back-scattered image. The areas responsible for initiating the cracks were located. Figure 141 shows an image of a fractured surface obtained by the binocular microscope. the Figure exemplifies how a crack initiated on the surface of the sample had propagated inwards to cause failure after the sample was subjected to a stress of 70 MPa at 20 °C and which lasted for 30 M cycles. The figure also reveals that the sample failed shortly after the initiation of the cracks, by showing only a small fatigue area prior to catastrophic ductile/cleavage failure.

Figure 142 shows a secondary electron micrograph, taken at low magnification, of a fractured sample subjected to a stress of 113 MPa at 20°C, which lasted for 6.5 M cycles. The crack had initiated at the centre of the sample from a large pore.

Figure 143, which was taken at a high magnification, shows cleavage through a largely eutectic area adjacent to the pore.

Figures 144 and 145, taken at two different magnifications, show a fractured surface of a sample fatigue tested at 20°C when subjected to a stress of 70 MPa, which lasted for 23 M cycles.

Figure 144(a) reveals a general view of the fracture in topographical (SE) mode, whilst Figure 144(b) shows the back-scattered image revealing the structural damage on the sample. Pores of various depths and sizes are seen in this figure. These pores initiated the cracks in the sample and were randomly distributed around the sample and, in fact, some of these cracks, travelling in a direction perpendicular to the major cracks, could have also contributed to delay the failure of the sample.

The very white areas, seen in Figure 144, and more clearly in Figure 145, mostly represent ductile surface extension around the cusped regions, and are associated with the aluminium-rich former β region. These figures also showed that pores surrounded by the η particles, due to different magnitudes of surface energy between the gas and the low energy of η during solidification. Figures 144 and 145 have also indicated a transgranular fracture. Cleavage and twinning can also be seen in these figures.

Another fractured sample was examined, and is shown in Figures 146 and 147, at two different magnifications. This fracture surface resulted from a fatigue test conducted at 20°C when subjected to a stress of 110 MPa, which lasted for 1.5 M cycles. The figures were taken using secondary electron and back-scattered electrons. Severe cleavage can be seen in these figures as a result of high stress. The cleavage is mainly seen in the η and the eutectic areas. The fracture went through in a transgranular manner.

Cross sections were taken from fractured samples and polished down to 1μm to investigate the possibilities of subsidiary microcracks. Figure 148 reveals the development of microcracks from a number of shrinkage pores, found very close to each other in a cross section from a fatigued sample, subjected to a stress of 0.5 MPa at 20°C and left to run for 30 M cycles. If the fatigue test had been allowed to continue then probably those cracks would have been responsible for the failure. Figure 149 shows a cross section of a fractured sample which was fatigue tested at 20°C when subjected to a stress of 89 MPa which lasted for 7 M cycles. The figure also shows the development and linkage of cracks parallel to, and below, the main fractured surface. When a sample was fatigue tested at a high stress of 115 MPa at 20°C, the sample lasted for 1.5 M cycles. Figure 150 depicts a cross section of that sample and indicates that a large crack had initiated from a pore and advanced parallel to the fractured surface, opening out during its propagation.

ZA8Ksamples were also fatigue tested at 100°C, an example of which is revealed in the cross-section in Figures 151 and 152. The sample was subjected to a stress of 86 MPa and it lasted for 630 k cycles.

Figure 151 shows a general area of the cross- section indicating a crack forming at a high angle to the fractured surface. Figure 152, at a high magnification, shows some microcracks that had developed parallel to the fractured surfaces, splitting a primary β particle into halves. The figure also shows a pore coated by the zinc-rich η particle.

The tensile fracture surfaces of alloy ZA8K were also examined and are shown in Figures 153 and 154, at two different magnifications. Figure 153 shows a photograph of a general fracture, obtained by the use of a mixed signal of secondary electrons and back-scattered images. Cracks which originated from stress concentrated areas (pores) can be seen avancing through the fractured surface in a transgranular manner. The figure also shows cleaved areas resulting from the twinning deformation and the severe tensile force. Figure 154 shows a large cleavage due to tensile force.

Figure 155 shows a cross-section taken from a tensile fractured sample, and polished down to 1 μm to show the development of cracks in the stress concentrated areas (pores). The figure also shows the development of the cracks from pores. The severity of the crack depends on the size of the original pore and location of their stress concentration in relation to the tensile stress direction.

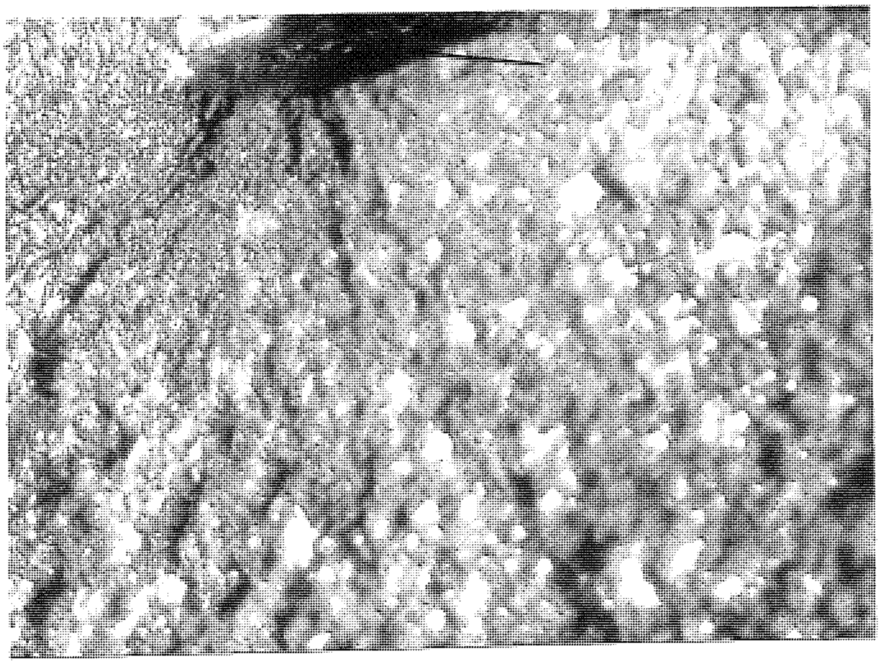

Figure 141. Light micrograph of ZA8K, 70 MPa at 20 °C/ 30 M cycles. Surface defect and crack initiation (arrowed).

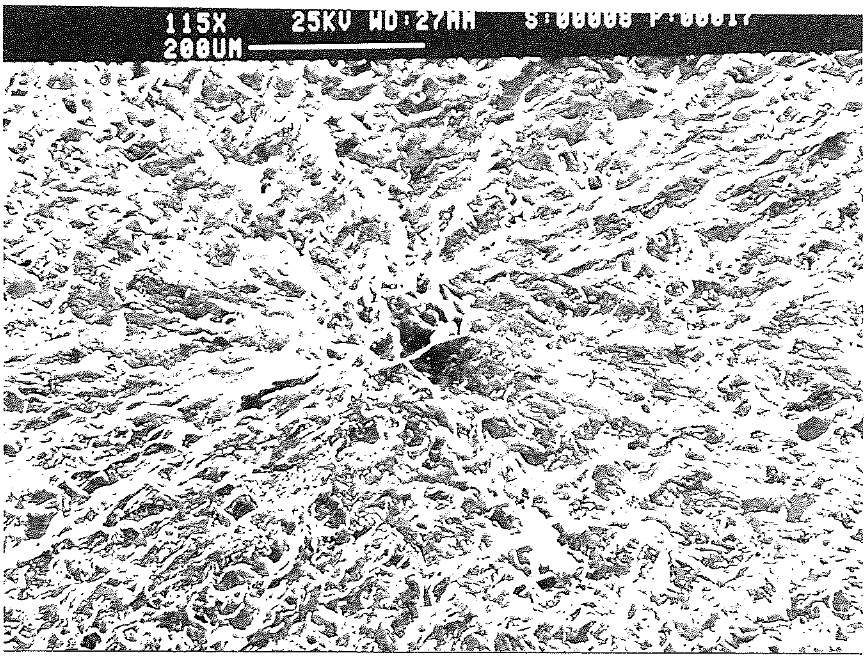

Figure 142. SEM.Secondary electron. ZA8K, 113 MPa at 20 °C/6.5 M cycles. Cracks radiating from the central defect.

Figure 143. High magnification of Figure 142, showing cleavage in the eutectic area resulted from the advanced cracks from the nearby defect (pore).

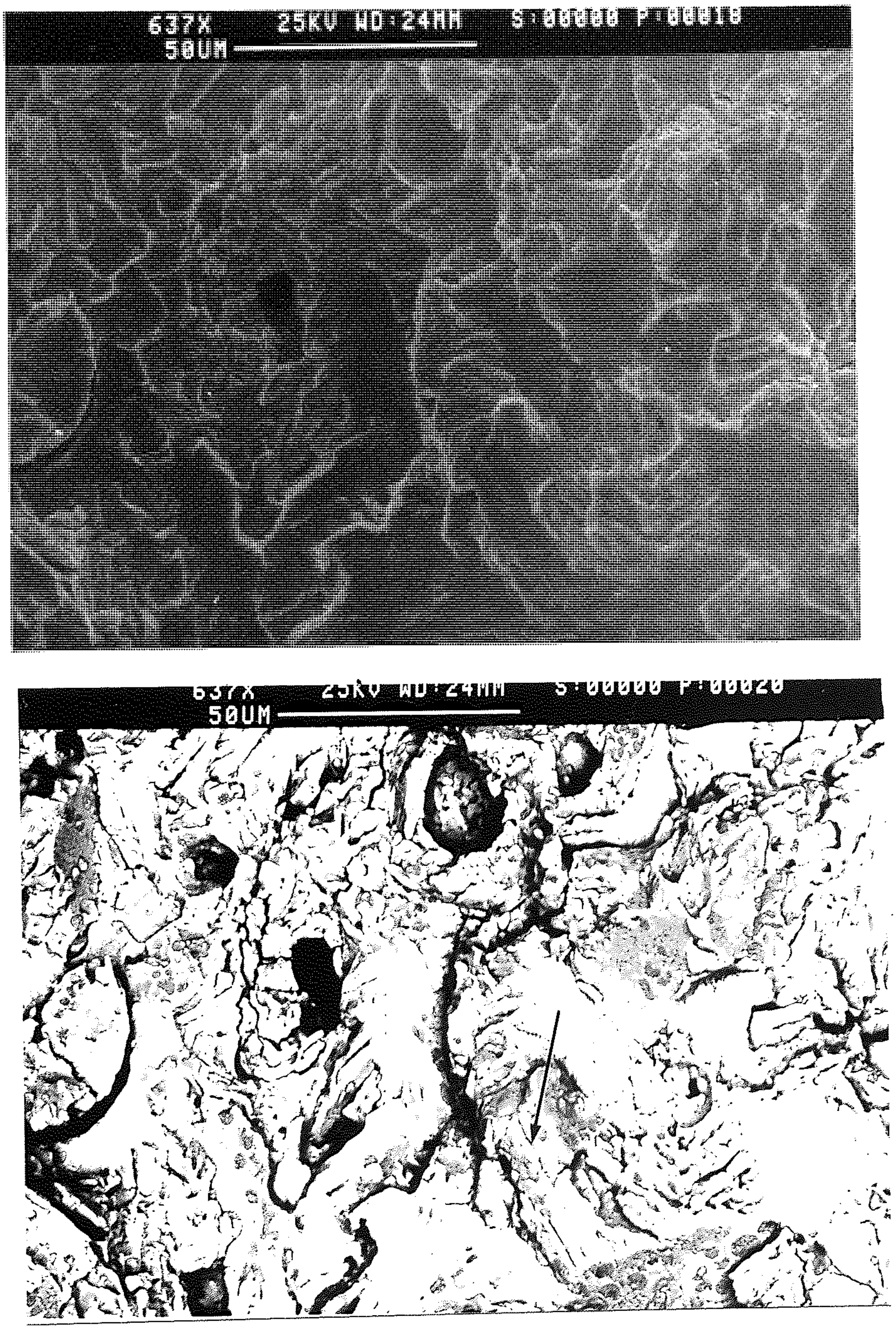

Figure 144. a) SEM.Secondary electron. ZA8K, 70 MPa at 20 °C/23 M cycles.

b) Back-scattered image of (a), revealing the structural damage.

Cracks radiating from pores and linking up to form larger cracks.

Twinning (arrowed).

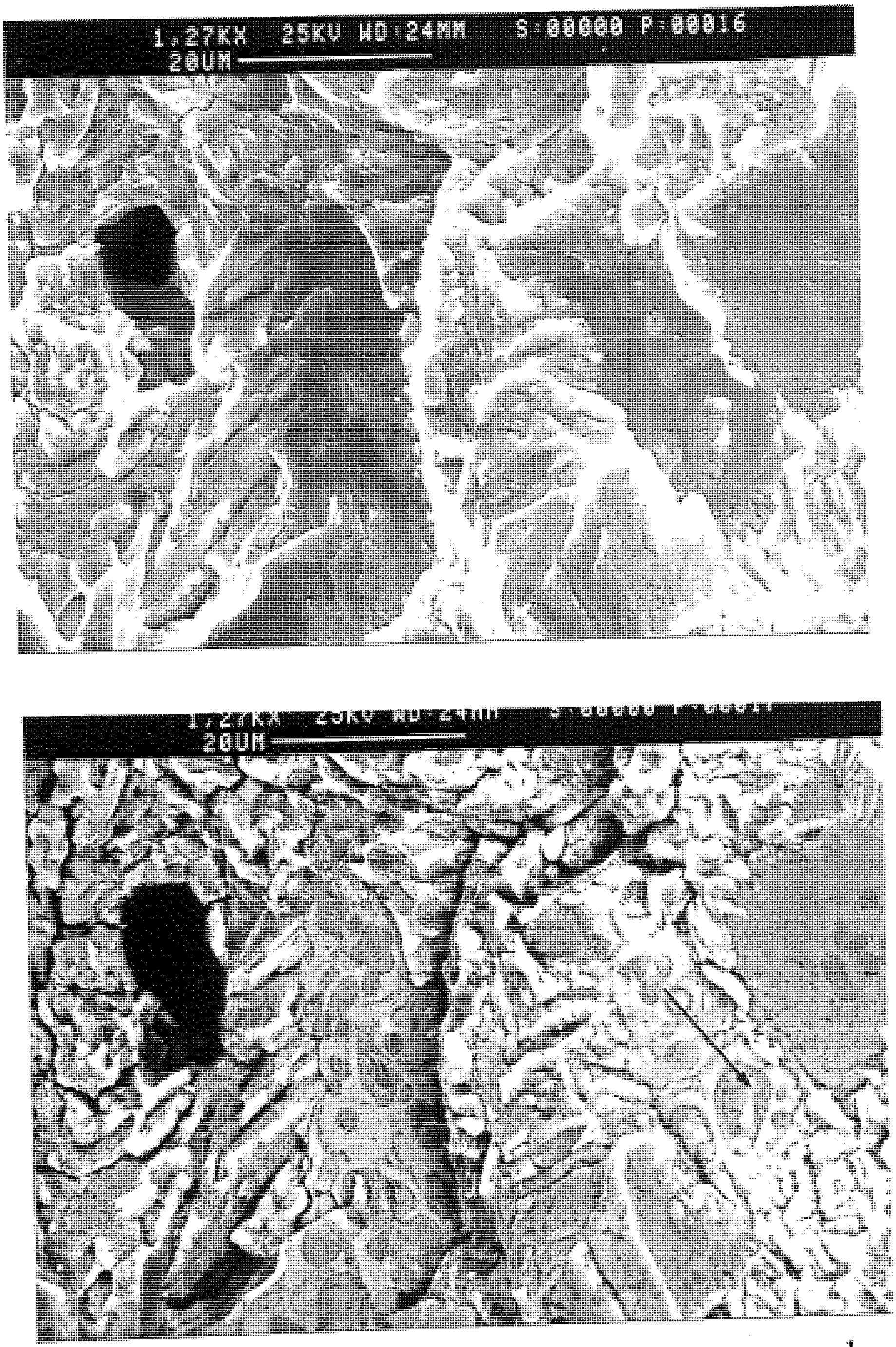

Figure 145. High magnification of Figure 144, showing transgranular propagation. White cusps (arrowed) are associated with the pseudoprimary β.

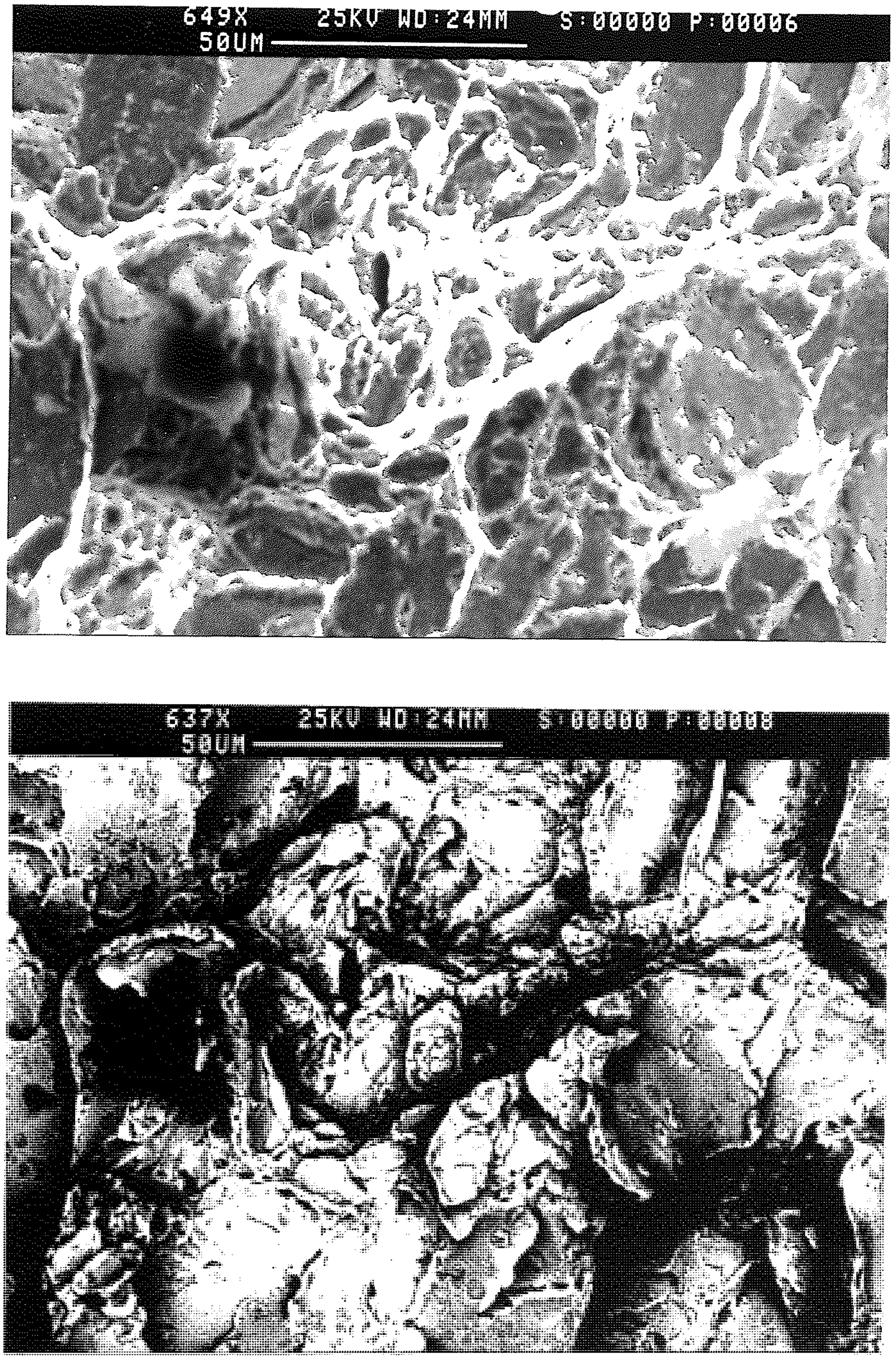

Figure 146. a) SEM.Secondary electron. ZA8K, 110 MPa at 20 °C/1.5 M cycles. b) Back-scattered image of (a), showing cracks going through the structure in a random maner depending on the stress concentrations orientations (pores, cleavages).

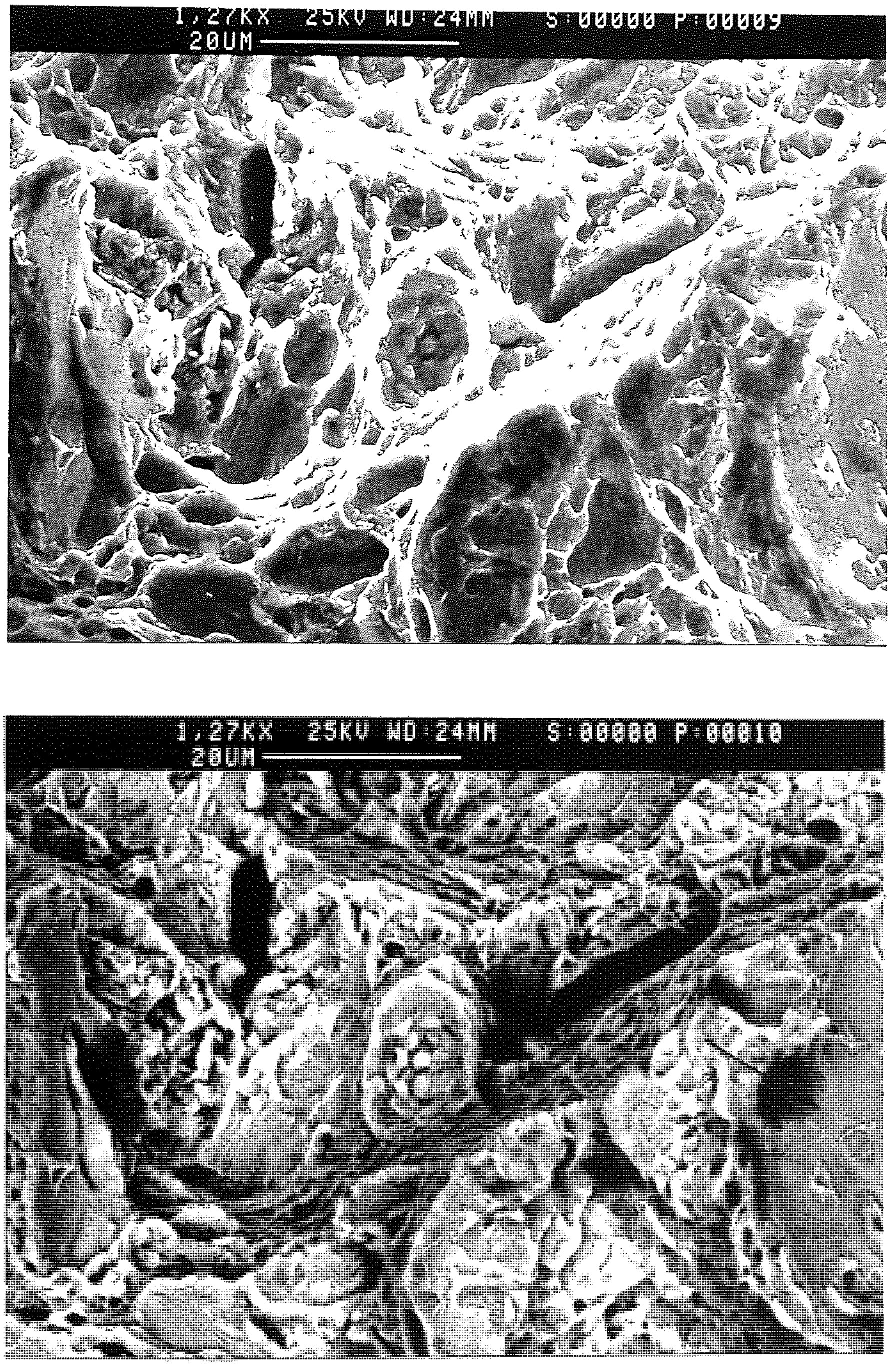

Figure 147. High magnification of Figure 146, showing massive cleavage (arrowed).

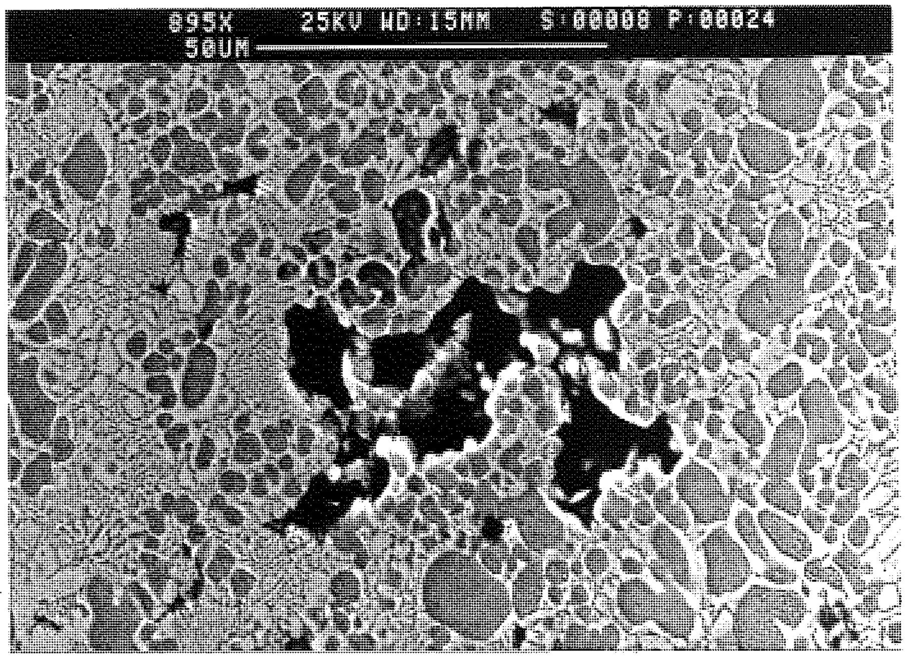

Stress Direction

Figure 148. SEM. Back-scattered image of cross-section; ZA8K at 20 °C/ 65 MPa at 20 °C/stopped at 30 M cycles. Voids started to link up.

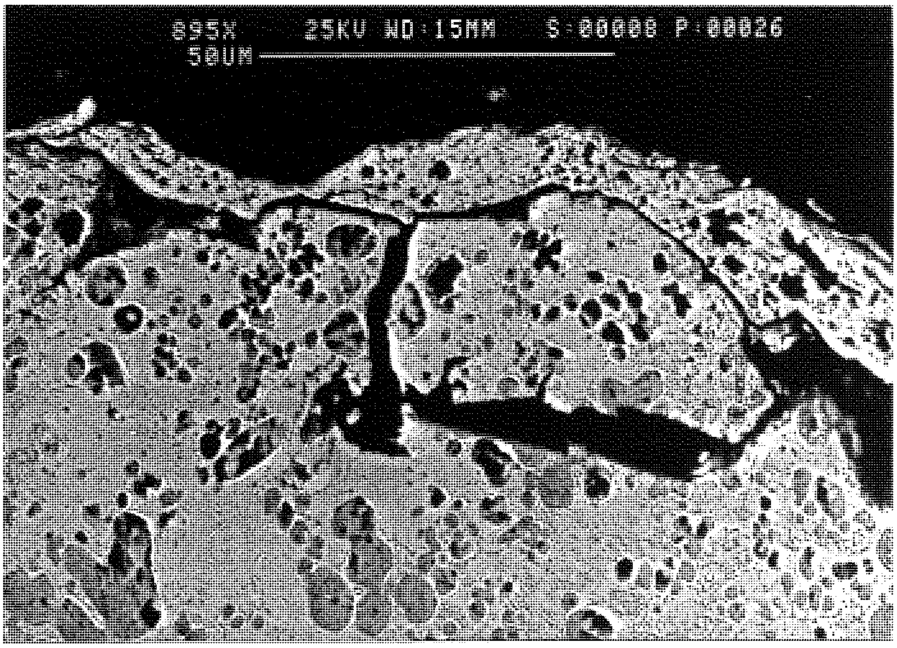

Stress Direction

Figure 149. SEM. Back-scattered image of cross-section. ZA8K 89 MPa at 20°C/7 M cycles. Subsidiary cracks with high angle to the stress direction.

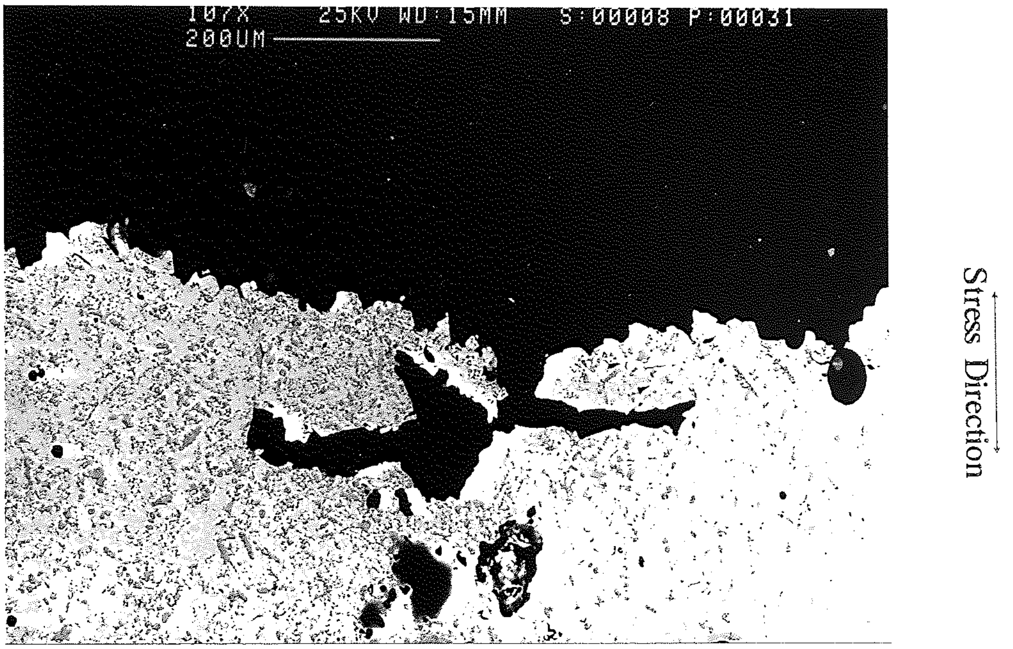

Figure 150. SEM. Back-scattered image of cross-section. ZA8K 115 MPa at 20 °C/1.5 M cycles. Susidiary cracks developed from apore in right angle to the stress direction.

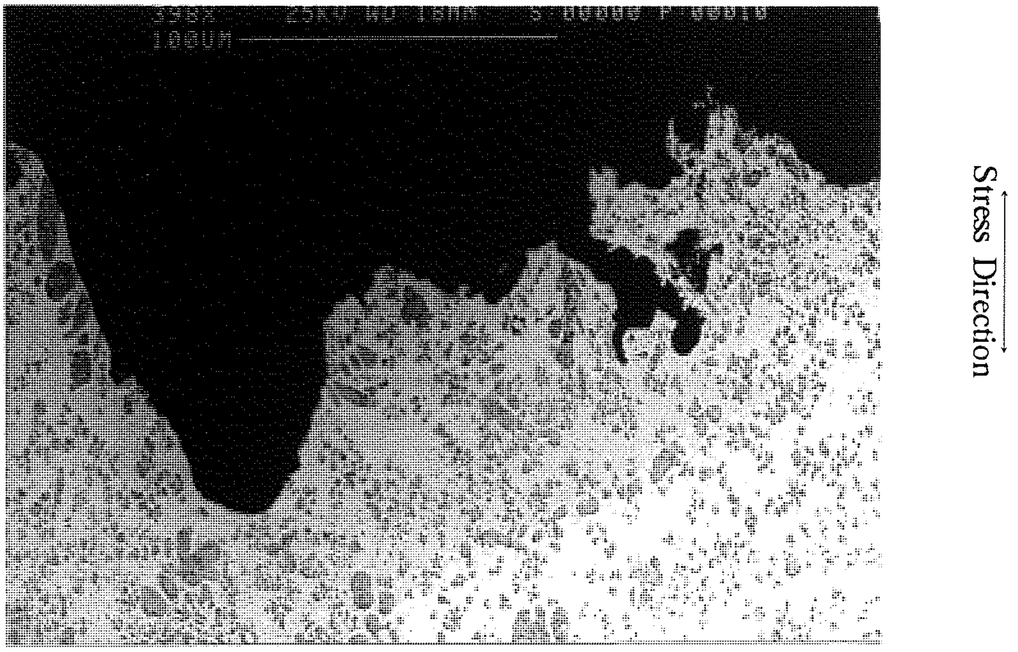

Figure 151. SEM. Back-scattered image of cross-section. ZA8K 86 MPa at 100 °C/630 k cycles. Severe temperature effect with tension causing rough fracture.

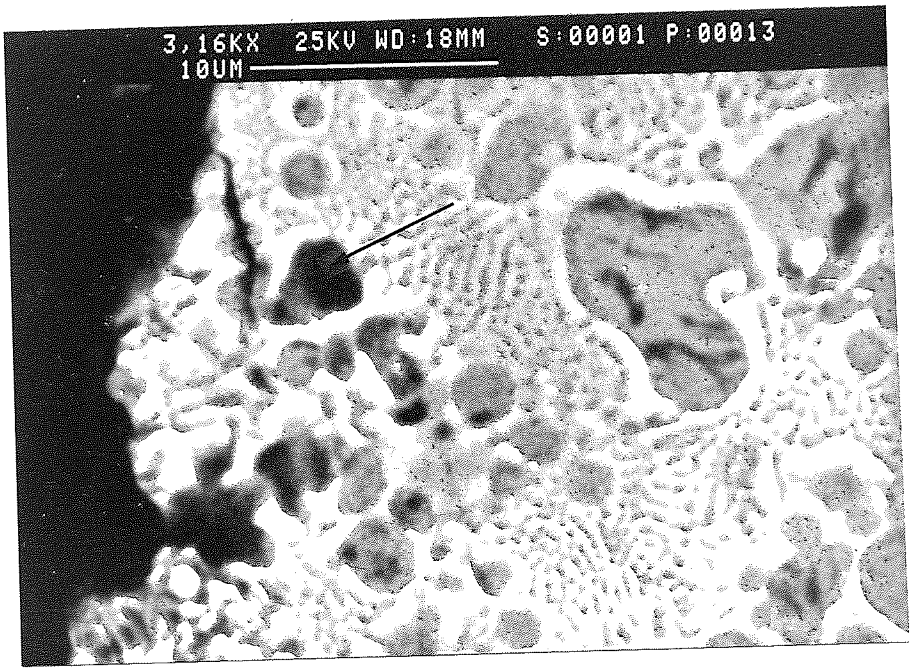

Stress Direction

Figure 152. High magnification of Figure 151 focused on some part of the fracture sample, shwoing evidence of subsidiary cracks parallel to the fracture surface. Also showing that crack was developed from a pore coated with an η particle during castings (arrowed).

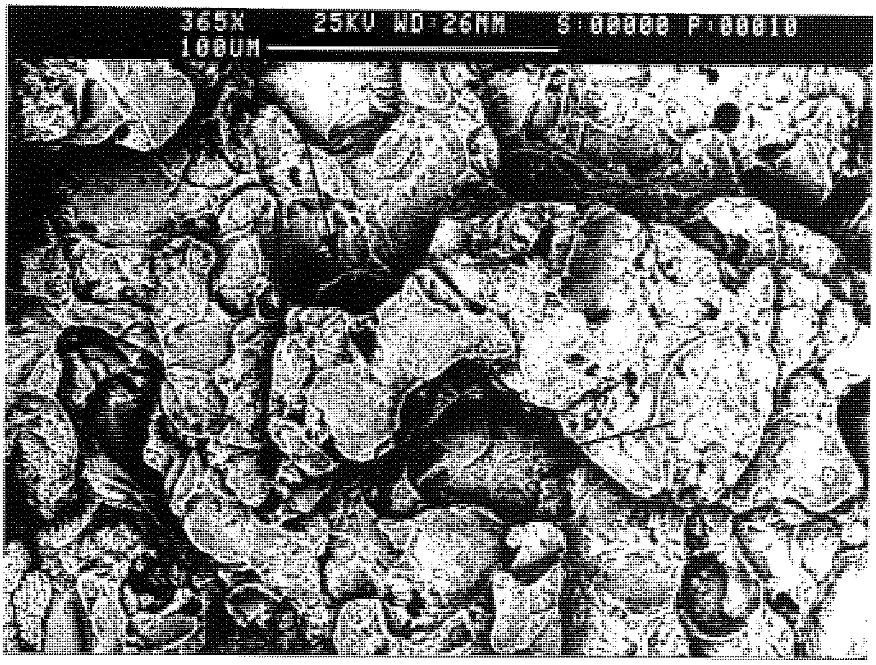

Figure 153. SEM. Mixed Secondary electron/Back-scattered image. ZA8K tensile fracture. Large number of cleavages (arrowed) caused by the tensile force.

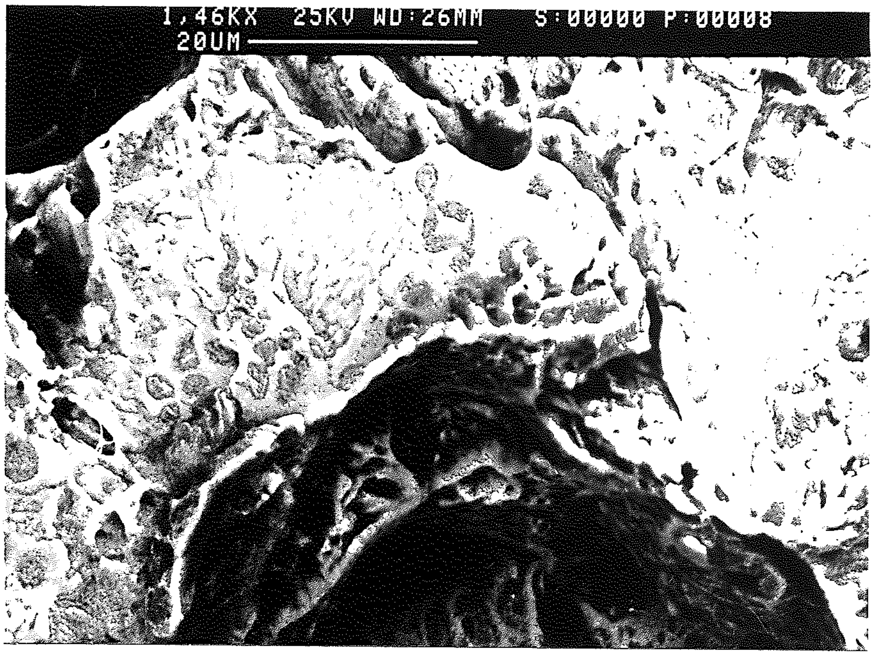

Figure 154. High magnification of Figure 153, showing large cleavage.

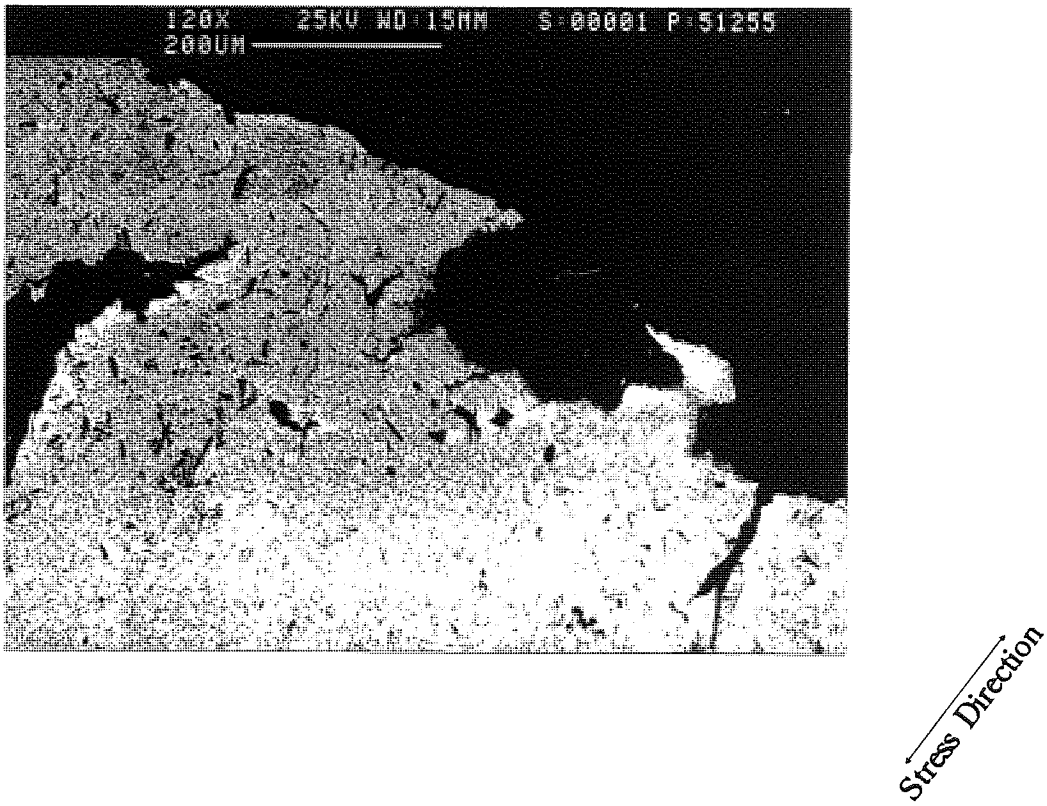

Figure 155. SEM. Back-scattered image of cross-section. ZA8K tensile fracture. Subsidiary cracks are formed in a right angle to the nearest stress concentrated area of fracture.

5.6.3 Fracture Morphology of ZA27K

The fractured surfaces of the ZA27K alloy were studied using the same SEM techniques as before, to obtain information on both the fracture morphology and the microstructure. Figures 156 and 157 show a fatigue fracture of the ZA27K sample subjected to a stress of 86 MPa at 20°C and lasting for 10.9 M cycles. Figure 158 reveals that the cracks initiated from a pore on the bottom of the micrograph. Figure 157, at high magnification, reveals small cracks linking up between the pores and shrinkage. The fracture is of transgranular type. Large cleavage areas can also be seen in Figures 156 and 157.

Figure 158 shows a general area of fractured samples, subjected to a high stress of 131 MPa at 20°C which lasted for 241 k cycles. The figure shows a randomly selected area of the fracture surface consisting of large pores, large shrinkages and small cracks progressing to link the pores and shrinkages together. The figure also reveals large cleavages, resulting from the high tensile force, to fail the sample prematurely.

Figures 159 and 160, at two different magnifications, depict a fatigue fractured sample subjected to a stress of 70 MPa at 20°C, which lasted for 22 M cycles. A SEM secondary image of Figure 159(a) shows numerous large and small pores in the sample. Figure 159(b), which is the back scattered image of the fractured sample, shows that the highly irregular fracture surface was forced due to the very inhomogeneous structure. Figure 160(a) shows the same area at higher magnification. Figure 160(b) shows that, in some cases, the cracks went through the hard α particles to split them up into halves. In some cases the cracks seem to have progressed through the interface between the hard α particles and the zinc-rich η particles. The white areas seen in this figure are believed to be the former aluminium-rich β particles (ductile).

Figure 161 shows a cross-section taken from a sample before fracture. This sample was subjected to a low stress of 65 MPa at 20°C, and the test was stopped at 30 M cycles. The sample was cut longitudinally into 4 cross-sections from the gauge length and polished down to 1 μm on a diamond wheel. All these cross-sections were examined thoroughly on the SEM by back-scattered imaging. The area seen in Figure 161 was the largest colony of pores, and it is believed that with prolonged fatigue testing, this area could have caused the failure. As seen from Figure 161 the pores had stated to link together with some form of cracks between them.

Figure 162 shows a cross-section taken from a sample tested at 20°C when subjected to a stress of 106 MPa that lasted for 1.46 M cycles. The figure shows the linkage between the pores below the fractured surface. Subsidiary cracks are also seen parallel to the fractures surface. Figure 163 shows a cross-section of a sample subjected to a high stress of 131 MPa at 20°C for 241k cycles. The figure shows the severe damage caused by tensile stress which caused a wide opening of the pores.

Figures 164 and 165, taken at two different magnifications, show a cross-section of fractured samples subjected to a stress of 72 MPa at 100°C for 300 k cycles. Pores have linked together through the structure and widely opened in the zinc-rich η particles and the aluminium-rich former β dendrites. No damage can be seen on the α particles. Figure 165, at higher magnification, shows the linkage between pores below the fractured surfaces. The linkage is formed by small cracks running through the interface between α particles and the zinc-rich η areas. One example of these cracks is illustrated by an arrow on the micrograph.

Figures 166 and 167, at two different magnifications, show a fractured surface subjected to tensile testing at 20°C. The mircographs were obtained by using a mixed signal between secondary electron and back scattered images.

Figure 166 shows cracks progressing from pores or shrinkage areas. The figure also shows cleavage caused by the severe tensile force. The cracks have developed in a random way depending on the stress concentration in relation to the applied stress. Figure 167, at higher magnification, shows the severe cleavage produced by the tensile force.

Figure 168 shows a cross-section taken from a tensile fractured sample at 20°C. The figure shows the tensile effect on pores near the fractured surface. The arrow indicates a linkage between a pore and a shrinkage that are very close to each other. The linkage occurred easily as the distance between the pore and the shrinkage was very small, to withstand the tensile force.

Figure 156. SEM. Secondary electron. ZA27K, 86 MPa at 20 °C/10.9 M cycles. Void and crack initiation (arrowed).

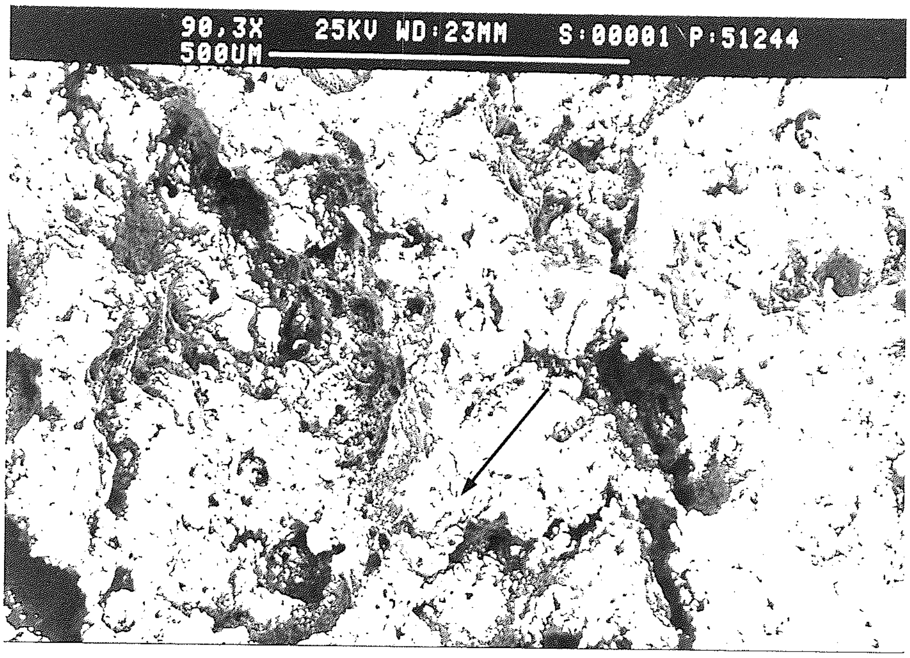

Figure 157. High magnification of Figure 156. Showing large number of shrinkages. microcracks developed from shrinkage (example arrowed).

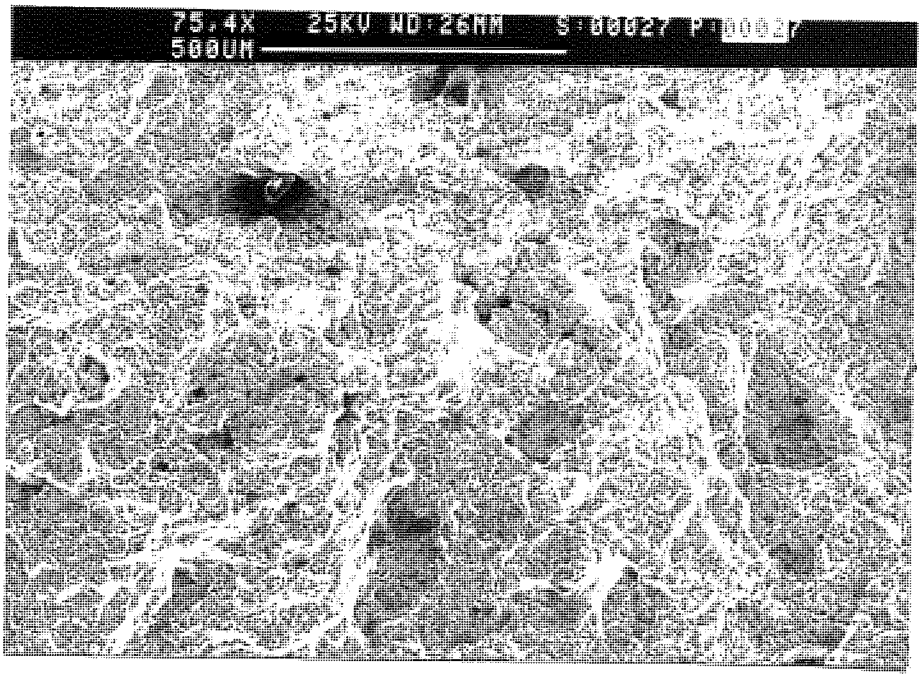

Figure 158. SEM. Secondary electron. ZA27K, 131 MPa at 20 °C/241 k cycles. The sample contained more the less the same number of pores and shrinkages as in Figure 157.

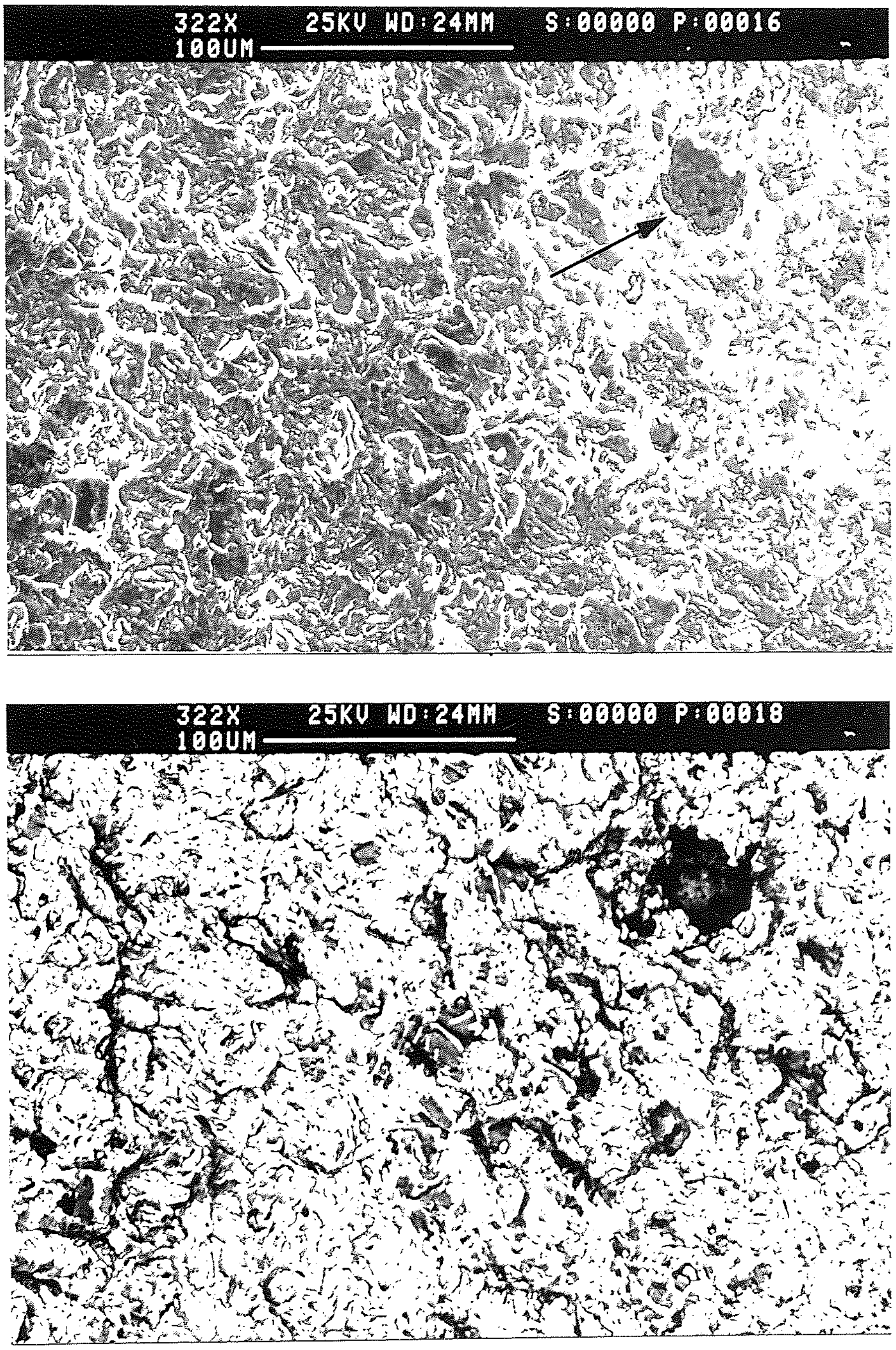

Figure 159. a) SEM.Secondary electron. ZA27K, 70 MPa at 20 °C/22 M cycles. Large shrinkage (arrowed)

b) Back-scattered image of (a). Cracks developed from the shrinkage and linked up with other smaller cracks developed from smaller shrinkages and voids. Transgranular propagation.

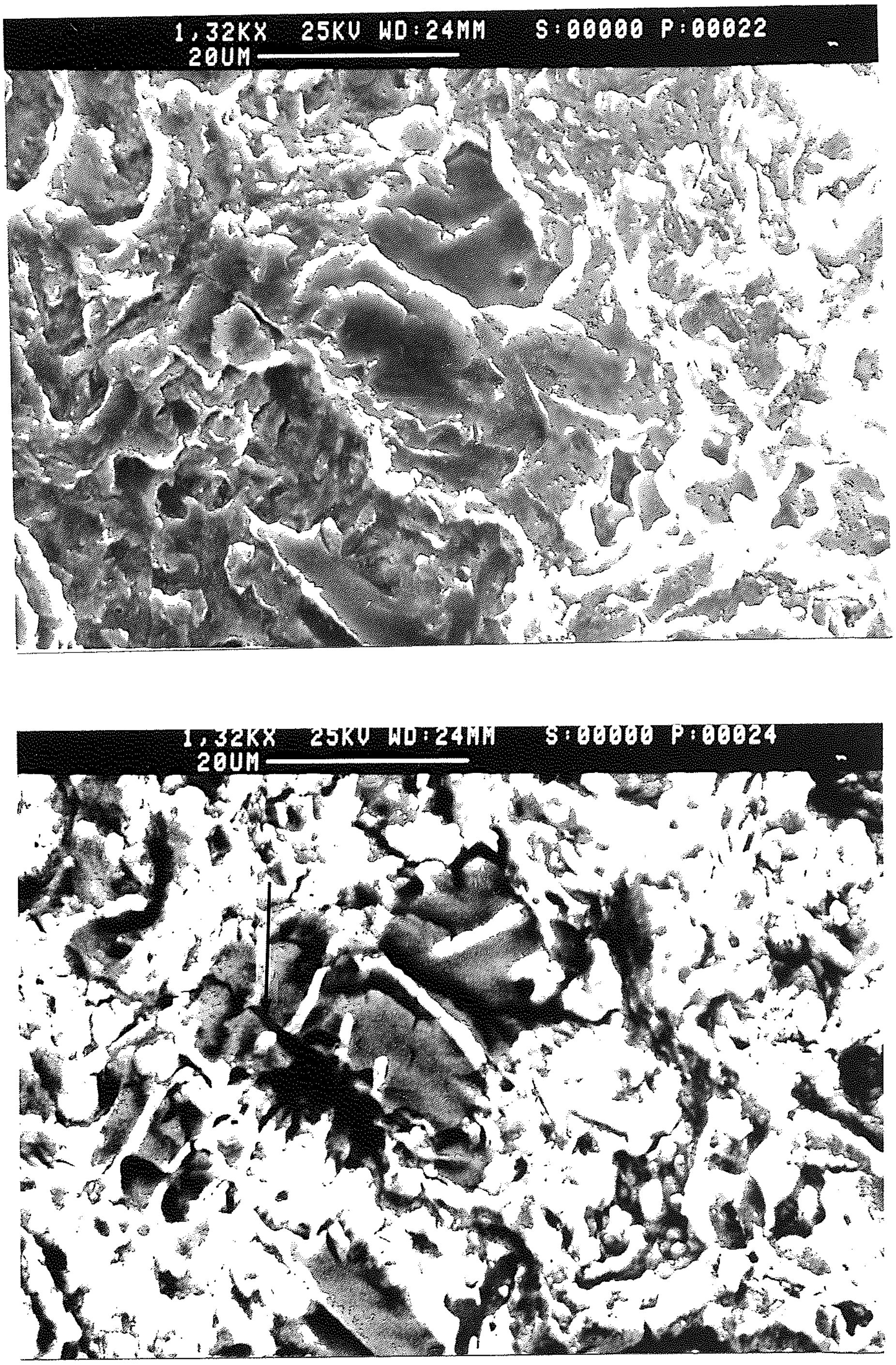

Figure 160. High magnification of Figure 159. Cracks going through α dendrites (arrowed). Also cracks went through the interface between the soft η and the hard α dendrites. White cusps are the β particles.

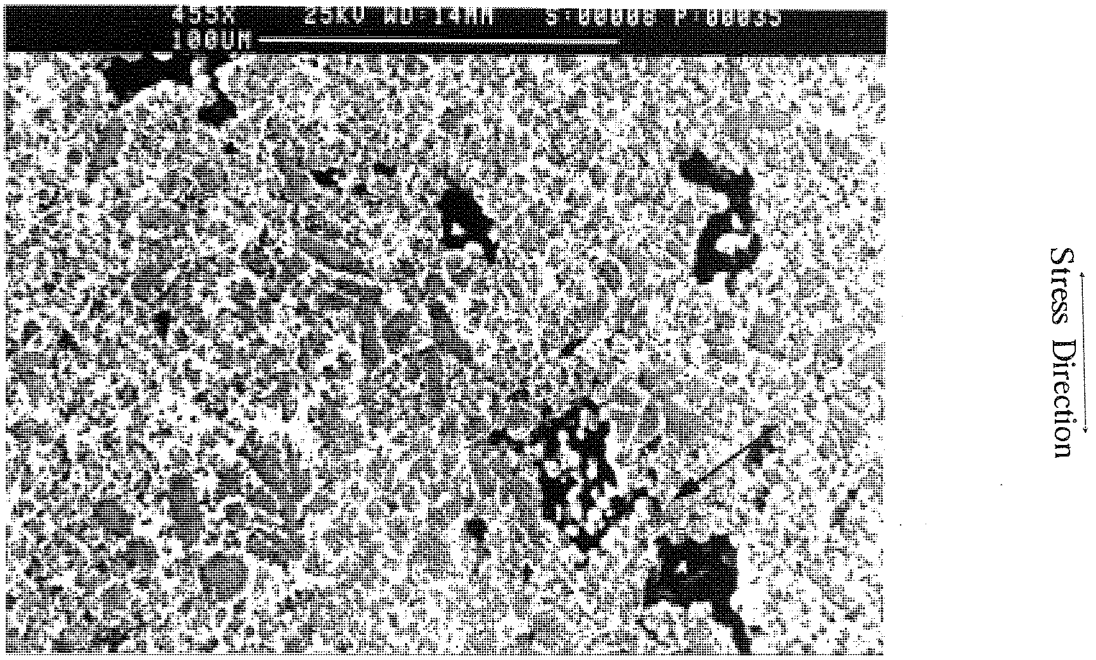

Figure 161. SEM. Back-scattered image of cross-section. ZA27K 65 MPa at 20 °C/stopped at 30 M cycles. Evidence of a linkage started between the shrinkages (arrowed).

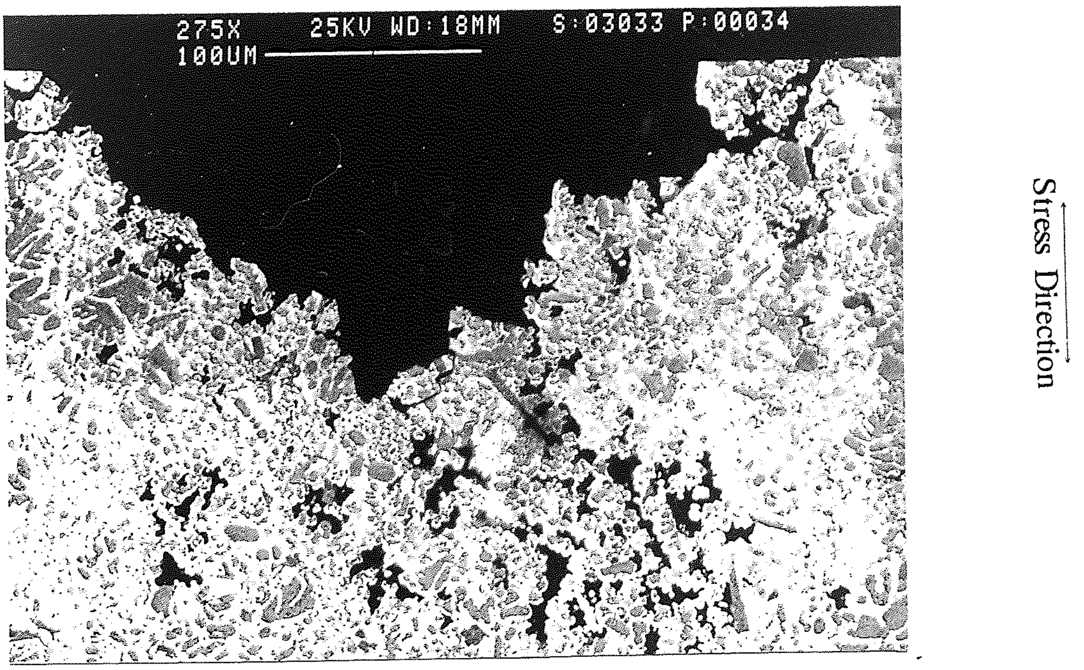

Figure 162. SEM. Back-scattered image of cross-section. ZA27K 106 MPa at 20 °C/1.4 M cycles. Subsidiary linkages between voids.

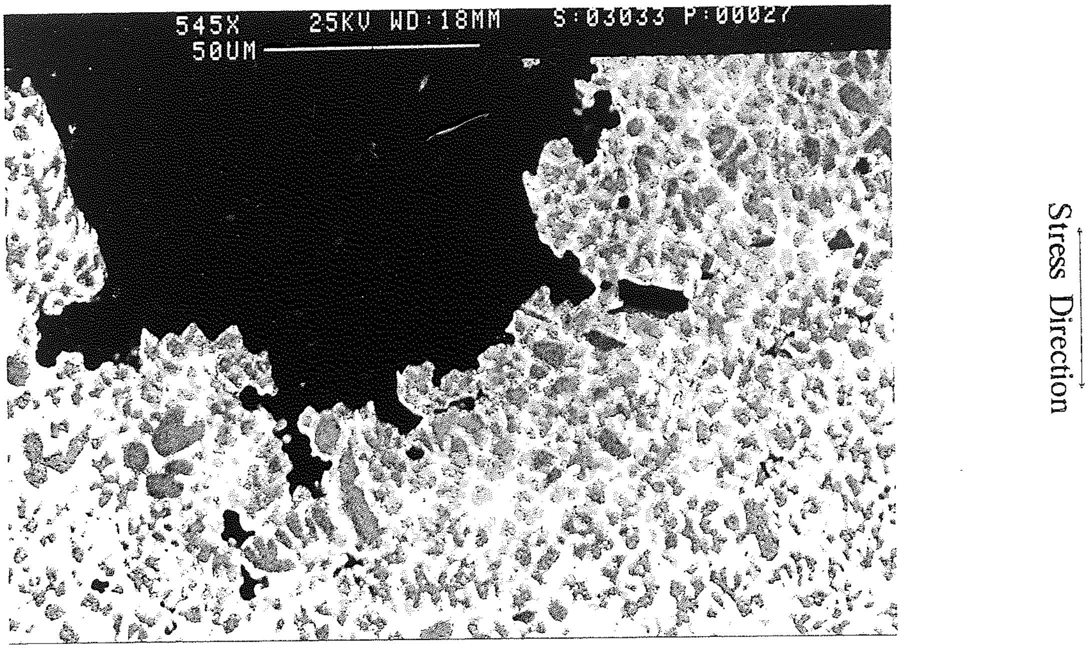

Figure 163. SEM. Back-scattered image of cross-section. ZA27K131 MPa at 20 °C/241 k cycles. Rough fracture caused by shearing at high tensile force.

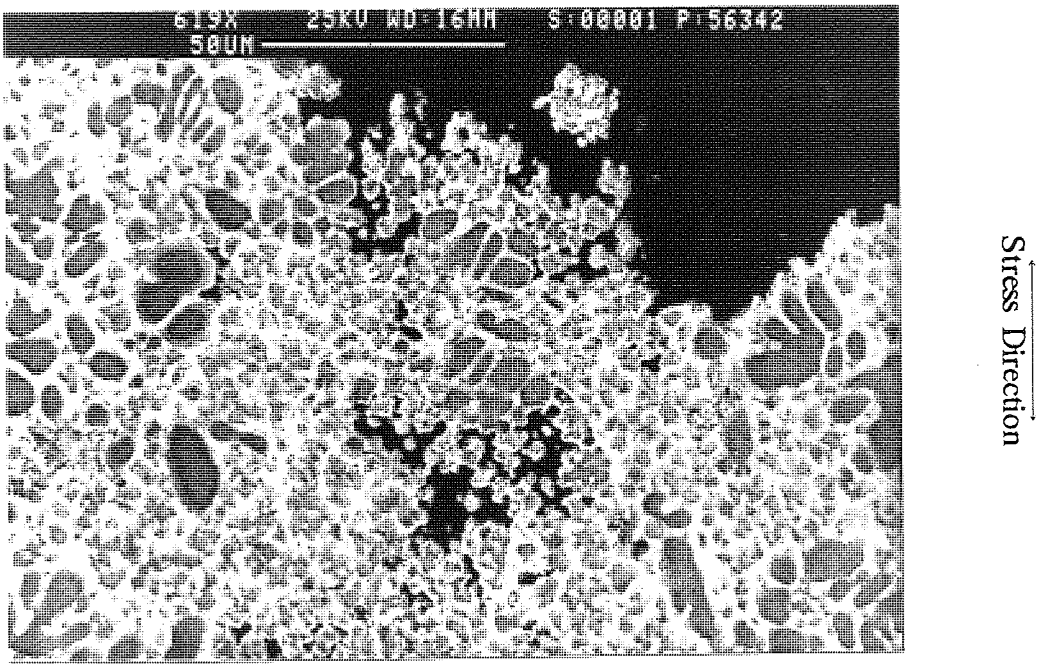

Figure 164. SEM. Back-scattered image of cross-section. ZA27K72 MPa at 100 °C/300 k cycles. Subsidiary linkage between voids.

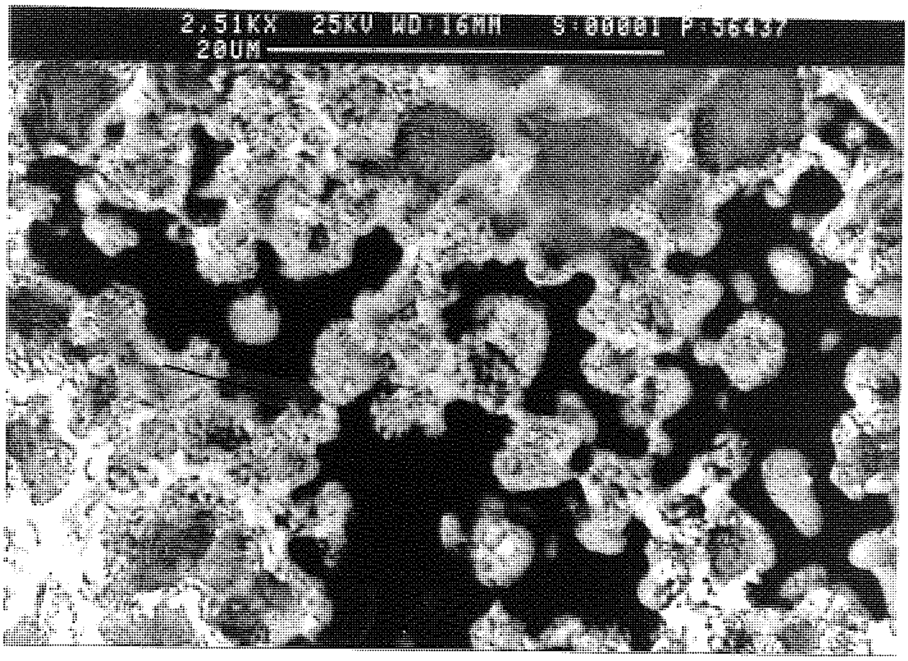

Figure 165. High magnification of Figure 164. Concentrated area of voids below the fracture surface with claer indications of linkage (arrowed).

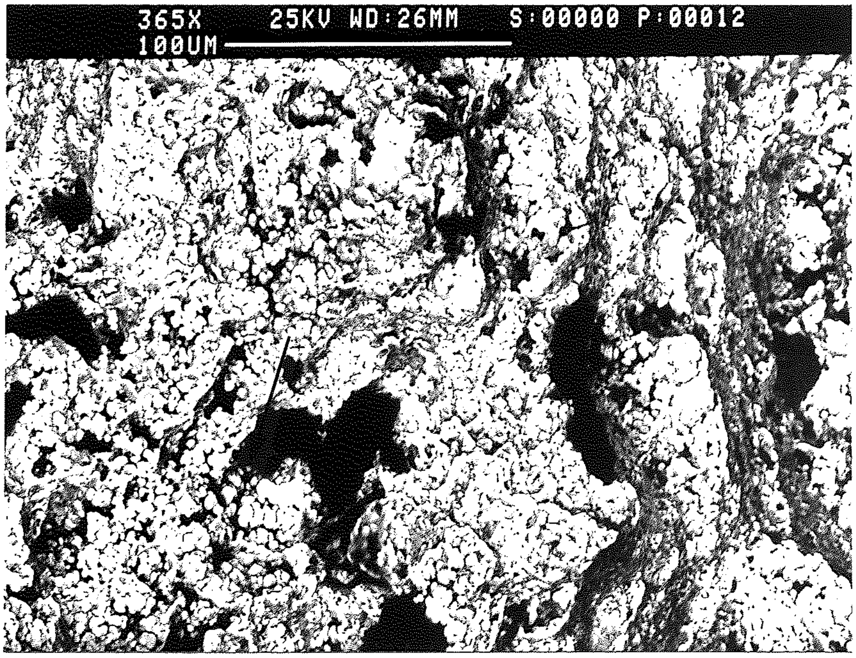

Figure 166. SEM. Mixed signal of Secondary electron/back-scattered electron. ZA27K/ tensile fracture sample. Cracks developed from shrinkage (arrowed).

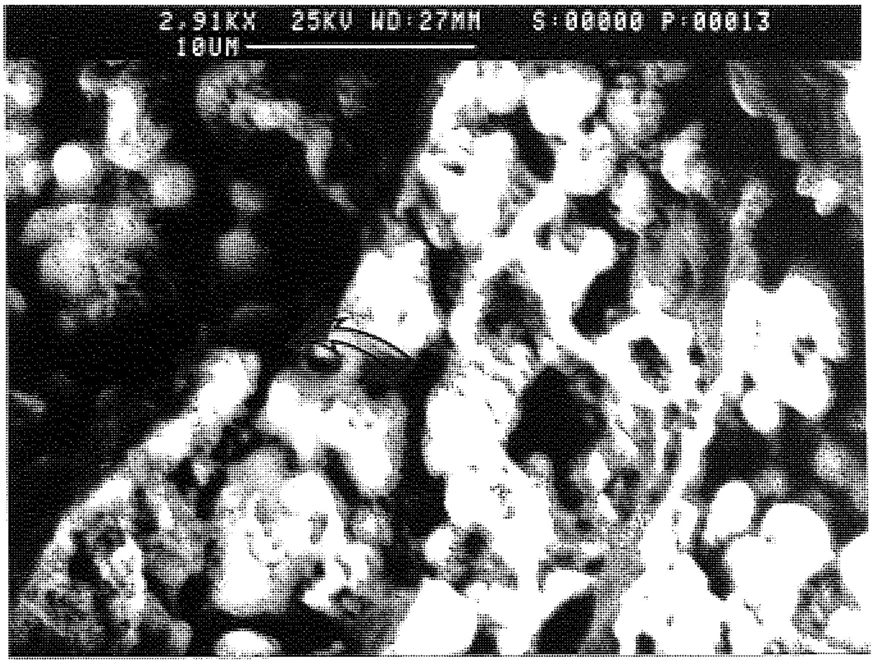

Figure 167. High magnification of Figure 166. Cleavage (arrowed).

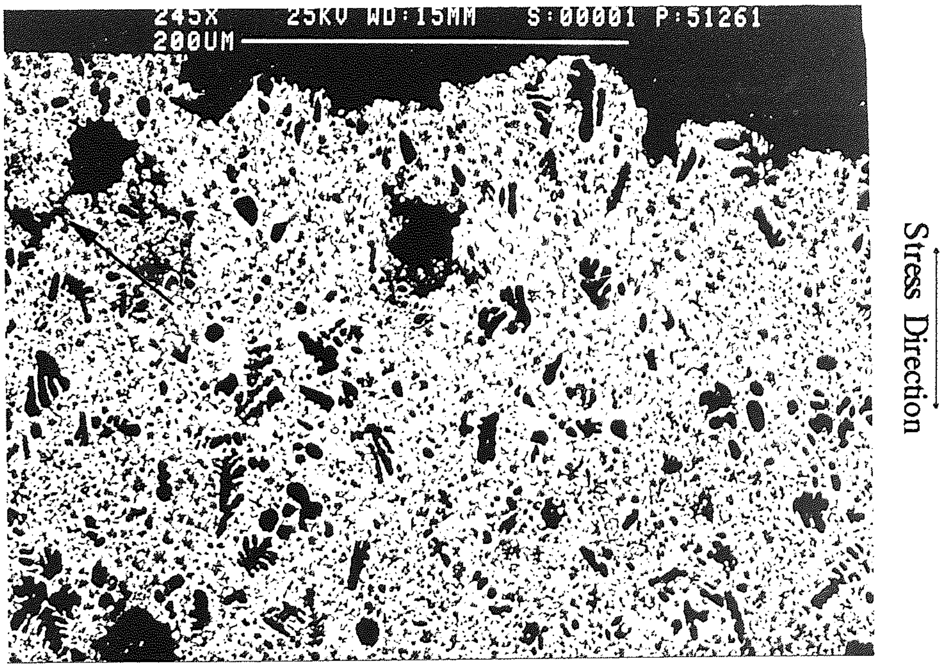

Figure 168. SEM. Back-scattered image of cross-section. ZA27K tensile fracture. Subsidiary cracks are seen to develope between a large pore and small shrinkage (arrowed).

CHAPTER 6

6.0 DISCUSSION OF THE EXPERIMENTAL RESULTS

6.1 Metallography of the Mazak3 and M3K Alloys

The Mazak3 and M3K alloys are meant to be the same as they both originated from commercial Mazak3 alloy. This can be confirmed by their chemical composition which was determined by the Atomic Absorption Spectro-analyser, and were revealed in Table 11.

Furthermore, the as-cast structure of the Mazak3 and M3K alloys, shown in figures 55-57 and 64-67 respectively, reveals the same structural phases. The structure of both alloys was heterogeneous but it was clearly hypoeutectic and consisted of a few large (about 20 μm in the M3 and 14 μm in the M3K) and many small (about 8 μm in the M3 and 5 μm in the M3K) dendritic particles of the primary Zn-rich η phase surrounded by a relatively small volume of eutectic matrix. Many small rounded particles of about 1 μm were attached to the primary η - phase dendrites. Figures 56 and 65, taken at a medium magnification, showed that these small dark particles were a pseudoprimary aluminium-rich β phase which had formed on the primary phase at high undercooling during solidification of the eutectic. As β is unstable below 275 °C (eutectoid temperature), it had subsequently decomposed into zinc-rich η and aluminium-rich α phases. Figures 66 and 67, taken at a high magnification, show in detail the nucleated pseudoprimary β and the radial eutectic on the primary η. The Figure also shows the presence of fine precipitates within the primary η - dendrites. These fine precipitates were studied in greater depth with the use of the TEM, and are shown in Figures 68, 69 and 70, at three different magnifications. Figure 69, taken at a medium magnification, shows the precipitates formed in the primary η grain. Figure 70, displays a primary η particle taken at a high magnification. It shows in greater detail the precipitates of the aluminium-rich α within the η particle. This phenomenon was due to the fact that the solid solubility of aluminium in zinc is very little at room temperature and the excess aluminium is removed by precipitation of the aluminium-rich α phase in zinc matrix. When studying Figures 69 and 70, it can be noted that the precipitation of the excess aluminium in the primary η has one habit in respect to the zinc matrix. This phenomenon was then revealed by the SADP's shown in Figure 71. The Figure shows a diffraction pattern taken from Figure 70. The SADP's showed the reflections of the zinc matrix with a beam direction of $\left[1\bar{2}10\right]$ and failed to show any double diffraction effects.

Returning to the SEM micrographs in Figures 65, 66 and 67, it can be seen that the eutectic had formed radially on the primary η. The TEM micrograph, revealed in Figures 68 and 69, shows that the eutectic Al-rich α phase had formed into the shape of thin haloes. These thin haloes of the eutectic might have been caused by the process of removing the excess aluminium from the supercooled liquid as a thin β layer before normal eutectic solidification took place. Upon subsequent cooling, this had transformed into a string of $\alpha + \eta$ particles as shown in the TEM micrographs in Figures 72, 73 and 74. These figures indicate that the eutectic firstly grew asymmetrically to form irregular ribbon-like lamellae, which acted as nuclei for further growth of irregular lamellae in a complex morphology. Upon cooling through the β-transformation, the lamellae had transformed into strings of α and eutectoid η particles. Three TEM micrographs showed a large number of small dark particles enclosed within the α phase of the eutectic. These micrographs are shown in Figure 68 and more clearly in Figures 72 and 73. These particles were rounded or elongated and had distinct boundaries with the surrounding α phase. These particles were seen in a smaller number within the α phase of the Mazak3 alloy, but they could not be identified and it was suspected that they might be transitional phases almost completely removed after five years of ageing at ambient temperature. However, in the case of M3K, which was freshly cast, the particles were more numerous and some of them were large enough to analyse quantitively by SED using STEM mode to minimise the beam diameter. The matrix α phase had an aluminium content corresponding to the α'_t phase found previously in a quenched-aged alloy(114) and this did not correspond to the equilibrium state of the α phase. The unknown phase had a larger zinc content than that of the β phase, which is presumed to be its precursor. Several attempts were made to obtain diffraction evidence for the structure of the transitional zinc-rich phase, but no separate diffraction reflection could be obtained. It is a fact that Mazak3 is a copper-free alloy and the amount of copper expected was merely up to an impurity level, but the results of the analyses showed that there was a reasonable amount of copper and that the zinc-rich phase was relatively higher in copper than in the aluminium-rich phase. This cannot be the case, however, and these results could have occurred due to an error introduced by the background fitting process to the characteristic peaks of the elements, or to redeposition of copper on the surfaces of the foil during electropolishing. The same problem occurred in the case of magnesium, where analyses showed an enormously high overall magnesium content within the aluminium-rich phase. Despite the analyses, this is thought to indicate that the majority of magnesium in the alloy must have been in solid solution in the aluminium-rich phase.

Figure 69 revealed that the primary η contained internal precipitates, whilst the higher magnification micrograph of Figure 70 showed these to be a group of rounded or plate-like dispersed small particles with a single habit plane or growth direction. The different contrast within the precipitates indicated more than one grain orientation relationship. Distinct precipitate-free regions, some 0.3 μm thick round the edges of the dendrite, together with a layer of aluminium particles coating the outer surface were also clearly shown. Identification of these interior precipitates was attempted using chemical analyses (EDS) and by crystallographic analyses using SADP's. Chemical analyses of individual particles was not possible owing to the fine scale of precipitation, even though the STEM mode was used to produce a finely focussed beam. However, comparison of the EDS spectra from the precipitate-free region with that from the interior region, showed that the latter had a substantial aluminium content, whereas the former had not.

In view of the undoubted overlap of phases in the thin foils, a fully-quantitative analyses of the precipitates was not attempted, but quantitative analyses from the precipitate-free region gave the following composition: 98.9wt% Zn-0.3wt% Al-0.5wt% Cu- 0.3wt% Mg(198). The zinc and aluminium contents are thought to be reliable and show that the primary phase contained very little aluminium, but the copper and magnesium contents were too high because of the reasons discussed earlier.

The solid solubility of aluminium in zinc is very low at room temperature, therefore it was concluded that the excess aluminium had been removed by precipitation of an Al-rich phase from the supersaturated zinc matrix. A SADP diffraction pattern, taken from the η dendrites, showed that the matrix zone was $[11\bar{2}0]$ of hcp zinc and the subsidiary reflections were from fcc zones of the form $\langle 110 \rangle$. The c/a ratio of the hcp phase corresponds closely to that of zinc, and in view of the fact that chemical analyses showed very little aluminium in the matrix, a calibration factor was obtained from the zinc reflections which allowed the lattice parameter of the fcc phase to be determined as a = 0.404 nm. It was then demonstrated by this diffraction pattern that the precipitates were aluminium and that two families of the fcc α phase particles were present in the hcp η phase matrix, each of which had adopted a different variant of a single orientation relationship between the matrix.

At this stage it is worth while indicating the differences between the Mazak3 and the M3K alloy. As both the Mazak3 and the M3K alloys originated from the same ingots of Mazak3, one expects the outcome to be the same. The analyses shown in Table 11 confirmed that both alloys have the same chemical composition. Upon examination of their structure, the SEM micrographs showed that Mazak3 had an overall coarser structure than that of the M3K alloy. The average size of the primary zinc-rich η phase, found in the M3K, was almost 60% of that of the Mazak3 alloy.

The other difference between these two alloys was discovered during the TEM work on their eutectic morphology and, more specifically, the small dark particles enclosed within the α phase. These particles could not be identified in the case of Mazak3.

However, they were succesfully identified in the case of M3K. This incidence indicated that these dark particles were transitional phases and they were almost completely removed after five years of ageing at ambient temperature. In the M3K case, these phases were large enough to analyse quantitively by EDS using the STEM mode, and the results are shown in Table 12. The aluminium content of this matrix corresponded to the α'_t phase found previously in the quench-aged alloy (114) and this did not correspond to the equilibrium state of the α phase. The unknown phase had a large zinc content even above that of the β phase, which is presumed to be its precursor. Several attempts were made to obtain diffraction evidence for the structure of the transitional zinc-rich phase, but no separate diffraction reflections could be obtained.

6.2 Metallography of the ZA8 and ZA8K

The as cast structure of the alloys ZA8 and ZA8K are shown in SEM figures 58-60 and 75-80 respectively. The structure consisted of the primary β phase comprised of different sizes and shapes with an average size of 12 μm in the case of ZA8 and 6 μm in the case of ZA8K. Eutectic pools can also be seen surrounding the primary β particles. The general structure was similar to that of the M3 alloy, but the primary β particles replaced primary η particles and were more uniformly distributed. Figures 59-60 and 76-77 showed that as ZA8 is hypereutectic, β dendrites had decomposed into lamellar products in the central portion of the grains, surrounded by a matrix of irregular phases. In addition to the primary β, η phase particles with similar sizes and shapes to the primary β were observed, although less frequently. These η particles are believed to be of eutectic composition rejected from the highly supersaturated zinc-rich liquid below the eutectic temperature during rapid cooling of the castings. In some cases the eutectic η can be seen as haloes around the β dendrites, as shown in Figures 77, 78 and 79 taken at three different magnifications. The α haloes formed around the primary η in the M3 alloy were observed to be thinner than these eutectic η haloes as shown in Figure 65. It was first thought that this was due to the higher undercooling applied to ZA8 from the melt, since the casting temperature of ZA8 was theoretically higher than that of the M3 alloy. One can argue that in most cases the castings of M3K were cast at temperatures as high as those applied to the castings of ZA8K, to compensate for heat losses when transfering the molten metal from the furnace to the feeder of the die-cating machine. An alternative hypothesis for this phenomenon can be explained by the amount of aluminium present in the M3 and ZA8.

The TEM micrographs in Figures 81-82 show the general structure of the alloy ZA8K taken at two different magnifications. The structure consisted of the primary β (white) surrounded by pools of eutectic. Here the eutectic consists of more irregular and shorter aluminium lamellae than those found in the eutectic of the M3K alloy. Each ribbon of aluminium encloses a small dark particle of a different phase. These particles were either round or, occasionally, elongated, as shown in Figure 83, and were similar in all respects to those found in the M3K alloy. These dark spots were analysed by STEM and the results are shown in Table 13. Comparing the results of the analyses in Table 13 with similar analyses* conducted on the dark particles of the long term aged ZA8 alloy, the latter showed that these dark particles contained only 11% Al. The aluminium content seems to have dropped by almost 50% after long-term natural ageing at ambient temperature. There is no equilibrium phase in the Zn-Al-Cu system with these compositions, which confirms that these dark spots are transitional phases and it is believed that they might completely disappear with prolonged natural ageing at ambient temperature. In the case of Mazak3, it was not possible to identify such particles after five years of natural ageing, as they had virtually disappeared by then. The freshly made alloy M3K was a different case as these phases were easily identified because they were both numerous and large in size. Figure 85 shows a SADP of the aluminium-rich α phase in the eutectic region taken from an area marked 2 in Figure 83. The diffraction pattern had a beam direction of [110]. This diffraction pattern also had the symmetry of the fcc structure of the α phase. The lattice parameter calculated by using an internal calibration from the nearby zinc-reflection was found to be a little smaller than that of pure aluminium, as expected in the α region, since the lattice parameter of aluminium decreases in the α and β region with increasing zinc content. The SADP shown in Figure 86 was taken from the area marked 1 in Figure 83 from one of the dark particles embedded in the α constituent of the eutectic. The diffraction pattern had a beam direction of $[110]$ which confirmed that the dark phases were the fcc α'_m phase with smaller lattice parameters than the neighbouring α.

A number of SADP's were taken from the areas of precipitates in the zinc of the eutectic regions in Figures 84 and 87. One example of these diffraction patterns is shown in Figure 88 which corresponded to a beam direction of $[0\bar{1}11]$ of the hcp structure of η matrix, but failed to show any clear evidence of the presence of precipitate phases. Further SADP's investigations on these precipitates in Figure 87 have revealed a different diffraction pattern, shown in Figure 89. This time streaked reflections were observed on the diffraction pattern from $[1\bar{2}10]$ zones and the pattern indicated two sets of streaked reflections with the same symmetry deviated by 5°. In order to ensure clarity, however, only one set of reflections was indexed. The streak's reflection was found to correspond to the hcp ε-phase ($CuZn_4$) with the same $[1\bar{2}10]$ beam direction as the η matrix, but with $[0001]_\eta$ not-parallel to $[0001]_\varepsilon$. In order to carry out further examinations of these streaks in relation to the matrix, a stereographic projection was then established as shown in Figure 169. From this figure the projection of ε on $[0001]$ was rotated by an angle of 5° in the clockwise direction around $[0\bar{1}10]$ * and superimposed on a $[0001]$ standard projection of the zinc matrix (η). Similar proximities of planes in the stereographic projection are also observed in the diffraction pattern in Figure 89. To find a unique orientation relationship, two sets of these parallel planes were selected, ie $(0\bar{1}10)_\eta // (0\bar{1}10)_\varepsilon$ and $(\bar{2}112)_\eta // (\bar{2}112)_\varepsilon$. The precipitates were needle-like and were about 20-30 Å thick and 800 Å long parallel to $(2\bar{1}\bar{1}2)$ and $(2\bar{1}\bar{1}2)$ planes of zinc-matrix.

* *Co-Worker. M.DURMAN.*

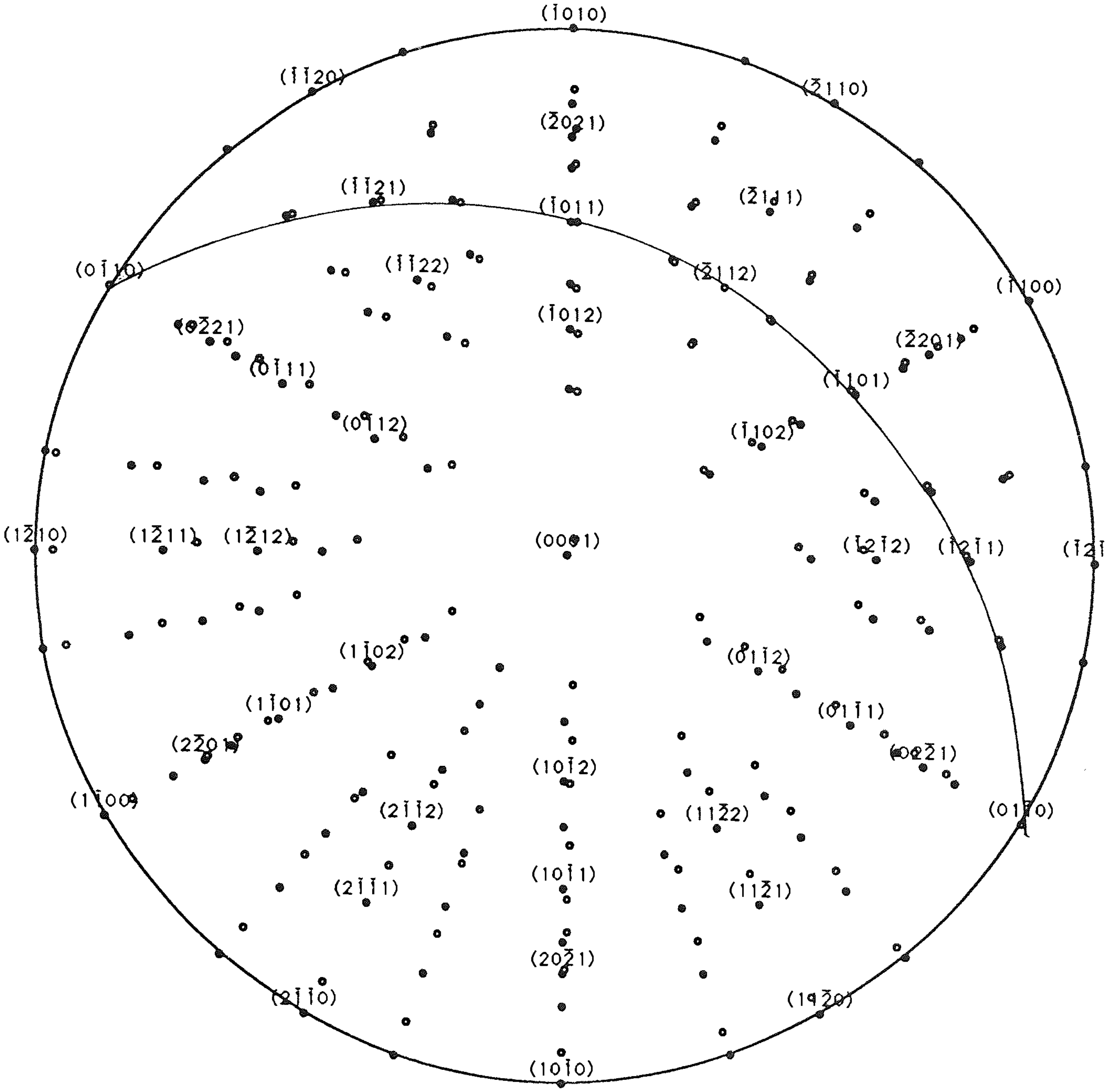

Figure 169. Stereographic projection of Zn and ε phases representing the orientation relationship between the two phases.

The diffraction pattern consisting of $[1\bar{2}10]$ zone revealed that the streak runs towards $(2\bar{1}\bar{1}7)$ and $(\bar{2}117)$ plane normal to the zinc-matrix. Regarding the formation of diffraction patterns in reciprocal space, if a crystal is thin in direction normal to the beam, streaks are expected in the diffraction pattern parallel to this direction, due to lower scattering intensity along this direction(199). Thus streaks observed in the diffraction pattern (Figure 89) indicated that the precipitates were needle-like with $(2\bar{1}\bar{1}7)$ and $(\bar{2}117)$ habits. Therefore, it should be expected that the ε-phase would form on a particular habit plane, along which the atomic planes facing each other across the matrix-precipitate interface would have very similar arrangements, ie coherent interface with minimum misfit. Returning to the stereographic projection in Figure 169, and upon examination of planes on the great circle, the $\langle 2\bar{1}\bar{1}3 \rangle$ zone indicates that the planes of both phases in the zone were parallel. The parallelism was achieved by rotating one crystal relative to the other away from a symmetrical orientation relationship, therefore, all other sets of planes were made non-parallel including the (0001) close-packed planes.

The decomposition of the primary β phase was firstly observed by the SEM micrographs in Figures 77-79. The primary β had decomposed specifically into well-formed lamellae near the edges, while regular lamellae tended to occupy the centre. In addition to that a coarse mixture of phases had also resulted from the decomposition of the primary β phase. In conjunction with the SEM, a more detailed study on the decomposition of the primary β was conducted on the TEM as shown in Figures 82 and 90. The primary β had decomposed into a final product in the form of $\alpha + \eta$ lamellae, granular η and a mixture of the same phases in the form of irregular particles as shown in Figure 90.

STEM analyses in Table 13 showed that both α and η lamellae from the decomposed β were generally in equilibrium, although some dark metastable particles (seen in Figure 90) formed within the α lamellae, were similar to the metastable α'seen within the eutectic α (seen in Figure 83). A comparison between those metastable phases was made by co-worker Durman. He found that the metastable phases found in the Al-rich α matrix had a higher aluminium content of about 22.7% than the α' found in the eutectic α. Furthermore, the copper content was lower by about 0.5% at 1.4%. This was also in accordance with the metastable extensions of the binary Zn-Al system, but in this case it was bounded by the extension of the ($\alpha + \alpha'$) region to low temperatures.

Thus, the metastable phase here was an analogue, not of the β phase but of the α' phase, due to the more aluminum-enriched nature of the primary particles than the eutectic β. This may also explain the lower copper content of the latter phase since the β phase dissolves more copper than the α phase at high temperatures (79).

Under equilibrium conditions β decomposes into η and α at above 275 °C. However, in this case the β undergoes two different transformations depending on its zinc-aluminium ratio. Upon rapid cooling, solidification firstly occurs with considerable undercooling followed by retention of the high temperature β phase to low temperatures at which decomposition takes place. At low temperatures the diffusion rates are very small and probably the cellular decomposition products would not be the same. In the case of the aluminium-rich cores of the primary β, it is suggested that a lamellar or sub-lamellar product of η and transitional alumimium-rich metastable α'_t was formed, due to the difficulty of reducing the zinc content of the aluminum-rich plates to that of α in one step . α'_t and α are crystallographically identical and differ only in chemical composition and thus lattice parameter and α'_t is known to persist for a substantial time on low temperature ageing (93-95). Furthermore, the η plates of the eutectic mixture would be very thin due to the fact that α'_t contains more zinc than α. Figures 82,83 and 90 show the products of the decomposed β, in which the α'_t is mostly transformed into α after the diffusion of zinc from the α'_t into η resulting in strings of elongated α particles in the middle of the aluminium-rich lamellae .

In addition, the same case applies to the β lamellae forming an integral part of the eutectic. Because of the higher zinc content of the β in this case, however, the metastable phase formed in the cellular decomposition reaction would be the lower aluminum metastable phase indicated by extension of the (α + β) phase field to lower temperatures, resulting in the decomposition of β into η plus another higher aluminium version of β, metastable at the transformation temperature .

There is evidence to suggest that such a diffusion mechanism can only apply to certain conditions and depends mainly upon the chemical composition of this alloy as well as upon the cooling rate involved. The copper-free M3 alloy did not show any signs of the α'_T in the eutectic, therefore the presence of copper acting in combination with the magnesium and the other alloying elements may be responsible for the stabilisation of the α'_T phase. Thus an alternative to the proposed (α + β) products as a first stage in the eutectic β decomposition in alloy ZA8 is simply another ($\eta + \alpha'_T$), where the composition of the α' is different from that formed from primary β due to the lower aluminum and increased copper contents of the eutectic β.

6.3 Metallography of the ZA.27 and ZA 27K Alloys

Unlike the M3 and the ZA8 alloys, the ZA27 has a higher aluminium and copper content. It is expected, therefore, that the ZA27 alloy will reveal a more complex multi-phase microstructure than the M3 and ZA8 alloys. The as-cast microstructure of ZA.27 and ZA.27K is shown at a low magnification on the SEM micrographs in Figures 61 and 91. The Figures revealed a fine dendritic structure formed in a mass of much smaller aluminium-rich particles and some pools of eutectic zinc.The average size of the α particles was about 14 μm in the case of ZA.27. In the case of ZA.27.K, the average size of the α particles was about 7 μm. Due to the very small volume of eutectic liquid, a regular eutectic such as that seen in M3 and ZA8 is not formed. Instead, a pool of eutectic zinc occupied the interdendritic spaces and the α phases joined the α phases from the decomposed β of the dendrites. From the SEM micrographs in Figures 62-65 and 92-94 of ZA27 and ZA27K respectively, it is clear that the solidification of this alloy began with the formation of Al-rich (α + α') dendrites, followed by the formation of much more Zn-rich β phase. The Zn-rich β phase formed around the primary dendrites through a peritectic reaction between the first formed α phase and residual liquid. Some cores had decomposed into coarse lamellar products but the majority decomposed into a very fine mixture of Zn-rich phases in an aluminium matrix. The β subsequently transformed eutectoidally into lamellae or irregular particles of α and η, with eutectic pools occupying the remaining interdendritic areas. Due to the similarity of their atomic number (Cu, Zn), it was not possible to differentiate the copper-rich precipitates from zinc by the atomic number contrast technique. However, the TEM micrograph in Figure 99 shows two distinct morphologies of the precipitation of the copper-rich ε-phase :-

a) Heterogeneous, high-density precipitate particles of the ε-phase similar to those found in both the eutectic zinc and the zinc from the decomposed β lamellae of the ZA8K alloy. Durman* found that the average copper content of these areas was about 6.3% in the ZA27 alloy. This indicates that copper was preferentially dissolved in the available η in both the eutectic matrix and the decomposed β.

b) Various size of irregularly distributed ε-particles, much larger than the precipitated form were also noticed in the interdendritic channels. Durman* studied the latter form of ε-phase in ZA27 and proved that those phases had the cph structure of the ε-phase and a composition of 84.2% Zn, 0.7% Al, 14.8% Cu. ZA27K was examined in this work and the results shown in Table 14 are in agreement with Durman. The close nature of these results suggests that the formation of these discrete ε-particles could have occurred in the copper-enriched liquid during the eutectic reaction. Figure 99 highlights the afore-mentioned complex structure of the ZA27K alloy. Here the α dendrites had decomposed into cellular precipitates, continuously decomposed matrix and large precipitates of a metastable phase. The lamellar structures seem to have developed from the interface of the large precipitates of the metastable phase, if the matrix had not already undergone any continuous reaction. The continuously decomposed matrix was very frequently seen surrounded by a coarse lamellar structure (Figure 99). Figure 95, taken at a high magnification, examined the continuously decomposed matrix found in Figure 99. From Figure 95, it is revealed that the equiaxed mixture of the phases was very fine. The results of the analyses (Table 14), which were carried out on the overall spinodal matrix (Figure 95 area 1) indicated that the spinodal matrix was from the first formed α-dendrites which are richer in aluminium. These results are in accordance with Durmans' results[*] carried out on the ZA27 alloy. The development of the two previously mentioned completely different morphologies must have been due to the real differences in composition of the cores of the α-dendrites to the β surfaces.

The metastable phases in the ZA27K alloy were found to be in much larger quantities and be larger in size than those in the ZA8K. This is probably due to the higher copper content in the ZA27K alloy compared with that of ZA8K.

There is a similarity between the eutectic α lamellae in Figure 99 to that of eutectic α found in Figure 83 in the ZA8K alloy. It was found that the eutectic α lamellae in ZA27K (Table 14 area 4) contained a metastable phase similar to α'_T found in ZA8K. The amount of zinc and copper found in the metastable phases of ZA27K was higher than that found in the ZA8K alloy.

The amount of copper in the ZA alloys plays an important role in the development and maintenance of the metastable phases. This can be proved by forming a comparison between the state of the metastable phases found in the naturally aged alloys, Mazak3, ZA8, ZA27 and the freshly made alloys M3K, ZA8K, ZA27K. The metastable phases seem to have disappeared in the case of Mazak3, but were found to be large in size and quantitiy in the M3K alloy. In the case of the 1% Cu (ZA8, ZA8K), the metastable phases found in the ZA8K were larger in size than those of ZA8. Furthermore, the ZA8K alloy was found to contain almost twice the amount of metastable phases than the ZA8. In the case of 2% Cu (ZA27, ZA27K), it seems that even after ageing the alloy for more than five years (ZA27) at ambient temperature, the metastable phases dropped only slightly in their aluminium content from 18.1% Al to

14.8% Al. Therefore, the copper, probably with the aid of magnesium, has influence in stabilizing the α'_T phases.

The decomposition morphology of the β phase found in the ZA27K alloy was similar in nature to that of the alloy ZA8K. The β had decomposed into lamellae products as shown in Figures 96 and 97. STEM analyses (Table 14) were carried out on the central portion of the aluminium lamellae (area 3, Figure 97). These analyses revealed a non-equilibrium composition of the α phase containing 26.1% Zn. This also confirms the evidence of the two-stage development of the lamellae structure. The SADP, shown in Figure 98 taken from one lamelar in Figure 97, provided a second confirmation that these lamellae are the aluminium α phase with a beam direction of [211] zone of the fcc structure.

6.4 Metallography of K1, K2 and K3

As mentioned earlier, these alloys were based on the ZA8K with variation of copper contents to study the effect of copper on the U.T.S, elongation and the fatigue strength. The microstructures of these alloys were only studied by the SEM. The SEM micrographs revealed that there was no structural difference between these alloys and the ZA8K. The reason for that was the fact that the atomic numbers of copper and zinc are very close and could not be differentiated by the power of the SEM. There was, however, some intermetallic particles seen in the case of the 2.0% Cu alloy (K3). These intermetallics were Cu Zn_4, and they were formed due to the excess copper which could not be completely dissolved in zinc.

* CO-Worker. M.DURMAN

6.5 Primary Size Variation

The alloys M3K, ZA8K and ZA27K have revealed a finer microstructure than that of alloys Mazak3, ZA8 and ZA27. The pressure die-castings of these experimental alloys should now be explained briefly. The cavity first fills with molten metal, turbulence and fluid flow ceases and solidification then proceeds under steady-state thermal conditions. When the molten metal enters the cavity through the gate in a high velocity stream, in a simple rectangular cavity, the stream strikes the face opposite the gate and flows back around the periphery of the cavity at high velocity. As more metal enters the cavity, it causes increased turbulence in the liquid metal already present. The growing dendrite nuclei are thus rotated violently within the cavity. A high degree of turbulence is experienced(200) in the cavity during the production of most modern commercial castings. The energy involved in stirring the metal during cavity fill can be as high as 20 kw for a 70 g casting. The effectiveness of the turbulence caused by the dissipation of the kinetic energy in the metal stream in influencing the microstructure depends on :

1) The effective length over which the stream from the gate has to travel before striking a wall (ls). The value of ls depends also on the number and types of turns in the flow path within the cavity.

2) The time lapse between the ends of cavity fill and the start of solidification.

Another important factor which might also contribute to the altering of the size of the primary phase, is the die-temperature. The lower the die temperature the smaller the primary size. It is also associated with the higher degree of casting integrity obtained with the higher die temperature, especially when the shear rate at the gate is low. This is based on experimental work conducted by Robinson and Murray(200).

In the case of the experimental alloys, the Mazak3, ZA8 and ZA27 were pressure die-cast as plates of 330 mm long and 90 mm wide with ribs and bosses. The M3K, ZA8K and ZA27K alloys, however, were produced as simple rectangular shapes, 120 mm long and 25 mm wide. The turbulence was, therefore, more severe in the shorter rectangular castings than in those of the long and wider plates. Furthermore, the ribs and bosses cause destruction to the turbulence flow.

It is not clear, however, if the prolonged ageing at ambient temperature has any coarsening effect on the microstructure.

6.6 Tensile Strength Properties of the Experimental Alloys

A study of the U.T.S, 0.2% Proof Stress and elongation to failure, which was conducted on M3K, ZA8K and ZA27K at temperatures of 20, 50 and 100°C, is revealed in Figures 122-124 respectively. The ZA27K revealed a superiority in its U.T.S values over the ZA8K and M3K alloys at all the above temperatures, as shown in Figure 122. The figure shows that at 20 °C, the ZA27K alloy had a U.T.S value of about 26% higher than that of ZA8K and 73% higher than that of the M3K alloy. At 50 °C, the U.T.S value of ZA27K was about 7% higher than that of ZA8K and 40% higher than that of M3K. At 100°C, the U.T.S value of ZA27K was also 14% higher than that of ZA8K and 53% higher than the M3K alloy. If the U.T.S value at 20°C is to be considered as standard, then it can be seen that at 50 °C this value was dropped by 12% in the case of M3K, 15% in the case of ZA8K and 29% in the case of ZA27K. At 100 °C, however, this value was dropped by 33% in the case of M3K, 35% in the case of ZA8K and 41% in the case of ZA27K.

The U.T.S values and 0.2% proof stress of the above alloys is directly proportional to their aluminium contents. The high strength nature of α and α' are responsible for the high tensile strength of the ZA27K alloy, as the structure of this alloy is dominated by the α and α' phases. The M3K structure is different to that of ZA27K. This structure is heterogeneous and is dominated by the low strength η phase. In addition, the eutectic nature of the M3K alloy is of low to medium strength. In the case of ZA8K, the tensile strength of this alloy was intermediate between the M3K and the ZA27K alloys. The structure of this alloy is similar to that of M3K, but is less heterogeneous and is dominated by the primary β phase which is of medium strength between the low strength of the η and the high strength α phases. The eutectic nature found in this alloy was also of medium strength.

The 0.2% proof stress of ZA27K was also revealed to be higher than that of ZA8K alloy and the M3K alloy at all the given temperatures (see Figure 123). Figure 124 shows the effect of temperature on the % elongation of alloys M3K, ZA8K and ZA27K. At 20 °C, the M3K alloy suffered an elongation of almost twice that of ZA8K and three times that of ZA27K. At 50 °C, the ZA8K and ZA27K alloys elongated 10% further than at 20°C, whilst the M3K alloy suffered a 100% increase compared to the elongation at 20 °C. At 100 °C, the ZA8K suffered an increase of 30% in elongation compared to the 20 °C result, whilst the ZA27K suffered an increase of 30%. The M3K alloy had suffered the most. Its elongation increased by 200% compared to that at 20 °C. This rapid increase in elongation in the M3K alloy is due to the fact that the primary η phase is very ductile even at room temperature. Similar experimental work was conducted(16) on Mazak3, ZA8 and ZA27 at higher temperatures. The work showed that at 160 and 165 °C, the properties of the alloys were virtually equal. The rate of increase in elongation of the ZA27 alloy was very slow below 100 °C, but it was found that at higher temperatures the rate of increase exhibited the expected characteristics of the superplasticity of the alloy. At higher temperatures the Mazak3 exhibited different characteristics to the ZA27. There was a rapid initial rise in elongation and this increase peaked between 150-200°C and decreased thereafter. The ZA8's elongation behaviour exhibited an elongation range between that of the ZA27 and Mazak3 alloys. It elongated in a way similar to that of ZA27 up to a temperature of 150 °C, and then peaked at about 200 °C. It then decreased in a likewise manner to that of Mazak3.

Tensile tests were also carried out on alloys K1, K2 and K3 which were based on the ZA8K alloy, but which have different copper contents of 0.0%, 0.5% and 2.0% respectively. These alloys were produced in order to study the effect of copper on the mechanical properties of the ZA8K alloy. From the results in Figure 125, it can be seen that the U.T.S value of these alloys is directly proportional to their copper contents. If the U.T.S value of the free copper (K1) alloy is taken as a standard value, then upon adding 0.5% Cu (K2), the U.T.S value increased by 5.0%. When 1.0% Cu (ZA8K) was added, the U.T.S value increased by 6.5%. An increase of 11.3% was noticed when the alloy contained 2.0% Cu (K3). The ratio of increase in the U.T.S is insignificant compared to the ratio of increase in copper. A further increase in copper to the K3 alloy might cause a very small increase in the U.T.S value. The increase of copper content in the K3 alloy can only be effective to a certain extent and any further increase could lead to negative effects. The solubility of copper in zinc is very limited at low temperatures, and the remaining copper might not be soluble and could form into intermetallic compounds ($CuZn_4$), as shown in the case of the K3 alloy in Figure 106. The content of copper in the ZA alloys can only be chosen to a compromised level between the possible increase in U.T.S and the hardness and decrease in ductility. This is, however, true as can be seen in Figures 125 and 127.

6.7 Fatigue of The Experimental Alloys

The fatigue-life data, or the S/N curves, for all the alloys involved in this work have now been established and are shown in Figures 109-121. Upon examination of these curves, the effect of temperature on the fatigue-life of these alloys can be determined. Furthermore, the superiority of the ZA8K fatigue life over alloys ZA27K and M3K is manifest. In order to examine the effect of temperature on the fatigue life of these alloys, the test results for each alloy were superimposed onto a single graph, as shown in Figures 170-172

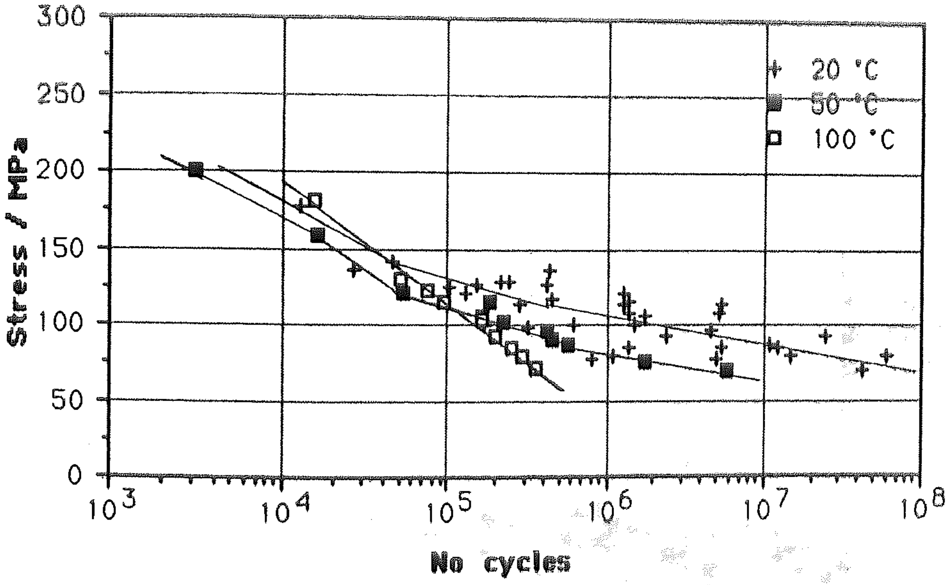

Figure 170. S/N Curves of M3K at Different Temperatures.

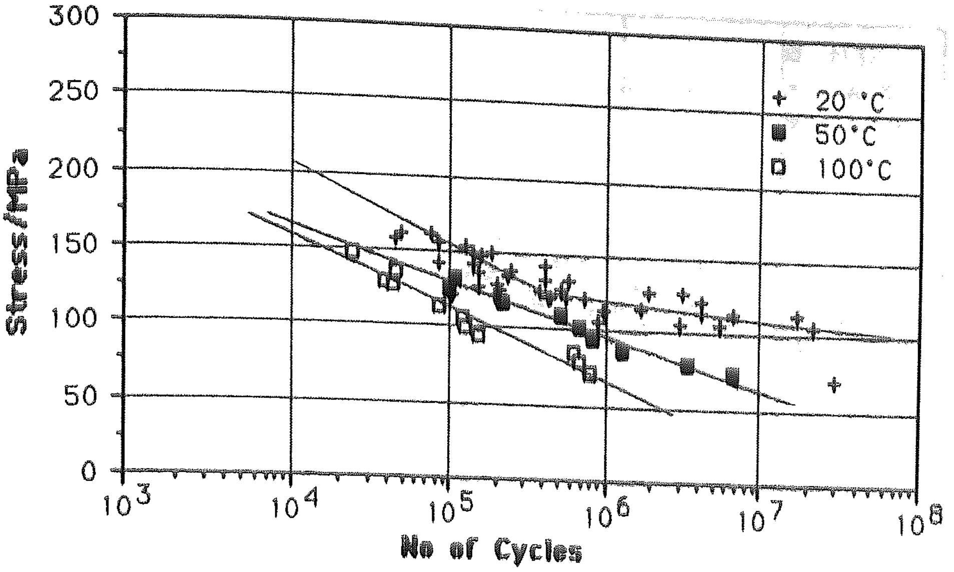

Figure 171. S/N Curves of Alloy ZA8K at Different Temperatures

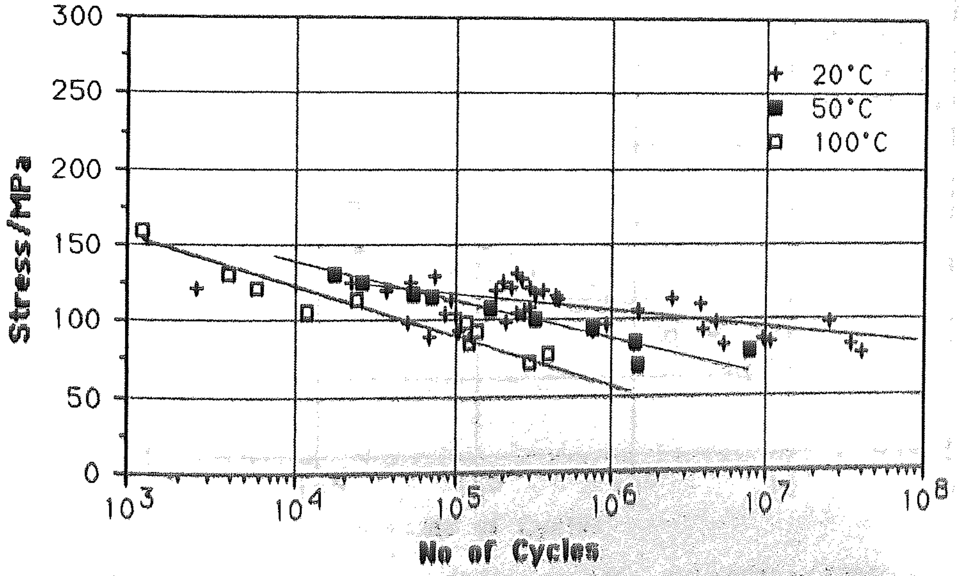

Figure 172. S/N Curves of Alloy ZA27K at Different Temperatures

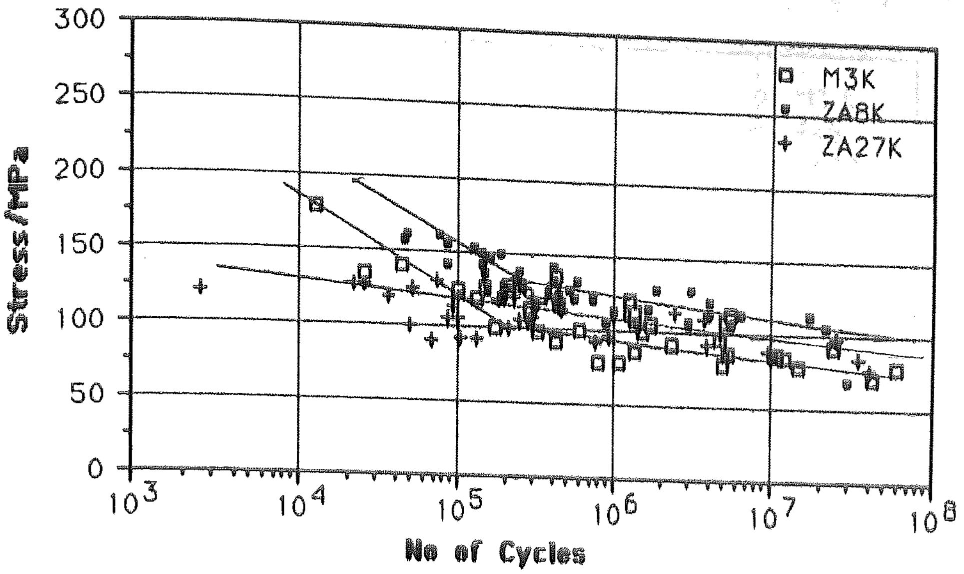

Figure 173 S/N Curves of Alloy M3K, ZA8K and ZA27K at 20°C.

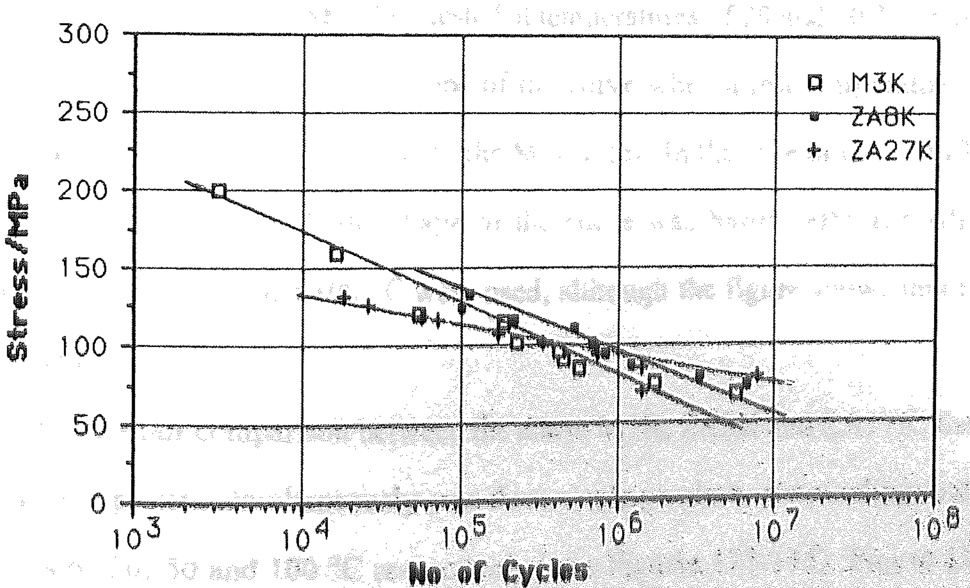

Figure 174 S/N Curves of M3K, ZA8K and ZA27K at 50°C.

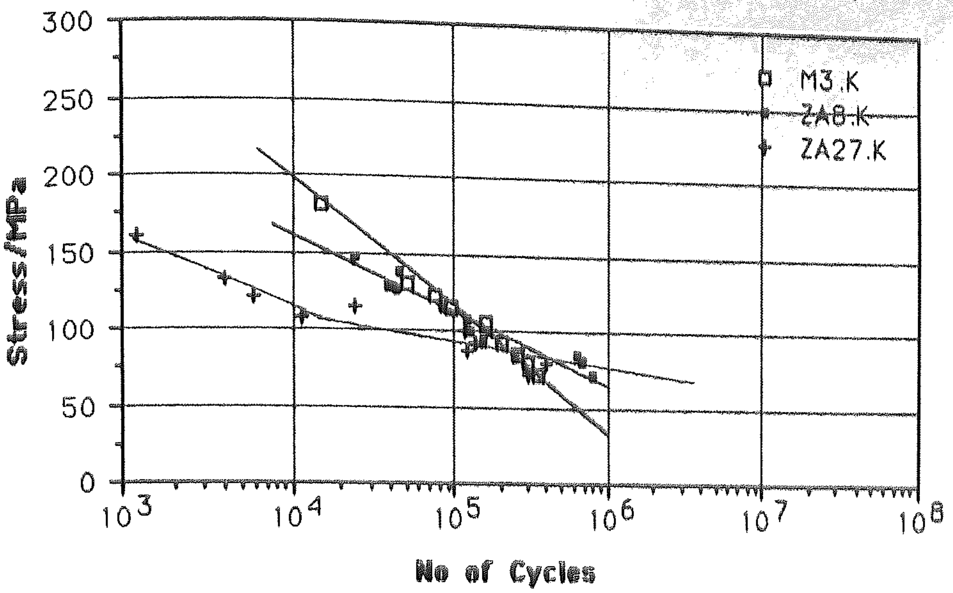

Figure175. S/N Curves of alloy M3K, ZA8K and ZA27K at 100°C.

Figures 170 and 171 show that there is a negligible difference in the shape of the fatigue curves of M3K and ZA8K when tested at temperatures of 20 and 50 °C. There was, however, a sharp change in the slope of the curve when a test temperature of 100 °C was used , especially in the case of the M3K alloy. In the case of the ZA27K alloy, as shown in Figure 172, the shape of the curve was hardly affected when temperatures of 50 and even a 100 °C were used, although the figure shows that the fatigue life had dropped.

In order to make a fair comparison between the alloys M3K, ZA8K and ZA27K, their S/N curves were plotted simultaneously onto three single graphs corresponding to the temperatures of 20, 50 and 100 °C respectively (see Figures 173-175). Figure 173 shows the 20 °C results. From this figure, the ZA8K alloy revealed a superiority over the M3K and the ZA27K alloys, with an average fatigue life that is about 20% higher than the M3K alloy and 25% higher than the ZA27K alloy. It is clear from this figure that in the range of 10^5 cycles, the ZA8K alloy clearly showed that it could withstand much higher stresses than the M3K and ZA27K alloys. Even at lower stresses the ZA8K revealed that it can achieve a longer fatigue life than the M3K and ZA27K alloys. When 50 °C tests were applied, as shown in Figure 174, the ZA8K alloy still revealed a higher fatigue life than the M3K and ZA27K alloys. This time the fatigue life of ZA8K was averaged to be about 15% higher than ZA27K and 25% higher than M3K. The fatigue life of M3K was exceeded by that of ZA27K.

In Figure 175, when the alloys were tested at 100 °C, it is shown that the effect of temperature is very clear. The ZA8K alloy still showed a higher fatigue life than ZA27K. The M3K alloy, however, had suffered the most and its resistance to fatigue at that temperature was very low, as revealed in Figure 175. The ZA8K and ZA27K alloys had offered a reasonable resistance at that temperature.

At the 20 °C temperature, the fatigue life of these alloys (Figure 173) had exceeded 10^7 cycles, whilst at 50 °C (Figure 174), the fatigue life of these alloys ended just before 10^7 cycles. At 100 °C, however, the fatigue life of the M3K and ZA27K alloys had reached almost 500 K cycles. The fatigue life of ZA8K, however, exceeded this and rose to almost 10^6 cycles. If lower stresses were used at 50 and 100 °C, the fatigue life of these alloys will doubtless increase, but this would be of no practical use. The idea, however, was to conduct the fatigue tests at similar ranges of reasonable stresses to enable there to be a fair comparison between the fatigue lives of the experimental alloys.

Figure 121 shows the S/N curves of the alloys K1, K2 and K3 in relation to the ZA8K alloy. The tests were carried out at 20 °C using a reduced range of stresses. The copper free K1 alloy revealed a low fatigue strength and the 0.5%Cu (K2) alloy had a longer fatigue life than that of K1. The 2.0%Cu (K3) offered a higher fatigue strength than K1 and K2. Alloy K3 enjoyed a potential fatigue strength even higher than ZA8K in some cases.

Furthermore, the freshly made alloys M3K, ZA8K and ZA27K showed a higher fatigue strength than the aged alloys Mazak3, ZA8 and ZA27 respectively.

As there were merely a limited number of samples from the alloys Mazak3, ZA8 and

ZA27, these samples were only fatigue tested at 20 °C. The S/N curves of these commercial alloys are shown in Figures 109, 113 and 117. A fair comparison was made to reveal that the ZA8 alloy had the highest fatigue strength, followed by Mazak3 and then the ZA27 alloy, which revealed the least fatigue resistance.

6.8 Correlation of Fatigue Data

The fatigue-life, as defined by the S/N curve, depends on two variables, namely stress-range and temperature. The alternating frequency and the R ratio were fixed throughout all the fatigue tests. In order to establish a formula to fit the fatigue data from the experimental results, one variable, referring to stress will now be considered. The temperature for the purpose of this formula will remain constant. Multiple regression analyses were conducted using a Statwork programme on the Macintosh computer. The programme assumes a model which can be expressed as :

$$Y_i = a_1 X_{1i} + a_2 X_{2i} + a_3 X_{3i} + \text{----} + a_k X_{ki} + b + \text{error}$$

The dependent variable involved in this work was the number of cycles to failure. The independent variables were the stress in MPa and absolute temperature in Kelvin. In order to obtain a greater degree of accuracy, two more independent variables were supplied to the computer. These were the inverse of the stress (σ^{-1}) and the inverse of the temperature (T^{-1}).

The first set of correlations corresponding to constant temperatures are shown in Table 18. In this case the independent variables were stress and the inverse of stress (MPa). The second set of correlations are shown in Table 19. Here the formula includes both the independent variables stress and temperature, and their inverses. The number of cycles in this formula can be predicted at any given stress and temperature.

The equations in Tabe 18 offered a good correlation except for that of the alloy ZA27K at 20 °C. In this case the coefficient of determination was lower than 0.5. The coefficient of correlation was also low and the standard error of estimates was very high. The prediction formula is, therefore invalid in this case, but it can be altered by dropping some of the unreasonable results on the S/N curve. The difficulty in the prediction of the ZA27K alloy at 20 °C can be related to the fact that some samples had a high degree of porosity and failed unexpectedly. Furthermore, Table 18 shows, that at temperatures of 50 and 100 °C, the correlated data nearly matched the actual data. It must be noted, however, that the fatigue tests were conducted on fewer samples at these temperatures than at 20 °C. A lower amount of data reduces the risk of error and deviation which will then give higher coefficients of determinations and correlations. Table 19 shows the correlated prediction at any given temperature. The equations show a good degree of accuracy. Here the analyses were conducted on a combination of data and contained a ratio of 4 - 1 - 1 from the 20, 50 and 100 °C tests respectively. The accuracy cannot be guaranteed as the alloys are heterogeneous and the samples produced by pressure die-casting methods have various degrees of porosity.

6.9 Fractography of the ZA Alloys

The fatigue behaviour of the experimental alloys is directly related to their strength, toughness and microstructure. The experimental results showed that the ZA27K alloy had a much higher U.T.S value than those of M3K and ZA8K alloys. The ZA8K alloy had a higher fatigue strength than M3K and ZA27K alloys. The M3K alloy had a slightly higher fatigue resistance than the ZA27K alloy. It was expected that the ZA27K should have a higher fatigue strength than ZA8K and M3K. The ratio between the fatigue strength and the tensile strength of the experimental alloys was determined and shown in Table 20. This ratio is acceptable, except for the case of ZA27 and ZA27K alloys, as their ratios were too small and unconvincing. This phenomenon lead to further examinations of factors which might influence the fatigue strength. These factors are, the test and environmental conditions, the specimens' conditions and microstructural and chemical compositions.

At this point it is worth mentioning that the tests and environmental conditions were fixed. All the above-mentioned factors indicated that the ZA27K alloy should have a higher fatigue strength than the rest of the experimental alloys, except for the specimens' conditions. The castings procedure of these alloys was carried out with painstaking care and consideration. The SEM micrographs of both the microstructure and the fractured topography revealed micropores which could not be detected by the X-ray radiographs. All the pressure die-cast experimental alloys were heterogeneous and contained porosity, with the exception of the ZA27K alloy which contained, on average, a lot more porosity than the rest of the alloys. The large number of pores found in the ZA27K alloy were the results of the shrinkage mechanism. The high aluminium content of ZA27K was responsible for the shrinkage, due to the high freezing range between aluminium and zinc.

The pressure die-cast experimental alloys are heterogeneous with a large number of pores. After examining their fractography, there was no evidence of any signs of crack nucleation. the cracks started from internal defects, but this is not actually a nucleation process because the defects are effectively embryo cracks. Therefore, it is possible that only the crack propagation mechanism was responsible for the overall failure of the experimental alloys.

6.9.1 Effect of Temperature

The relatively high cooling rate resulting in the pressure die-casting of the zinc alloys is known to produce non-equilibrium phases which transform gradually to more stable phases by ageing at ambient temperature(17). This results in the reduction of mechanical properties as time elapses, as in the case of the Mazak3, ZA8 and ZA27 alloys in relation to the freshly made alloys M3K, ZA8K and ZA27K. By increasing the exposure temperature, the general kinetics of ageing become more vulnerable, thereby accelerating the process.

At ambient temperature, zinc is approximately 0.4 of its melting point on the absolute scale (Kelvin). At 100 °C it is at 0.5 of its melting point. It is not surprising, therefore, to see the gradual decrease in tensile and fatigue strengths with increasing temperature. This is clearly related to high atomic mobility in the experimental ZA alloys.

6.9.2 Plastic Deformation

Plastic deformation is generally temperature dependent ; the higher the temperature, the easier the plastic deformation. At low temperature, the prevailing mechanism of fracture is brittle fracture. At high temperature, the fatigue process can be combined with creep and with enhanced diffusion. Zinc is by far the major content of the experimental alloys and varies from 72% in the ZA27K alloy to 96% in the M3K alloy. Zinc has an hcp structure with a limited number of slip systems which restrict its ductility. In the hcp structure the basal plane [0001] is the closest packed plane and is the common slip plane for hcp metals with a high c/a ratio, such as zinc. It was often observed that cracks nucleated in particular grains, whilst other grains appeared to have suffered no damage at all. This may be due to the difference in crystal orientation and the constraining effects of surrounding grains. Therefore, the fatigue damage varies from one place to another in the specimens. Fatigue striations could not be observed in the fracture topography of the experimental alloys, due to their brittle nature. This argument is in agreement with Forsyth(132), who stated that fatigue striations are only dominant in ductile metals and alloys.

The limited number of slip systems and the absence of striations in the fractured surfaces of the experimental alloys, can rule out the possibility of plastic deformation by slip dislocation. The other alternative plastic deformation is the twinning dislocation. Twinning is unavoidable in hcp structures due to the limited number of slip systems. Twinning occurs during tension tests and can be heard forming with a click or load report (similar to the "tin cry"). Further evidence of twinning in the experimental alloys was obtained. Firstly, the tensile tests showed the occurrence of serrations in the stress/strain curve. Secondly, twins were noticed on the fractured topography of the alloys. In the twinning process, part of the atomic lattice is deformed so that it forms a mirror image of the undeformed lattice next to it, as shown in Figure.176. The crystallographic plane of symmetry between the undeformed and deformed parts of the metal is called the twinning plane. Twinning, like slip occurs in a specific direction called the twinning direction. However, in slip the atoms on one side of the slip plane all move equal distances, whereas in twinning the atoms move distances proportional to their distance from the twinning plane, as shown in Figure 176. Although twinning only involves a small fraction of the total volume of the ZA alloys crystals (13.0%)(201), the important role of twinning in plastic deformation comes not from the strain produced by the twinning, but from the fact that orientation changes resulting from twinning may place new slip systems in favourable orientation with respect to the stress axis, so that additional slip can take place.

The fractured ZA alloys could have possibly gone through three stages before failure.

1) Plastic deformation concentrates dislocations along planes at obstacles.

2) Shear stress builds up in planes where dislocations are blocked and as a result microcracks are nucleated.

3) Further stress propagates the microcracks, and stored elastic strain energy may also contribute to the propagations of the cracks.

It is known that the grain size is a relevant factor influencing the fatigue and tensile strengths. Indeed, the smaller the grain size, the higher the strength at a given temperature. The grain sizes of the experimental alloys were measured and the results showed that, the average grain size was about 30 μm for M3K, 30 μm for ZA8K and 15 μm for ZA27K.

Alloy at Temperature°C	Formulas Obtained From Multiple Regression Analyses	C . D	C . C	S . E . E	D-W. Stat
M3K at 20 °C	$\ln N = 19.715 - 0.060\,\sigma + 77.765/\sigma \pm 1.27299$	0.61845	0.78642	1.27299	2.58069
M3K at 50 °C	$\ln N = 9.6570 - 0.020\,\sigma + 486.635/\sigma \pm 0.37104$	0.97799	0.98894	0.37104	2.63128
M3K at 100 °C	$\ln N = 15.174 - 0.031\,\sigma + 10.543/\sigma \pm 0.14350$	0.98262	0.99127	0.14350	1.84616
ZA8K at 20 °C	$\ln N = 18.355 - 0.057\,\sigma + 265.316/\sigma \pm 1.004$	0.666	0.816	1.004	2.143
ZA8K at 50 °C	$\ln N = 14.868 - 0.043\,\sigma + 286.676/\sigma \pm 0.326$	0.962	0.981	0.326	2.149
ZA8K at 100 °C	$\ln N = 12.970 - 0.030\,\sigma + 207.293/\sigma \pm 0.348$	0.937	0.968	0.348	2.516
ZA27K at 20 °C	$\ln N = 9.1080 - 0.026\,\sigma + 701.677/\sigma \pm 1.717$	0.402	0.634	1.717	1.854
ZA27K at 50 °C	$\ln N = 35.826 - 0.160\,\sigma + 678.544/\sigma \pm 0.612$	0.927	0.963	0.612	3.126
ZA27K at 100 °C	$\ln N = 12.213 - 0.045\,\sigma + 297.642/\sigma \pm 0.625$	0.924	0.961	0.625	2.811

Where N is Number of Cycles to Failure. σ is Peak Stress (MPa)
C.D is Coeffecient of Determination C.C is Coeffecient of Correlation
S.E.E is Standard Error of Estimates D-W.Stat is Durbin-Watson Statistic

Table 18 Fatigue-Life Prediction of The Experimental Alloys at Different Temperatures.

Alloy at any Temperature	Formula Obtained From Multiple Regression Analysis	C . D	C . C	S . E . E	D-W. Stat
M3K	$\text{Ln } N = 23.6294 - 0.017\, T\,(°K) + \frac{34.56}{T\,(°K)} - 0.061\,\sigma + \frac{72.362}{\sigma} \pm 0.882$	0.730	0.855	1.126	2.350
ZA8K	$\text{Ln } N = 23.6294 - 0.017\, T\,(°K) + \frac{34.56}{T\,(°K)} - 0.061\,\sigma + \frac{72.362}{\sigma} \pm 0.882$	0.738	0.859	0.882	1.884
ZA27K	$\text{Ln } N = 26.85636 - 0.038\, T\,(°K) + \frac{6.451}{T\,(°K)} - 0.053\,\sigma + \frac{340.496}{\sigma} \pm 1.469$	0.611	0.782	1.469	1.890

Where N...Number of Cycles to Failure, T (°K)...Temperature in Kelvin, σ...Stress in MPa
C.D is Coeffecient of Determination C.C is Coeffecient of Correlation
S.E.E is Standard Error of Estimates D-W.Stat is Durbin-Watson Statistic

Table 19 Fatigue Life Prediction of the Experimental Alloys at any Given Temperature.

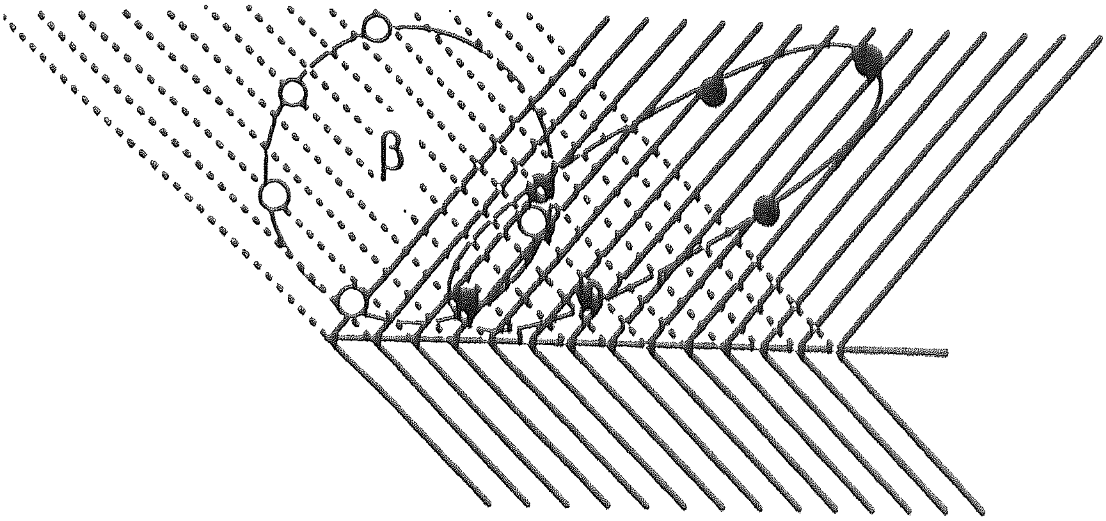

Figure 176. Schematical Drawing for Twinning Mechanism. Where, small white circles represents situation before twinning Dark small circles represents the new location after twinning.

Alloy	Fatigue Strength (MPa at 10^7 Cycles)	U.T.S (MPa)	Fatigue Strength ------------------- Tensile Strength
Mazak 3	85	270	0.32
ZA8	100	315	0.32
ZA27	85	420	0.20
M3 K	90	240	0.38
ZA8 K	115	330	0.35
ZA27 K	95	415	0.23
K 1	75	310	0.24
K 2	92	325	0.28
K 3	100	345	0.29

Table 20. The Relationship Between Fatigue Strength and Tensile Strength of the Experimental Alloys at 20 °C.

6.9.3 Fractography of the M3K Alloy

The M3K alloy has a simple structure consisting mainly of primary η particles surrounded by eutectic matrix. The structure of this alloy was heterogeneous and consisted of a considerable amount of porosity distributed throughout the structure. The alloy revealed reasonable fatigue and tensile strengths at room temperature, but it failed dramatically at a higher temperatures of 50 °C and fared even worse at 100 °C. The reason for this occurrence is probably due to the amount of η occupying the majority of the structure. The η phase is very weak and has a low strength, therefore it offered a small resistance to cracks, whilst the majority of the resistance was given by the low to medium strength eutectic.

Generally fatigue fracture leaves two distinct types of surface areas that can be recognized, these are :

1) A smooth surface region due to propagation action of the fine cracks across the section.

2) A rough surface area which is formed by the fracture when the load becomes too high for the remaining cross section.

In the case of the M3K alloy, the first type could be seen occupying a small region of the fracture. It is possible however, that cracks propagated for a short distance before it went to the final ductile fracture. Therefore, the fatigue life of the M3K alloy depended on the time required to propagate the cracks from the pre-existing pores for a significantly short distance. No significant difference can be seen between the fatigue fractured surface in Figure 128 and that of Figure 129. The failure in both cases was caused by surface pores. Figures 130-133 show a different kind of failure. In this case the pores responsible were seen in the sample's interior. In all the above-mentioned figures, there is evidence of plastic deformation in the form of deformed η particles. Figures 130-133, also show that the cracks followed a transgranular path through the sample. This was also revealed in the cross-section in Figure 134. Here the pore had developed whiskers parallel to the fractured surface. A similar case was also seen in Figure 135, where microcracks propagated parallel to the fractured surface. There seems to be no difference in the manner of propagation between samples subjected to low or high stress. When fatigue tests involved a high temperature of 100 °C, severe damage was caused to the structure, as shown in Figures 136 and 137 taken at two different magnifications. The figures show a very rough ductile fracture which occurred due to the opening of the pores. Furthermore the primary η particles were elongated.

The tensile fractured surfaces in Figures 138 and 139 are somehow similar to those caused by fatigue fracture. The pores developed into cracks and went through the structure leaving a cleavage and rough ductile fracture. The cross-section of the tensile fractured sample, shown in Figure 140, revealed the occurrence of the same kind of damage to the η particles observed in Figure 137.

6.9.4 Fractography of the ZA8K Alloy

The structure of the ZA8K alloy was similar to that of the M3K alloy, but the primary in this case was the β particles occupying the majority of the structure and surrounded by a eutectic matrix. Here the structure was a modification of that of M3K because it was less heterogeneous and it contained fewer voids.

The fatigue fractured surface in Figure 141 was different to that of M3K (Fig,128,129). In this case it seems that the sample was either free of pores or the pores were too small and scattered. Two distinct types of surface areas can be seen in Figure 141: 1) a smooth surface region due to the smooth propagation of the cracks across the section. 2) a rough surface area (ductile) which is formed by the fracture when the load becomes too high for the remaining cross-section. Although area 1 was comparatively small, it at least indicated that in the absence of voids or pores, the precurser events would be located at regions where the local geometry of grain type and orientation was such as to initiate the weakening effect. In this case the weakening was located at the surface of the specimen. With the presence of pores, cracks were propagated from the pore, as shown in Figure 142. In this occasion, the fracture topography was similar to that of M3K. The pore in Figure 142 was studied at a higher magnification and is shown in Figure 143. This figure reveals evidence of the embryo cracks in the deep pore. These cracks propagated to meet the medium strength eutectic which allowed the cracks to propagate for a reasonable distance until the remainder of the cross section could not stand any further loading. The rest of the cross section failed, therefore, under ductile fracture which peeled off the layers of the eutectic. The fracture topography, seen in Figures 144 and 145 taken at two different magnifications, was similar to those seen in the fractured surfaces of the M3K alloy. The figures show a disturbed structure due to the deformation on the voids' edges near the middle of the sample. As in the case of M3K, twinning may have contributed to a few ductile areas. These ductile sections are seen as white areas, as in Figure 145b. Twinning favours higher stresses as shown in Figures 146 and 147 taken at two different magnifications. The figures show a twinning effect on the β particles. The propagation of the cracks adopted a transgranular manner through the structure of the sample. No difference was observed between fractured samples at low or high stresses. The cross-section shown in Figure 148 was taken from a fatigued, but unfailed sample. The sample was fatigue tested up to 30 m cycles. The Figure shows that the pores started to link together by means of microcracks developing from each pore and extending towards a neighbouring pore. If the fatigue test was left for a longer period, it is possible that these cracks could have been responsible for the failure. Further proof to this phenomenon can be seen in Figure 149. In this case the cracks have completed the linkage between the pores and have caused failure. Sometimes cracks propagate from both sides of the pores in a whisker-like shape parallel to the fractured surface, as shown in Figure 150. This occurrence, however, depends on the geometry of the pore. The same case was also seen in the fractured surfaces of the M3K alloy.

The 100 °C fatigued fractured sample is shown in Figures 151 and 152 taken at two different magnifications. This sample lasted more than the M3K sample which was subjected to the same conditions. Unlike the η phase, the β phase has a higher strength and did not elongate. The figure also shows that the major contribution to failure was the rapidly-formed cracks which developed from the pores.

As mentioned in the previous chapter, the gas pores were found to have formed on the zinc-rich η in both the M3K and the ZA8K alloys. It can be concluded, therefore, that the zinc-rich η was responsible for the failure of these alloys. It must be born in mind, however, that the ZA8K alloy was less heterogeneous and contained less pores than the M3K. Plus the fact that the ZA8K alloy contained less η dendrites than that of the M3K. The fatigue and tensile strengths of the ZA8K were derived from its primary β phase occupying most of its structure.

There was no observable difference between the tensile fracture and the fatigue fracture of the ZA8K alloy. The tensile fracture was also due to a transgranular propagation caused by twinning dislocation. Figure 155, shows a cross-section of the tensile fractured ZA8K sample. It seems that the microcracks developed parallel to the nearest stress concentrated areas. The difference between this fracture and that of the M3K tensile fracture lies in the fact that the primary β particles and the eutectic of ZA8K have a higher strength than that of M3K. This strength enables the tension force to be resisted giving the microcracks chance to propagate through.

6.9.5 Fractography of the ZA27K Alloy

The ZA27K revealed a complex heterogeneous structure consisting of α' dendrites surrounded by the aluminium-rich β and the eutectic zinc η. The ZA27 and ZA27K alloys revealed a much higher tensile strength, but a lower fatigue strength than the experimental alloys . The average number of pores found in the ZA27K structure was much higher than in the rest of the experimental alloys, and most were irregular shrinkage cavities. The alloy also contained a higher aluminium content than the other alloys. The shrinkage was due to the high freezing range of this alloy. The large number of pores prevented the opportunity for any precursor events to be allocated. The fatigue failure of this alloy was purely due to the large number of voids and it can be noted that the plastic deformation and cracks are concentrated around the pores. If the ZA27K alloy contained fewer voids, or as many voids as found in the ZA8K alloy, then the ZA27K alloy should have a higher fatigue strength than that of ZA8K. This hypothesis was checked by fatigue testing specimens produced by squeeze casting(pore free) both the ZA8 and the ZA27 alloys. The results were as expected. The ZA27 alloy showed a higher fatigue strength than that of ZA8.

From the fracture topography, no evidence of crack initiation can be seen in the ZA27K alloy, as the internal defects are effectively embryo cracks and the failure depended on the linkage of cracks. Cracks were seen to have advanced from a pore or shrinkage. This was seen in Figure 156 at low magnification. When Figure 156 was examined at higher magnification in Figure 157, smaller cracks were seen developing from small pores and linked up together. The Figure also showed that, as in the case of M3K and ZA8K, the ZA27K fractured surface shown in Figure 156 revealed that cracks propagated from pores or shrinkages and advanced to link up with other cracks. This stage only covered a small area of the sample before the final ductile fracture. At higher magnification as shown in Figure 157, tiny cracks were seen to link up together to meet the major cracks advancing from large pores or shrinkages. The direction of these cracks is random and did not follow any standard direction. The directions of these cracks was monopolised by the resultant of the applied stress and the stress concentrations (stress raisers) and directions. The cracks propagated transgranularly through the structure.

At higher stresses, the damage was severe and resulted in the formation of large cleavages. This is shown in Figure 158, the Figure also shows large shrinkage with cracks propagated from their edges to link with neighbouring shrinkages and pores. At lower stresses (high cycles), it was much easier to identify and to follow the directions of the cracks through the first stage of propagation. In Figure 159 and 160, at two different magnifications, it was very easy to observe the cracks and their origins (pores). Here it is clear that the major cracks were developed from a pore and then formed linkage with other cracks from other pores and shrinkages. In the first stage of crack propagation, the cleavages caused by the applied stress were very small. In Figure 160 at higher magnification, it showed that the cracks followed the shortest easiest path depending on the orientation of the stress concentration areas. The advancing cracks did not differentiate between hard or soft areas. Here the Figure showed that the cracks had to go through the high strength α particle to meet up with the nearest advancing crack. In some cases the cracks went through the interface between the hard and soft phases (α and η). The white cusps seen in the Figure are the aluminium-rich former β dendrites.

The fatigue life of the ZA27K alloy depended on the time and the stress needed to form linkage between the voids (pores and shrinkages). If the stress was high, the time needed was short. Examples of these cases are shown in Figures 161-163. In the case of Figure 161 at low stress, obviously the time needed to form linkage was long and the test had to be stopped after 30 m cycles. The Figure shows that there were some signs of propagations to form linkage between the pores. Figure 162 showed a fractured sample tested at medium stress, the time needed to form linkage was adequate at that stress. When high stress was used, as in Figure 163, the sample failed in a short time under the severe tensile force. When elevated temperature was involved, the parameters have then changed. Here the variable to form linkage became stress, temperature and time. Dislocation was easier with temperature, even when using what was considered to be a low stress at 20 °C. This stress became too high as far as the temperature was concerned. There might have been some phase transformation at that temperature, but the SEM micrographs could not identify them. Therefore, basing this argument upon what was seen in the SEM micrographs, it was not possible to differentiate between fractured surfaces at low temperature (Figure 162) and that of high temperature (Figure 164). Both Figures showed that failure was caused by the linkage between the pores.

The tensile fracture surfaces were a mirror image to those of fatigue fractures. Comparing Figures 166 and 157, no significant difference can be seen. The two fractures were based on the linkage between the pores or shrinkages. The cross-sections taken from tensile fracture showed no difference to that of fatigue fracture. This can be seen when comparing Figure 168 to any cross-section taken from a fatigue fractured sample of ZA27K.

CHAPTER 7

7.0 CONCLUSION

1) The tensile and fatigue strengths of alloys M3K, ZA8K and ZA27K were slightly higher than the commercial alloys Mazak3, ZA8 and ZA27 respectively. The reasons for such phenomenon are:

a) The commercial alloys (Mazak3, ZA8 and ZA27) were subjected to room temperature ageing for more than 5 years, hence losing some of their mechanical properties (Transformed into equilibrium state).

b) The casting parameters such as castings geometry and size, the die temperature and cooling rates were different. Therefore, the M3K, ZA8K and ZA27K alloys had a finer structure than the Mazak3, ZA8 and ZA27 respectively.

2) The fatigue life curves (S/N) of the experimental alloys revealed no fatigue limit, even though, as it might seem from the S/N curves, there could be. To achieve this it would be necessary to carry out prolonged fatigue tests over several months at very low stresses, and this would not be practical.

3) The ZA27 and ZA27K offered much higher tensile strengths than the ZA8, ZA8K and Mazak3 and M3K at all the given temperatures. Therefore the U.T.S value was directly proportional to the aluminium content of these alloys.

4) The ZA8 and ZA8K alloys had a higher fatigue strenth than the ZA27, ZA27K, Mazak3 and M3K alloys. It was expected, however, that the ZA27 and ZA27K should have the highest fatigue strengths, but the only set back was that the ZA27 and ZA27K had a much higher number of voids and shrinkages than the rest of the alloys.

5) At elevated temperature fatigue tests, the ZA27K revealed a higher resistance to temperature than the M3K and ZA8K.

6) The higher the copper content the higher the tensile and fatigue strengths. This was

demonstrated by comparisons between K1, K2, ZA8K and K3. This, however, can only be achieved at the expense of ductility, which was reduced by increasing the copper content.

7) The fatigue to tensile strengths ratio was very low in the case of ZA27 and ZA27K, but it was reasonable in the cases of the other experimental alloys.

8) The fatigue life prediction formula seems to be adequate in most cases, but it was less adequate in the case of ZA27 and ZA27K which contained a large number of pores and shrinkages with various sizes and shapes.
All the experimental alloys were heterogeneous and contained large numbers of pores. The pores had a large influence in determining the fatigue life of these alloys.

9) There was no significant difference in the fracture topography from either tensile or fatigue samples. Both tests were based on applying tension to the specimens.

10) Due to the limited number of slip sysytems in the cph zinc, there was no alternative for plastic deformation except for twinning. The topographs showed a large number of cleavages due to the twinning mechanism.

11) It seems from the fracture topography of the experimental alloys, that most of the fracture was of ductile nature. This might have looked the case, but the fact is that a small part of the sample had already failed in a brittle manner for a short distance. The remaining part of the sample could not stand any further stressing, therefore it was sheared in a ductile manner.

12) The reason for the large variation in fatigue and tensile strengths of the experimental alloys was due to their microstructure :

η revealed a low strength (Mazak3, M3K)

β revealed a medium strength (ZA8, ZA8K)

α revealed a high strength (ZA27, ZA27K)

There was no difference between the eutectic morphology of Mazak3, M3K and that of ZA8 and ZA8K.The eutectic had low to medium strength.

13) The SEM micrographs revealed no signs of phase transformation which might happen at test temperatures of 100 °C.

14) The metastable phases seen in the TEM micrographs of the experimental alloys are believed to be transitional phases and can be removed by ageing process. The Mazak3, ZA8 and ZA27 alloys were aged for more than 5 years at ambient temperature. In the Mazak3 case, these phases were completely removed. In the ZA8 case, almost 50% were removed. In the ZA27 case almost 10% were removed. It can be concluded that aluminium and copper were very influential in maintaining and delaying the transformation of these phases after ageing.

CHAPTER 8

8.0 Suggestions for future work

1) The present work has established the S/N curves of the experimental alloys at different temperatures up 100 °C. It is necessary at this stage to investigate the fatigue life of these alloys through the fracture mechanics approach.

2) The fatigue tests were conducted by using pull-pull stresses, it is useful therefore to examine the samples under compressive stresses.

3) All the experimental results were based on the as-cast conditions, therefore determination of the mechanical properties (fatigue, tensile) of these alloys would be useful at heat-treated conditions.

4) The experiments were conducted in a normal atmospheric environment. It is advisable to conduct fatigue and tensile tests in a sea water environment and also under vacuum environment.

5) Since the pressure die-casting parameters have a large influence on the microstructure and, hence, on the mechanical properties, it is therefore important to investigate the mechanical properties in relation to die temperature, plunger speed, pressure etc. It is also worthwhile conducting further pressure die-casting practice to eliminate porosity. It is also advisable to produce the experimental alloys by using a hot chamber die-casting machine.

6) The fatigue and tensile fractured surfaces were examined by using the secondary electron microscopes and the back-scattered imaging. It is important to investigate the fracture morphology in relation to the microstructure by using TEM replicas of the fractured surfaces.

7) K1, K2 and K3 alloys were examined by the SEM to study the effect of copper content on the microstructure. The SEM showed that there was no structural difference between these alloys, except for some intermetallic particles ($CuZn_4$) seen in the case of the high copper K3 alloy. TEM work might reveal the differences between these alloys.

REFERENCE

1) H.L.Evans; Met. Ind.(Lond). 1937, 51(5) 105-109; (6) 139-142.

2) H.E.Brauer and W.M.Price; Trans. A.I.M.M.E. 1922, 22 (1) 13 pp.

3) A.J.Murphy 1954. University of Birmingham, Non-Ferrous Foundry Metallurgy.

4) Engineering Properties of Zinc Alloys. Published by Int. Lead Zinc Research Organisation Inc, 2nd., Newyork. 1981.

5) A Technical Data Sheet for Mazak 3 Pressure Die-cast Zinc Alloy Ingot, Mazak Ltd, Bristol, U.K.

6) A Technical Data Sheet for Mazak 5 pressure Die-cast Zinc Alloy Ingot, Mazak Ltd, Bristol, U.K.

7) Mazak Zinc Alloys for Pressure Die-casting. A Booklet for Designers, Mazak Ltd, Bristol, U.K, 1972.

8) R.W.Balliett. Mechanical Properties of Creep Resistant Zinc Die-casting Alloys.Paper No. G575-OB, 8th SDCH Int. Die-casting Exposition and Congress, Detroit, Michigan, March 17-20, 1975.

9) G.D.Sosa, T.Greday and D.Coutsouradis. Les alliages de zinc moules leur resistance au fhiage a chaud et leur agressivite vis-a-vis de l'acier. ATB Metallurgie XXIV, No.3, 253-273, 1984.

10) E.H.Rennhack and G.P.Conard. Creep Deformation of Rolled Zn-Ti Alloys.Trans Metall. Soc. AIME, Vol. 236, 1441-1444, 1966.

11) E.H.Rennhack and G.P.Conard. Structural Aspects of Fibering in Rolled Zn-Ti Alloys and their Relation to Creep. Trans. Metall. Soc. AIME, Vol. 236, 694-698, 1966.

12) E.A.Anderson and G.L.Werkey. A new Zinc Alloy for Gravity-Casting. ILZRO Research Summary, Project ZM-5, July 1962.

13) E.Gervais, H.Levert and M.Bess. Development of a Family of Zinc Based Foundry Alloys. Presented at the 84th Casting Congress and Exposition, and published in the Transactions of the American Foundrymen's Society,

St. Louis, Missouri, U.S.A., April 21-25, 1980.

14) C.A.Loong, E.Gervais and M.Lefebure. Properties and Die-Casting ZA Alloys. Trns.13th SDCE Int. Die-Casting Congress and Exposition, Paper No. G-T85-O55, June 3-6, Milwaukee, U.S.A, 1985.

15) J.Rutherford. ZA.8 Hot-Chamber Die-Casting Alloys and Process Development.Trans.13 th SDCE Int. Die-Casting Congress and Exposition, June 3-6, Milwaukee, U.S.A, 1985.

16) S.Murphy, J.Hill and M.Durman. Creep Behaviour of Commercial Pressure Die-Cast Zinc Alloys. Presented at 12th Int. Pressure Diecaster Conf. Florence, Italy, 1987.

17) C.A.Loong. Temperature and Ageing and Thickness Effects on Die-Casting Alloys. Proc. 25th CIM Conf., 157-170, Toronto, Canada, 1986.

18) W.V.Youdelis and G.W.Dallin. Effect of Magnesium and Copper on the Decomposition Kinetics and Mechanical Properties of Zinc-Aluminium Alloys. Conference of Metallurgists, The Canadian Inst. Mining Metall., Paper 40, University of Toronto, August 28-31, 1966.

19) G.V.Kleshchev, A.M.Yelistratov, A.I.Sheynkman, D.V.Shumilov and V.A.Toldin, (Nature of the metastable states in Al-Zn during ageing), Fiz. tverd tel., 9, 2811-2819 (1967).

20) V.A.Toldin, G.V.Kleshchev, D.V.Shumilov and A.I.Sheynkman, (Generalized scheme of the sequence of metastable phases in alloys Al-Zn), Fiz. metal. metalloved, 40, 1223-1226, 1975.

21) G.A.Kleshchev, V.A.Toldin, I.Sheynkman, D.V.Shumilov, Yu.G. Raspopov and V.N.Panov, (Nature of the metastable states during the ageing of Al-Zn), Izv. vuzov, Fizika, 2, 30-35, 1971.

22) G.V.Kleshvhev, (On the sequence and priority of the metastable states in Al-Zn and Al-Ag Alloys), Auther's abstract of dissertation, Moscow, TSN, IICHM, 1972.

23) G.V.Kleshchev, Yu.G.Raspopov, V.A.Toldin and A.I.Sheynkman, (Influence of small additions of magnesium on precipitation of an equilibrium β phase in Al-Zn alloys), Fiz. metal. metalloved., 33, 653-656, 1972.

24) Metals Handbook, 8th edn, Metals Park, Ohio, 1973. (Amer. Soc.for Metals), Vol.8, p 265.

25) J.A.Belk, Met. Technol., 1976, 3, 161.

26) J.A.Belk, Micron (London), 1974, 5, 201.

27) L.A.Neumeier and J.S.Risbeck. U.S. Bureau of Mines Report of Investigation No. 7538, 1971, p.27.

28) E.Pelzel, Metall, 1954, 8, 83.

29) L.Habraken, G.Crocq, N.Dreulle and A.Hannick, ATB Metallurgie, 1974, 14, 125.

30) M.Hirohashi, E.Kawai, M.Mutsuzaki and M.Miyagawa. J. Jpn. Inst. Met., 1977, 41, 487.

31) E.Gebhardt, Z. Metallkd., 1941. 33. 328.

32) M.L.Fuller and R.L.Wilcox, Trans. AIMME, 1935, 117, 338.

33) V.A.Toldin, A.A.Burykin and G.V.Kleshchev, Phys Metallogr. (U.S.S.R), 1981, 51, 147.

34) K.E.Geary and W.Showak, International Lead and Zinc Research Organisation, Newyork, Contract No ZM-246, Final Report, June 1977.

35) E.Gebhardt, Z. Metallkd., 1946, 37, 87.

36) E.Gebhardt, Metallforschung, 1946, 1, 87.

37) A.Koniger and P.Sahm, Giesserei Technishe Wissenschaftliche Beiheft, 1960, 30, 1673.

38) W.P.Roe and V.R.Friebel, Modern Castings, 1963, 42, 117.

39) V.R.Friebel and W.P.Roe, Modern Castings, 1963, 44, 388.

40)E.A.Anderson, M.L.Fuller, R.L.Wilcox and J.L.Rodda, Trans.

AIMME,1934, 111, 264.

41) K.Lohberg. Rontgenogrphische bestimmug des Losurgsvermogens des zink fur aluminium und kupher. Z. Metallkunde, Vol. 32, 86-90, 1940

42) E.W.Horvick, Trans.SDCE Int. Congr. & Exposition. 9th. 1977, Milwaukee Wisconsin, Paper G-T77-094, p 5.

43) H.Johnen, Metall. 1978, 32, 910.

44) A.M.Zahra, C.Y.Zahra, J.Dutkiewicz and R.Ciach. The influence of Cu and Mg additions on the decomposition of Al-(40% to 50%) wt%Zn alloys during isothermal and continuous heating. Journal of Materials Science 25 (1990) 391-398.

45) E.Wassermann and H.Falke, Z. Metallkd., 1969, 60, 623.

46) E.Trela, Trans. 4th Nat. Die-Casting Congr., 1966, Cleveland, Ohio, Paper 202.

47) M.M.Blouke, N.Holonyak Jr, B.G.Streetman and H.R.Zwicker, J.Phys. Chem. Solids, 1970, 31, 173.

48) C.D.Thurmond and M.Kowalchik, Bell System Tech. J., 1960, 39, 169.

49) P.J.Morell, United States Patent No. 1815479, application field 18 June 1930 (Serial No 462141), patented 21 July 1931.

50) J.C.Fox, Zinc : The Science and Technology of the Metal, Its Alloys and Compounds (ed. C. H. Mathewson), Newyork, 1970 (Hatner Pub. Co), p.423.

51) N.Mykora, Y.H.Zhu and S.Murphy. Solid-State Reactions in Zn-Al Based Alloys. Aston University . Canadian Metallurgical Quarterly, Vol 25, No 2, pp 151-159, 1986.

52) Zinc. The Science & Technology of the Metal, Its Alloys and Compounds. C.H.Mathewson. American Chemical Society Monograph Series No 142.

53) H.Auer and K.E.Mann. Z. Metalk. 1936, 28 (10) 323-326.

54) D.Hanson and M.L.V.Gayler. Further Study of the Alloys of Aluminium and Zinc. J. Inst. Met., Vol. 27, 267-306, 1922.

55) T.Tanabe. Studies in the Aluminium-Zinc System. J. Inst. Met., Vol. 32, 415-453, 1924.

56) T.Isihara. On the Equilibrium Diagram of Aluminium-Zinc System. J. Inst. Met., Vol.33, 73-90, 1925.

57) E.A.Owen and L.Pickup. X-ray Study of Aluminium-Zinc Alloys at Elevated Temperatures. Phil. Mag., Vol. 20, 761-777, 1935.

58) E.C.Ellwood. An X-ray Study of the Constitution of Aluminium-Zinc Alloys of High Purity Above 275°C, with a Description of a New High Temperature X-ray Camera. J. Inst. Met., Vol. 66, 87-96, 1940.

59) E.C.Ellwood. The Solid Solutions of Zinc in Aluminium. J. Inst. Met., Vol. 80, 217-224, 1951-1952.

60) W.L.Fink and L.A.Willey. Equilibrium Relations in Aluminium-Zinc Alloys of High Purity, II. Trans. Amer. Inst. Min. Met. Eng., Vol. 122, 244-265, 1936.

61) M.L.V.Grayler and E.G.Sutherland. The Constitution of Aluminium-Zinc Alloys of High Purity, the Nature of the Thermal Change at 443°C. J. Inst. Met., Vol.63, 123-147, 1938.

62) A.A.Presnyakov, Yu.A Gorban and V.V.Chervyakova. The Aluminium-Zinc Phase Diagram. Russian Journal of Physical Chemistry, Vol.35, No.6, 632-633, 1961.

63) G.R.Goldak and J.G.Parr. A High Temperature X-ray Diffractometer Study of the Zinc-Aluminium System in the Region. 40-75wt% Zinc. J. Inst. Met., Vol.92, 230-233, 1963-64.

64) L.F.Mondolfo. Aluminium Alloys-Structure and Properties, Butterworth, London, 1976.

65) W.B.Pearson. A handbook of the Lattice Spacing and Structures of Metals and Alloys. Vol. 2, Pergamon Press, London, 1967.

66) T.B.Massalski and H.W.King. The Lattice Spacing Relationship in h.c.p. ε and η Phases in the System Cu-Zn, Ag-Zn and Ag-Cd. Acta Met., Vol.10, 1171-1181, 1962.

67) M.Hansen and K.Andreko. Constitution of Binary Alloys. 2nd Ed., McGraw Hill Book Company Inc., USA, 1958.

68) Handbook , Bick & Otham.

69) A.Burkhardt, Z. Metallk. 1936, 28 (10), 299-308 Technologie der Zinklegierungen. Julius Sprnger, Berlin 1940.

70) W.Koster and K.Moeller. Uber den Aufbau und die Volumenanderungen der Zinc-Kupter-Aluminium-Legierungen; I. Die Aufteilung der Konzentrationsebene bei 350°C. Z. Metallkunde, Vol. 33, 278-283, 1941.

71) W.Koster and K.Moeller. Uber den Aufbau and die Volumenanderungen der Zink-Kupte-Aluminium-Legierungen; II. Der Zusammenhang von CuAl mit der ternaren kristallart. Z. Metallkunde, Vol.33, 284-288, 1941.

72) W.Koster and K.Moeller. Uber den Aufbau und die Volumenanderungen der Zink-Kupte-Aluminium-Legierungen; V. Die aufspaltung der ternaren kristallart bei tiefen temperaturen, Z. Metallkunde, Vol. 34, 206-207, 1947.

73) E.Gebhardt, Zeitschrift fur Metallkunde, Vol.32, pp. 78-85, 1940.

74) A.J.Bradley and H.Lipson, Proc. Roy. Soc., (A), Vol. 167, pp. 421-438, 1938.

75) L.A.Willey. Aluminiu-Copper-Zinc. Metal's Handbook, 8th Edition, Vol.8,390-391, American Society for Metals, Ohio, 1973.

76) H.H.Arndt and K.Moeller. Die ternare phase im system kupter-aluminium-zink; I.Der Zerfall der T-phase zwischen 200 und 300°C.Z. Metallkunde, Vol. 51, 596-600, 1960.

77) H.H.Arndt and K.Moeller. Die ternare phase im system kupter-aluminium-zink;II. Das Zustandsgbiet der T-phase oborhalb 500°C. Z. Metallkunde, Vol.51,656-662, 1960.

78) S.Murphy. The Structure of the T' Phase in the System Al-Cu-Zn. Met. Sci., Vol.9, pp.163-168, 1975.

79) S.Murphy. Solid-Phase Reaction in the Low Copper Part of the Al-Cu-Zn System.Z. Metallkunde., Vol.71, pp. 96-102, 1980.

80) W.Koster and K.Moeller, Z. Metallkunde, Vol.33, 278-283, 1941.

81) W.Koster and K.Moeller, Ibid, pp. 206-207 + p. 289.

82) W.Koster, Ibid, Vol.33, p.299, 1941.

83) E.Gebhardt, Ibid, Vol. 33, p.297, 1941.

84) E.Gebhardt, Ibid, Vol. 34, p.208, 1942.

85) A.Gurnier, Solid State Physics, Vol. 9, Academic Press, Newyork, p.294, 1959.

86) G.Borelins, J. Metals, Vol.3, pp. 477-484, 1951.

87) R.D.Garwood, A.L.Davies and G.L.Richards. A transition Phase in the Ageing of Aluminium-Zinc Alloys. J. Inst. Met., Vol. 88, 375-378, 1959-60.

88) G.L.Richards and R.D.Garwood. An Electron-Microscope Study of the Isothermal Decomposition of an Aluminium-25% Zinc Alloy. J. Inst. Met., Vol.93,393-397, 1964-65.

89) W.Merz and V.Gerold. Strukturelle Untersuchungen der ausscheidung in aluminium-zinc-legierungen. Z. Metallkunde, Vol. 57, 607-615, 1966.

90) G.J.C.Carpenter and R.D.Garwood. Hardness Reversion and the Metastable Phase Boundary for G.P.Zones in Aluminium-Zinc Alloys. J. Inst. Met., Vol.94, 301-303, 1966.

91) M.Simerska and V.Synecek. The Mechanism of Stucture Transformations in Supersaturated Al-Zn Alloys. Acta. Metall., Vol.15, 223-230, 1967.

92) G.J.C.Carpenter and R.D.Garwood. The Ageing of a Quenched Aluminium-22.5% Zinc Alloy. Met. Sci. J., Vol.1, 202-211, 1967.

93) M.H.Jacobs. The Morphology of Crystal Structure of a New Precipitate in

Rapidly Quenched Aluminium-Zinc Alloys. Met. Sci. J., Vol.6, 143- 148, 1972.

94) M.Simerska and V.Synecek. The Mechanism of Stucture Transformations in Supersaturated Al-Zn Alloys. Acta. Metall., Vol.15, 223-230, 1967.

95) W.Merz, T.R.Anantharaman and V.Gerold, Phys. Status Solid. Vol.8, K5, 1965.

96) R.P.Wahi and T.R.Anantharaman. Corr. Sci., Vol.38, 1, 1969.

97) V.Ramaswamy, E.D.Butler and P.R.Swann. Direct Observation of Discontinuous Precipitation in Al-28at% Zn. J. Microscopy, Vol. 97, 259-260, 1973.

98) M.Vijayalakshmi, V.Seetharaman and V.S.Raghunathan. Cellular Decomposition in Al-Zn Alloys. Acta Metall., Vol. 30, 1147-1155, 1982.

99) M.Vijayalakshmi, V.Seetharaman and V.S.Raghunathan. Morphological Features of Discontinuous Reactions in Al-Zn Alloys. Mat.Sci. Eng., Vol.52, 249-256, 1982.

100) R.A.Fournelle and J.B.Clark. The Genesis of the Cellular Precipitation Reaction. Metall. Trans., Vol.3, 2757-2767, 1972.

101) P.G.Boswell and G.A.Chadwick. Eutectoid Decomposition of Zn-Al Splat-Quenched and Bulk Specimens. acta. Metall., Vol. 25, 779-792, 1977.

102) D.Cheetham and N.Ridley. Isothermal-Transformation and Directional-Growth Studies on a Zn-Al Eutectoid Alloy, J. Met., Vol.99, 371-376, 1971.

103) R.D.Garwood and A.D.Hopkins. Journal of the Inst of Metals., Vol. 81, 407- 415, 1952-53.

104) A.J.Ardell, K.Nuttal and R.B.Nicholson. Proc. International Conference, University of Manchester, The Metallurgy Committee of the Institute of Metal, pp.22-26, 1966

105) K.Nuttal and R.B.Nicholson. Phil. Mag., Vol.17, pp.1089-1091, 1969.

106) C.Panseri and T.Federighi. Acta. Met., Vol.8, p.217, 1960.

107) L.Huston, J.W.Oahi and J.E.Hillard. Acta. Met., Vol. 14, p.1053, 1960.

108) A.E.W.Smith and G.A.Hare. Journal of the Institute of Metals ., Vol.101, pp 320-328, 1973.

109) V.A.Toldin, A.A.Burykin and G.V.Kleshchev. Natural Ageing of Aluminium-Zinc Alloys with a High Zinc Concentration. Phys. Met. Metall., Vol.45, No.2, 97-100, 1978.

110) V.A.Toldin, A.A.Burykin and G.V.Kleshchev. Influence of Magnesium Additionsof the Phase Sequence During Ageing of Al-Zn Alloys with a High Zinc Content. Phys. Met. Metall., Vol.51, No.1, 116-124, 1981.

111) A.Krupkwski, R.Cach and J.Krol. Decomposition of the a' Phase in the Al-Zn Alloys with 60-78% Zinc. Bulletin De L'Academie Polonaise des Sciences, Vol.115, No.11, 975-979, 1967.

112) W.Truszkowski and J.Dutkiewicz. Bulletin de Lacademie Polonaise des Sciences des Sciences Techniques., Vol.XIX, No.11-12, 1971.

113) E.Gebhardt. Gleichgewichtsuntersuchungen in den systemen zinc-aluminium und zinc-aluminium-kupter. Z. Metallkunde., Vol.40, 136-140, 1932.

114) Y.H.Zhu. Phase Relationships in Zn-Al Based Alloys. Ph.D. Thesis, Aston University in Birmingham, 1983.

115) S.Murphy, N.Mykura and Y.H.Zhu. Solid-State Reactions in Zn-Al Based Alloys. 24th. Ann. Conf. of Metallurgist, CIM, Vancouver-Canada, 1985.

116) W.Koster. Zeitschrift fur Metallkunde., Vol.33, pp.289-296, 1941.

117) A.E.W.Smith and G.A.Hare. Controlling the Zinc-Aluminium Eutectoid Reaction. J. Inst.Met., Vol.101, 320-328, 1973.

118) N.Mykura, S.Murphy and Y.H.Zhu. Volume Change in Ternary Zn-Al-Cu Alloys. Mat. Res. Soc. Proc., Vol.21, 841-846, 1984.

119) Mechanical Metallurgy (H.B), By George.E.Dieter, p. 404, 1976, Mcgrow Hill.

120) Fatigue at High Temperatures (H.B), ASTM. 459, 1968.

121) W.E.Mayo.Microscopic Damage-based criterion for fatigue failure prediction.Int. J. Fatigue.9. No.4. pp. 203-209, 1987.

122) H.J.Gough and W.A.Wood. Deformation and fracture of mild -steel under cyclic stress in relation to crystalline structure. Inst. Mech. Engrs.J and Proc. Vol.141. pp.175-185. 1939.

123) T.Sato and H.Shimda. Evaluation of fatigue crack initiation life from a notch. Int. J. Fatigue.10.No.4. pp. 243-247, 1988.

124) T.H.Topper and M.T.Yu. The effect of overloads on threshold and crack closure. Int. J. Fatigue. 7. No.3. pp.159-164, 1985.

125) W.J.Plumbridge and D.A.Ruder. Metall. Rev. Vol.14. No.136, 1969.

126) International Conference on Mechanisms of Fatigue in Crystalline Solids. Acta. Metallurgica. Vol.11. No.7. p.639, 1963.

127) H.J.Gough. Am. Soc. Test. Mater. Vol.33, pt, 2. pp.3-114, 1933.

128) Metal Fatigue (H.B), By : N.E.Frost, K.J.Marsh and L.P.Pook. p.7, 1974. Clarendon Press, Oxford.

129) G.C.Smith. Proc. R. Soc. London. Vol.142A. pp.189-196, 1957.

130) N.Thompson, N.J.Wadsworth and N.Louat : Phil. Mag. Vol.1. p.113, 1956.

131) Morris.E.Fine. Fatigue Resistance of Metals. Am. Soc.Metals. Campbell Memorial Lecture, 1979.

132) P.J.E.Forsyth and C.A.Stubbington. J. Inst. Met., Vol.83. p.395, 1955-56.

133) W.A.Wood. Some Basic Studies of Fatigue in Metals, in Fracture. John Wiley & Sons. Inc. Newyork, 1959.

134) W.A.Wood, Bull. Inst. Met., Vol.3, pp.5-6, Sept 1955.

135) Fatigue of Metallic Materials (H.B), By : M.Klesnel and P.Lukas. Materials Science Monographs. 7, p.81-83, 1980.

136) D.J.Duquette, M.Gell and J.W.Pitto. Met. Trans. 1, 3107, 1970.

137) N.E.Frost and D.S.Dugdale. The propagation of fatigue cracks in sheet

specimens. J. Mech. Phys. of solids. 6. p.92-110, 1958.

138) H.W.Liu. Crack propagtion in thin metal sheet under repeated loading. Trans. Am. Soc. Mech. Engrs. Series. D. 83, 1961, 23.

139) H.W.Liu. Fatigue crack propagation and applied stress range-An energy approach. Trans . Am. Soc. Mech. Engrs. Series. D, 85, 1963, 116.

140) D.S.Kemsley. Phil. Mag. 2, 131, 1957.

141) D.S.Kemsley. Nature. 178, 653, 1956.

142) The Fatigue of Metals (H.B). The Institution of Metallurgests, London, 1955.

143) H.E.Moore and J.B.Kommers. The fatigue of metals.p.154. Mcgrow Hill, 1927.

144) H.J.Gough and D.G.Sopwith. J. Inst. Met., 49, 93, 1932.

145) W.Weibull. Statistical Representation of Fatigue Failures in Solids. Trans. Royal. Inst.of Tech., Stockholm, No.27, pp.49, 1949.

146) R.P.Singh and A.Gupta. S/N Curve vs Fracture Mechanics Approach to Fatigue Analysis of Steel Jacket Platforms. Int. J. Fatigue. 10. No.1. pp.49-53, 1988.

147) P.C.Paris and G.C.Sih. Stress Analysis of Cracks" Fracture Toughness Testing and its Applications". ASTM. STP.381. pp.30-81, 1965.

148) H.M.Westergaard. "Bearing Pressure and Cracks". Trans. ASME. J. App. Mechs, 1939.

149) S.T.Rolfe and J.M.Barson, ibid. Ref 73. Sec.2.2.

150) A.A.Griffith " The phenomena of rupture and flow in solids. Royal Soc of London, a-221, 1920.

151) C.E.Inglis " Stress in a plate due to the pressure of cracks and sharp corners". Proc. Inst of Noval Architects, 60, 1913.

152) G.R.Irwin " Fracture Dynamics ", in fracturing of metals , Am. Soc. Metals. Cleveland, 1948.

153) E.Orowan " Fracture strength of solids " in report on progress in physics,

Vol. 12, phys. Soc. of London, 1949.

154) G.R.Irwin " Analysis of stress and strain near the end of a crack transversing a plate ". Trans. ASME. J. of Appl. Mechs, 24, 1957.

155) M.A.Miner. J. Appl. Mech. 12, 159, 1945.

156) H.J.Grover, in ASTM Spec. Tech. Pub. 274, p.120, 1959.

157) H.Corten and T.J.Dolan, in Proc. Int. Conf. Fatigue, Inst. Mech. Engrs, p.235. London, 1956.

158) S.S.Manson, A.J.Nachtigal and J.C.Freche. Proc. ASTM.61, 679, 1961.

159) S.M.Marko and W.L.Starkey. Trans. ASME. 76, 627, 1954.

160) D.L.Henry. Trans. ASME. 77, 913, 1955.

161) S.V.Serensen and L.A.Kozlov. Industrial Laboratory. 7 (1958). 1378.

162) A.Buch, T.Seeger and M.Vormwald. Improvement of fatigue life prediction accuracy for various realistic loading spectra by use of cooection factors. Int. J. Fatigue.8.No.3.pp.175-185, 1986.

163) W.Schutz. Problematik der Lebensdauervohersage fur Schwingend beanspruchte Bauteile ' Aluminium 61 No 4, pp.204-208. The prediction of fatigue life in the crack initiation and propagation stages - A state of the art survey '. Engng. Fract. Mech 11 No 2, pp. 405-421, 1979; IC AF Document No 1363.

164) Buxbaum, O.Opperman, H.Kobler, H.G.Shutz, D.Boller. Ch, Henler,P and T.Seeger "Vergleich der lebensdauervorhersage nach dem Kerbgrundkonzept und demNennspannungskonzept ". LBF Bericht. FB-169 (LBF Darmstadt, ERG 1983).

165) Buch, A.Vormwald, M and Seeger, T." Anwendung von Korrektur Facktoren fur die Verbesserung der rechnerischen Lebensdauervorhersage " Fg werk stoffmechanik FF-16/1985 (Technion, Haifa, Israel and Tech Hochschule Darmstadt FRG.

166) Nihei, N, Heuler, P.Boller, ch and Seeger, T. " Damage parameters for

constant strain controlled fatigue data with several levels of mean strain and mean stresses " Fg Werkstoffmechanik Ff-12/1983 (Tech Hochschule Darmstadt, FRG).

167) The Mechanical World., Vol.71-72, 1922, pp.133-134.

168) C.S.Shin and R.A.Smith. Fatigue crack growth from sharp notches. Int. J. Fatigue. 7 No.2, pp.87-93, 1985.

169) D.Morkovin and H.F.Moore." Third Progress Report on the effect of size of specimen on fatigue strength of three types of steel. Proc. Amer. Soc. Test. Mat., Vol.44, pp.137-158, 1944.

170) R.E.Peterson." Methods of correlating data from fatigue test of stress concentration specimens " in contributions of mechanics of solids dedicated to Stephen Timoshenko by his friends on the occusion of his sixtieth birthday anniversary" Macmillan Company, pp.179-183, 1938.

171) J.Morrow, R.M.Wetzel and Topper. ASTM. STP.462, 74, 1970.

172) T.H.Topper et al. J. Mater ., Vol 4, p.200, 1969.

173) J.M.Barson and R.C.McNicol. ASTM. STP. 559, p.183, 1974.

174) S.J.Hudak. Engn. Mater. Tech 103, p.26, 1981.

175) H.Shimada and M.Obata. Tohoku University. Tech. Rep, No 36, p.187, 1971.

176) H.Neuber. Theory of notch stresses : Principles for exact stress calculation, J.W.Edwards. Ann Arbor, Michigan, 1946 (Translation of Kerbspannungslere Grund lagen fur genaue spannungsrechssung).

177) H.F.Moore, S.W.Lyon and N.P.Inglis. Tests of the fatigue strength of cast iron Univ. Ill., Eng. Exp. Sta. Bull. No164, 1927.

178) J.O.Smith. The effect of range of stress on the fatigue strength of metals. Univ. Ill. Eng. Exp. Sta. Bull. No 334, 1942.

179) K.Gunn. The effect of yielding on the fatigue properties of test pieces containing stress concentrations. Aer. Quat., 6, Nov., 1955.

180) G.Forrest. Internal or residual stresses in wrought aluminium alloys and their structural significance. J.Roy. Aer. Soc. April 1954, 58, 261276.

181) M.L.Becker and C.E.Philips. Internal stresses and their effect on fatigue resistance of spring steels, J. Iron Steel. Inst., 133, pp 427-442, 1936.

182) D.Rosenthal and G.Sines. Effect of residual stress on the fatigue strength of notched specimens. Proc. Amer. Soc. Test. Mat . 51, pp.593-608, 1951.

183) H.J.Gough. Fatigue of Metals. Ernest Benn Limited, 1926.

184) H.F.Moore and J.B.Kommers. An investigation of the fatigue of metals. Univ. III. Eng. Exp. Sta. Bull. No 124, 1921.

185) L.Formmer and E.H.Lloyds. The measurement of residual stresses in metals by the X-ray back reflection methodm, with special reference to industrial components in aluminium alloys. J. Inst. Met, 1944, 70, 91124.

186) N.P.Allen and P.G.Forrest. International conference on fatigue of metals . Inst. Mech. Engrs. London 1956, p.327.

187) R.D.McGammon and H.M.Rosenberg. P.R.S., 1957, A 242, 203.

188) N.E.Frost, K.J.Marsh and L.P.Pook. Metal Fatigue (H.B). Oxford Engineering Science Series, 1974.

189) J.G.Tweedale. Mechanical properties of metals, Allen & Unwin, London, 1964.

190) G.Forrest. "The Fatigue properties of aluminium Alloys". Chapter in Metal Fatigue. Chapman & Hall, 189, 1959.

191) R.L.Templin." Fatigue of Aluminium ". Proc. Amer. Soc. Test. Mat. 54, (1954), 641.

192) H.J.Grover, S.A.Gordon and L.R.Jackson.Fatigue of Metals and Structures. U.S. Bureau of Aeronautics (1954). Thames & Hudson, London, 1956.

193) Anon. " Fatigue Properties of Some Noral Wrought Aluminium Alloys ". Aluminium Labs. Ltd. Research Bulletin No. 1 (1952).

194) T.T.Oberg." When Will it Fail ?". Metal Progress 60 (July 1951) 74.

195) J.L.Waisman, L.Soffa, P.W.Kloeris and C.S.Yen." Effect of Internal Flaws

on The Fatigue Strength of Aluminium Alloys ". Nondestructive Testing 16 (1958) 477.

196) C.S.Shin and N.A.Fleck. " Fatigue and Fracture of Zinc Die-casting Alloy " J. Fatigue.11 No 5, pp.341-346, 1989.

197) R.C.Bates and W.J.Jr.Clark. Trans. Quart. ASM 62. 2, p.380, 1969.

198) M.Durman, K.Sawalha and S.Murphy. An Electron Microscopic Study of the Commercial Zinc-based Pressure-die-cast Alloy 3. Mat.Sci & Engineering A 130 (1990) pp 247-256.

199) P.B.Hirschy., A.Howiey., R.B.Nicholson., D.W.Pashley & M.J.Whelan. Electron Microscopy of Thin Crystals, 4th Ed, Butterworths, London, 1971.

200) P.M.Robibson & M.T.Murray. 10th SDCE International Die-Casting Exposition & Congress. Gateway Convention Centre, St. Louis, Missouri, March 19-22, 1979.

201) P.Hassen. Physical Metallurgy, C.U.P. Cambridge, 1978.

APPENDIX

Paper Published in the Material Science & Engineering Journal.

Materials Science and Engineering, A130 (1990) 247-256

An Electron Metallographic Study of the Commercial Zinc-based Pressure-die-cast Alloy 3

MEHMET DURMAN, KAMEEL SAWALHA and SAMUEL MURPHY
Aston University, The Aston Triangle, Birmingham B4 7ET (U.K.)

(Received May 8, 1990)

Pages removed due to Confidentiality reasons

Pages 247 - 255